UNIVERSITÉ CÔTE D'AZUR

ÉCOLE DOCTORALE
SCIENCES FONDAMENTALES ET APPLIQUÉES

THÈSE DE DOCTORAT

Modélisation stochastique de particules non sphériques en turbulence

Lorenzo Campana

Laboratoire CaliSto INRIA

Présentée en vue de l'obtention du grade de docteur
en Sciences pour l'ingénieur **d'**Université Côte d'Azur **et de** INRIA
Dirigée par : Mireille Bossy
Soutenue le : 29 Mars 2022

Devant le jury, composé de :

Sergio Chibbaro	Professeur à l'Université Paris-Saclay, Orsay	Rapporteur
Gabriel Stoltz	Professeur à l'École des Ponts ParisTech, Marne-La-Vallée	Rapporteur
Elisabetta De Angelis	Maître de Conférences, (Reader) à l'Université de Cardiff, Cardiff	Examinatrice
Alain Pumir	Directeur de Recherche CNRS, École Normale Supérieure de Lyon, Lyon	Examinateur
Gautier Verhille	Chargé de Recherche CNRS, Laboratoire IRPHÉ d'Aix-Marseille	Examinateur
Dario Vincenzi	Chargé de Recherche CNRS, Université Côte D'Azur, Nice	Examinateur
Mireille Bossy	Directrice de recherche, Inria - Sophia Antipolis	Directrice de thèse

Inria

ABSTRACT

Stochastic modelling of non-spherical particles in turbulence: The motion of small non-spherical particles suspended in a turbulent flow is relevant for a large variety of natural and industrial applications such as aerosol dynamics in respiration, red blood cells motion, plankton dynamics, ice in clouds, combustion, to name a few. Anisotropic particles react on turbulent flows in complex ways, which depend on a wide range of parameters (shape, inertia, fluid shear). Inertia-free particles, with size smaller than the Kolmogorov length, follow the fluid motion with an orientation generally defined by the local turbulent velocity gradient. Therefore, this thesis is focused on the dynamics of these objects in turbulence exploiting stochastic Lagrangian methods. The development of a model that can be used as predictive tool in industrial computational fluid dynamics (CFD) is highly valuable for practical applications in engineering. Models that reach an acceptable compromise between simplicity and accuracy are needed for progressing in the field of medical, environmental and industrial processes.

The formulation of a stochastic orientation model is studied in two-dimensional turbulent flow with homogeneous shear, where results are compared with direct numerical simulations (DNS). Finding analytical results, scrutinising the effect of the anisotropies when they are included in the model, and extending the notion of rotational dynamics in the stochastic framework, are subjects addressed in our work. Analytical results give a reasonable qualitative response, even if the diffusion model is not designed to reproduce the non-Gaussian features of the DNS experiments.

The extension to the three-dimensional case showed that the implementation of efficient numerical schemes in 3D models is far from straightforward. The introduction of a numerical scheme with the capability to preserve the dynamics at reasonable computational costs has been devised and the convergence analysed. A scheme of splitting decomposition of the stochastic differential equations (SDE) has been developed to overcome the typical instability problems of the Euler–Maruyama method, obtaining a mean-square convergence of order $1/2$ and a weakly convergence of order 1, as expected. Finally, model and numerical scheme have been implemented in an industrial CFD code (*Code_Saturne*) and used to study the orientational and rotational behaviour of anisotropic inertia-free particles in an applicative prototype of inhomogeneous turbulence, i.e. a turbulent channel flow. This real application has faced two issues of the modelling: the numerical implementation in an industrial code, and whether and to which extent the model is able to reproduce the DNS experiments. The stochastic Lagrangian model for the orientation in the CFD code reproduces with some limits the orientation and rotation statistics of the DNS.

The results of this study allows to predict the orientation and rotation of aspherical particles, giving new insight into the prediction of large scale motions both, in two-dimensional space, of interest for geophysical flows, and in three-dimensional industrial applications.

Keywords: Turbulent flows, anisotropic particles, wall shear, Lagrangian stochastic model, numerical scheme for SDEs, weak and strong numerical convergence

RÉSUMÉ

Modélisation stochastique de particules non sphériques en turbulence: Le mouvement de petites particules non-sphériques en suspension dans un écoulement turbulent a lieu dans une grande variété d'applications naturelles et industrielles. Par exemple, ces phénomènes impactent la dynamique des aérosols dans l'atmosphère et dans les voies respiratoires, le mouvement des globules rouges dans le sang, la dynamique du plancton dans l'océan, la glace dans les nuages ou bien la combustion. Les particules anisotropes réagissent aux écoulements turbulents de manière complexe. Leur dynamique dépend ainsi d'un large éventail de paramètres (forme, inertie, cisaillement du fluide). Les particules sans inertie, dont la taille est inférieure à la longueur de Kolmogorov, suivent le mouvement du fluide avec une orientation généralement gouvernée par le gradient local de vitesse turbulente. Cette thèse est axée sur la dynamique de tels objets en turbulence en ayant recours à des méthodes Lagrangienes stochastiques. Le développement d'un modèle qui peut être utilisé comme outil prédictif dans le cadre de la dynamique de fluides numérique (CFD) au niveau industriel est d'un grand intérêt pour les applications concrètes en ingénierie. Par ailleurs, pour progresser dans le domaine de la médecine, de l'environnement et des procédés industriels, il est nécessaire que ces modèles atteignent un compromis acceptable entre simplicité et précision.

La formulation d'un modèle stochastique pour l'orientation de telles particules est tout d'abord présentée dans le cadre d'un écoulement turbulent bidimensionnel avec un cisaillement homogène. Des simulations numériques directes (DNS) sont produites pour guider et évaluer la proposition de modèle. Les questions abordés dans ce travail portent sur la représentation de formes analytiques du modèle, sur les effets des anisotropies inclues dans le modèle, et sur l'extension de la notion de dynamique rotationnelle dans le cadre de cette approche stochastique. Les résultats obtenus avec le modèle, comparés avec la DNS, produisent une réponse qualitative acceptable, même si ce modèle diffusif n'est pas conçu pour reproduire les caractéristiques non-gaussiennes des expériences numériques (DNS).

L'extension au cas tridimensionnel du modèle d'orientation pose le problème de son implémentation numérique efficace. Dans ce travail, un schéma numérique capable de simuler la dynamique d'orientation de telles particules, à un coût de calcul raisonnable, est introduit. La convergence de ce schéma est également analysée. Pour ce faire, un schéma fondé sur la décomposition de la dynamique a été développé pour résoudre les équations différentielles stochastiques (EDS) de rotation de ces particules. Cette décomposition permet de surmonter les problèmes d'instabilité typiques de la méthode Euler–Maruyama; on a ainsi obtenu une convergence en norme L^2 d'ordre $1/2$ et une convergence faible d'ordre 1, comme classiquement attendu. Enfin, le schéma numérique a été implémenté dans un code CFD industriel (*Code_Saturne*). Ce modèle a ensuite été utilisé pour étudier l'orientation et la rotation de particules anisotropes sans inertie dans le cas d'un écoulement turbulent inhomogène, à savoir un écoulement de canal plan turbulent. Cette application dans un cas pratique a permis de mettre en evidence deux difficultés liées au modèle : d'abord, l'implémentation numérique dans un code industriel, ensuite la capacité du modèle à reproduire les expériences numériques obtenues par DNS. Ainsi, le modèle stochastique Lagrangien pour l'orientation de sphéroïdes implémenté dans *Code_Saturne* permet de reproduire, avec certaines limites, les statistiques d'orientation et de rotation de sphéroïdes mesurées dans la DNS.

Cette thèse propose un modèle et son implémentation numérique, permettant de prédire l'orientation et la rotation de particules non-sphériques dans un contexte turbulent, ouvrant ainsi la voie vers une meilleure prédiction des mouvements de tels objets à grande échelle à la

fois dans le cas bidimensionnel (avec des applications dans les écoulements géophysiques) et dans le cas tridimensionnel (avec des applications industrielles).

Keywords: Écoulement turbulent, particules anisotropes, écoulement de paroi, modèles Lagrangiens stochastiques, schémas numériques pour les EDS, analyse de convergence faible et forte

CONTENTS

1 INTRODUCTION

A thorough understanding of the behaviour of two-phase systems, made up by discrete objects as fibres and particles in a wide range of shapes and sizes (polymeric chains, solid particles, droplets or bubbles) in a turbulent fluid flow, is a challenging, open issue of interest for many environmental, biological, physical and industrial processes.

Pollutant transport by atmospheric flows, ice crystals in clouds, colloidal particle dynamics in filtration systems, combustion, design of new material-surface properties, plankton motion in oceans, red blood flow through blood vessels are example of possible applications of two-phase flows. In all of these fields, the knowledge of the complex dynamics of non-spherical particles suspended in a turbulent flow is crucial for any novel device and any technological advancement.

One of the most striking examples of the dispersed two-phase flow is represented by the water cycle (ice, water, vapour), involving several situations, including the air/ocean interface, and the precipitation (evaporation, condensation and formation of clouds and rain). Here droplets in a very wide dimension range, also departing from sphericity, are an example of poly-dispersed two-phase flow. Raindrop size distributions are key elements for a reliable precipitation prediction, and inputs to hydrological and environmental modelling.

A second example of two-phase flow is the dynamics of eruptions and ashes dispersion in the atmosphere. The motion of liquid magma inside the chimney, together with formation of a bubbly regime, and the subsequent stream of hot gases with particles of a large variety in size and shape, represent a vivid illustration of a poly-dispersed multi-phase turbulent flow, whose predictions of the spread in the atmosphere are of utmost importance for air traffic.

A relevant industrial example is brought by boilers used in thermal generation. In a combustion chamber, inert sand and solid fuel or coal particles of different sizes are transported by an injected gas, as we can see in Fig. 1.1 (left panel). Optimal use of the process that guarantees a minimum of pollutants is based on the dynamics of the flow of solid particles inside the boiler, which are separated and eventually reinserted in the cycle. Methods of simulating these processes are really needed to improve the efficiency.

Another field of interest is the cavitation problem, concerning the evolution of bubbles and whether they grow or collapse in the flow, as displayed in Fig. 1.1 (right panel). Severe erosions of turbine blades and propellers can be caused by bubble collapse on the material surface and avoided by in-depth research on the cavitating flow in thermosensitive fluids.

Pumping clogging is equally an ongoing subject of investigation, extensively studied to optimise the geometries for the flow passage that can resist clogging by foreign substances, and in many cases fibrous materials. Due the high cost of testing the anti-clogging performance of pump designs, developing models and performing simulations in industrial codes is highly required.

The disperse two-phase flows show complex phenomena associated to both, transport of particles by fluid motion, and particle-particle interactions. Fluid-particle interactions have the potentiality to modify particle shape, temperature, composition as well as the fluid local Reynolds number, phase and density. Particle-particle interactions can lead to agglomeration or fragmentation in case of solid particles, and to coalescence or break-up of droplets and bubbles. It is easy to imagine that complexity is prone to be afforded by a variety of methods. In fact, the description levels attempted to study turbulent flows in physics span from the microscopic to the mesoscopic and macroscopic scales, greatly differing in the information

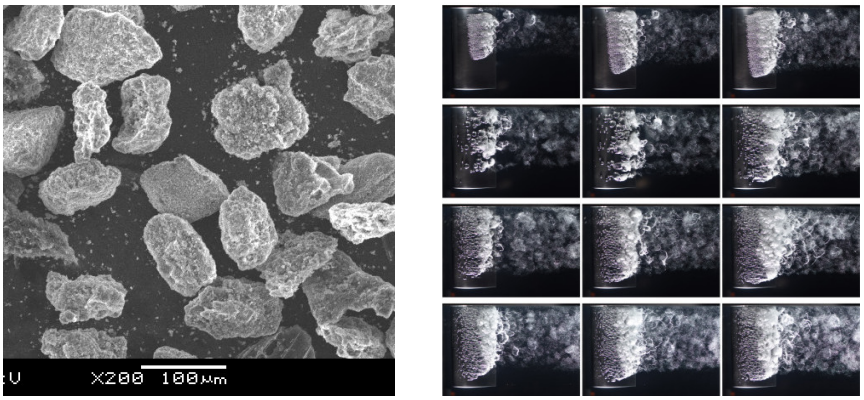

Figure 1.1: Left panel: Example of fly ash particles within boiler's combustion chamber generated by burning the molten pulverized mineral coal in electric power generating plants. Image reproduced from Dong et al. (2013). Right panel: Example of cavitation on marine propeller at different angular speed of the propeller. Image reproduced from van Terwisga et al. (2021).

content, assumptions, kind of description, and techniques developed for data simulation and data analysis.

Using the terminology in the realm of the classical statistical physics, at the microscopic scale, molecular dynamics (MD) has been studied and typical molecular behaviour investigated in terms of global variables of the molecule ensemble, as mean molecular free path or inter-collision time. The mesoscopic level of description is intermediate, and replaces molecular dynamics with stochastic models in which distribution functions carry out particle informations evolving in turbulence. A variety of models as, among the others, the Smoothed Particle Hydrodynamics (SPH) or the Dissipative Particles Dynamics (DPD), Stochastic Rotation Dynamics (SRD), Smoothed Dissipative Particle Dynamics (SDPD), has been worked out. The macroscopic level, finally, supersedes any microscopic information with locally averaged variables, representing very large ensembles of molecules, and is the case treated by the Navier–Stokes equations.

1.1 HYDRODYNAMICAL LEVELS OF DESCRIPTION

Three levels of descriptions are also used in the study of single-phase and disperse two-phase flow turbulence. In this case the classification refers to the degrees of freedom rather than to physical scales. The microscopic approach deals with all degrees of freedom considered in the formulation, while mesoscopic approach applies some form of reduction of variables, and macroscopic models study relations among averaged quantities.

The complete solution of the Navier–Stokes equations corresponds to the microscopic level of description of single-phase turbulent flows, since all degrees of freedom are calculated. Numerical simulations are used to solve the equations (Direct Numerical Simulations, DNS), with appropriate initial and boundary conditions, producing single realisations of the flow, eventually analysed by statistical methods. In principle, it is possible to simulate the degrees of freedom of a fine-grained model relying on the mathematical description of the phenomena through the Navier-Stokes equations. In practice, when a large number of particles moves into a high Reynolds-number flow, the problem becomes rapidly untractable, as the computational time increases approximately with $Re^{11/4}$. Therefore, considering that most of the real life turbulent flows have high Reynolds numbers, variables-reduction techniques have been introduced, and the macroscopic and mesoscopic approaches developed.

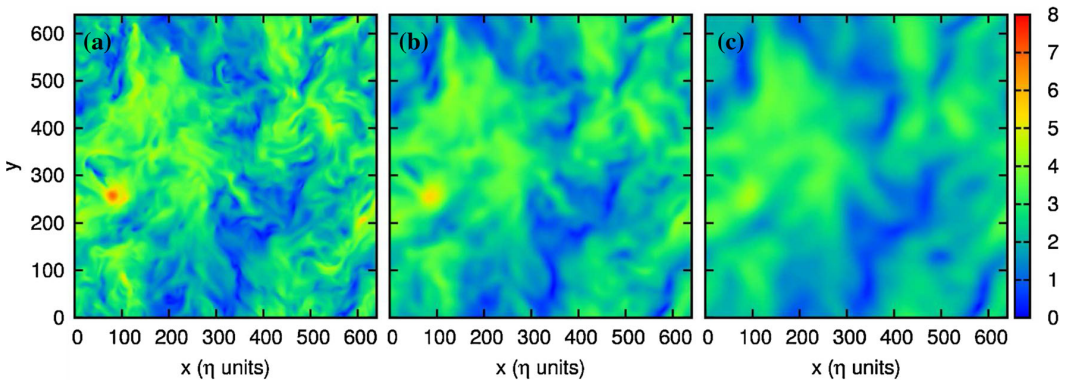

Figure 1.2: Effect of filtering of the flow structures (identified by means of a $2D$ slice of the fluid vorticity) in HIT. In (a) DNS, no filter applied, (b) LES with filter width $\Delta = 5\eta_K$, (c) LES with filter width $\Delta = 10\eta_K$, where η_K is the Kolmogorov length scale. The progressive loss of small-scale details of the flow, which are not felt by the Lagrangian particles as they evolve within the fluid domain, is apparent. Image reproduced from Calzavarini et al. (2011).

The macroscopic level deals with mean-flow equations, as conceived in the fundamental work of Reynolds in 1894. The Reynolds-averaged Navier-Stokes (RANS) approaches provide insights on the mean-flow evolution, sensitive mostly to the geometry of the flow domain, boundary and external conditions. In RANS, flow variables are split into mean and fluctuating parts using Reynolds-decomposition. The insertion of decomposed variables into the Navier-Stokes equations, followed by an averaging, gives rise to the closure problem of Reynolds-stress tensor. RANS models are widely used in industrial applications where the geometry and physics of the problem are complicated, and the averaged flow variables are helpful to characterise the system.

Mesoscopic approaches address more particle-turbulence interaction details than mean values treated by the RANS. Simulations of particle interactions with fluid fields are grid-based and characterised by a mesh-length determining the spatial resolution of the model. Deterministic and stochastic components are both present, with the stochastic contribution obtained from direct simulation of large-scale processes. Filtering functions are used by the large-eddy simulations (LES) to define the spatial grid. Large scale motions, on the scale of the mesh-length, are explicitly treated while the others are modelled by sub-grid scale (SGS) fields description. A visualisation of LES spatial filtering effects is provided in Fig.1.2, which shows the impact on the flow structures in homogeneous isotropic turbulence for different filter widths. The underlying concept is that only SGS interactions, in the inertial and dissipative regime, are universal and prone to be modelled. LES constitutes nowadays a widespread technique, with affordable computational costs and good predictivity, including statistical fluctuations pertaining to the large-scale phenomena. LES is well suited to study those practical applications with shear-dominated flows and turbulence reacting by large-scale mixing, where the simulation of statistical properties on large-scales is really relevant.

Alternative mesoscopic models, which lies in between DNS/LES and RANS methods, have been developed with the purpose to reintroduce information on the whole range of fluctuations. These approaches are referred to as PDF and FDF methods, where their name derive from the information that they produce, which indicates that they aim at simulating the probability density function (PDF) and the filtered density function (FDF). Compared to the previous approaches, they are formulated in terms of particle systems where stochastic models are used to represent the evolution of the instantaneous variables attached to each particle. Although the interest of these methods is marked for scalar variables when single-phase reactive flows are

involved, in the following we essentially concentrate on the dynamical variables which are the positions and velocities of a large number of fluid particles. Central to these methods are the *stochastic Lagrangian models*, which involve new concepts and require additional mathematical tools. The mathematical background comes from the concepts of *diffusion processes* and *stochastic differential equations* (SDE). One of the simplest Lagrangian stochastic models is the *Langevin equation*, which provides a model for the velocity following the motion of a fluid particle. These methods are commonly used for predicting the disperse two-phase flows since the Lagrangian point of view seems a natural choice when an ensemble of 'real' particles are embedded in a flow.

1.2 OUTLINE OF THE THESIS

The goal of this thesis is to study the dynamics of small non-spherical particles suspended in a turbulent flow which is relevant to many natural and industrial processes, ranging from the deposition of aerosol in respiratory organs and the motion of red blood cells travelling through blood vessels, to plankton dynamics in ocean, ice-crystal formation in clouds, combustion systems, distribution of cellulose fibres in paper, and pulp industry.

In particular my interest focuses on the modelling of the dynamics of non-spherical particles in turbulence by means of the stochastic Lagrangian approach. The dissertation starts with a brief *excursus* on most intriguing results concerning particles with non-spherical shape and on recent advances in their modelling. Firstly, a coarse-grained stochastic model to describe the dynamics of non-spherical particle is introduced. In two-dimensional case, analytical results are discussed against DNS. Secondly, a numerical scheme for the model, extended to the three-dimensional case, is developed and examined by investigating its numerical convergence. Finally, the model is implemented in an industrial CFD code (*Code_Saturne*), where both, modelling challenges, and numerical issues are faced. Indeed, the behaviour of both, the physical model and its numerical scheme are examined in the practical context of a turbulent channel flow.

General context and motivations

In Chapter 2, an overview on the motion of small ($\simeq$ Kolmogorov length) non-spherical particles in turbulence is presented. Moreover, a short review on stochastic modelling approaches for small turbulent scales and their coupling with non-spherical particle dynamics is given. Anisotropic particles react on a turbulent flow in complex ways which depend on a wide variety of parameters, with great emphasis in literature on particle shape, inertia and fluid shear. Inertialess particles, with a size smaller than the Kolmogorov length, behave as tracers which passively follow the fluid motion and assume an orientation $\boldsymbol{p}$ which preferentially samples certain directions defined by the local turbulent velocity gradient. This picture, already quite intricate in the homogenous isotropic turbulence (HIT), becomes even more difficult to treat in a turbulent channel due to the presence of near wall structures. When inertial particles are considered, the preferential alignment changes from tracers, becoming as inertia increases, less and less impacted by the fluid velocity gradient tensor. Furthermore, preferential alignment causes the non-spherical particles to tumble and to spin, characterising their rotational dynamics. Despite the advances in the studies of preferential alignment and rotation using direct numerical simulation (DNS) in HIT and wall turbulence, the modelling of small scale turbulence dynamics still remains an open issue. In fact, the orientation and rotation of non-spherical particles are strongly affected by turbulent structures in the viscous range which are not directly accessible by fluid modelling approaches.

From DNS perspective, computer simulations are widely used to understand and improve the description of the complex dynamics of such processes. However, due to the limitations in computational power, a wide range of approaches have been developed for particle dynamics in turbulent flows, related to the multi-scale character of the problem. These models, that have been developed for different purposes, present various levels of description and information content. At fundamental hydrodynamic level, DNS have been largely used to get access to a microscopic level of description by capturing all the information about the fluctuations in space and time. Conventionally, DNS have been performed to characterise the dynamics of non-spherical particles in reduced settings such as limited domain size, simple geometry, small number of particles and moderate Reynolds number. Conversely, from a macroscale point of view, our aim is to develop a model that can be used as a predictive computational tool in CFD codes. In this framework, the fluid phase is modelled by a small set of statistical mean fields which are described by Reynolds averaged Navier–Stokes (RANS) models. Meanwhile, the dispersed-phase, composed by solid particles, is modelled by a set of stochastic differential equations (SDEs) describing their dynamics. In this context, we propose an SDE which models the orientation of an axisymmetric ellipsoidal inertialess particle in turbulent shear flows that can be coupled to classical Lagrangian stochastic models.

Dynamics of rigid fibres in two-dimensional shear flow

Non-spherical particles transported by an anisotropic turbulent flow preferentially align with the mean shear and intermittently tumble when the local strain fluctuates. In Chapter 3, such intricate behaviour is studied for inertialess, rod-shaped particles embedded in a two-dimensional turbulent flow with homogeneous shear. We start by developing a Lagrangian stochastic model for the rods angular dynamics and its results have been compared with DNS ones. The model consists in superposing a short-correlated random component to the steady large-scale mean shear, and can thereby be integrated analytically. To reproduce the single-time orientation statistics obtained from DNS, it is found that such approach has to properly account for the effect of the mean shear onto the Lagrangian statistics of the turbulent velocity gradients. This leads to include anisotropic correlations in noise fluctuations by measuring an effective correlation tensor for the velocity gradient fluctuations from DNS data. The model is calibrated by introducing a tuning parameter which has the effect of rescaling in time the diffusion part with respect to the drift one, and the results are compared with DNS. Then, the model is used to address the two-time statistics of the rods orientation. Besides, to extend the notion of rotation rate statistics, an alternative definition with respect to what has been previously investigated in DNS literature under the notion of 'tumbling rate' has been proposed. It allows to identify the mode of rotation in the stochastic model. Indeed, the tumbling rate can be associated to the stationary probability flux of the rods unfolded angle. While the complex behaviour observed in the DNS indicates a stretched-exponential tails in the probability distribution of the unfolded angle in a diffusive regime, the diffusion model gives a reasonable qualitative response, even if it is not designed to reproduce the characteristics of the Lévy walk.

Lagrangian stochastic model: an efficient numerical method

Chapter 4 focuses on studying and developing a semi-implicit splitting numerical method to integrate in time the non-linear SDE which forms the particle's orientation model in three dimensional case. Moreover, in the same spirit of Chapter 3, an alternative definition of the rotational modes of a non-spherical particle in three dimensions has been introduced for the stochastic model and its numerical convergence has been analysed. Interestingly, the solution of the SDE is constrained to stay on a manifold $SO(3)$ which arises a significant issue whether

or not this geometric constraint is preserved by the numerical scheme used. Classical Euler–Maruyama method commonly fails to converge with optimal rate or eventually diverges, when coefficients have non-bounded first derivative (i.e., globally Lipschitz condition fails). This last scenario includes the SDE orientation model, that involves polynomial coefficients. Thus, specific numerical methods need to be tailored for this problem. We construct a scheme by using the splitting decomposition of the SDE. The numerical scheme is shown to be mean-square convergent of order 1/2 and weakly convergent with order 1, pointing the ability of the proposed method to preserve the geometric features with a reasonable computational cost. Moreover, the long time behaviour has been analysed by observing the marginal probability density functions in time. These converge to the invariant measures which have been derived analytically. In the last part of the work, the model and its numerical scheme is illustrated in a semi-real applicative case by considering the non-spherical particles embedded in a homogeneous shear flow.

Dynamics of inertialess spheroids in a channel flow

The aim of Chapter 5 is to experiment the stochastic Lagrangian model previously developed and to study the orientational and rotational behaviour of inertialess non-spherical particles in a turbulent channel. Whereas the translational motion of non-spherical particles is controlled by the turbulent motion at large scales, rotational motion is determined by the fluid velocity gradient tensor, at small scales. The latter poses a modelling challenge when predicting the rotational dispersion of non-spherical particles by means of an hybrid Eulerian/Lagrangian PDF method. This is due to lack of information on the velocity gradient tensor, which is dominated by the turbulence structure in the viscous range. The proposed stochastic model in Chapter 3 and its numerical scheme discussed in Chapter 4 have been implemented in an industrial CFD code (*Code_Saturne*) and detailed comparisons with DNS are carried out. Indeed, this last part of the work represents the bridge between two different issues of the modelling: the first concerns whether and to which extent the model is able to reproduce (features of the) 'reality'; the second is about its numerical implementation within an industrial code framework. Moreover, a detailed statistical investigation on the orientation and rotation has been performed by considering the mean-field information by filtering the DNS dataset, which can be treated as a 'perfect' RANS providing finer details on time-filtered DNS trajectories, as well as on the mean velocity gradient tensor in the buffer layer. The DNS results indicate that, similarly to earlier studies, rod-like particles preferentially align their symmetric axes parallel to the wall, whereas disk-like particles were normal to the wall.

The shape-dependence of the particle orientations affects their rotation where two qualitatively different modes of rotations are found, at the centre and near the wall, respectively. The stochastic differential equation (SDE) model for the orientation reproduces, with some limits, the orientation and rotation statistics out of the viscous layer employing 'perfect' RANS approach. Conversely, for the RANS case, results are less close to DNS, due to its limit to reproduce the mean-field above the turbulent log-layer. The aforementioned findings reveal the time-reversal invariance of the model that constitutes a major limit of the model for accurately reproducing the distinctive behaviour of rod- and disk-like particles.

2 NON-SPHERICAL PARTICLES IN TURBULENCE

Outline. In this chapter we present an overview about the motion of small ($\simeq$ Kolmogorov length) non-spherical particles in turbulent flows. There is a vast literature about this, since the study of the dynamics of such particles is relevant in many natural and industrial applications. Non-spherical particles interact with turbulent flows in a complex way, depending on a wide variety parameters; namely their shape, inertia and fluid shear. We will discuss about how the orientation and rotation dynamics of both inertial and inertialess particles can be described, for the particular case of spheroidal particles. Then, we will investigate how the preferential orientation is affected by the turbulent velocity gradient in homogeneous and inhomogeneous turbulent flows, as well as the associated rotational rate statistics. To conclude, we will list existing stochastic modelling approaches for non-spherical particles in turbulence and their importance in order to make the study of orientation accessible within the industrial framework.

2.1 INTRODUCTION

The investigation of aerosol transport processes has attracted considerable attention since they are relevant for the understanding and for the optimization of many environmental and industrial applications. Industrial processes include the combustion of pulverised solid fuels (Stein et al. (2013), polymers processing (Jarecki et al. (2012)), molding of fibre-reinforced composites (Yashiro et al. (2012)) or colloidal particles deposition/resuspension for filtration systems, as well as spray cooling processes (Henry et al. (2012)). Aerosol transport is also affecting natural phenomena, including dust storms (Lu and Shao (2001)), ice-crystal in clouds (Pinsky and Khain (1998); Korolev et al. (2003)) or plankton in the oceans (Jumars et al. (2009); Guasto et al. (2012)). These examples are only few of the fields in which the knowledge of particle dispersion plays a crucial role. Such kind of flows (referred to as polydispersed two-phase flows), are made of discrete particles (solid particles, droplets, bubbles), all having a wide range of sizes and shapes embedded in a turbulent fluid flow.

The particles behaviour is expected to be affected by their size and shape, deformability, translational/rotational diffusivity, collision rate, aggregation or fragmentation, electrostatic force and gravitational acceleration (Minier (2016)). Most of the works on particle dispersion in fluids deals with idealized spherical particles (Balachandar and Eaton (2010)); however, as one can expect, most natural and industrial solid aerosol particles are non-spherical. The shape and orientation of particles can affect industrial processes, as in papermaking where mechanical properties are regulated by the alignment of the cellulose fibres in the pulp (Lundell et al. (2011)), or in the case of fractal soot emitted by combustion engines, where shape and orientation determine the radiative properties of the aerosols (Moffet and Prather (2009)). The non-spherical shape plays an important role in the study of the dispersion of pollen and seeds (Sabban et al. (2017)), the dynamics of ice clouds (Heymsfield (1977)), the lifecycle of diatom plankton (Musielak et al. (2009)) and sediment transport in rivers (Vercruysse et al. (2017)). Moreover, the addition of fibres in a fluid flow can significantly alter the suspension rheology (Butler and Snook (2018); Daghooghi and Borazjani (2015)).

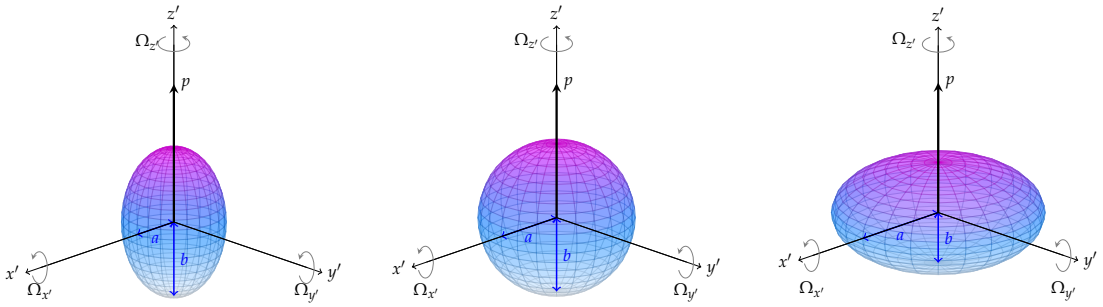

(a) Prolate (b) Sphere (c) Oblate

Figure 2.1: Sketch of spheroid shapes used to investigate the dynamics of anisotropic particles with $\boldsymbol{p}$, the unit vector along their symmetric axis, and their possible rotations. In (a) prolate ellipsoid with $\lambda > 1$ corresponds to rigid rod; (b) spherical particle with $\lambda = 1$ and (c) oblate ellipsoid with $\lambda < 1$ corresponds to rigid disk. The *tumbling* motion is referred to the rotations $\Omega_{x'}$ and $\Omega_{y'}$; the *spinning* motion is referred to the rotation $\Omega_{z'}$.

Beyond the complexity of turbulence and two-phase flow with spherical particles, which is already a challenging problem to solve, the motion of non-spherical particles in turbulent flows is even more intricate, due to their rotational dynamics that is already complicated in simple laminar flows. The presence of turbulence makes the problem even more challenging, with forces and torques that vary according to the particle orientation. In particular, within this intriguing framework, we want to focus our attention on a crucial issue for non-spherical particles in turbulence: the investigation of translation, orientation and rotation of small spheroidal particles at low concentration in turbulent flows. We are going to assume that the suspension of spheroidal particles is diluted, with particle size smaller than the Kolmogorov length scale. In other words, we are considering a *one-way coupling* where the feedback from spheroidal particles on the fluid phase is ignored and particle-particle collisions neglected.

It is worthwhile to mention that the assumption of small spheroidal particle is fundamental to justify point-particle approach, since when particles have at least one dimension larger than the Kolmogorov length scale, they interact with the non-linear spatial variation of the velocity field. Conversely, large particles have been studied with particle-resolved approach (Tenneti and Subramaniam (2014)). The exception is the slender rod limit, for which Olson and Kerekes (1998) and Shin and Koch (2005) develop expressions for the response of a thin fibre to a spatially varying velocity field.

A spheroid, i.e. an axisymmetric ellipsoid, is often adopted as a model of non-spherical particle, nonetheless many others shapes have been considered, we refer to Jeffery (1922); Bretherton (1962); Brenner (1963); Harris and Pittman (1975); Chevillard and Meneveau (2013), to name a few. Any spheroid shape is parametrised by a single aspect ratio $\lambda = b/a$, defined as the ratio of the distance from centre to the pole along the symmetry axis b and the equatorial radius of spheroids with semi-axis a. The aspect ratio $\lambda > 1$ corresponds to a prolate spheroid or fibre (Fig. 2.1a), $\lambda = 1$ to a sphere (Fig. 2.1b) and $\lambda < 1$ corresponds to an oblate spheroid or disk (Fig. 2.1c). The rotations of axisymmetric particles are naturally decomposed into a component along the symmetry axis, called *spinning*, and components perpendicular to the symmetry axis, called *tumbling* (see Fig. 2.1).

The study of non-spherical particles suspended in a viscous fluid flow has been a topic for research through many decades. The case of an ellipsoidal particle immersed in a creeping viscous fluid was studied by Jeffery (1922). In addition, analytical work on particles of different shapes has been investigated by Brenner (1963, 1964a) and a general monograph on the subject has been provided by Happel and Brenner (1973). All these different analytical studies assume

Stokes flow conditions around the particles, i.e. particles are assumed small enough so that inertial effect and rotational diffusion can be neglected. Many researchers have subsequently extended these works to study non-spherical particle suspensions in more general terms, considering inertial effects and turbulent flow. For example, Karnis et al. (1963, 1966) observed that at large Reynolds number, inertial effects become significant, so that the behaviour of non-spherical particles differs from the Jeffery's theory.

Inertialess and inertial particles imply a different treatment of the problem, leading to a distinct kind of dynamics. In general, solid particles are usually identified by a characteristic particle response (or relaxation) time τ_p, which is the response of the particle to perturbations produced by the underlying turbulence, and the flow Reynolds number. The particle Stokes number, St, is then the ratio of the particle response time τ_p, to a characteristic time of the flow, τ_f. This relaxation time for a spheroidal particle depends on the particle shape and can be expressed analytically (Shapiro and Goldenberg (1993)) for either oblate or prolate spheroids as a function of particle aspect ratio (λ). Conversely, for inertia-free particles ($St = 0$) the relaxation time τ_p is much shorter than the shortest time scale of turbulence, i.e. the Kolmogorov time scale τ_η, and the particle responds almost immediately to turbulent fluctuations. Such inertia-free particles are often referred to as *tracers* since they passively translate along with the flow.

In general, turbulent dispersed flows are characterised by a wide range of length- and time-scales that bring to a possible classification according to different levels of descriptions (or information contents). Details span from *microscopic* to *macroscopic* levels, with a possible intermediate step constituted by *mesoscopic* descriptions (Fox (2012)).

In principle, all levels of coupling between particles and fluid can be applied to the three different approaches for the description of turbulence. Firstly, the *microscopic* approach deals with all details of the flow around each particle and resolves all scales of fluid motion up to the Kolmogorov scale by means of direct numerical simulations (DNS). Secondly, the *mesoscopic* description resorts to a filtered fluid velocity, as in large-eddy simulations (LES). In this case, the fluid velocity at the particle position is not exactly known, being replaced by its filtered value. Finally, the *macroscopic* approach, giving a statistical description of the fluid flow, is employed, based on the Reynolds-averaged Navier-Stokes equation (RANS) and additional models for the effects of the turbulence on the particles need to be developed.

Alternatively, at either *mesoscopic* or *macroscopic* level, Lagrangian stochastic models can be used for both, single-phase, and dispersed two-phase turbulent flows (Minier and Peirano (2001)). These approaches are referred to as PDF (Probability Density Function) methods, since pdfs of relevant variables are simulated, giving a statistical description of either single- and two-phase flows. Moreover, for the dispersed two-phase flows, Lagrangian stochastic models have been developed in the context of RANS, and also used within LES framework for extending predictivity to particle dynamics.

Following the growing interest in the subject, different physical and numerical modelling approaches have been used to study the motion of non-spherical particle in various flow fields. A modern exhaustive review of these models used to describe non-spherical particles motion, alongside with numerical and experimental methods for measuring particle dynamics, has been done by Voth and Soldati (2017).

Direct numerical simulations have been largely used to study many aspects of the motion of non-spherical particles in turbulent flow. In particular, a wide range of classes of spheroids (in terms of their aspect ratio) have been considered using this approach, where the particles are characterised either by the presence of inertia (quantified by the particle relaxation time τ_p) or by the absence of inertia, and both are transported in flows with different levels of turbulence.

The dynamics of tracers spheroidal particles in homogeneous isotropic turbulence (HIT) has been subjected to several numerical studies (Shin and Koch (2005); Pumir and Wilkinson (2011); Chevillard and Meneveau (2013); Gustavsson et al. (2014); Ni et al. (2014); Byron et al. (2015)).

Moreover, tracers particles were investigated by Challabotla et al. (2015b) and Zhao et al. (2015) in turbulent channel flow. On the other hand, the majority of the literature on the dynamics of inertial spheroidal particles has been performed in turbulent channel flow (Mortensen et al. (2008); Marchioli and Soldati (2013)).

At the same time, a wide variety of experimental measurements have been developed for determining the motion of non-spherical particles. The full motion has been studied by Marcus et al. (2014), where they measure the orientation and rotation of spheroidal particles across a range of aspect ratio in the HIT framework. Conversely, with respect to inhomogeneous flows, Carlsson et al. (2010a) provide some measurements on fibre orientation in the bulk and near wall regions of headbox geometry relevant to the paper industries.

Currently, fully resolved simulations in multiphase flows (based on DNS approach for the fluid and Lagrangian particle tracking for the solid particle phase) are computationally expensive approaches. Indeed, these methods are not designed to handle suspensions of a large number of small finite size particles, as often met in engineering applications, and as required to obtain reliable particle statistics in a turbulent flow environment. Among very practical applications, Asgharian and Anijilvel (1995) analysed the deposition of fibres in human and rat airways developing an empirical formulation of the problem. Moreover, more analytical work has been done by Tian et al. (2012) using commercial CFD software to study low Reynolds number flows in a circular duct reporting that the particle aspect ratio, different size of particles and particle-to-fluid density ratio, all these situations significantly affect the transport and deposition of non-spherical particles. A similar kind of investigation at a high shear Reynolds number, with an approach based on LES to predict a fully developed solid-gas flow in a channel geometry has been conducted by Njobuenwu and Fairweather (2015, 2016).

This chapter is organised as follows: Section 2.2 reports the two different mathematical models largely used to describe the orientation and rotation dynamics of inertial and inertialess spheroidal particles, respectively. Furthermore, an alternative approach to describe the orientation dynamics of non-spherical tracers particles is provided. In Section 2.3, the preferential orientation in homogeneous and inhomogeneous turbulent flows will be discussed. Section 2.4 presents the rotation rate statistics associated to the rotational dynamics and their strong dependence on aspect ratio. Section 2.5 highlights the statistical models used to describe the behaviour of non-spherical particles in turbulence and their importance in order to make accessible the study of orientation within the industrial framework. These models are strictly related with the stochastic models for the velocity gradient tensor, for which we will list a small existing literature. Conclusions are reported in Section 2.6.

2.2 EVOLUTION EQUATIONS FOR ANISOTROPIC PARTICLE ORIENTATION

While different models are used to describe particle translation and rotation in turbulent flows, here we intend to focus our attention on two models among the others, by considering as entering parameters the particle shape and particle relaxation time; clearly the latter does not enter in the inertialess model.

The motion of rigid fibres in a turbulent flow is commonly studied through an Eulerian-Lagrangian approach (Balachandar and Eaton (2010)). The Eulerian formulation of the fluid phase is governed by the mass and momentum conservation equations (incompressible Navier–Stokes equations). In addition, the presence of the fibres is assumed not to affect the underling flow, i.e. there is no reaction force from the fibres in the fluid. Therefore, the fluid particle system is one-way coupled and we consider only dilute fibre suspensions. The particle phase is represented in the Lagrangian framework, and fibres are modelled as point-wise spheroidal particles given that their size is considered smaller than the Kolmogorov length scale.

2.2.1 *Inertial particles*

The mathematical model for the inertial fibres has been derived from the methodology outlined by Zhang et al. (2001) and subsequently adopted by Mortensen et al. (2008). The translational and rotational motion of a single inertial fibre (in subscript p) of mass m_p is governed by the kinematic and dynamical equations of rigid-body, in vector form:

$$\frac{d\mathbf{X}_p}{dt} = \boldsymbol{u}_p, \tag{2.1}$$

$$m_p \frac{d\boldsymbol{u}_p}{dt} = \boldsymbol{F}_D, \tag{2.2}$$

$$\frac{d(\boldsymbol{I}' \cdot \boldsymbol{\Omega}'_p)}{dt} + \boldsymbol{\Omega}'_p \times (\boldsymbol{I}' \cdot \boldsymbol{\Omega}'_p) = \boldsymbol{N}'. \tag{2.3}$$

Equation (2.2) is written in the inertial frame of reference ($\boldsymbol{x} = (x, y, z)$) and Eq. (2.3) is formulated in the fibre frame ($\boldsymbol{x}' = (x', y', z')$); $\boldsymbol{I}'$, $\boldsymbol{\Omega}'_p$ and $\boldsymbol{N}'$ represent the moment of inertia tensor, the angular velocity of the particle and the torque in the fibre frame, respectively. The expressions for the torque on prolate and oblate spheroids can be found in Challabotla et al. (2015a). For non-spherical particles, the drag force, $\boldsymbol{F}_D$ can be expressed as

$$\boldsymbol{F}_D = \mu \, \boldsymbol{Q}^{\mathsf{T}} \boldsymbol{K}' \boldsymbol{Q} \left(\boldsymbol{u} - \boldsymbol{u}_p \right), \tag{2.4}$$

where μ is the kinematic viscosity of the fluid and $\boldsymbol{u}$ is the fluid velocity at fibre position. Finally, $\boldsymbol{K}'$ is the resistance tensor for spheroidal particles (Brenner (1964b); Challabotla et al. (2015a)). The orthogonal transformation matrix $\boldsymbol{Q}$ converts particle coordinates to the co-moving frame ($\boldsymbol{Q}^{\mathsf{T}}$ is its transpose).

From a numerical perspective, the matrix $\boldsymbol{Q}$ has been expressed in terms of four Euler parameters, and its time evolution was solved using rigid-body kinematic equations (e. g., Zhang et al. (2001); Mortensen et al. (2008); Marchioli et al. (2010)). Moreover, the associated numerical scheme to solve the Eq. (2.2) in terms of Euler parameters uses a fourth-order Runge–Kutta scheme, while Eq. (2.3) is solved using a mixed explicit-implicit differencing procedure developed by Fan and Ahmadi (1995), which is specifically tailored for solving stiff ordinary differential equations. The method has been ameliorated by Zhao and Van Wachem (2013a), using quaternions dynamics by removing the need to explicitly compute the transformation matrix $\boldsymbol{Q}$, improving numerical efficiency.

2.2.2 *Tracers particles*

For a small tracer particle with size smaller than the Kolmogorov length scale η_K, the local flow around the particle can be considered inertia-free and Stokes flow solutions can be used to relate the rotational dynamics of the particle to the local velocity gradient tensor. The problem was afforded by Jeffery, who considered spheroids, showing that particle shape enters in the orientation dynamics through the shape parameter Λ (Jeffery (1922); Bretherton (1962)),

$$\Lambda = \frac{\lambda^2 - 1}{\lambda^2 + 1}. \tag{2.5}$$

The shape parameter Λ takes values in the range $[-1, 1]$, with $\Lambda = -1$ corresponding to infinitely thin discs ($\lambda \to 0$), $\Lambda = 0$ to spherical particles and $\Lambda = 1$ to infinitely elongated rods ($\lambda \to \infty$).

Following reference (Monin and Yaglom (2013)), we can define a mapping between Eulerian and Lagrangian coordinates $\mathcal{M}_{t_0,t} : \boldsymbol{x}^0 \in \mathbb{R}^3 \to \mathbf{X} \in \mathbb{R}^3$, where $\mathbf{X}(t; \boldsymbol{x}^0, t_0)$ denotes the position

at time t of a fluid particle which was at the position $\mathbf{X}(t_0; \boldsymbol{x}^0, t_0) = \boldsymbol{x}^0$ at the initial time t_0. Given the initial position of a fluid particle, this mapping is fully defined at any time by

$$\frac{d\mathbf{X}}{dt} = \boldsymbol{u}(\mathbf{X}, t). \tag{2.6}$$

Then, the orientation $\boldsymbol{p}$ of a spheroidal tracer particle with a shape parameter Λ owning a centre of mass velocity that matches the fluid velocity at the particle position, is described by the Jeffery's equation (Jeffery (1922)),

$$\frac{d\boldsymbol{p}}{dt} = \boldsymbol{O}\,\boldsymbol{p} + \Lambda\left(\boldsymbol{S}\,\boldsymbol{p} - \boldsymbol{p}\,\boldsymbol{p}^{\mathsf{T}}\,\boldsymbol{S}\,\boldsymbol{p}\right), \tag{2.7}$$

where $\boldsymbol{S} = (\boldsymbol{A} + \boldsymbol{A}^{\mathsf{T}})/2$ is the rate-of-strain tensor, and $\boldsymbol{O} = (\boldsymbol{A} - \boldsymbol{A}^{\mathsf{T}})/2$ is the rate-of-rotation tensor which are the symmetric and antisymmetric part of the velocity gradient tensor $A_{ij} = \partial u_i/\partial x_j$ along its Lagrangian trajectory. Equation (2.7) is valid for axisymmetric particles, and it has also been extended (new derivation) to tri-axial ellipsoid by Junk and Illner (2007).

The first term on the right-hand side of Eq. (2.7) denotes the rotation rate caused by the vorticity and the second term denotes the rotation rate caused by the strain, where the elongation of $\boldsymbol{p}$ due to the contribution of $\boldsymbol{S}$ is subtracted by the non linear term $\boldsymbol{p}\,\boldsymbol{p}^{\mathsf{T}}\,\boldsymbol{S}\,\boldsymbol{p}$, such that the orientation vector $\boldsymbol{p}$ is constrained to be a unit vector.

From a numerical point of view, in DNS, Eq. (2.7) is integrated along the particle trajectory. The presence of a non-linear term in Eq. (2.7) requires higher order integration schemes in time, such as second/fourth order Adam–Bashforth or Runge–Kutta (Press et al. (1986)), used for example by Parsa et al. (2012).

As said, Eq. (2.7) is a non-linear vector equation, and it is seemingly hard to solve. However, the non-linearity is only apparent: it is due to the geometric constraint that $\boldsymbol{p}$ is a unit vector. The underlying dynamics is in fact linear. The vorticity $\boldsymbol{O}$ rotates $\boldsymbol{p}$, and the strain $\boldsymbol{S}$ aligns and stretches $\boldsymbol{p}$ towards its strongest eigendirection. The non-linear term is simply the stretching component of the strain, which is subtracted in order to prevent elongation of $\boldsymbol{p}$. Bretherton (1962) realised that one may instead model the orientation of the particle with any vector $\boldsymbol{q}$ which obeys the same linear terms, but without compensating for any elongation:

$$\frac{d\boldsymbol{q}}{dt} = (\boldsymbol{O} + \Lambda\boldsymbol{S})\,\boldsymbol{q}. \tag{2.8}$$

Owing to the common linear terms in Eq. (2.7) and (2.8), the vector $\boldsymbol{q}$ will have the same angular dynamics as $\boldsymbol{p}$. In addition, $\boldsymbol{q}$ may be stretched and compressed by the strain $\boldsymbol{S}$. But since we are only interested in the angular degrees of freedom, we can at any instant recover $\boldsymbol{p}$ by normalising $\boldsymbol{q}$ to unit length. Thus, the general solution of the Jeffery's equation is given by solving Eq. (2.8) for $\boldsymbol{q}$, then the solution to Eq. (2.7) is given by normalising $\boldsymbol{q}$ to unit length:

$$\boldsymbol{p} = \frac{\boldsymbol{q}}{\|\boldsymbol{q}\|}. \tag{2.9}$$

The advantage of this approach is that it is easier to solve the linear Eq. (2.8) than the non-linear Eq. (2.7). In addition, this consideration is useful to present the next paragraph since it furnishes the link between the Jeffery's equation and the upcoming discussion.

2.2.2.1 *Cauchy–Green tensor*

A different picture can be adopted in order to investigate the orientation of non-spherical particles in turbulent flows. Furthermore, we anticipate that this picture will be used in next chapters to develop a macroscopic stochastic Lagrangian model for the orientation.

In the case of a rod tracer particle ($\Lambda = 1$), the orientation dynamics can be reduced to the study of a passive vector problem. Among the many applications related to the problem of passive vectors we find the orientation of a thin rod (Parsa et al. (2011); Pumir and Wilkinson (2011); Einarsson et al. (2013); Gustavsson et al. (2014)), and of material line segments (Dresselhaus and Tabor (1992); Lüthi et al. (2005)). In particular, there are two studies (Parsa et al. (2011); Wilkinson et al. (2011)) that used the eigenvector of the Cauchy–Green strain tensor to understand the orientation of rods in two-dimensional flows. This means that a simple description can be used by studying the local alignment of the rod direction with the eigenvalues of the left Cauchy–Green strain tensor (Wilkinson et al. (2009); Bezuglyy et al. (2010); Wilkinson et al. (2011); Ni et al. (2014); Hejazi et al. (2017)), since the infinitesimally thin rods must converge to the leading eigenvector of this tensor (Ni et al. (2014)).

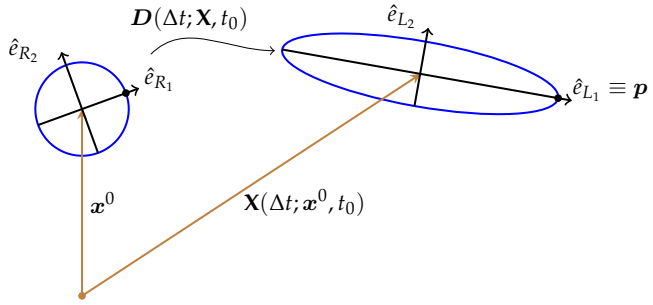

Figure 2.2: Sketch of deformation. A fluid element at initial position $\boldsymbol{x}^0$ at time t_0 is mapped to final position $\mathbf{X}$ after time Δt by the flow. The circular fluid element is also deformed by the flow to an ellipse. The eigenvectors of the left $(\hat{e}_{L_1}, \hat{e}_{L_2})$ and right $(\hat{e}_{R_1}, \hat{e}_{R_2})$ Cauchy–Green tensors are shown in two-dimensional case.

In continuous mechanics, the Eulerian coordinates system can be considered as the present configuration, while the Lagrangian one as the configuration of reference. In the absence of material deformation caused by the velocity field, the present (Eulerian) and the reference (Lagrangian) frames should be the same. Thus, the effect of the velocity field is to deform the configuration rendering the present coordinate different from the reference coordinate frame. The transformation (deformation) tensor between the two frames contains important information about the material deformation.

In fact, considering a fluid element (blob), having a size L much smaller than the viscous length η_K of the velocity, that is initially spherical. After a certain time Δt it will be stretched into an ellipse by the flow, as in Fig. 2.2. The stretching is the ratio between the semi-major axis of the ellipse and the radius of the circle. The evolution between the initial configuration $\boldsymbol{x}^0$ and final one $\mathbf{X}$ of the blob can be described in terms of the deformation gradient tensor $D_{ij}(t; \mathbf{X}, t_0) = \partial \mathrm{X}_i(t; \boldsymbol{x}^0, t_0)/\partial x_j^0$. Then the solution of $\boldsymbol{D}$ is obtained by integrating the linear differential equation,

$$\frac{d\boldsymbol{D}}{dt} = \boldsymbol{A}(t)\boldsymbol{D}(t), \quad \text{with intial condition } \boldsymbol{D}(0) = \mathbb{1} \tag{2.10}$$

where $\mathbb{1}$ is the identity matrix. The deformation gradient tensor describes the evolution of the infinitesimal separation vector $\boldsymbol{r}$ between two neighbourhood points in the fluid $\boldsymbol{r}(t) = \boldsymbol{D}(t, t_0)\boldsymbol{r}(t_0)$, where $\boldsymbol{r}(t_0)$ is the initial infinitesimal separation at time t_0.

The deformation gradient tensor includes both rotation and strain, $\boldsymbol{D} = \boldsymbol{V}\boldsymbol{R} = \boldsymbol{R}\boldsymbol{U}$ (called also 'polar decomposition'), where $\boldsymbol{R}$ is the rotational matrix and $\boldsymbol{U}$, $\boldsymbol{V}$ are the left and right stretch tensor respectively (Ni et al. (2014)). The left Cauchy–Green strain tensor, $\boldsymbol{C}^{(L)} = \boldsymbol{D}\,\boldsymbol{D}^\intercal = \boldsymbol{V}\boldsymbol{R}\boldsymbol{R}^\intercal\boldsymbol{V}^\intercal = \boldsymbol{V}\,\boldsymbol{V}$, has eigenvectors $(\hat{e}_{L_1}, \hat{e}_{L_2}, \hat{e}_{L_3})$ along the principal axis

of the ellipse formed after the fluid element is deformed over Δt. The right Cauchy–Green strain tensor, $\boldsymbol{C}^{(R)} = \boldsymbol{D}^\intercal \boldsymbol{D} = \boldsymbol{U}^\intercal \boldsymbol{R}^\intercal \boldsymbol{R}\boldsymbol{U} = \boldsymbol{U}\boldsymbol{U}$, has eigenvectors $(\hat{e}_{R_1}, \hat{e}_{R_2}, \hat{e}_{R_3})$ along the initial direction that will become the principal axis after deformation. Thus, the eigenvector of the left Cauchy–Green strain tensor gives the preferred direction toward which a rod at that location will rotate due to the deformation of the fluid. These two tensors have the same eigenvalues $\sigma_1 > \sigma_2 > \sigma_3 > 0$, corresponding to extension for the largest one, compression for the smallest and both extension or contraction for the intermediate one. The leading eigenvector $\hat{e}_{L_1}$ associated to the largest eigenvalue σ_1 is called Lagrangian stretching direction, while the eigenvector $\hat{e}_{L_3}$ that corresponds to the smallest eigenvalue σ_3, is the compressing direction. The middle one $\hat{e}_{L_2}$, forms an orthogonal bases with the other two. A simplified picture of this mechanism is presented in Fig. 2.2 for two-dimensional case, where we have only stretching and compression directions. Furthermore, the properties of these eigenvalues are of great interest in studies of turbulence since they are directly related to the Lyapunov exponent (Pierrehumbert and Yang (1993); Bec et al. (2006)).

It has been shown (Balkovsky and Fouxon (1999); Ni et al. (2014)) that the rod orientation vector will be perfectly oriented along with the Lagrangian stretching direction $\hat{e}_{L_1}$, in the long time limit. Thus, for a small rod ($\Lambda = 1$), when $\boldsymbol{p}_0$ is the initial direction of the rod at time t_0, the orientation at time t is given by,

$$\boldsymbol{p}(t) = \frac{\boldsymbol{r}(t)}{\|\boldsymbol{r}(t)\|}, \quad \boldsymbol{r}(t) = \boldsymbol{D}(t, t_0)\, \boldsymbol{p}_0. \tag{2.11}$$

This solution was first given by Szeri and Leal (1993) and corresponds to Eq. (2.7) for a slender rod ($\Lambda = 1$).

2.3 PREFERENTIAL ALIGNMENT

Non-spherical particles in turbulence are oriented by the effect of the deterministic part of the velocity gradient tensor and randomised by the stochastic fluctuating part of it. The preferential orientation has been widely investigated and it is the result of the competition between the alignment by the mean velocity gradient and/or (depending on the flow field) by the fluctuating contributions.

Tracers spheroidal particles are randomly oriented with respect to the laboratory frame of reference in homogeneous isotropic turbulence (HIT). Nonetheless, the complex angular dynamics has been investigated, using DNS, in terms of the alignment with respect to the vorticity vector $\boldsymbol{\omega}$ and the eigensystem of strain rate $\boldsymbol{S}$. Pumir and Wilkinson (2011) integrate Eq. (2.7) for rods-like particles ($\Lambda = 1$) studying how slender rods induce a preferential alignment with the local velocity gradient tensor. In particular, it has been shown that rod-like particles tend to align their symmetry axis $\boldsymbol{p}$ with the instantaneous vorticity vector of turbulent flow $\boldsymbol{\omega} = \nabla \times \boldsymbol{u}$ (Pumir and Wilkinson (2011); Parsa et al. (2012); Byron et al. (2015)), whereas disk-like particles preferentially orient $\boldsymbol{p}$ perpendicular to $\boldsymbol{\omega}$ (Gustavsson et al. (2014); Byron et al. (2015)). Moreover, many authors (Guala et al. (2005); Parsa et al. (2012); Pumir and Wilkinson (2011); Gustavsson et al. (2014); Ni et al. (2014); Chevillard and Meneveau (2013)) have analysed how $\boldsymbol{p}$ aligns with the eigenvectors of the local strain rate tensor $\boldsymbol{S}$, showing that rod-like particles $\boldsymbol{p}$ tends to align strongly with the intermediate eigenvector of the strain rate tensor, slightly less with the largest one (most extensional) and strongly perpendicular to the smallest (most compressive). For thin disk-like, particles are preferentially aligned with the smallest eigenvector of the strain rate tensor. The aforementioned findings are encapsulated in Fig. 2.3. Experimentally, Ni et al. (2015) have been able to access both the orientation of non-spherical particles and the velocity gradients tensor in order to obtain consisting results with the previous numerical studies.

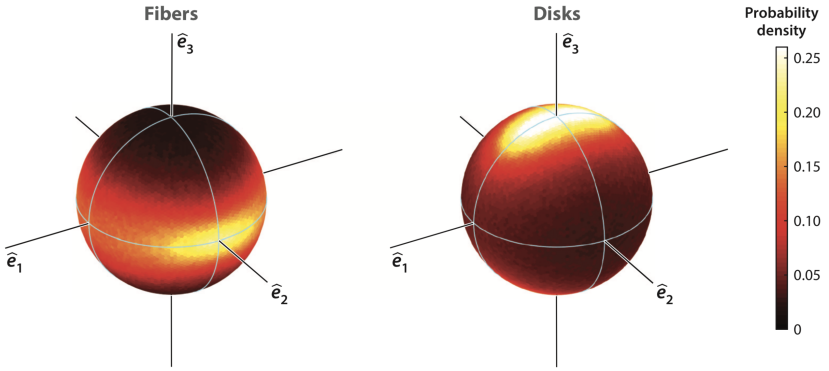

Figure 2.3: Spherical probability density functions of the orientation of fibres (left panel) and disks (right panel) in the coordinate system defined by the eigenvectors of the strain rate tensor in HIT. Image reproduced from Voth and Soldati (2017).

The orientation of tracer spheroids have been also investigated in turbulent channel flow. Zhao and Andersson (2016) have uncovered the mechanism that gives rise to preferential particle alignment with the vorticity and left Cauchy-Green strain tensor in anisotropic turbulence. They showed that the alignment of the fluid vorticity vector with the strongest Lagrangian stretching direction in the bulk of the channel, just as in HIT (Ni et al. (2014)), vanishes close to the walls. Moreover, all over the channel they found that the symmetry axis of the prolate spheroid aligns with the direction of the strongest Lagrangian stretching, whereas oblate spheroids are oriented with the direction of the Lagrangian compression. Furthermore, their analysis revealed that the directions of the strongest Lagrangian stretching and compression in near-wall turbulence are in the streamwise and wall-normal directions, respectively.

As analysed by Andersson et al. (2015), in the centre of the channel, particles are almost randomly oriented since the velocity field is nearly isotropic, whereas near the walls the alignment strongly depends on the particle shape. In disk-like particles $\boldsymbol{p}$ strongly aligns along the wall-normal direction, but rod-like becomes parallel to the wall with $\boldsymbol{p}$ mostly aligned in the stream-wise direction (Challabotla et al. (2015b)).

In the case of inertial spheroids, the same analysis has been largely investigated mainly in turbulent channel flow (Zhang et al. (2001); Mortensen et al. (2008); Marchioli et al. (2010); Marchioli and Soldati (2013); Challabotla et al. (2015a); Zhao et al. (2015)). As an example, a totally different alignment is observed (with respect to the inertial-free particles) with disk-like particles becoming aligned perpendicular to wall-normal direction.

2.4 ROTATION RATE

The qualitatively different preferential orientation of non-spherical particles, depending on their aspect ratio λ, has a profound impact on their rotational behaviour.

As said, the rotational dynamics in the case of inertialess spheroidal particle in turbulent flow is described by the temporal evolution of the unit vector $\boldsymbol{p}(t)$ indicating the orientation of the particle axis and the time derivative of $\boldsymbol{p}(t)$, the rotation rate. Thus, a spheroid rotates with a total angular velocity $\boldsymbol{\Omega}$ which is distributed into two motions: the tumbling, which corresponds to the rotation of the axis of symmetry of the particle, and the spinning, corresponding to the rotation about that axis. The evolution of the vector $\boldsymbol{p}$ can be rewritten as,

$$\frac{d\boldsymbol{p}}{dt} = \boldsymbol{\Omega} \times \boldsymbol{p}. \tag{2.12}$$

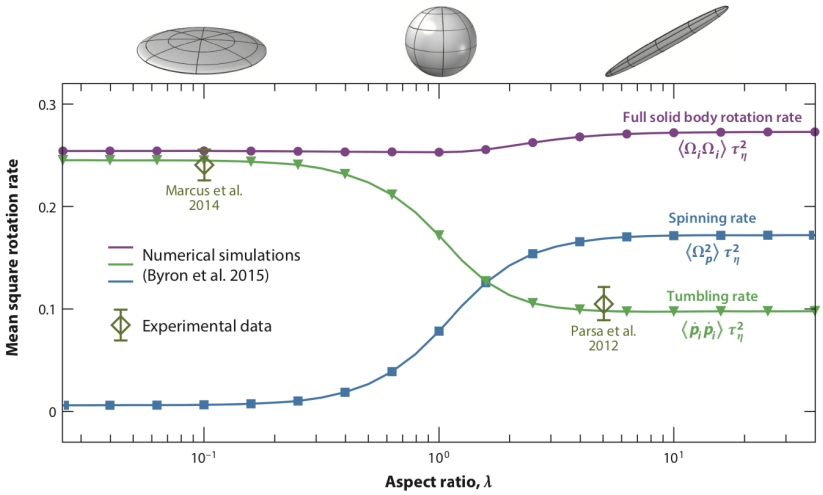

Figure 2.4: Mean square rotation rate as a function of aspect ratio for tracer particles in homogeneous isotropic turbulence. Image reproduced from Voth and Soldati (2017).

With respect to Eq. (2.7) the total angular velocity of the particle can be identified as $\boldsymbol{\Omega} = \boldsymbol{\omega}/2 + \Lambda \boldsymbol{p} \times \boldsymbol{S}\boldsymbol{p}$. Here the antisymmetric part of the velocity gradient $\boldsymbol{A}$ has been rewritten as $\boldsymbol{O}\,\boldsymbol{p} = (\boldsymbol{\omega} \times \boldsymbol{p})/2$, where the vector $\boldsymbol{\omega}$ is equal to the vorticity vector.

The particle angular velocity $\boldsymbol{\Omega}$ can be decomposed into two components, one parallel and one orthogonal to the orientation vector $\boldsymbol{p}$; they read respectively:

$$\boldsymbol{\Omega}_{\perp p} = \boldsymbol{p} \times (\boldsymbol{\Omega} \times \boldsymbol{p}) \tag{2.13}$$

$$\boldsymbol{\Omega}_{\parallel p} = |\boldsymbol{\Omega} \cdot \boldsymbol{p}|\, \boldsymbol{p}, \tag{2.14}$$

such that $\boldsymbol{\Omega} = \|\boldsymbol{\Omega} \cdot \boldsymbol{p}\|\, \boldsymbol{p} + \boldsymbol{p} \times \dot{\boldsymbol{p}}$, with a norm $\|\boldsymbol{\Omega}\|^2 = |\boldsymbol{\Omega} \cdot \boldsymbol{p}|^2 + \|\boldsymbol{p} \times \dot{\boldsymbol{p}}\|^2$. Finally, the magnitude of these two quantities refers to the definition of spinning and tumbling rate respectively (Byron et al. (2015)).

The variance of tumbling rate, $\langle \|d\boldsymbol{p}/dt\|^2 \rangle$ (a way to rewrite $\langle \|\boldsymbol{\Omega}_{\perp p}\|^2 \rangle$), for a rod-like particle ($\Lambda = 1$) has been investigated, using DNS. In HIT, by Shin and Koch (2005) who observed that this quantity was smaller than the expectations for a randomly oriented rod-like particle. Parsa et al. (2011) presented experimental and DNS results on the probability distribution of tumbling rate of a spheroid as a function of aspect ratio. Marcus et al. (2014) develop an experimental technique to measure the tumbling rate for a wide range of aspect ratios, including disk-like particles ($\Lambda = -1$).

The full body rotation rate, including tumbling and spinning rate has been studied by Byron et al. (2015) both, numerically and experimentally. They observe that the variance of the total rotation rate is almost independent from the aspect ratio. Furthermore, they found that a rod spins more than it tumbles, while a disk tumbles more than it spins. The effect of the particle shape on tumbling and spinning rate saturates at a constant value, remaining insensitive to the change of the aspect ratio outside the range $0.1 < \lambda < 10$.

Most of these features crucially depend on the precise dynamics of the spheroids and fluid vorticity, in relation to the alignment with the eigensystem of the local stain rate. The slower tumbling rate of a rod has been explained with the fact that the component of the vorticity along the rod axis does not contribute to its tumbling rate. Conversely, disk behaviour shows that the axis aligns perpendicular to the vorticity, explaining the larger variance of the tumbling rate for disks than for rods. Figure 2.4 summarizes DNS and experimental measurements in

HIT for the variance of total rotation rate, given by the sum of spinning and tumbling rate as a function of the aspect ratio.

These quantities have also been investigated for inertialess spheroidal particles in turbulent channel flow by Challabotla et al. (2015b). An extensive study including both, inertialess and inertial spheroids has been provided by Zhao et al. (2015). They conclude that rotation rate statistics for a tracer spheroid in the bulk of the channel are close to the HIT case. On the other hand, spheroids in the near wall region are affected by both the mean shear and anisotropic fluid vorticity, and their rotational behaviour is totally different from the channel centre.

The addition of particle inertia has been considered in many works (Marchioli and Soldati (2013); Zhao et al. (2015)). It has been observed that the inertia reduces tumbling and spinning rate, leading to a more isotropic rotation at the centre channel, whereas near to the wall inertial spheroids respond strongly to the mean shear by causing for example, inertial disks to spin much faster than inertial rods, having an opposite trend with the HIT case in Fig. 2.4.

2.5 LAGRANGIAN STOCHASTIC MODELS FOR THE ORIENTATION

Jeffery equation (2.7) is fully characterized in terms of the velocity gradient tensor. The velocity gradient tensor $A_{ij}(t) = \partial u_i/\partial x_j(t)$ fluctuates, being dominated by the small-scale motions, of the order of the Kolmogorov length scale η_K, and it results similar in many different turbulent flows. In addition, it identifies many fundamental and intrinsic properties of small-scale motions in turbulence. Indeed, this tensor encodes interesting geometric and statistical information such as the alignment of vorticity with respect to the strain-rate eigenvectors, rate of deformation and shapes of fluid material volumes, non-Gaussian statistics, and intermittency, as explained by Meneveau (2011).

Here we want to briefly recall that, the time evolution of $\boldsymbol{A}$ following fluid particles can be obtained by taking the gradient $(\partial/\partial x_j)$ of the Navier-Stokes equations. For incompressible flow, the resulting equation reads

$$\frac{DA_{ij}}{Dt} = -A_{ik}A_{kj} - \frac{\partial^2 P}{\partial x_i \partial x_j} + \nu \frac{\partial^2 A_{ij}}{\partial x_k \partial x_k} \tag{2.15}$$

where D/Dt stands for the Lagrangian material derivative (i.e., $D/Dt \equiv \partial/\partial t + u_k \partial/\partial x_k$), P is the pressure divided by the density of the fluid, and ν is the kinematic viscosity. Equation (2.15) is not closed in terms of $\boldsymbol{A}$ at position $\boldsymbol{x}$ and time t due to the last two terms in the right-hand side of the equation, the pressure Hessian $\partial^2 P/\partial x_i \partial x_j$ and the viscous term $\nu \nabla^2 A_{ij}$. The trace of the above equation with the incompressibility condition $A_{ii} = 0$ leads to the Poisson equation $\nabla^2 P = -A_{ik}A_{kj}$, showing that the pressure field is highly non-local (Meneveau (2011)).

Equation (2.15) represents a non-trivial dynamical equation (unclosed), that gathers inside several geometric, statistical, and dynamical turbulence phenomena. As said, many practically important applications can be strongly affected by the properties of the velocity gradient tensor. Moreover, here, we want to underline that, from a modelling point of view, resort a model for Eq. (2.15) represents an hard task by the presence of pressure Hessian and viscous effects.

Despite the highly complexity of Eq. (2.15), several Lagrangian stochastic models for the velocity gradient tensor have been proposed in literature (Girimaji and Pope (1990); Cantwell (1992); Brunk et al. (1998); Chertkov et al. (1999); Jeong and Girimaji (2003); Chevillard and Meneveau (2006); Biferale et al. (2007); Vincenzi et al. (2007); Pumir and Wilkinson (2011); Pereira et al. (2018)), as reviewed by Meneveau (2011). Some of these models are for coarse-grained velocity gradients and obey to isotropic Gaussian statistics, e. g., are the result of linear Ornstein–Uhlenbeck processes (Brunk et al. (1998); Vincenzi et al. (2007); Pumir and Wilkinson (2011)) or constructing a phenomenological model by considering the Lagrangian dynamics of four points (the tetrads of fluid particles, see Chertkov et al. (1999)), as well as multi scale model

(Biferale et al. (2007)). Alternatively, others describe transient or quasi-steady state behaviour (Cantwell (1992); Jeong and Girimaji (2003)). Girimaji and Pope (1990) introduced a model for the pressure Hessian and viscous Laplacian in the evolution dynamics of $\boldsymbol{A}$ designed to reproduce log-normal stationary statistics for the pseudo dissipation, leading to more realistic strain-vorticity but their model introduces several additional free parameters. A more complex and refined model is the recent fluid deformation approximation (RFDA) model (Chevillard and Meneveau (2006)), which predicts a variety of local, statistical, geometric and anomalous scaling properties of 3D turbulence.

2.5.1 *Modelling context*

In order to understand the dynamics of inertialess spheroidal particles in turbulence, the Lagrangian statistics of the velocity gradient tensor has to be included, to properly take into account the orientation dynamics coming from integration of Eq. (2.7) along the particle trajectory. This sheds light on both, the complexity of understanding particle orientation statistics with respect to difficulty to identify what are the important features in the dynamics of the velocity gradient that mainly affect particle orientation.

In this context, most of the present studies of non-spherical tracer particles in turbulent flows has been done using DNS. In fact, the advantage of DNS over macroscopic and mesoscopic description is that it yields a complete information about the velocity field on the finest Kolmogorov scale, by providing a microscopic description of the influence of the velocity gradient tensor on the non-spherical particle dynamics.

The need to develop and investigate statistical models on the small scale fluctuations aiming to reproduce the orientation statistics of the unitary vector $\boldsymbol{p}$, are different:

(i) In theoretical studies, it is necessary to introduce models in order to gather analytical expressions to face the problem. Specifically, these studies have mainly focused on the derivation of the model equations for the probability of the orientation in which turbulent fluctuations are described by an effective isotropic diffusion term (Olson and Kerekes (1998); Shin and Koch (2005)). Turitsyn (2007) derived an analytical expression for the probability density function of a rod-like polymer in a random flow overlapping a mean shear and a short correlated isotropic fluctuation model. Vincenzi (2013) derived the exact probability density function of a spheroidal tracer particle transported by an homogeneous random flow, introducing the simplest form of statistical anisotropy (axisymmetric statistics).

(ii) The comparison of DNS results for the particle rotation with those obtained by models, is instructive to understand which aspects of the particle dynamics are influenced by the nature of turbulence and which aspects can be explained by simple statistical models (Byron et al. (2015)).

(iii) The statistics of the velocity gradient tensor are of both practical and theoretical importance in the study of turbulence (Wallace (2009)). In particular, the dynamics of turbulence, including velocity gradient, can be better understood in a Lagrangian frame following the flow (Falkovich et al. (2001)). Moreover, the velocity gradients in turbulence are highly non-Gaussian with considerable spatio-temporal complexity. The highly non-trivial dynamics can be important for a wide range of applications where the velocity gradients enclose a rich description of the local flow.

Meanwhile, from a theoretical perspective, the statistics of the velocity gradient are essential in exploring internal intermittency and multifractality (Kolmogorov (1962); Oboukhov (1962); Parisi and Frisch (1985)). These features brought out the increasing

interest to investigate, in isolate manner, the evolution equation of the velocity gradient along Lagrangian path. In fact, the equation for $\boldsymbol{A}$ contains two unclosed terms that have to be modelled: the deviatoric part of the pressure Hessian, and the viscous Laplacian (Meneveau (2011)). These two terms have motivated a number of studies (Girimaji and Pope (1990); Cantwell (1992); Chertkov et al. (1999); Chevillard and Meneveau (2006); Biferale et al. (2007); Pereira et al. (2018)) to attempt closure models for governing the Lagrangian evolution of the velocity gradient tensor.

More recently, the study of Jeffery's equation (2.7) and the particle rotation rate as a function of the shape parameter, turned out to be a precise and demanding way to test the accuracy of different models for the velocity gradient tensor (Chevillard and Meneveau (2013); Pereira et al. (2018)).

(iv) In the context of mesoscale models description, LES is becoming progressively attractive in view of the continuous improvement of sub-grid scale (SGS) models for both fluid and particle phase. Indeed, a large part of turbulent kinetic energy may be resolved by replacing the fine-scale details of the flow with SGS models. While such approach, in many cases, succeeded to simulate high Reynolds number turbulence, some applications require a more detailed representation of the fine-scale properties of the velocity gradient dynamics that are not resolved in LES modelling context.

Examples include particle dispersion (Sawford (2001)), rotation and orientation dynamics (Chevillard et al. (2008); Pumir and Wilkinson (2011)), break up and coalescence of drop and bubbles (Maniero et al. (2012); Biferale et al. (2014)) and polymer stretching-relaxation dynamics (Balkovsky and Fouxon (1999); Chertkov (2000); Procaccia et al. (2008)).

Indeed, a possible approach to recover small scale details of turbulence dynamics is to employ Lagrangian stochastic models. These models have been developed to predict particle dispersion, deposition and re-suspension, especially in the context of RANS for industrial applications (Minier (2016)). However, efforts have been devoted to the extension of stochastic closure to LES with SGS modelling.

In this context, the Lagrangian stochastic approaches deal with the modelling of the fluid velocity seen by the particle which determines the filtering error impacting the estimation of the velocity field acting on particles in LES. Furthermore, adopting a stochastic closure for the fluid velocity seen, typically involves a Wiener process with uncorrelated independent increments and continuous trajectories that are nowhere differentiable and are not realizations of the fluid like in Navier–Stokes equations. Rather, they represent actually different realizations of a stochastic process associated to a one-point probability distribution function equation for the fluid velocity seen. Thus, the notion of the local velocity gradient is missed in the classical Lagrangian stochastic approach (Peirano et al. (2006)).

Results from a priori tests demonstrate that SGS fluctuations mostly affect particles orientation and rotation, leading to error prediction on the particle alignment with the vorticity and eigenvectors of the strain rate tensor (Chin and Geiser (2011); Johnson and Meneveau (2018)). Thereby, a Lagrangian stochastic model for SGS velocity gradient tensor seen by the particle has been adopted in order to recover small scale details.

(v) Despite the ever present toll of DNS, it will be not very handy to design large scale system at practical Reynolds number (used in industrial applications), therefore a contracted probabilistic description is needed.

In particular, just for a single-phase flow, a macroscopic statistical description of the fluid flow can be employed based on RANS, which greatly reduces the computational efforts.

However, in such a simulation an additional model for the effects of turbulence on the particle is required (Minier (2016)). In order to take into account the effect of turbulence on particle motion, a stochastic turbulence dispersion model is introduced.

Indeed, over the last decades, Lagrangian stochastic models have been more and more used for both single-phase flows and dispersed two-phase turbulent flows. These approaches are referred to as PDF (probability density function) methods. Following the presentation of standard Lagrangian stochastic model for dispersed two-phase flow in Minier (2016), the particle state vector (which gathers the variables of interest attached to each particle) is made up by particle location and velocity as well as the velocity of the fluid seen by the particle $\boldsymbol{Z} = (\mathbf{X}_p, \boldsymbol{u}_p, \boldsymbol{u}_s)$ for a spherical inertial particle.

Conversely, in case of non-spherical particle, the fibre state vector is complemented with the particle rotation $\boldsymbol{\Omega}_p$ (or orientation) and the modelled Lagrangian velocity gradient seen, i.e. $\boldsymbol{Z} = (\mathbf{X}_p, \boldsymbol{u}_p, \boldsymbol{u}_s, \boldsymbol{\Omega}_p, \boldsymbol{A}_s)$. From this point of view, a useful discussion has been given by Minier (2016), but no attempts are present in literature to solve either, analytically or numerically a mesoscopic model or macroscopic (depending on the number of components and the hierarchy of the particle/fibre state vector), based on Lagrangian stochastic approach, that could be interesting for many industrial applications.

In the following part, we want to describe some examples where the different models for the velocity gradient tensor have been applied to the study of the orientation dynamics of non-spherical particles.

The simple case, when the particle orientation vector and the velocity gradient tensor $\boldsymbol{A}$ are assumed to be statistically independent, has been proposed by Shin and Koch (2005) to analytically investigate a rod-like particle in HIT. In particular, an analytical expression for the variance of tumbling rate has been derived, and later on the same calculation has been extended by Parsa et al. (2011) to non-spherical particles with a finite aspect ratio. They observe that the assumption of statistical independence makes no difference between rod- and disk-like particles, in contrast with DNS result that leads to marked differences between these two cases (e. g., DNS result in Fig. 2.4).

Byron et al. (2015) numerically explore the simple model in an isotropic homogeneous Gaussian random velocity field focusing on the behaviour of the variance of both tumbling and spinning rates. They explain that the main difference between turbulence and random Gaussian velocity field is that turbulence breaks time reversal invariance such that the velocity gradient tensor $\boldsymbol{A}$ and $\boldsymbol{A}^\intercal$ have different probabilities, which is not the case for a Gaussian model. This difference results to be fundamental for the orientation statistics because the orientation dynamics of a rod- and disk-like particle are settled by $\boldsymbol{A} = \boldsymbol{O} + \boldsymbol{S}$ and $-\boldsymbol{A}^\intercal = \boldsymbol{O} - \boldsymbol{S}$, respectively. Moreover, they observe that turbulent flows show a stronger vorticity fluctuations than the random flow model, leading to long-living vortex structures responsible for the particle alignment, which impact the relation between spinning and tumbling rates.

Several models for $\boldsymbol{A}$ have been tested by Chevillard and Meneveau (2013) in order to solve Eq. (2.7) in HIT. Among these, a linear Ornstein–Uhlenbeck process where the relaxation terms involve the simple Kolmogorov time scale τ_η. For this Gaussian model no preferential alignment of $\boldsymbol{p}$ with the vorticity can be observed, as well as no preferential alignment with the intermediate eigendirection of strain rate as found in DNS. This model correctly predicts only the preferential alignment of disk-like particles with the most contracting eigendirection. Furthermore, in line with others studies (Shin and Koch (2005); Pumir and Wilkinson (2011); Byron et al. (2015)), the model finds out that, assuming statistically independent $\boldsymbol{A}$ and $\boldsymbol{p}$, as well as Gaussian process for $\boldsymbol{A}$, a poor prediction of the tumbling rate is obtained with respect to DNS results.

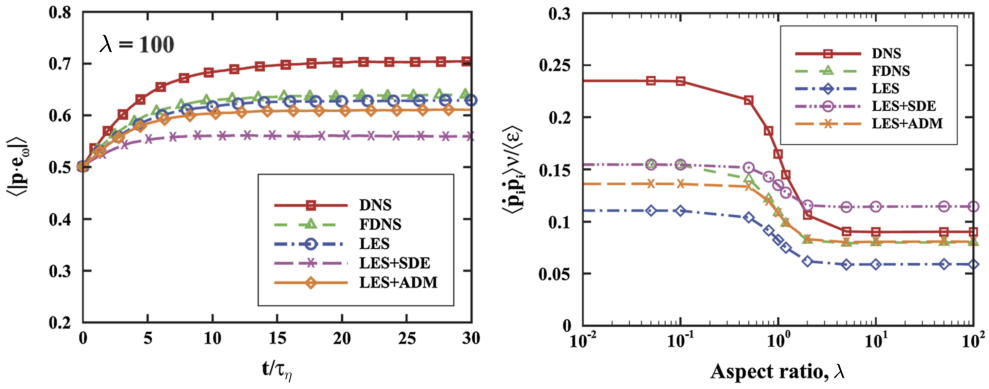

Figure 2.5: (Colour online) Comparative assessment of the particle SGS models for ellipsoidal particles in HIT. Left panel: time behaviour of the mean particle alignment with vorticity, $\langle |\boldsymbol{p} \cdot \boldsymbol{e}_\omega| \rangle$. Right panel: particle mean square rotation rate, $\langle \dot{p}_i \dot{p}_i \rangle$, as a function of particle aspect ratio, λ. Labels FDNS and LES indicate a priori and a posteriori tests without particle SGS model, respectively. Labels LES+SDE and LES-ADM indicate simulations with the stochastic and the ADM-based particle SGS model, respectively. Image reproduced from Chin and Geiser (2011).

A more realistic Gaussian process has been proposed for the velocity gradient statistics. Pumir and Wilkinson (2011) have considered an Ornstein–Uhlenbeck process for $\boldsymbol{A}$ with different correlation time scales for the symmetric and antisymmetric part. Indeed, from DNS they measured that, in turbulence, the correlation time scale for the rotation rate of velocity gradient is significantly longer than that of the strain rate. They observed some degree of alignment between $\boldsymbol{p}$ and vorticity; nonetheless this effect is weak, and their results are overall in line with the Gaussian model studied by Chevillard and Meneveau (2013).

The stochastic model of Girimaji and Pope (1990) has been used to compute the long-time variance of tumbling rate for rod-like particles in HIT by Shin and Koch (2005). This model incorporates an approximate description of the correlation between the strain and rotation rate of $\boldsymbol{A}$ by means of the prescription of a log-normal probability density function for the pseudo-dissipation. It gives a reasonable approximation of the variance of tumbling rate that is about 13% smaller than obtained by DNS.

More refined stochastic models have been developed and tested using Eq. (2.7) in order to provide an accurate level of intermittency for the dissipation and enstrophy fluctuations and multifractality (Chevillard and Meneveau (2013); Pereira et al. (2018)). In these cases the non-linear dynamics of the velocity gradient tensor in the viscous range is taken into account and the tensorial structure is captured with remarkable accuracy by the model. This includes the degree of alignment trend of vorticity with the strain rate eigendirections, as well as the relative probability of prolate and oblate deformation in the strain eigendirections. Furthermore, the preferential alignment and rotation rate of spheroidal tracer particles are better predicted in HIT using this advanced model. In particular, the variance of tumbling rate is accurately reproduced for a prolate particle ($\lambda > 1$), but underestimated for oblate particles ($\lambda < 1$). These results point out the necessity for further improvements in stochastic Lagrangian models for the velocity gradient tensor. Specifically, a model that successfully leads to a more accurate prediction of tumbling rate for disk-like particles.

The prediction of orientation and rotation statistics of tracers spheroidal particles using LES method has been presented by Chin and Geiser (2011). These authors have considered the effect of including a sub-grid closure in the equation of motion (2.7) evolving in HIT and have quantified this effect in terms of particle alignment within the rotation and strain tensor and particle orientation distribution. In particular, the turbulent energy dissipation rate results to

be reduced when SGS velocity fluctuations are not accounted for. To recover these small scale effects, the stochastic Ornstein–Uhlenbeck model of Pumir and Wilkinson (2011) for SGS and a model based on approximate deconvolution method (ADM, see Marchioli (2017)) have been tested. The results of the behaviour of different tests is shown in Fig. 2.5.

The preferential alignment of $\boldsymbol{p}$ with the unit direction vector of vorticity field for a rod-like particle is presented in the left panel of Fig. 2.5. The stochastic model (LES-SDE) under-predicted the preferential alignment compared to DNS results since the stochastic model is Gaussian with a vorticity and strain rate that are not directly related. The ADM-based model has a little influence on preferential alignment compared to a-priori (FDNS) and a-posteriori (LES) results, emphasizing the effect of ADM to recover fluid enstrophy near cut-off scale. The mean squared tumbling rate as a function of aspect ratio is shown in the right panel of Fig. 2.5. Overall, the difference between reference DNS and results obtained with or without any of the particle SGS models is either marginal or increased, indicating that small scale quantities are extremely complex to model.

A notable exception is the work of Johnson and Meneveau (2018), to extend the stochastic model of Johnson and Meneveau (2016) (in isotropic turbulence) to predict velocity gradients and, at the same time, the deformation features of small droplets in an inhomogeneous turbulent channel flow, by coupling the model to an LES solution for the large scale flow. As said, while straight use of coarse-grained velocity gradients in a large scale flow simulation leads to a significant error, the stochastic modelling technique can be coupled to LES to provide small scale information about trajectories.

The authors showed the capability of this approach to the channel flow case to capture the main small scale effects in inhomogeneous flow. Still, they remark that the closures for the pressure Hessian and viscous Laplacian terms used in isotropic turbulence, require to be revised to capture important near-wall effects in the buffer region and viscous sublayer, i.e. accounting near-wall deviations from the approximate isotropy hypothesis of the current model.

2.6 CONCLUSIONS

Anisotropic particles are present in many natural and industrial flows. These particles react on a turbulent flow in complex ways which depend on a wide variety of parameters, with great emphasis in literature on particle shape, inertia and fluid shear. Inertialess particles, with a size smaller than the Kolmogorov length, behave as tracers which passively follow the fluid motion and assume an orientation $\boldsymbol{p}$ which preferentially samples certain directions defined by the local turbulent velocity gradient. This picture, already quite intricate in the homogeneous isotropic turbulence (HIT), becomes even more difficult to treat in a turbulent channel due to the presence of near wall structures. When inertial particles are considered the preferential alignment changes from tracers, becoming as inertia increases, less and less impacted by the fluid velocity gradient tensor. Furthermore, preferential alignment causes the non-spherical particles to tumble and to spin, characterising their rotational dynamics. Direct numerical simulation (DNS) in HIT and wall turbulence are widely used to understand and improve the description of the complex dynamics of preferential alignment and rotation of non-spherical particles.

Despite the advances in the DNS studies, the modelling of small scale turbulence dynamics, which impacts the orientation and rotation of a non-spherical particle, still remains an open question since it is not directly accessible using fluid modelling approaches. A strategy that has been proposed by several authors in order to mimic the behaviour of non-spherical particles in turbulent flows consists in coupling existing stochastic models for the Lagrangian velocity gradient with the equation for the orientation.

3 PARTICLES IN 2D TURBULENCE

Outline. In this chapter, the complex behaviour of inertialess rod-shaped particles embedded in a two-dimensional turbulent flow, with homogeneous shear, is studied. We introduce s Lagrangian stochastic model for the rods angular dynamics. It consists in superposing a short-correlated random component to the steady large-scale mean shear, and can be thereby integrated analytically. Within the model, an effective anisotropic correlation tensor is introduced, to properly account for the effect of the mean shear onto the Lagrangian statistics of the turbulent velocity gradients. Then, single-time orientation statistics obtained from DNS, are compared with the models results derived from the semi-analytical expression for the stationary distribution of the folded angle. We propose an alternative definition of tumbling rate applicable to diffusive dynamics, in terms of the stationary probability flux of the rods unfolded angle, to address the two-time statistics of the rods orientation. While the complex behaviour observed in the DNS shows a non-Gaussian distribution of the unfolded angle in a diffusive regime, the diffusion model is intended to provide a reasonable qualitative response, even if it is not designed to reproduce such a behaviour.

3.1 INTRODUCTION

The manifestation of turbulence is everywhere in nature, at all scales from quantum systems, for example in super-fluid helium 4, to Universe, for instance in galaxy formation. Two-dimensional (2D) turbulence is nowhere realised in nature or in laboratory but only in computer simulations. Nevertheless, there are numerous situations, in natural flow and in laboratory experiments, which are constrained to quasi-two-dimensional or layer-wise motion. Most examples arise in geophysical and planetary flows. For example, 2D turbulence is relevant to the dynamics of oceanic currents, the motion of intense eddies such as tropical cyclones, the existence of polar vortex, the dispersion of tracers in the oceans or of chemical species in the polar stratosphere, a key factor in the production of the ozone hole and in other large scale motions of planetary atmospheres (Charney (1971); Dritschel and Legras (1993); Waugh et al. (1994)). Figure 3.1, showing an image of Jupiter's northern hemisphere (left panel) illustrates the similarity with a vorticity field in numerical simulation of 2D Navier–Stokes equations (centre panel) as measured in different systems. The theory and phenomenology of 2D turbulence in homogeneous isotropic case has been largely investigated and is quoted in several reviews (Kraichnan and Montgomery (1980); Tabeling (2002); Boffetta and Ecke (2012)) and books (Batchelor (1953); Lesieur (1987); Frisch (1995)). It should also be added that many important turbulent configurations exist that deviate from the idealized situation of homogeneous isotropic turbulence (HIT), where pure 2D Navier–Stokes equations can be amended by the addition of extra-terms, e. g., in the presence of external mechanisms such as rotation, stratification, confinement, shear, or magnetic fields where the dynamics depends on the value of a control parameter (rotation rate, magnetic field strength, aspect ratio, shear rate, etc...) in order to represent physically relevant situations. These different physical situations have been investigated in numerical simulations and experiments of thin/thick layers (Xia et al. (2009); Benavides and Alexakis (2017)), in rotating and stratified turbulence (Godeferd and Lollini (1999); Deusebio et al. (2014); Machicoane et al. (2016)) and in magnetohydrodynamic

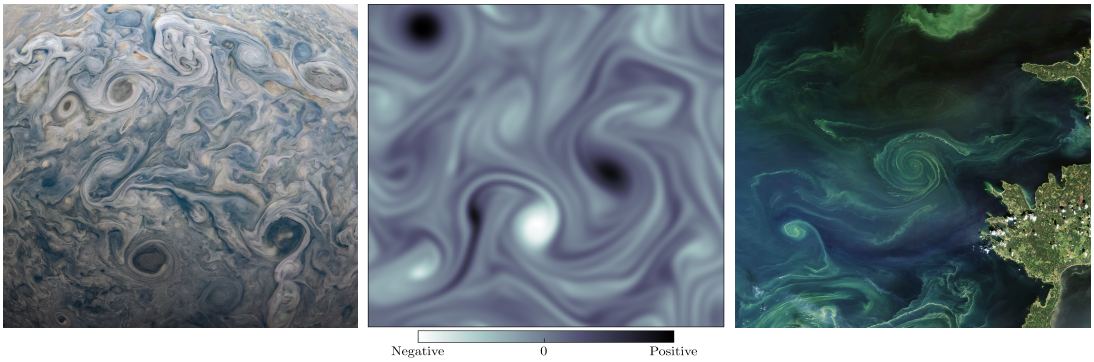

Figure 3.1: Left panel: Image (from NASA's Juno spacecraft) of storms and turbulence in the folded filamentary region of Jupiter's northern hemisphere. Center panel: Snapshot of a vorticity field in a numerical simulation of the 2D Navier–Stokes equations. Right panel: Large green bloom of phytoplankton in the Gulf of Finland (Baltic Sea), that spread across hundreds kilometres (images by NASA's Landsat satellite, on July 2018).

(MHD) turbulence (Favier et al. (2010); Alexakis (2011); Baker et al. (2017)). They have been observed in different geophysical flows: e. g., where the atmosphere acts like a 2D flow at large scale and as a three-dimensional (3D) flow at small scales (Charney (1971); Byrne and Zhang (2013)), or in the ocean (King et al. (2015)). Similar behaviour has been attributed to astrophysical flows (like the atmosphere of Venus and Jupiter (Izakov (2013))), and accretion discs (Gressel and Pessah (2015)), in plasma flows (Yoshizawa et al. (2003)) and in industrial applications like in Tokamak (Diamond et al. (2005)) and wind turbines (Devinant et al. (2002)), either due to the thinness of the layer, to fast rotation or to the presence of strong magnetic fields.

Among other reasons or prospects to get involved in studies on 2D turbulence, there is the connection to the 3D turbulence problem. The current literature has shown the existence of a common conceptual framework between two- and three-dimensional turbulence. Phenomena, such as cascades, coherent structures, dissipative processes, filamentation mechanisms take place in both systems. On the other hand, turbulence is simpler to represent and easier to compute in two than in three dimensions, and physical experiments provide much more information when the flow is thoroughly visualized and probed through a combination of special sensors and cameras. Therefore, working in 2D space may be instructive to test ideas or theories, prior to considering them in the three-dimensional world. Besides, the idealised 2D turbulence provides a starting point for modelling phenomena and it can be used as a simplified framework for certain turbulence problems allowing a systematic investigation of the control parameters and ultimately easier to handle from an analytical view point. Alongside this, it is noteworthy that 3D turbulence is not three dimensional in all respects; an example is represented by the worms (elongated structures), which populate the dissipative range: they are long tubes and thus can be tentatively viewed as two-dimensional objects. One may also add that 2D turbulence is helpful for understanding turbulence in general. Turbulence is a general phenomenon, involving non linear dynamics and broad range of scales, including as particular cases two- and three-dimensional fluid turbulence; so that a common conceptual framework exists, and 2D turbulence can obviously be used to understand several aspects of the general problem.

This chapter is devoted to analyse and model the orientation statistics of non-spherical particles immersed in a 2D homogeneous turbulent shear flow. The motivation arises from the

importance of controlling and predicting flows seeded with non-spherical particles (fibres, discs, or inclusions with more general shapes) which occurs in many natural and industrial processes. Sediment transport in dams (Vercruysse et al. (2017)), ice crystals in the atmosphere (Heymsfield (1977)), pulp fibres in paper making (Lundell et al. (2011)) or swimming microorganisms in the ocean as particular application of quasi-2D case in Fig. 3.1 (right panel) (Musielak et al. (2009)), are some examples. Moreover, recent work (Parsa et al. (2011); Calzavarini et al. (2020)) has renewed the interest in the Lagrangian studies with anisotropic particles, specifically in 2D turbulence.

In most of these applications the flow is highly turbulent and particles rotational dynamics, their alignment trends and correlations with the flow, become of considerable interest. When their size falls in active turbulent scales, the particles filter the fluid in a complex manner and show a very intricate dynamics (Qureshi et al. (2007); Ouellette et al. (2008); Brown et al. (2009)). Particles with sizes in the dissipative range have a more tractable behaviour. When their slip velocity is small enough, the local flow has a weak inertia and Stokes solutions can be used to relate particle rotational dynamics to the local velocity gradient tensor. This problem was first considered in the classic paper of Jeffery (1922) to derive evolution equations for the orientation of general ellipsoidal objects.

In turbulent flows the velocity gradient tensor $A_{ij} = \partial u_i / \partial x_j$ is dominated by small-scale motions and fluctuates on length and time scales of the order of the Kolmogorov dissipative length η_K and time scale τ_η. From an experimental perspective, the orientation dynamics of particles smaller than η_K has been studied in atmospheric flows (Krushkal and Gallily (1988); Newsom and Bruce (1998)) and in water tunnels (Bernstein and Shapiro (1994)). As to numerical studies, they consist in simulating, in addition to the fluid flow, the orientation of particles by integrating Jeffery's equation along Lagrangian trajectories. Simulations have been carried out in homogeneous isotropic turbulence (Shin and Koch (2005); Pumir and Wilkinson (2011); Parsa et al. (2012)), as well as in turbulent channel flows (Zhang et al. (2001); Mortensen et al. (2008)) and in chaotic velocity fields (Wilkinson et al. (2009)). At a theoretical level, most studies consisted in deriving model equations for the probability distribution of orientations, in which turbulent fluctuations are approximated by an effective isotropic diffusion term (Olson and Kerekes (1998); Shin and Koch (2005)). Much still needs to be understood in the presence of flow anisotropies. For instance, it was found by Turitsyn (2007) that the superposition of a constant mean shear to short-correlated isotropic fluctuations deeply influences the rotation of extensible polymers and consequently their size distribution.

Here, we focus on the orientation and rotation of a rod-like particle in the presence of a mean shear, since we expect that spheres and rods will rotate in qualitatively different fashions. As long as the Reynolds number at the particle scale is small, the local flow is well approximated by a Stokes flow. If in addition their inertia can be neglected, spheres will rotate with an angular velocity given by half of the flow vorticity. An inertialess anisotropic particle, however, will also couple with the strain-rate. In a 2D Stokes flow with uniform velocity gradients, the unit orientation vector $\boldsymbol{p}$ of a rod-like particle follows Jeffery (1922) equation,

$$\frac{dp_i}{dt} = A_{ij}p_j - p_i p_k A_{kl} p_l \tag{3.1}$$

where $A_{ij}(t) = (\partial u_i / \partial x_j)(\boldsymbol{X}(t), t)$ is the gradient tensor of the fluid-velocity field $\boldsymbol{u}$, evaluated along the particle trajectory $\boldsymbol{X}(t)$, which is assumed to be that of a tracer, i.e. $d\boldsymbol{X}(t)/dt = \boldsymbol{u}(\boldsymbol{X}(t), t)$.

To study the dynamics of ellipsoidal particles in turbulence, it is necessary to extend the understanding of the Lagrangian statistics of the velocity gradient tensor, and to include the orientation dynamics, resulting from integrating Eq. (3.1) along the particle trajectory. This is a challenging problem, because of the complexity of quantifying statistically the particle orientation with respect to the velocity gradient tensor. In this frame, the rod orientation

is solved numerically, performing direct numerical simulations (DNS). At the same time a Lagrangian stochastic model is developed. In more detail, the flow viewed by the rods is modelled by the superposition of a constant shear and a random component corresponding to a chaotic velocity field. In the spirit of classical works (Batchelor (1959); Kraichnan (1968)), the chaotic velocity part is assumed to be Gaussian and to have zero correlation time. The assumption of temporal decorrelation is adequate when the correlation time of the flow is short compared to the characteristic time scale of the velocity gradient tensor. Furthermore, such models are a great simplification of real flows and can be successfully applied for the analysis of advection by turbulent flows, as pointed out by Falkovich et al. (2001). As long as statistical properties of real flows are unknown, our approach is one possible way to model single rod in chaotic flows. This approach, albeit restrictive, allows to derive most of the results analytically and can form a basis for future studies of more intricate problems.

We report the main results in this chapter. First, we propose a stochastic model to describe the dynamics of thin rods in a turbulent shear flow. The model is derived by coarse-graining the deformation gradient tensor that fully characterises the orientation of fluid blob which evolves within a turbulent flow. We assume that the fluctuations of the velocity gradient tensor are Gaussian and delta-correlated in time and distinguished by an effective anisotropic diffusion correlation tensor.

In addition, the model contains the information about the integral Lagrangian correlation time that leads to define the validity of the model in terms of a Kubo number $Ku = \tau_I/\tau_\omega \ll 1$, i.e. the ratio between the integral time scale and the characteristic turnover time of the velocity gradient tensor. Under this hypothesis, the probability density function of the Lagrangian stochastic model associated to the folded angle of the rod is derived analytically. Moreover, three different ways to model the effective correlation tensor are tested: firstly assuming the tensor to be isotropic without any knowledge about the Kubo number, secondly introducing an anisotropic character through the simple measurement of instantaneous correlations letting Ku to be a constant parameter. Lastly, we measure the Kubo number Ku in the DNS by providing the model with an effective anisotropy correlation tensor for the velocity gradient fluctuations. Then, the angular distribution of the model is compared with the DNS. Both model and DNS results show that the angular distribution is concentrated in the region of small angles for large values of the shear rate, and this preferential alignment strengthens as the mean shear increases. In particular, in the DNS results the shear rate parameter and the amplitude of the velocity gradient fluctuations suffice to fully characterise the shape of the angle distribution. By contrast, in the stochastic model, a calibration parameter is introduced to rescale in time the model with respect to DNS. The model is tuned either to fit the probability density function (PDF) or to reproduce the average value of the orientation angle in the three declinations of the model. In particular, a good agreement with the DNS measurements is found using an effective correlation tensor, underlying the importance of anisotropy fluctuations within homogeneous shear flow turbulence.

Second, we study the statistics of time periods between consequent events of rod tumbling. Particularly, the classical measurement of tumbling rate in the DNS case (Parsa et al. (2012)) are not well defined in the model since the stochastic process which describes rod orientation is not differentiable in time. For this purpose, an alternative definition of tumbling rate is presented, providing another way to measure the tumbling rate experimentally. We show that this alternative definition can be identified through the long term evolution of the mean angular displacement (angular increment with respect to an initial point). The analytic results of the model are then compared with the DNS measurements revealing that the model is able to reproduce the DNS for some values of the calibration parameter. Finally, the variance of the angular displacement is investigated, revealing the limits of the stochastic model. Indeed, the unfolded angle trajectory in DNS resembles a Lévy walk. Furthermore, the fluctuations of

the angular displacement around its average are non-trivial in DNS and exhibit a highly non-Gaussian behaviour, which is confirmed by the PDF of the variance of the angular displacement showing some exponential tails. This underlies the presence of the anomalous diffusion, and the limits of the stochastic model to reproduce these features.

The plan of this chapter is as follows. In Section 3.2 we describe the numerical method for direct numerical simulation (DNS) in turbulent homogeneous shear flow and present the results on the preferential alignment of rods. Section 3.3 is devoted to introduce the Lagrangian stochastic model for the rods orientation and the analytical derivation of the stationary PDF for the orientation angle. Moreover, the results are compared with DNS. In Section 3.4 we introduce two-time statistics, by presenting an alternative definition for the tumbling rate which is investigated both numerically (DNS) and analytically with regards to the Lagrangian model. Some conclusions are drawn in Section 3.5.

3.2 TWO-DIMENSIONAL HOMOGENEOUS TURBULENCE WITH SHEAR

We consider two-dimensional turbulence described by the Navier–Stokes equations for an incompressible flow in the presence of mean shear,

$$\begin{aligned} \partial_t \boldsymbol{u} + \boldsymbol{u}\cdot\nabla\boldsymbol{u} &= -\nabla P + \nu\nabla^2\boldsymbol{u} - \alpha\,(\boldsymbol{u} - \sigma\, y\,\hat{e}_x) + \boldsymbol{f}, \\ \nabla\cdot\boldsymbol{u} &= 0. \end{aligned} \tag{3.2}$$

Here $\boldsymbol{u}(\boldsymbol{x},t) = \{u_x(x,y), u_y(x,y)\}$ is the divergence-free velocity field with a constant unit density, P is the pressure per unit density that enforces incompressibility and ν is the kinematic viscosity. The flow is put in motion by a linear friction, with coefficient α to an underlying linear flow along the y axis. In the absence of external forcing ($\boldsymbol{f} = 0$), the fluid velocity relaxes to the 2D shear flow $\boldsymbol{u}_\infty = \sigma\, y\,\hat{e}_x$ with amplitude σ, which is a stable stationary solution of Eq. (3.2). In order to maintain a developed turbulent state, an input of kinetic energy is provided by the stochastic forcing $\boldsymbol{f}$.

The incompressible turbulent fluctuations $\boldsymbol{u}' = \boldsymbol{u} - \boldsymbol{u}_\infty$ are then homogeneous in space and stationary in time. Equation (3.2) can be rewritten for the scalar fluctuating vorticity field $\omega = (\nabla\times\boldsymbol{u}')\hat{e}_z \equiv (\partial_x u'_y - \partial_y u'_x)\hat{e}_z$ solving

$$\partial_t\omega + \boldsymbol{u}\cdot\nabla\omega = \nu\nabla^2\omega - \alpha\,\omega + f_\omega, \tag{3.3}$$

with $f_\omega = \nabla\times\boldsymbol{f}$. The equations of motions are complemented by appropriate boundary conditions, which are taken to be periodic on a square domain of size L^2. The forcing in Eq. (3.3) is assumed Gaussian, homogeneous, isotropic, white in time, with correlations,

$$\langle \hat{f}_\omega(k,t)\,\hat{f}_\omega(k',t')\rangle = C\exp\left(\frac{-(k-\bar{k}_f)^2}{2\mu_f^2}\right)\delta(k+k')\,\delta(t-t'), \tag{3.4}$$

where the forcing $\hat{f}_\omega$ is expressed in the Fourier space and $\bar{k}_f$, μ_f need to be set properly, such that the forcing will be concentrated over large spatial scales (C is a constant factor). Here the angular brackets $\langle\cdot\rangle$ stand for ensemble average.

Conversely to the 3D turbulence, the non-linearity in Eq. (3.3) conserves the enstrophy $\mathcal{Z} = (1/2)\langle\omega^2\rangle$, that together with the kinetic energy $\mathcal{E} = (1/2)\langle|\boldsymbol{u}'|^2\rangle$ characterise the resulting turbulent state. Namely, the budgets of these two inviscid quadratic invariants satisfy,

$$\frac{\mathrm{d}\mathcal{E}}{\mathrm{d}t} = 0 = -2\nu\,\mathcal{Z} - \alpha\,\mathcal{E} - \sigma\,\mathcal{R} + \varepsilon_I, \tag{3.5}$$

$$\frac{\mathrm{d}\mathcal{Z}}{\mathrm{d}t} = 0 = -2\nu\,\mathcal{P} - \alpha\,\mathcal{Z} + \eta_I, \tag{3.6}$$

where we have introduced the Reynolds shear stress $\mathcal{R} = \langle u'_x u'_y \rangle$ and the palinstrophy $\mathcal{P} = (1/2)\langle |\nabla\omega|^2 \rangle$. The quantities ε_I and η_I are the injection rates of kinetic energy and enstrophy, respectively, and are fully determined by the stochastic forcing. As already said, in 2D the vorticity of each fluid parcel is conserved, which implies the existence of two quadratic invariants: the energy and the enstrophy. These two constrains led Kraichnan (1967) to propose the existence of two different inertial ranges for 2D turbulence: one with constant energy flux, extending from the injection scale toward larger scales and one with constant enstrophy flux, extending from the injection scale down to the viscous scale. The first leads to an inverse energy cascade and the latter to a direct enstrophy cascade. When dissipation is present, an external forcing $\boldsymbol{f}$ is necessary to produce a statistically stationary state characterised by the injection of turbulent fluctuations at a scale ℓ_f.

Those fluctuations are removed, either at much larger scale $\ell_\alpha \gg \ell_f$ by the friction, or at much smaller scales $\ell_\nu \ll \ell_f$ by viscosity. The two intervals of scales $\ell_f \ll \ell \ll \ell_\alpha$ and $\ell_\nu \ll \ell \ll \ell_f$ are the inertial ranges over which universal statistics are expected. A more quantitative approach is detailed in Kraichnan (1967); Eyink (1996). The energy and enstrophy dissipated by friction at large scales, ε_α and η_α, respectively, are balanced by energy/enstrophy input and by viscous dissipation, i.e. $\varepsilon_I = \varepsilon_\alpha + \varepsilon_\nu$ and $\eta_I = \eta_\alpha + \eta_\nu$. The two scales characteristic of friction and viscosity are $\ell_\alpha^2 = \varepsilon_\alpha/\eta_\alpha$ and $\ell_\nu^2 = \varepsilon_\nu/\eta_\nu$. With the relation at the forcing scale, $\ell_f^2 \simeq \varepsilon_I/\eta_I$, one obtains

$$\frac{\varepsilon_\nu}{\varepsilon_\alpha} = \left(\frac{\ell_\nu}{\ell_f}\right)^2 \left(\frac{\ell_f}{\ell_\alpha}\right)^2 \frac{\eta_\nu}{\eta_\alpha}, \tag{3.7}$$

$$\frac{\eta_\nu}{\eta_\alpha} = \frac{\left(\ell_\alpha/\ell_f\right)^2 - 1}{1 - \left(\ell_\nu/\ell_f\right)^2}. \tag{3.8}$$

In the limit of an extended direct inertial range $\ell_\nu \ll \ell_f$, one has from Eq. (3.7) that $\varepsilon_\nu/\varepsilon_\alpha \to 0$; all the energy is flowing to large scales in an inverse energy cascade. Furthermore, when $\ell_\alpha \gg \ell_f$ one obtains $\eta_\alpha/\eta_\nu \to 0$; all the enstrophy goes to small scales to generate the direct enstrophy cascade (e.g., Kraichnan and Montgomery (1980); Boffetta and Ecke (2012)).

Similarly, by balancing the different dissipative rates in Eqs. (3.5) and (3.6), one can express the friction scale $\ell_\alpha = (\mathcal{E}/\mathcal{Z})^{1/2}$ and the viscous dissipation scale $\ell_\nu = (\mathcal{Z}/\mathcal{P})^{1/2}$. These length scales define two Reynolds numbers: an outer-scale Reynolds number $R_\alpha = \ell_\alpha/\ell_f$ which measures the ratio between inertial and frictional forces, and a viscous Reynolds number $R_\nu = (\ell_f/\ell_\nu)^2$, which balances inertial and viscous forces. These two numbers prescribe the extensions of the inverse energy cascade and of the direct enstrophy cascade, respectively.

Here, we focus on the direct cascade of energy, which corresponds to $\ell_\alpha \gtrsim \ell_f \gg \ell_\nu$, and thus $R_\alpha \sim 1$ and $R_\nu \gg 1$. In the presence of shear ($\sigma > 0$), the flow develops anisotropies and the energy budget is affected by the Reynolds stress. The importance of shear has to be measured by non-dimensionalising it with a characteristic time scale of the flow. Still, the flow time scales are themselves modified by shear, so that the choice cannot be made a priori. In our protocol, the only time scale that is prescribed by the simulation setup is the forcing time scale $\tau_f = (\ell_f^2/\varepsilon_I)^{1/3} = \eta_I^{-1/3}$. The influence of shear on the energy and enstrophy budget is then measured by the non-dimensional shear rate parameter $\bar{\sigma} = \tau_f\sigma$. In the developed regime attained once σ has been prescribed, the shear needs to be compared to the typical dynamical timescale of the direct cascade, namely $\tau_\omega = (2\mathcal{Z})^{-1/2}$. The associated shear rate parameter is then $\sigma^* = \tau_\omega\sigma$.

3.2.1 *Numerical method*

We perform direct numerical simulations by using a pseudo-spectral solver. To construct periodic solutions that account for the mean flow, we follow (Rogallo (1981); Rogers and Moin (1987); Pumir (1996)) and integrate Eq. (3.3) on a distorting frame defined by $x' = x - t\,\sigma\,y$, $y' = y$. The integration domain is the two-dimensional torus $[0, 2\pi]^2$ at resolution 128^2. The distorted grid is regularly shifted back to the Cartesian grid at times multiple of $1/\sigma$. We make use of the vorticity formulation Eq. (3.3), together with the Biot–Savard law to obtain the fluctuating velocity $\boldsymbol{u}'$ as a function of the vorticity ω. The stochastic forcing is approximated as the sum of independent modes whose variances behave as a Gaussian centred at wave number $\bar{k}_f = 4$ and variance $\mu_f = 0.5$, in Eq. (3.4)in order to reduce the anisotropy of the box. Time marching uses a second-order Runge–Kutta method, which is explicit for the non-linear term and implicit for the friction and viscous terms. Furthermore, simulations are performed with an hyperviscosity and hypofriction in place of the viscous dissipation and linear friction term in the right-hand side of Eq. (3.2), that is by replacing it with $(-1)^{p+1}\nu_p\nabla^{2p}\boldsymbol{u}$ and $(-1)^{q+1}\alpha_q\nabla^{-2q}\boldsymbol{u}$, respectively. The motivation for the use of hyperviscosity ($p \geq 1$) and hypofriction ($q \geq 0$) is to reduce the range of scales over which dissipative terms contribute substantially, whereby extending the inertial range for a given spatial resolution (Lindborg and Alvelius (2000); Haugen and Brandenburg (2004)). It has been observed that such a modified dissipation might affect velocity statistics at the transition between inertial and dissipative scales (Frisch et al. (2008)). Still, the situations and effects that we consider here are related to the direct cascade of enstrophy, which is only weakly perturbed. The double cascade scenario (Kraichnan (1967)) can be affected by the weak values of frictional dissipation (α_q), where a semi-stable equilibrium can be set up so that an unstable regime emerges (Tabeling (2002)), as shown below.

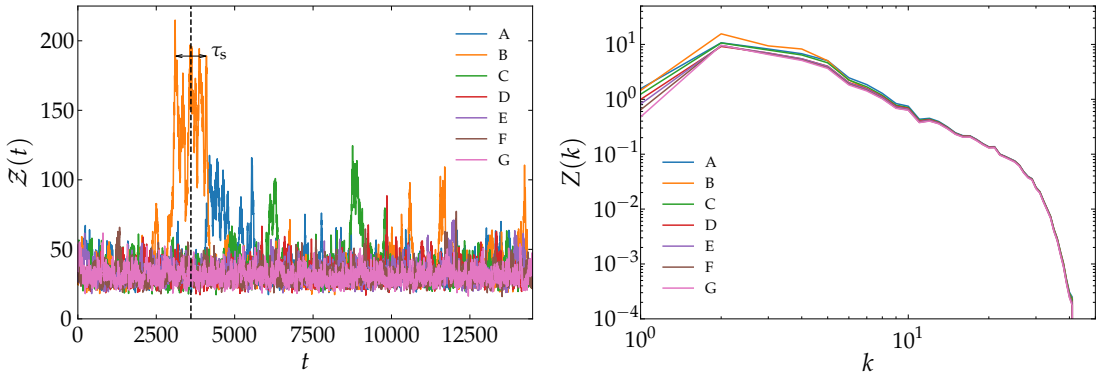

Figure 3.2: Left panel: Enstrophy $\mathcal{Z}(t)$ in time for seven values of friction dissipation α_q labelled in capital letters; (A: $\alpha_q = 0.9$), (B: $\alpha_q = 1$), (C: $\alpha_q = 1.5$), (D: $\alpha_q = 2.5$), (E: $\alpha_q = 3.5$), (F: $\alpha_q = 5$), (G: $\alpha_q = 7$). Here τ_s is the correlation time of the super-structure formation. Right panel: Enstrophy spectrum $Z(k)$ for different values of α_q.

In order to find a stable configuration on long times, in units of turnover time (based on τ_ω), we carried out runs in the case of homogeneous isotropic turbulence (mean shear rate $\sigma = 0$). Different values of the friction coefficient α_q have been tested by covering almost one order of magnitude. These values are labelled in increasing order with capital letters from A to G, and are summarised in the caption of Fig. 3.2.

In Fig. 3.2 (left panel) the enstrophy in time for different runs is shown. The presence of large values for the cases A to C is related to the presence of a semi-stable state. Indeed, at large scales, when neglecting the viscosity effect, the competition between advection, which

redistributes energy among the scales, and friction, which dissipates energy at large scales, becomes a key factor. Accordingly, the dependency of friction dissipation on the enstrophy is confirmed by the spectrum of enstrophy in Fig. 3.2 (right panel).

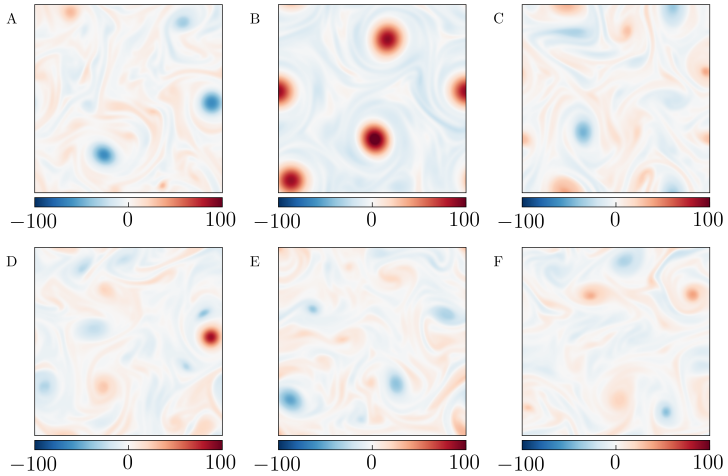

Figure 3.3: Snapshot vorticity field ω for different values of friction dissipation α_q (A-F, G has been omitted resulting very similar to F) taken at a fixed time corresponding to vertical dotted line in Fig. 3.2 (left panel). Blue corresponds to negative values (cyclonic eddies) and red to positive values (anticyclonic eddies).

The instantaneous vorticity fields are shown in Fig. 3.3, where time has been taken within a single burst of enstrophy (and corresponds to the vertical dotted line of Fig. 3.2 (left panel)). These bursts in time of enstrophy lead to the formation of intense vortex structures (counter- or clockwise) which are four times larger, in terms of amplitude, for the cases A and B compared to the others. The origin of these super-structures within the flow can be explained assuming that in some regions of the domain the vorticity becomes parallel to the velocity, that implies the formation of Beltrami regions (as a solution of Euler equation at large scale), where the advection term becomes zero. This means that if the frictional term is not large enough to dissipate the contents of energy at large scale, the emergence at some localised wave number of these super-structures will occur. The correlation time τ_s associated to the permanence of bursts in time of $\mathcal{Z}$ is visually depicted in Fig. 3.2 (left panel). This characteristic time can be estimated considering the vorticity Eq. (3.3) in the Fourier space as an Ornstein–Uhlenbeck process. That is, replacing the linear friction with the hypofriction term, neglecting the viscous effect at large scale and assuming the advection term zero under the Beltrami property, this leads to,

$$\partial_t \hat{\omega} = -\alpha_q \ell_f^{2q} \hat{\omega} + \hat{f}_\omega \tag{3.9}$$

where $\hat{f}_\omega$ is a white noise. Therefore, the correlation time of this process can be read as $\tau_s \approx \alpha_q^{-1} \ell_f^{-2q}$ (as in Fig. 3.2 (right panel)) and can result to be very long for small α_q.

The spontaneous emergence of these super-structures along time affects the probability distribution of the vorticity as shown in Fig. 3.4 (left panel), where the cases A to C result to be strongly skewed. From this last observation, a question arises: either the system explores all accessible phase space with equal probability, or it can be trapped for long in a part of it. This question wants to shed light on the mechanism ensuring ergodicity in 2D turbulence, and on the role of the friction parameter in order to reach an equilibrium state in a finite time (even longer but finite). The convergence of the vorticity field (i.e. ergodicity assumption) has

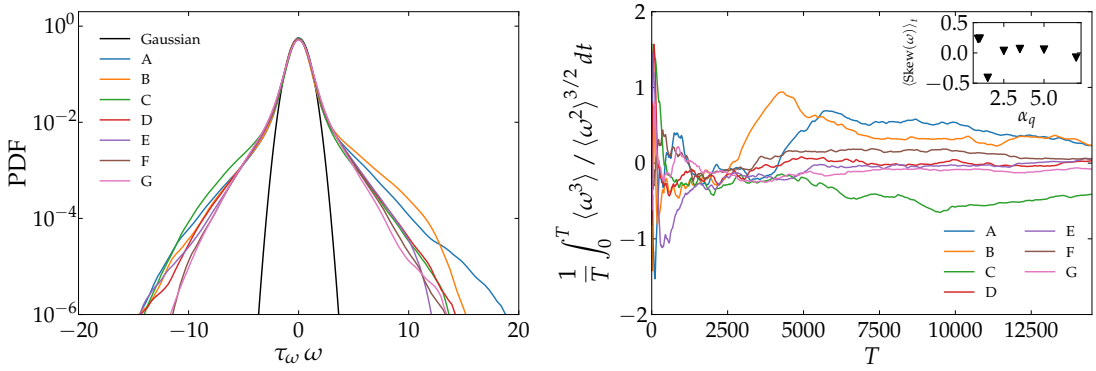

Figure 3.4: Left panel: Probability density function (PDF) of the vorticity for different values of friction dissipation α_q. Right panel: Cumulative integral for the skewness of vorticity. The inset shows the average values in time of the skewness of vorticity as a function of α_q.

been tested, as shown in Fig. 3.4 (right panel). As we can see, the cumulative integral for the skewness of the vorticity, in cases A to C, does not reach an equilibrium state and we can assert that even for longer times other bursts of enstrophy occurs driving away the system far from the equilibrium state. In conclusion, this analysis exhibits the strong dependence of friction dissipation α_q on the statistics of vorticity and on the tendency of 2D turbulent systems to reach a steady statistical equilibrium at long times. Hereinafter, the case F is chosen to investigate the rods' orientation in a turbulent shear flow since its distribution seems to be the most symmetric one.

Several numerical experiments varying the mean shear rate σ have been performed. The forcing mechanism has been kept constant by producing an injection rate ε_I and η_I and the forcing scale $\ell_f \approx 1.56$ (in units where the box size is 2π). Figure 3.5 shows how the global quantities, i.e. $\mathcal{E}$, $\mathcal{Z}$, $\mathcal{P}$ and $\mathcal{R}$, vary when the shear rate σ is increased. The left panel demonstrates that the kinetic energy is depleted down to $\approx 20\%$ of its value at $\sigma = 0$. This change of kinetic energy is partly explained by a decrease of the Reynolds stress, as observed on the centre panel of Fig. 3.5. The three quantities $\mathcal{E}$, $\mathcal{Z}$ and $\mathcal{P}$ characterise the fluid and the structures within the flow. Another important quantity, in the presence of shear flow, is the Reynolds stress (centre panel) which decreases as σ increases (not for the last value); the negative sign comes from the imposed direction of the mean shear rate.

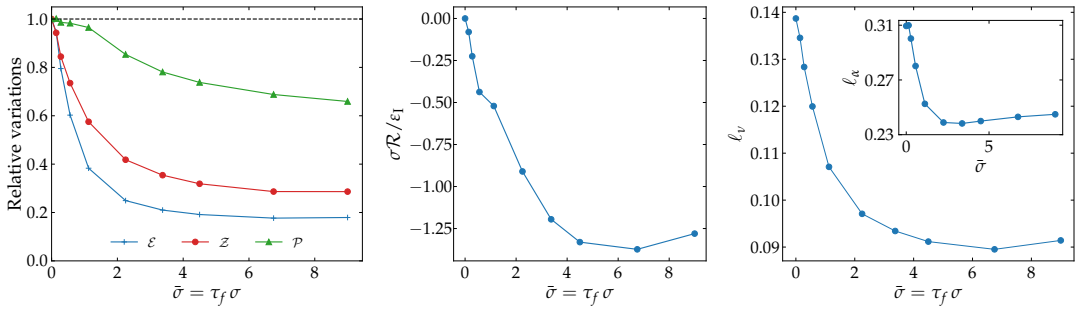

Figure 3.5: Left panel: Variations of the kinetic energy ($\mathcal{E}$), enstrophy ($\mathcal{Z}$) and palinstrophy ($\mathcal{P}$) as a function of the shear rate σ, here expressed in units of the forcing time $\tau_f = (\ell_f^2/\varepsilon_I)^{1/3}$. Global quantities are rescaled by their values at $\sigma = 0$. Centre panel: Reynolds stress (normalized by the kinetic energy), as a function of σ. Left panel: Viscous length scale ℓ_v associated to small scale, as a function of the shear rate parameter $\bar{\sigma}$. In Inset: Variations of the friction length scale ℓ_α associated to large scale.

The resulting modifications of the turbulent properties are summarized in the right panel of Fig. 3.5, which represents the two typical scales ℓ_ν and ℓ_α (in inset). These are the typical variation scales of the vorticity and velocity, respectively. Particularly, in 2D turbulence, the characteristic friction length scale is associated to the inverse energy cascade, while the viscous length scale is characterised by the direct cascade of enstrophy. These two decrease as the shear rate increases, which is confirmed by the relative variations of energy and enstrophy, in the left panel.

To get further insights on the spatial properties of the turbulent field, we have plotted on Fig. 3.6 the kinetic energy spectrum $E(k)$, obtained for different values of the mean shear rate. The spatial scaling of the turbulent velocity field does not depend strongly from the value of the shear. For all σ^*, one observes a clear inertial range where $E(k) \sim k^{-n}$, with $n > 3$, that is a spectrum steeper than Kraichnan's prediction. The energy content of the smallest mode seems to strongly vary as a function of the shear rate. This is due to the fact that the spectrum is evaluated from discrete modes that are defined with respect to the distorted coordinates. In addition, the peak values observed in the energy spectrum matches with the imposed mean forcing mode $\bar{k}_f = 4$.

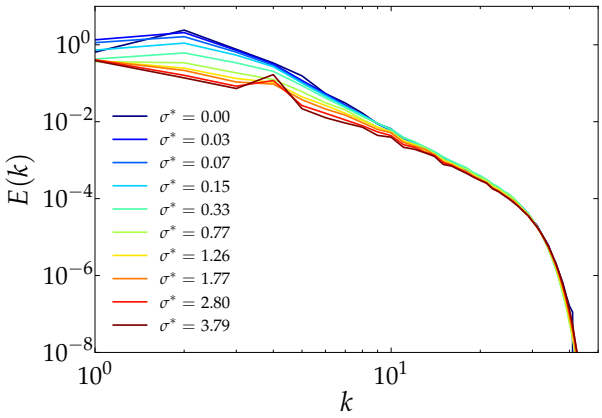

Figure 3.6: Shell-averaged kinetic energy spectra of the turbulent fluctuations, defined as $E(k) = \sum_{k \leq |\boldsymbol{k}'| < k+1} \langle |\hat{\boldsymbol{u}}'(\boldsymbol{k})|^2 \rangle$ for various values of the shear rate.

3.2.2 *Preferential alignment of rods*

The flow is seeded with uniformly distributed tracers that are tracked during its time evolution. Each tracer is provided with an orientation which is integrated numerically along its trajectory. In general this orientation is described by Jeffery's equation (3.1). In 2D, this equation can be conveniently simplified rewriting the vector $\boldsymbol{p} = (p_x, p_y) = (\cos\theta, \sin\theta)$ in terms of a folded orientation angle $\bar{\theta} = \arctan(p_x/p_y) \in [-\pi/2, \pi/2]$ with respect to a fixed axis. Finally, the evolution of tracers' positions $\mathbf{X}(t)$ and unfolded orientations $\theta(t) \in \mathbb{R}$ is obtained according to,

$$\frac{\mathrm{d}\mathbf{X}}{\mathrm{d}t} = \boldsymbol{u}(\mathbf{X}, t), \tag{3.10}$$

$$\frac{\mathrm{d}\theta}{\mathrm{d}t} = \frac{\sigma}{2}(\cos(2\theta) - 1) + \frac{\omega}{2} - \partial_x u'_x \sin(2\theta) + \frac{1}{2}(\partial_x u'_y + \partial_y u'_x)\cos(2\theta), \tag{3.11}$$

here the incompressibility condition has been used to simplify the last equation.

The unfolded orientation angle θ, as for the Jeffery's dynamics, is driven from one side by the antisymmetric part of the velocity gradient $\omega/2$, and on the other, by its symmetric part.

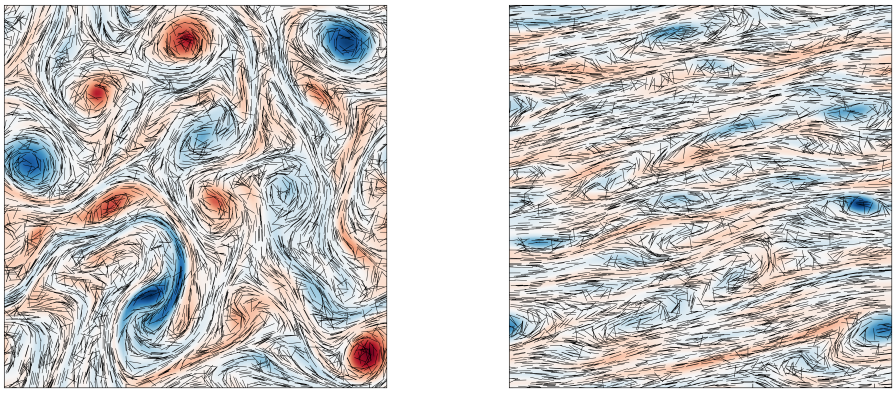

Figure 3.7: Vorticity field ω (coloured background) for two different values of the shear rate parameter σ^*. Blue corresponds to negative values (cyclonic eddies) and red to positive values (anticyclonic). On the top of this field, the orientations of fibres are shown as black segments.

Considering that Eq. (3.1) is invariant with respect to the transformation $\boldsymbol{p} \to -\boldsymbol{p}$, then the preferential alignment can be regarded in terms of the folded angle $\bar{\theta}(t) \in [-\pi/2, \pi/2]$.

Figure 3.7 shows two snapshots of an instantaneous orientation of rods, together with the vorticity field, in the developed regime, in the absence of shear (left panel) and when shear is present (right panel). The particle orientation is visually correlated with the vorticity structures, i.e. rods tend to be trapped in strong cyclonic and anticyclonic vortices for $\sigma^* = 0$ and to line up along stretched filaments, when σ^* becomes large. Furthermore, one clearly observes that anisotropies develop in the vorticity field. First, the vorticity becomes skewed toward negative values (shown in blue). This is due to the depletion of anticyclonic vortices by the shear. Second, vortex filaments tend to be stretched by the shear and to align with an oblique angle. In order to quantify these effects, the one-point one-time probability distribution (PDF) of vorticity is shown in left panel of Fig. 3.8. Even if the mean value remains zero, the distribution becomes strongly skewed toward cyclonic (negative) values when σ^* increases. At $\sigma^* = 0$, the distribution consists of a Gaussian core, followed by exponential tails, as predicted for instance by Falkovich and Lebedev (2011). Such a behaviour persists at negative values when shear is present. The positive tail is still exponential but with a decay rate that increases as a function of σ^*. The main effect of shear is thus to deplete anticyclonic vortices.

Figure 3.8 (left panel) shows the PDF of $\bar{\theta}$ for different values of the shear parameter σ^*. While it is almost uniform when shear is weak, it develops a peak that moves towards $\bar{\theta} = 0$ when the shear becomes stronger. In inset is reported the average value of folded orientation angle $\langle\bar{\theta}\rangle$ as a function of shear rate. The mean orientation can be directly related to the behaviour of the vorticity distribution, namely, as soon as it becomes skewed, the cyclonic vortices start to take down by the small effect of the shear resulting in an increase of the mean orientation (increasing part of the plot). When the shear becomes sufficiently large the vorticity structures are replaced by elongated filaments in the direction of the mean shear, and rods tend to align along them, so that the mean orientation decreases (decreasing part of the plot). In addition, $\langle\bar{\theta}\rangle$ can be interpreted as a direct measurement of the flow anisotropies since it expresses the pitch angle with respect to the horizontal direction, for vorticity filaments. Indeed, in perspective, it could be interesting to measure the mean angle between the components of vorticity gradient $\nabla\omega$ to understand if there is a perfect agreement between this measurement and $\langle\bar{\theta}\rangle$.

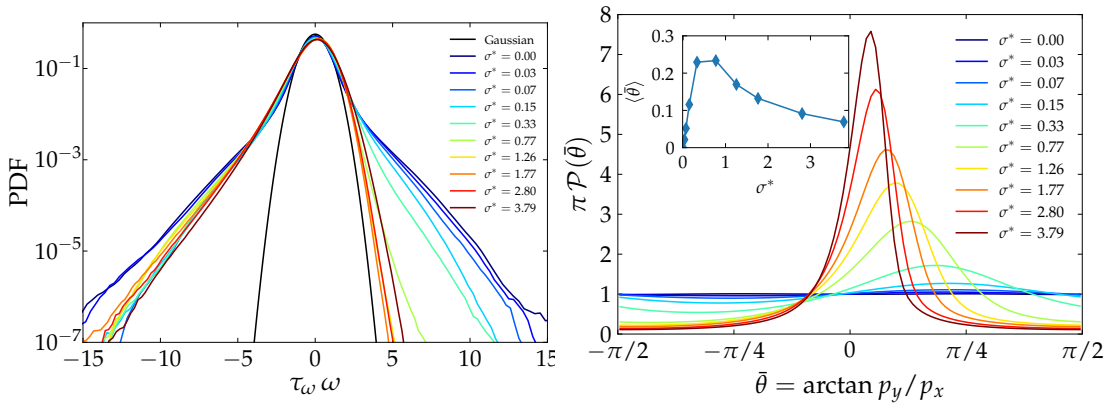

Figure 3.8: Left panel: Probability density function (PDF) of the vorticity ω for different values of the shear rate parameter σ^*. Right panel: Distribution of the rods angle $\bar{\theta} = \arctan p_y/p_x$ with respect to the horizontal for different values of the shear. Inset shows the average value of $\bar{\theta}$ as a function of σ^*.

3.3 ORIENTATION MODEL

The Jeffery's equation (3.1) can be investigated by modelling the velocity gradient tensor A_{ij} in the Lagrangian reference frame and then integrating along particles trajectories. A number of recent numerical and theoretical studies (presented in Chapter 2) attempted to recover the statistics of orientation of non-spherical particles (rod, ellipsoid, disk) by assuming that the velocity gradients obey to isotropic Gaussian statistics, e. g., are the result of linear Ornstein–Uhlenbeck processes (Brunk et al. (1998); Pumir and Wilkinson (2011); Vincenzi (2013)). Moreover, this Gaussian assumption, albeit restrictive, allowed a fully analytical solution for the probability density function of the angular orientation (Vincenzi (2013)). Otherwise, more refined model for A_{ij} (along Lagrangian trajectory) have been proposed in literature (e. g., Girimaji and Pope (1990); Chertkov et al. (1999); Chevillard and Meneveau (2006); Biferale et al. (2007)) with the aim of representing specific features encoded in the tensor, such as the alignment of vorticity with respect to the strain-rate eigenvectors, rate of deformation and shapes of fluid material volumes, non-Gaussian statistics or intermittency, and they have been the focus of extensive studies (Meneveau (2011)). In contrast with the HIT case, few analytical results seem to exists on shear flow geometry for the probability distribution of orientations in homogeneous shear turbulence. The orientation motion of rod-like polymers was examined either analytically (Turitsyn (2007)) or numerically (Chertkov et al. (2005); Celani et al. (2005)) in a random flow from the superposition of a mean shear and short correlated isotropic fluctuation. Otherwise, the dynamics of semi-flexible objects in an extensional flow was analysed by Plan and Vincenzi (2016).

In the following section a Lagrangian stochastic model for the rod orientation will be presented. Its formulation is not restricted to two-dimensional flows (the subject of this chapter) but its validity extends also to three-dimensions. To describe and model the behaviour of a rod-like particle injected in a turbulent flow, in the presence of a mean shear velocity component along the x-axis, some assumptions have to be made, due to the interplay between spatial and temporal properties of the velocity field.

As introduced in Chapter 2, the evolution between initial and final configuration of a fluid blob can be described in terms of the deformation gradient tensor $D_{ij}(t, t_0; \boldsymbol{x}^0) = \partial X_i(t; \boldsymbol{x}^0, t_0)/\partial x_j^0$ which expresses the evolution of the infinitesimal separation vector $\boldsymbol{r}$ of two points advected by the flow (Wilkinson et al. (2009)), (the dependencies on $\boldsymbol{x}^0$ will be omitted from now on). Furthermore, it has been shown (Balkovsky and Fouxon (1999); Ni et al.

(2014)) that the rod will be preferentially aligned with the longest principal axis of the ellipsoid, and at long times it will be perfectly oriented in the direction of the eigenvector corresponding with the largest eigenvalue of the deformation gradient tensor.

Thus, in the limit of small rod (ellipsoid with high aspect ratio), the rod approximates the separation vector, and one can determine the orientation $\boldsymbol{p}(t) = \boldsymbol{r}(t)/\|\boldsymbol{r}(t)\|$ in Eq. (3.1) from the characterisation of the deformation gradient tensor (by renormalising the vector $\boldsymbol{r}$). Thus, the stochastic Lagrangian model for the motion of rods in turbulence takes into account the dynamics of $\boldsymbol{r}(t)$, as we will detail hereafter.

To follow the evolution of the fluid element, it is natural to work in the Lagrangian reference frame where the velocity $\boldsymbol{u}(\mathbf{X}(t), t)$ simply follows the Lagrangian trajectories $\mathbf{X}(t)$. Since the variation of the velocity field on the scale of the fluid element ($L \ll \ell_v$) is smooth, due to the viscosity, it can be expanded in a Taylor series; namely the velocity difference between two fluid points is given by the velocity gradient multiplied by the distance (so called Batchelor (1959) regime). Then the kinematics of the fluid element is fully determined by the velocity gradient tensor. In this regime, the Lagrangian flow is described by the end-to-end separation vector $\boldsymbol{r} = \mathbf{X}_1 - \mathbf{X}_2$ between two fluid particles obeying to the ordinary differential equation,

$$\frac{dr_i(t)}{dt} = A_{ij}(t)\, r_j(t), \tag{3.12}$$

where $A_{ij} = \partial_j u_i(\mathbf{X}(t), t)$ is Lagrangian velocity gradient. In the presence of a mean shear contribution the velocity gradient can be decomposed into the sum of mean and fluctuating part, i.e. $A_{ij} = \langle A_{ij} \rangle + A'_{ij}$. The finite integral Lagrangian correlation time τ_{I}^{ijkl} of fluctuations is defined as,

$$\tau_{\mathrm{I}}^{ijkl} = \frac{1}{\langle A'^2_{ij}(0) \rangle^{1/2} \langle A'^2_{kl}(0) \rangle^{1/2}} \int_{-\infty}^{\infty} \langle A'_{ij}(0) A'_{kl}(\tau) \rangle \, d\tau \tag{3.13}$$

where the integrand is the correlation of the velocity gradient $\mathcal{C}_{ijkl}(\tau) = \langle A'_{ij}(0) A'_{kl}(\tau) \rangle$ and the signal of velocity gradient has been assumed stationary in time ($\tau = t - t'$). Moreover, the solution of Eq. (3.12) can be written in terms of the Lagrangian deformation tensor $D_{ij}(t, 0)$ (with $t > 0$) according to,

$$r_i(t) = D_{ij}(t, 0) r_j(0), \tag{3.14}$$

where $D_{ij}(t, 0)$ characterises the full history of the distortion withstand to the fluid element from the initial time $t = 0$ up to time t (see Section 2.2.2). We recall that the matrix $D_{ij}(t, 0)$ satisfies $dD_{ij}(t, 0)/dt = A_{ij}(t) D_{ij}(t, 0)$ with $D_{ij}(0, 0) = \delta_{ij}$ (where δ_{ij} is the Kronecker delta) and the solution can be written in the following form,

$$\begin{aligned} \boldsymbol{D}(t, 0) &= \mathcal{T} \exp\left[\int_0^t \boldsymbol{A}(s) ds \right] \\ &= \mathbb{1} + \sum_{n=1}^{\infty} \int_0^t \int_0^{s_n} \cdots \int_0^{s_2} \boldsymbol{A}(s_n) \boldsymbol{A}(s_{n-1}) \cdots \boldsymbol{A}(s_1) ds_1 \cdots ds_{n-1} ds_n, \end{aligned} \tag{3.15}$$

where $\mathcal{T}$ is the time ordering operator (or Dyson (1949) series). It is worth noticing that if the velocity gradient matrix and its integral commute, the series is truncated at the first order, and classical exponential solution is recovered; this means that all the difficulties rely on commutation operations, which make the time ordering operator not very handy for direct calculations. The semi-group property of evolution matrix allows to write $\boldsymbol{D}(t, 0) = \boldsymbol{D}(q\Delta t, (q-1)\Delta t) \cdots \boldsymbol{D}(\Delta t, 0)$ with $t = q\Delta t > (q-1)\Delta t \ldots 2\Delta t > \Delta t > 0$, where we have fixed the resolution time scale of our model to Δt. Somehow we are defocusing the signal associated to the evolution matrix by an amount above which, it becomes smooth. Namely, the model will be the result of a coarse graining procedure, where the finer details of the dynamics of

$D_{ij}(\Delta t, 0)$ will be discarded. In addition, by choosing a time scale resolution of the model smaller than the typical turnover time of the vorticity (which is of the order of the inverse of velocity gradient fluctuations) $\Delta t \ll \tau_\omega$, Eq. (3.15) can be is simplified by the following approximation. In this case, the series in expression (3.15) have been cut at $n = 1$ and the rest is of the order $\mathcal{O}(\Delta t/\tau_\omega)$. So the leading term within the time interval $[0, \Delta t]$ reads

$$D_{ij}(\Delta t, 0) \simeq \delta_{ij} + \int_0^{\Delta t} \langle A_{ij} \rangle (s) ds + \int_0^{\Delta t} A'_{ij}(s) ds + \mathcal{O}\left(\frac{\Delta t}{\tau_\omega}\right), \tag{3.16}$$

where the decomposition $A_{ij} = \langle A_{ij} \rangle + A'_{ij}$ has been used.

Considering the case where Δt is much larger than the maximum value of the integral Lagrangian correlation time of the velocity gradient $\tau_I = \max(\tau_I^{ijkl})$, the fluctuation contribution behaves as a sum of many independent, identically distributed, random variables Z_q^{ij} which allows to rewrite the integral fluctuations in Eq. (3.16) as,

$$S_n^{ij} = \sum_{q=1}^{n} Z_q^{ij} = \sum_{q=1}^{n} \int_{(q-1)\tau_I}^{q\tau_I} A'_{ij}(s) ds \tag{3.17}$$

where $n \propto \Delta t/\tau_I$. These fluctuations S_n^{ij} are governed by the central limit theorem $S_n^{ij}/(\sqrt{2n}\,\zeta)$, where ζ^2 is the variance of Z_q^{ij}, becomes, for large n, a Gaussian random variable. The case of short correlated strain was first solved by Kraichnan (1968) for the problem of passive scalar transport, and most of the analytic results have been obtained in this frame, so called 'Kraichnan model', where velocity statistics are assumed to be Gaussian and delta-correlated in time. The variance of white noise Gaussian fluctuations reads,

$$\begin{aligned} 2n\,\zeta^2 &= 2\,\frac{\Delta t}{\tau_I} \langle \int_{(q-1)\tau_I}^{q\tau_I} A'_{ij}(s) ds \int_{(q-1)\tau_I}^{q\tau_I} A'_{kl}(s) ds \rangle \\ &\simeq 2\,\frac{\Delta t}{\tau_I} \tau_I^2 \langle A'_{ij}(0) A'_{kl}(0) \rangle, \end{aligned} \tag{3.18}$$

where the velocity gradient fluctuations are assumed constant within the interval τ_I. Therefore, the 2-point correlation function can be written as (for $t > t'$),

$$\langle S_n^{ij}(t) S_n^{kl}(t') \rangle = 2\,\tau_I\, \mathcal{C}_{ijkl}(0) \min(t', t), \tag{3.19}$$

where $\mathcal{C}_{ijkl}(0) = \langle A'_{ij}(0) A'_{kl}(0) \rangle$. The maximum value of the integral Lagrangian correlation time τ_I provides a measurement of the Lagrangian velocity gradient memory. In (3.19), we remark that the information about the different components of τ_I^{ijkl} ((3.13)) has been not considered since we took the maximum over $ijkl$.

In order to recover that relevant information in anisotropic flows, i.e. considering the full tensor structure of the integral Lagrangian correlation time τ_I^{ijlkl}, we introduce also a different approximation for the 2-point correlation function of $S_n^{ij}(t)$ that depends upon the integral of correlation. We underline that when τ_I is finite in the prescribed regime $\Delta t \gg \tau_I$, an effective diffusive regime arises, as observed by Taylor (1922). Specifically, a general relation for an effective diffusion coefficient can be derived employing the *Leibniz rule* (following the same argument of Shalchi (2011)),

$$\mathcal{C}_{ijkl}^{\text{eff}} = \frac{1}{2} \left(\langle \int_0^\infty \mathcal{C}_{ijkl}(\tau) d\tau \rangle + \langle \int_0^\infty \mathcal{C}_{klij}(\tau) d\tau \rangle \right). \tag{3.20}$$

In this way, the case where fluctuations are stationary white in time Gaussian processes can be represented by the 2-point correlation function,

$$\langle S_n^{ij}(t) S_n^{kl}(t') \rangle \simeq 2\,\mathcal{C}_{ijkl}^{\text{eff}} \min(t', t). \tag{3.21}$$

It is important to remark that, in order to derive the model for the evolution matrix, two different hypotheses have been taken into account: the first, i.e. $\Delta t \ll \tau_\omega$, leads to consider only the leading term of the expression (3.15) and the second, i.e. $\Delta t \gg \tau_\mathrm{I}$, leads to assume a short correlated velocity gradient tensor. This means that the resolution time scale Δt of our model has to satisfy $\tau_\mathrm{I} \ll \Delta t \ll \tau_\omega$, implying that the validity of the model can be defined in terms of the Kubo number $Ku = \tau_\mathrm{I}/\tau_\omega \ll 1$.

The parameter Ku turns out to be a dimensionless measurement of the correlation time with respect to typical turnover time of the vorticity and it determines the domain of validity of various turbulent regimes, such as linear processes (diffusive) or more complex ones (sub- and super-diffusive). Furthermore, this parameter is a measure of particle capacity of exploring the spatial structure of the velocity field, before that it drastically changes in time and space. In other words, Ku determines the importance of the Lagrangian non-linearity within the velocity field. When $Ku \ll 1$ we are in the diffusive regime approximation, which confirms the above analysis.

In Eq. (3.16) we have identified A'_{ij} as a Gaussian process stationary in time, whose integral can be reinterpreted in terms of a Wiener matrix, such that the integral of fluctuating part becomes a stochastic one. The standard ambiguity between the choice of Itô or Stratonovich interpretation for the SDE associated to $\boldsymbol{r}(t)$, it is here solved by the presence of asymptotic expansion for the time order exponential (Castell (1993)). Namely, the generalisation of Dyson series to stochastic differential equations (SDEs) were proposed by several authors (Castell (1993); Blanes et al. (2009); Kamm et al. (2020)) and corresponds to the Stratonovich prescription of Eq. (3.14). The model for $\boldsymbol{r}(t)$ is recovered by replacing Eq. (3.16) into Eq. (3.14).

Finally, using the group property on the operator D_{ij} to recombine the evolution matrix up to the instant of time t, the solution of the Stratonovich stochastic equation in Eq. (3.12) can be expressed as,

$$r_i(t) = r_i(0) + \int_0^t \langle A_{ij} \rangle (s)\, r_j \, ds + \int_0^t \beta_{imj}\, r_j \circ d\mathrm{w}_t^m \tag{3.22}$$

where $\circ$ corresponds to the integral in Stratonovich form. The third order tensor β_{imj} has been introduced in order to link the model fluctuations and the Lagrangian correlation function through the equality,

$$\beta_{imj}\beta_{kml} = 2\, \mathcal{C}^{\mathrm{eff}}_{ijkl}. \tag{3.23}$$

To make a comparison between the model and DNS, it is useful to adimensionalise Eq. (3.22) with the characteristic quantity τ_ω,

$$\begin{aligned} dr_i(t) &= \langle A_{ij} \rangle\, \tau_\omega\, r_j\, d\left(\frac{t}{\tau_\omega}\right) + \beta_{imj}\sqrt{\tau_\omega}\, r_j \circ d\left(\frac{d\mathrm{w}_t^m}{\sqrt{\tau_\omega}}\right) \\ &= \langle A^*_{ij} \rangle\, r_j\, dt^* + \beta^*_{imj}\, r_j \circ d\mathrm{w}^m_{t^*}. \end{aligned} \tag{3.24}$$

To simplify the notation, we are going to omit the star $(*)$ referring all quantities in model (Eq. (3.24)) to dimensionless ones. Finally, the stochastic version of Jeffery's equation (3.1) can be obtained by normalising Eq. (3.22) by its length, i.e. $\boldsymbol{p}(t) = \boldsymbol{r}(t)/\|\boldsymbol{r}(t)\|$.

Limiting now ourself to the 2D case, it is possible to reduce the complexity of the analysis and the associated stochastic calculus, following the same procedure made in the DNS. Indeed, reintroducing the folded orientation angle $\bar{\theta}(t) = \arctan(p_y(t)/p_x(t)) = \arctan(r_y(t)/r_x(t))$ valued in the torus domain $\mathbb{T} = [-\pi/2, \pi/2]$, and applying the Itô formula to Eq. (3.22) (see derivation in Appendix A.1), the SDE for $\bar{\theta}(t)$ can be expressed as the toroidal equation,

$$d\bar{\theta}_t = a(\bar{\theta}_t)dt + b(\bar{\theta}_t)dW_t \quad \text{in } \mathbb{T}, \tag{3.25}$$

where W_t is introduced as a new one dimensional Brownian motion, after making use of the martingales representation of the scalar stochastic integral arriving with the Itô formula (see Appendix A.1). Besides, the coefficients of Eq. (3.25) are respectively,

$$a(\bar{\chi}) = \frac{\sigma^*}{2}\left(\cos(2\bar{\chi}) - 1\right) + \frac{1}{4}\partial_{\bar{\chi}} b^2(\bar{\chi}), \tag{3.26}$$

$$b(\bar{\chi}) = \left(\gamma_0 + \gamma_1 \sin(2\bar{\chi}) + \gamma_2 \sin(4\bar{\chi}) + \gamma_3 \cos(2\bar{\chi}) + \gamma_4 \cos(4\bar{\chi})\right)^{1/2}. \tag{3.27}$$

Here we made the distinction between the stochastic variable $\bar{\theta}_t$ and canonical variable $\bar{\chi}$. The parameters γ_i (with $i = 0, \ldots, 4$), as detailed in Appendix A.1 are

$$\begin{aligned}
\gamma_0 &= f + \frac{k}{2} + \frac{3}{4}(\ell + g) \\
\gamma_1 &= 2(h - j) \\
\gamma_2 &= -(h + j) \\
\gamma_3 &= (\ell - g) \\
\gamma_4 &= \frac{1}{2}\left(-2f + k + \frac{1}{2}(\ell + g)\right)
\end{aligned} \tag{3.28}$$

where $f = \mathcal{C}_{1111}$, $g = \mathcal{C}_{1212}$, $h = \mathcal{C}_{1112}$, $j = \mathcal{C}_{1121}$, $k = \mathcal{C}_{1221}$ and $\ell = \mathcal{C}_{2121}$. In the following the forth-order tensor $\mathcal{C}_{ijkl}$ is a generic tensor that need to be specified. Particularly, it will replaced by $\mathcal{C}^{\text{iso}}_{ijkl}$, $\mathcal{C}^{\text{aniso}}_{ijkl}$ or $\mathcal{C}^{\text{int}}_{ijkl}$, depending on the choice of the approach considered in order to model $\mathcal{C}^{\text{eff}}_{ijkl}$ in Eq. (3.23) as we will see in Section 3.3.1.

In an attempt to compare the results of orientation dynamics in the DNS case with the results produced by the model, we first derive the stationary distribution of the folded angle. It is useful to introduce the Fokker–Planck equation, associated to the dynamics of $\bar{\theta}_t$ described by Eq. (3.25), in the form of continuity equation,

$$\partial_t \mathcal{P}(\bar{\chi}, t) + \partial_{\bar{\chi}} j(\bar{\chi}, t) = 0, \tag{3.29}$$

having defined the *probability flux* or *current* to be,

$$j(\bar{\chi}, t) := a(\bar{\chi})\mathcal{P}(\bar{\chi}, t) - \frac{1}{2}\partial_{\bar{\chi}}\left(b^2(\bar{\chi})\mathcal{P}(\bar{\chi}, t)\right), \tag{3.30}$$

which represents the amount of flow of probability across a fixed point per unit time.

The probability flux associated to the Fokker–Planck equation (3.29) has been related in literature to the caustic formation rate, to study the clustering of particles suspended in a random flow, in cases where the inertia of the particles is significant (Wilkinson and Mehlig (2005)). In particular, the probability flux contains information about the mixing rate of particles, such as collision rate (Wilkinson and Mehlig (2005)). In the present work, new insights on the probability flux, that can be used to characterise the rotation rate ('tumbling rate') of an anisotropic particle, will be discussed in Section 3.4.

Due to the fact that SDE (3.25) is a folded toroidal diffusion, the Fokker–Planck equation is complemented with periodic boundary conditions $\mathcal{P}(-\pi/2, t) = \mathcal{P}(\pi/2, t)$, and the usual normalisation of unitary mass condition. Moreover, the process $\bar{\theta}_t$ is an ergodic diffusion as detailed in García-Portugués et al. (2019), so that a unique invariant measurement, describing the equilibrium of $\bar{\theta}_t$, exists, given as the stationary solution $\mathcal{P}_{st}(\bar{\chi})$ of Eq. (3.29),

$$\partial_{\bar{\chi}}\mathcal{P}_{st}(\bar{\chi}) = \frac{1}{b^2(\bar{\chi})}\left[2a(\bar{\chi}) - \partial_{\bar{\chi}} b^2(\bar{\chi})\right]\mathcal{P}_{st}(\bar{\chi}) + \frac{2\mathcal{J}}{b^2(\bar{\chi})}, \tag{3.31}$$

where the probability flux is constant in time for the stationary distribution and has been identified with $j(\bar{\chi}) = -\mathcal{J}$. It is important to remark that the diffusion coefficients $b^2(\bar{\chi}) > 0$ is required to be strictly positive, such that Eq. (3.31) turns out to be well defined. This assumption has been verified in Appendix A.2. Now, integrating Eq. (3.31) yields,

$$\mathcal{P}_{st}(\bar{\chi}) = \frac{e^{\Psi|_{-\pi/2}^{\bar{\chi}}}}{\mathcal{N}} \left(1 + 2\mathcal{A} \int_{-\frac{\pi}{2}}^{\bar{\chi}} \frac{e^{-\Psi|_{-\pi/2}^{s}}}{b^2(s)} ds \right). \tag{3.32}$$

To simplify the notation, the integral functional $\Psi|_{-\pi/2}^{s} = \int_{-\pi/2}^{s} \frac{1}{b^2(r)} \left(2a(r) - \partial_r \left[b^2(r) \right] \right) dr$ has been introduced. Imposing the periodicity and unitary mass, the condition the two constant factors $\mathcal{A}$ and $\mathcal{N}$ introduced in Eq. (3.32) are, respectively:

$$\mathcal{A} = \frac{e^{-\Psi|_{-\pi/2}^{\pi/2}} - 1}{2 \int_{-\pi/2}^{\pi/2} \frac{e^{-\Psi|_{\pi/2}^{s}}}{b^2(s)} ds}, \tag{3.33}$$

$$\mathcal{N} = \int_{-\frac{\pi}{2}}^{\frac{\pi}{2}} e^{\Psi|_{-\pi/2}^{r}} \left(1 + 2\mathcal{A} \int_{-\frac{\pi}{2}}^{r} \frac{e^{-\Psi|_{-\pi/2}^{s}}}{b^2(s)} ds \right) dr. \tag{3.34}$$

The asymptotic long time behaviour corresponds, in the presence of the mean shear $\sigma^* > 0$, to a non zero probability flux that reads,

$$\mathcal{J} = \mathcal{P}_{st}(\pi/2)\mathcal{A}. \tag{3.35}$$

Moreover, the positive (or negative) sign of the probability flux is related to the sign of the velocity component of the mean shear σ^*.

3.3.1 *Correlations of turbulent gradients induced by shear*

In order to compute the stationary distribution of the model Eq. (3.32) and compare it with DNS results, we need to specify the form of the effective diffusion tensor $\mathcal{C}_{ijkl}^{\text{eff}}$ and consequently β_{imj} (see Eq. (3.20)-(3.24)) associated to the homogeneous turbulent shear flow.

In 3D turbulence, models and simulations commonly assume the diffusion coefficient tensor to be homogeneous and isotropic. Namely, statistical turbulence modelling has been dominated by the ideas of Kolmogorov hypothesis, known as the 'K41' model (Frisch (1995)). The K41 hypothesis assumes that, in intense turbulence and far away from any boundaries or singularities, the statistics of turbulent flow should be universal at length and time scales that are small compared with the injection of energy into the flow. If these small-scale statistics are to be universal, they must be independent of the large-scale flow structures. In particular, K41 predicts that at small scales the turbulence should 'forget' any preferred directions of the large-scale flow and that the small-scale fluctuations should be statistically homogeneous and isotropic. Conversely, in 2D case this picture is not longer valid due to the presence of intense structures at all scales. Moreover, the coarse-grained model is aimed to reproduce the behaviour of the system on scales much larger than the Kolmogorov viscous scale ℓ_ν and an effective diffusion tensor arises which accounts for the presence of anisotropies within the turbulent flow. Thus, the isotropic homogeneous assumption on the correlations of the velocity gradient can not provide a realistic behaviour of the model in the presence of mean shear flow.

Here three different choices on the construction of velocity gradient correlation tensor have been considered. Indeed, we will proceed in the presentation from the straightforward case, where the correlations are assumed to be isotropic and can be explicitly written out, to the non-trivial case where the effective diffusion tensor $\mathcal{C}_{ijkl}^{\text{eff}}$ needs to be evaluated from DNS,

providing a full characterisation of the anisotropies for the model. An intermediate stage has been considered measuring the one-point, one-time correlation of the velocity gradient as a function of shear rate σ^*, which provides a first attempt to introduce some anisotropy within the model.

Briefly, we want to summarise the construction of correlations tensor in general, both to underline the hypothesis to construct it and to justify the three choices made. Here, we are going to consider the two-time correlations of the velocity gradient tensor $\mathcal{C}_{ijkl}(\tau) = \langle \partial_j u_i'(0) \partial_l u_k'(\tau) \rangle$ along the particle trajectory, assuming the velocity gradient tensor $\partial_j u_i'$ stationary in time. Considering an invertible map $\psi(i,j)$ that assigns to each pair of indices (i,j), $1 \leq i, j \leq n$ a single index $\psi(i,j)$ that ranges from 1 to n^2 (Moakher (2008)), it is possible to rewrite the 4-th order tensor in matrix form. Under this map the correlation tensor can be rewritten as,

$$\mathbb{C}_{\psi(i,j),\psi(k,l)}(\tau) = \begin{pmatrix} \mathcal{C}_{1111} & \mathcal{C}_{1112} & \mathcal{C}_{1121} & \mathcal{C}_{1122} \\ \mathcal{C}_{1211} & \mathcal{C}_{1212} & \mathcal{C}_{1221} & \mathcal{C}_{1222} \\ \mathcal{C}_{2111} & \mathcal{C}_{2112} & \mathcal{C}_{2121} & \mathcal{C}_{2122} \\ \mathcal{C}_{2211} & \mathcal{C}_{2212} & \mathcal{C}_{2221} & \mathcal{C}_{2222} \end{pmatrix} \tag{3.36}$$

The incompressibility of the flow field ensures that the elements in the first column of matrix (3.36) are the exact opposite of the elements of last column; in addition $\mathcal{C}_{1111} = -\mathcal{C}_{2211}$ (incompressibility condition), since

$$\langle \partial_1 u_1'(0) \partial_1 u_1'(\tau) \rangle + \langle \partial_2 u_2'(0) \partial_1 u_1'(\tau) \rangle = 0.$$

This means that we can rewrite the matrix (3.36) in the general form as,

$$\mathbb{C}_{\psi(i,j),\psi(k,l)}(\tau) = \begin{pmatrix} f(\tau) & h(\tau) & j(\tau) & -f(\tau) \\ h(-\tau) & g(\tau) & k(\tau) & -h(-\tau) \\ j(-\tau) & k(-\tau) & \ell(\tau) & -j(-\tau) \\ -f(\tau) & -h(\tau) & -j(\tau) & f(\tau) \end{pmatrix}. \tag{3.37}$$

Here we have reduced the tensor to six parameters and rewritten the lower triangular part as $\mathcal{C}_{ijkl}(\tau) = \mathcal{C}_{klij}(-\tau)$. It is worth noticing that the general incompressible case depends upon nine independent parameters, where $h(\tau) \neq h(-\tau)$, $j(\tau) \neq j(-\tau)$ and $k(\tau) \neq k(-\tau)$.

A simple description can be made regarding the isotropic case, which means to consider the symmetric transformation within a square. That is, using the parity with respect to the diagonal, i.e. $(x_1, x_2) \mapsto (x_2, x_1)$ leading to,

$$\begin{aligned} &\mathcal{C}_{1212}(\tau) = \mathcal{C}_{2121}(\tau) = g(\tau) = \ell(\tau), \\ &\mathcal{C}_{1112}(\tau) = \mathcal{C}_{2221}(\tau) = h(\tau) = -h(\tau) \Rightarrow h(\tau) = 0, \\ &\mathcal{C}_{1121}(\tau) = \mathcal{C}_{2212}(\tau) = j(\tau) = -j(\tau) \Rightarrow j(\tau) = 0, \\ &\mathcal{C}_{1221}(\tau) = \mathcal{C}_{2112}(\tau) = k(\tau) = k(-\tau). \end{aligned}$$

In the isotropic case, three independent parameters are necessary to describe the correlation tensor. In this simplest case the effective correlation tensor in Eq. (3.21) can be replaced by $\mathcal{C}^{\text{iso}}_{ijkl}$ assuming that it is isotropic and incompressible. The integral Lagrangian correlation time τ_{I}, in this case, does not depend on the space and $Ku = \tau_{\text{I}}/\tau_\omega$ represents a simple rescale parameter,

$$\mathcal{C}^{\text{iso}}_{ijkl} = \alpha_{\text{iso}} \frac{Ku}{\tau_\omega} (3\delta_{ik}\delta_{jl} - \delta_{ij}\delta_{kl} - \delta_{il}\delta_{jk}). \tag{3.38}$$

In addition, using isotropic hypothesis the model is strongly simplified since only the value of γ_0 is not null in Eq. (3.27).

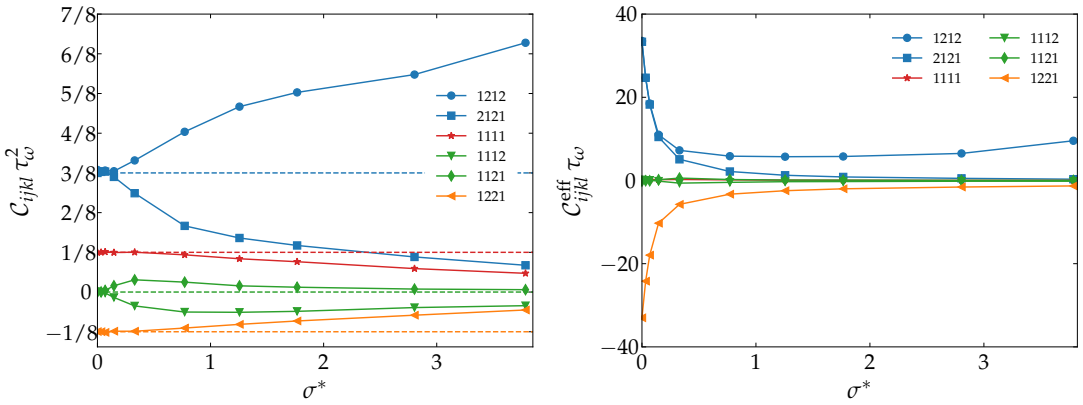

Figure 3.9: Left panel: One-point, one-time correlation $\mathcal{C}_{ijkl}(0)$ of the fluid velocity gradient tensor renormalised for the characteristic time scale τ_ω as a function of the shear parameter. The horizontal dashed lines correspond to isotropic statistics. Right panel: Effective correlation tensor $\mathcal{C}^{\text{eff}}_{ijkl}$ measured as in Eq. (3.20) renormalised for the characteristic time scale τ_ω as a function of the shear parameter.

The values of the three parameters for $\mathcal{C}_{ijkl}(0)$ are shown in left panel of Fig. 3.9 (constant dot lines). The $\mathcal{C}^{\text{iso}}_{ijkl}$ has been conveniently calibrated for different values of a constant parameter α_{iso} by considering that several approximations were made to develop the model.

More precisely, one can imagine that the model is the result of having applied a high pass filter to the signal of the evolution matrix $\boldsymbol{D}$. Consequently, the filter requires a tuning action in order to optimise some specific information coming from the original signal. This means that the choice of time scale Δt to drive the coarse-grained model is partly arbitrary in the sense that could depend up-to a constant value. Then, ten different values of α_{iso} linearly spaced have been selected within a range, to minimize the error in terms of both the peak of the orientation distribution and the average values $\langle\bar{\theta}\rangle$ with respect to the DNS results. These values are reported in x-axis of Fig. 3.13.

In left panel of Fig. 3.10 the results of the angle distribution of the model are shown, for $\alpha_{\text{iso}} = 0.075$, for different values of the shear rate. It immediately stands out that the distribution $\mathcal{P}_{st}$ is in good agreement at small values of σ^* but becomes less peaked than the DNS when shear rate increases. Moreover, the inset reports the average values of the orientation's model as a function of σ^* for different values of α_{iso} in increasing order (from violet to yellow solid lines). Only for small values of the shear rate the model is close to the DNS (markers), revealing that the usage of $\mathcal{C}^{\text{iso}}_{ijkl}$ in the modelling is not sufficient to represent the DNS statistics in the presence of a mean shear flow.

Increasing the model complexity and the information that the DNS has to provide, we choose to model the effective correlation tensor taking into account the anisotropic character of the velocity gradient tensor by introducing a $\mathcal{C}^{\text{aniso}}_{ijkl}$, and a tuning parameter is set up as α_{aniso}. In this case the integral Lagrangian correlation time τ_{I} remains constant but the one-time Lagrangian correlation tensor $\mathcal{C}_{ijkl}(0)$ is evaluated for the different values of the shear rate,

$$\mathcal{C}^{\text{aniso}}_{ijkl} = \alpha_{\text{aniso}}\, Ku\, \tau_\omega\, \mathcal{C}_{ijkl}(0). \tag{3.39}$$

Figure 3.9 (left panel) shows the dependency on the six parameters as a function of the shear rate. One observes that the most important deviations from the isotropic case occurs both for the component along the mean shear $\mathcal{C}_{1212} = \langle(\partial_y u'_x)^2\rangle$, which increases as a function of σ^*, and for the component $\mathcal{C}_{1212} = \langle(\partial_x u_y)^2\rangle$, which is depleted by shear. In this case the

matrix (3.37) is still symmetric but its values depend on σ^*. It should be emphasised that the choice, on how the correlation of the velocity gradient tensor is considered, relies on the easy access that the DNS information can provide, which is in the spirit of a, as much as, possible stand-alone modelling.

The stationary distribution of the model in Eq. (3.32) is shown in Fig. 3.10 (right panel), for $\alpha_{\text{aniso}} = 0.18$. In this case, a better agreement is obtained with the DNS results, in terms of peaks of PDF for large values of σ^*. The average value of the folded angle is shown in the inset, for different values of α_{aniso}, in increasing order (from violet to yellow solid lines). Here we find a good agreement with the DNS for small values of σ^* and an amelioration with respect to the isotropic case, also for large σ^*. We should point out that the value of $\alpha_{\text{aniso}} = 0.18$ fixed to plot the PDFs, corresponds to the second-last curve in violet, for $\langle\bar{\theta}\rangle$. This means that in this approach the best that the model can perform is to reproduce qualitatively the PDFs behaviour, but remaining sufficiently far in terms of average values for the fixed $\alpha_{\text{aniso}} = 0.18$ used for the PDF.

In order to better quantify the effects of the anisotropy on the model orientation and to understand its limits, we measured the nine components of the correlation matrix for different values of the shear parameter. Figure 3.11 shows the behaviour of the nine components of $\mathcal{C}_{ijkl}$ renormalised by their standard deviation as a function of time-lag. For $\sigma^* = 0$ (left panel) the correlation tensor is isotropic, where the symmetries of the matrix (3.37) are well preserved $g(\tau) = \ell(\tau)$, $j(\tau) = h(\tau) = 0$ and $k(\tau) = k(-\tau)$. Moreover, the main contribution is given by the components associated to the vorticity, which means that the cyclonic/anticyclonic structures within the flow have a very long lifetime compared with the strain surrounding regions. Moving to $\sigma^* = 2.8$ (right panel), the anisotropic behaviour of the correlations is detected, with the most significant deviation obtained for the components related to the vorticity, and the vortices tend to be twisted by the shear in a different manner.

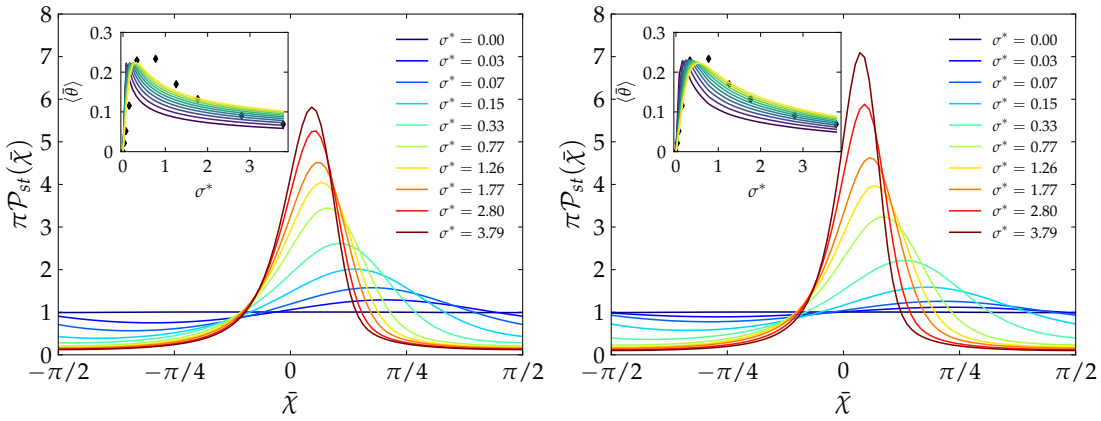

Figure 3.10: Stationary distribution of the rods angle $\mathcal{P}_{st}(\bar{\chi})$ with respect to the horizontal in the model for different values of the shear (in legend). Results using an isotropic correlation tensor $\mathcal{C}^{\text{iso}}_{ijkl}$, choosing $\alpha_{\text{iso}} = 0.075$ (left panel) and anisotropic correlation tensor $\mathcal{C}^{\text{aniso}}_{ijkl}$, choosing $\alpha_{\text{aniso}} = 0.18$ (right panel). Inset: average values of $\bar{\theta}$ for the DNS measurements (black diamond; as in inset of Fig. 3.8). In the model solid lines corresponds to ten values linearly spaced (see x-axis of Fig. 3.13) of α_{iso} (inset left panel) and α_{aniso} (inset right panel) from smaller to bigger values (from violet to yellow solid lines) as a function of σ^*.

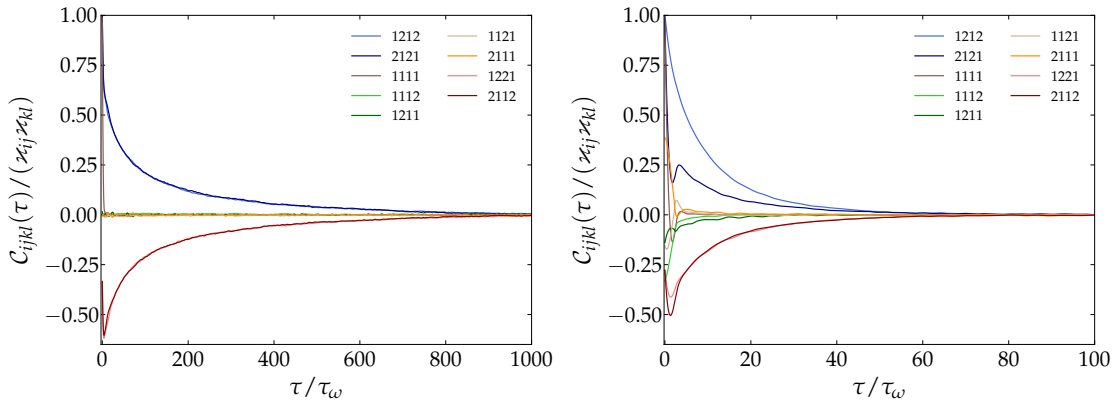

Figure 3.11: Correlations of the fluid velocity gradient tensor renormalised by their standard deviation $\varkappa_{ij} = \langle A'^2_{ij}(0)\rangle^{1/2}$ as a function of time-lag τ. Left panel: $\sigma^* = 0$. Right panel: $\sigma^* = 2.8$.

Having evaluated the matrix (3.37), we can compute the effective correlation tensor $\mathcal{C}^{\text{eff}}_{ijkl}$ according to Eq. (3.20). This expression corresponds to symmetrise the matrix (3.37) where the upper-triangular elements have been averaged with their lower-triangular counterpart.

Figure 3.9 (right panel) shows the measurement of $\mathcal{C}^{\text{eff}}_{ijkl}$ as a function of σ^*. For values smaller than $\sigma^* < 0.15$ the components of the integral Lagrangian correlation time rapidly decreases due to the presence of the shear and at larger values, the anisotropies start to develop, in particular for the component along the mean shear direction $\mathcal{C}^{\text{eff}}_{1212}$. Moreover, the $\mathcal{C}^{\text{eff}}_{ijkl}$ is very different from one-point, one-time $\mathcal{C}_{ijkl}$ (left panel), especially for small values of σ^*, where we find $\mathcal{C}^{\text{eff}}_{1212} = \mathcal{C}^{\text{eff}}_{2121} = -\mathcal{C}^{\text{eff}}_{1221}$, underling that the effective correlation tensor is dominated by the presence of vortex structures. This can be explained by considering that the total Lagrangian integral time is given by two contributions: the first is the fraction of time spent by a fluid tracer within a vortex structure T_{struct}, and the latter is the time spent by itself in a strain region T_{SR}. Therefore, $T_{\text{struct}} \gg T_{\text{SR}}$, where the integral time associated to the component of the antisymmetric part of the velocity gradient is larger than its symmetric counterpart.

After evaluating, from DNS, the effective correlation tensor $\mathcal{C}^{\text{eff}}_{ijkl}$, we can introduce for the model an integral correlation tensor containing the Lagrangian integral correlation information that reads,

$$\mathcal{C}^{\text{int}}_{ijkl} = \alpha_{\text{int}}\, \mathcal{C}^{\text{eff}}_{ijkl}, \tag{3.40}$$

where, in the same spirit of what we did before, a constant tuning parameter α_{int} is introduced. Moreover, in this case the Ku number depends on the space and is included in the definition of $\mathcal{C}^{\text{eff}}_{ijkl}$.

The angular distribution in the model is less peaked for small values of σ^* than the DNS counterpart. On the other hand a good agreement is re-established at large values, as shown in Fig. 3.12 (calibration parameter $\alpha_{\text{int}} = 0.053$). This behaviour is confirmed by looking at the average orientation (in inset) where the model perfectly reproduces the DNS (markers) trend within the interval parameters $0.045 < \alpha_{\text{int}} < 0.074$ as soon as $\sigma^* > 1.2$. In contrast, the model does not respond in the similar way for small values of the shear rate. In this range of σ^*, the model starts to be far from the hypothesis $Ku \ll 1$, since the flow is dominated by pure rotational region and a new characteristic scale of the order $1/\sigma^*$ arises. That is, the resolution time scale Δt chosen to coarse grain, becomes smaller than $1/\sigma^*$ and consequently the short correlation strain approximation becomes feeble (limit of validity of the model).

Finally, it is interesting to notice that, the choice of a $\mathcal{C}^{\text{eff}}_{ijkl}$ (by using $\mathcal{C}^{\text{int}}_{ijkl}$ in the model) for the model fluctuations is an important feature in the presence of anisotropic flow since this tensor contains a crucial information about level fluctuations. In perspective, this approach could be extended also to three dimensional anisotropic flows where, for example, in the case of a turbulent channel flow, the anisotropies close to the wall are of high relevance.

With the intent to provide a global picture between the different approaches presented above, we have defined a global error of the mean orientation of the model with respect to DNS, which could represent the goodness of these three stages. In more detail, this error globally estimates the trend of the model for different values of the calibration parameter in the regime of large σ^*, where the assumption of the model are still valid. The error can be defined as

$$err_{\langle\bar{\theta}\rangle}\,\% = \frac{\int_{0.7<\sigma^*<\max(\sigma^*)} \left(\langle\bar{\theta}\rangle_{\text{model}} - \langle\bar{\theta}\rangle_{\text{DNS}}\right)^2 d\sigma^*}{\int_{0.7<\sigma^*<\max(\sigma^*)} \langle\bar{\theta}\rangle^2_{\text{DNS}}\, d\sigma^*} \times 100. \tag{3.41}$$

The results are shown in Fig. 3.13 (from left to right panel) for different values of α_{iso}, α_{aniso} and α_{int} in the three approaches, respectively. In agreement with the results above, we find that the smallest error is provided by considering an effective correlation tensor $err_{\text{int}}\%$, whereas for the two other cases the error ($err_{\text{iso}}\%$, $err_{\text{aniso}}\%$) is overall higher. A global estimation on the error for the stationary PDF of $\bar{\theta}$ is provided evaluating the L^2-norm,

$$err_{\mathcal{P}_{st}}\,\% = \int_{-\frac{\pi}{2}}^{\frac{\pi}{2}} \left|\mathcal{P}^{\text{model}}_{st}(r) - \mathcal{P}^{\text{dns}}_{st}(r)\right|^2 dr \times 100. \tag{3.42}$$

Inset of Fig. 3.13 shows the results for the error of the PDF $err_{\mathcal{P}_{st}}$ for the three declinations for the correlations of velocity gradient tensor. Different curves (from deep violet to yellow) correspond to the values, in increasing order, of α_{iso}, α_{aniso} and α_{int}, respectively. Finally, the third declination of the model appears to be the proper one to consider and will provide the base to analyse the two-time statistics in the next section.

BOX SIZE EFFECT Here, we would like to give an insight into the peculiar behaviour of both $\mathcal{C}_{ijkl}$, and $\mathcal{C}^{\text{eff}}_{ijkl}$ results in Fig. 3.9, for the last two values of σ^*. In fact, for these values of

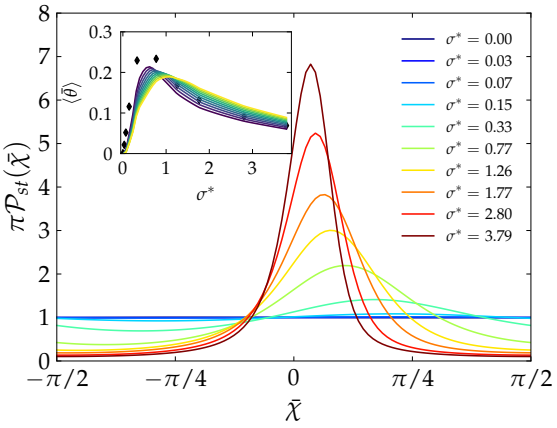

Figure 3.12: Stationary distribution of the rods angle $\mathcal{P}_{st}(\bar{\chi})$ with respect to the horizontal in the model with an integral correlation tensor $\mathcal{C}^{\text{int}}_{ijkl}$, choosing $\alpha_{\text{int}} = 0.053$ for various values of the shear. Inset: average values of $\bar{\theta}$ for the DNS measurements (black diamond; as in inset of Fig. 3.8). In the model solid lines correspond to ten values linearly spaced (see x-axis of Fig. 3.13) of α_{int} from smaller to bigger values (from violet to yellow solid lines) as a function of σ^*.

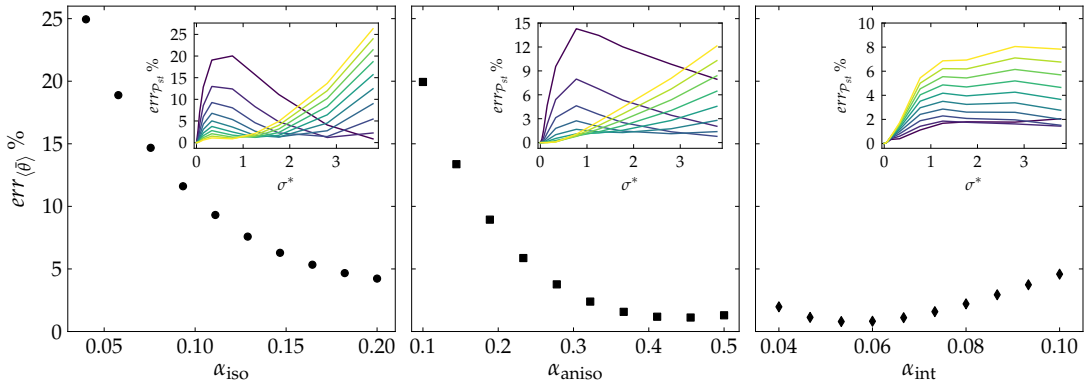

Figure 3.13: (Colour online) Error of $\langle\bar{\theta}\rangle$ (Eq. (3.41)) as a function of calibration parameter using $\mathcal{C}^{\text{iso}}_{ijkl}$, $\mathcal{C}^{\text{aniso}}_{ijkl}$ and $\mathcal{C}^{\text{int}}_{ijkl}$ (from left to right panels). Inset: Error of probability distribution function for the unfolded angle (Eq. (3.42)) as a function of calibration parameter using $\mathcal{C}^{\text{iso}}_{ijkl}$, $\mathcal{C}^{\text{aniso}}_{ijkl}$ and $\mathcal{C}^{\text{int}}_{ijkl}$. Solid lines (from deep violet to yellow) correspond to the values of tuning parameter (x-axis of the plot) in increasing order.

the shear rate we observe a non-monotonic trend for $\mathcal{C}^{\text{eff}}_{ijkl}$ or, equivalently, a non-monotonic derivative trend of $\mathcal{C}_{ijkl}$. In principle, as σ increases, the vorticity should decorrelate fast, since the presence of the shear rate tends to stretch the fluid in a chaotic manner. In order to clarify this effect, we show in Fig. 3.14 a snapshot of the vorticity field superposed with the rod alignment for the extremely large value of the shear rate parameter $\sigma = 64$.

Looking at Fig. 3.14, we observe that the vorticity field appears strongly elongated with an alternation of negative and positive bands, all parallel to each other. Moreover, the length of these bands corresponds to the size of the domain (L_x). This means that, if we compute the velocity gradient correlations, we should find that they stay correlated for infinite long time, due to the absence of enough chaotic motion. That is, a Lagrangian tracer would be trapped within a stripe (either positive or negative bands) without the possibility to escape, remaining confined periodically within either positive or negative vorticity structure.

The mechanism of appearance of these bands for large values of the shear rate seems to be associated to the size of the box L_x, which is not large enough with respect to the values of the shear rate.

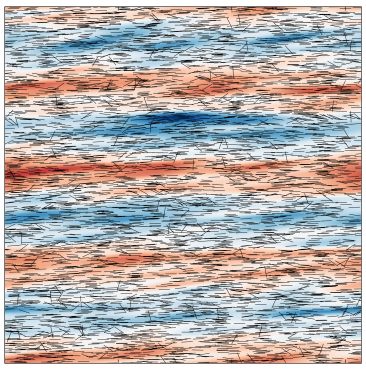

Figure 3.14: Test case: Vorticity field ω (coloured background) for the shear rate parameter $\sigma = 64$. Blue corresponds to negative values (cyclonic eddies) and red to positive values (anticyclonic). On the top of this field, the orientations of fibres are shown as black segments.

3.4 TUMBLING STATISTICS

In the previous sections we have studied the folded stationary distribution function which can be measured experimentally by averaging the rod orientation over large time periods, or equivalently over a large number of independent realizations. However, the dynamics of the rod is non-stationary, due to continuous tumbling. The usually called "tumbling rate" is the root-mean-squared speed of orientation defined as $\langle \|d\boldsymbol{p}/dt\|^2 \rangle^{1/2}$, i.e. the rate of change of the orientation vector $\boldsymbol{p}$ (see, e. g., Voth and Soldati (2017)). As discussed in Chapter 2, a wide range of studies has explored the tumbling rate statistics in DNS both numerically (e. g., Byron et al. (2015); Shin and Koch (2005)) and experimentally (e. g., Parsa et al. (2012); Marcus et al. (2014)). Moreover, we want to emphasize that experimental techniques for imaging the dynamics of individual non-spherical particles in a turbulent environment have recently become available. These techniques still represent a challenging problem and are affected by large experimental uncertainties when time and spatial resolution are greatly lowered (tens or hundreds of microns at high Reynolds numbers). Moreover, the tumbling rate in the framework of stochastic Lagrangian models, is not properly defined due to the presence of stochastic integral for the orientation vector $\boldsymbol{p}_t$.

Thereby, the natural question which arises is whether there are some quantities, which would allow experimental observations and quantitative model description of the tumbling process. Here we introduce another definition of the tumbling rate, which can be measured experimentally and used to describe the tumbling process.

Our aim is now to give some analytical and numerical results both for the stochastic Lagrangian model and the DNS as regarding some tumbling rate statistics in its reformulation.

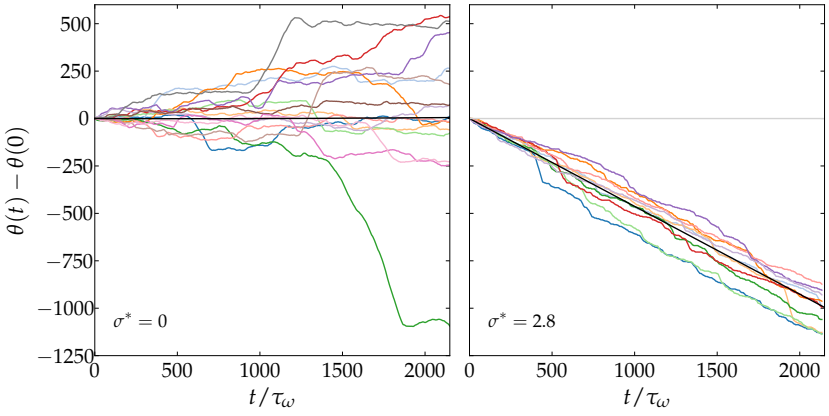

Figure 3.15: Typical trajectories of the angular displacement $\delta\theta(t) = \theta(t) - \theta(0)$ with the horizontal in the absence of shear (left panel) and for $\sigma^* = 2.8$ (right panel). Their average behaviour is shown in black lines.

The total number of rod's rotations can be described by considering the unfolded angle $\theta(t)$ on the real line of the folded angle $\bar{\theta}(t)$. More precisely, we are interested in looking at the dynamics of the angular displacement $\delta\theta(t) = \theta(t) - \theta(0)$ that represents the change in time of the unfolded angle with respect to its initial position. Figure 3.15 shows a sample of trajectories of angular displacement (extracted from DNS) in the absence of shear (left panel) and for moderate value of σ^* (right panel). In the first case, trajectories fluctuate along their mean $\langle \theta(t) \rangle = \theta(0)$. Still, one observes that this is certainly not diffusion because fluctuations involve strong ballistic excursions during which $\theta(t)$ varies quasi linearly. This corresponds to events during which tracers are captured by a vortex structure. They are also present in the

sheared case but with a negative bias that reflects the skewness of the vorticity distribution. Note that the random motion of the angle, which is a combination of diffusion with long-range excursions resembles the behaviour of Lévy walks.

Indeed, from this visual assessment, we can define the tumbling as the account of turns of a rod for the unfolded dynamics $\theta(t)$. When the rod is in an unstable equilibrium configuration $\theta(t) = k\pi,\ k \in \mathbb{Z}$ the velocity gradient fluctuations can bring the rod out of the region, and this induces a fast rotation which is globally linear in time. This means that the tumbling rate can be associated to the mean behaviour of the trajectories of the angular displacement.

Thus, we can define the tumbling rate as the long time behaviour of the rotation rate of the orientation $\dot{\theta}_\infty$

$$\dot{\theta}_\infty \simeq \frac{d}{dt} \langle \delta\theta(t) \rangle \ \text{ for large } t, \tag{3.43}$$

when the time becomes large (i.e. when the increment is large with respect to the initial point $\theta(0)$). Moreover, it is important to notice that the above definition remains valid in the presence of mean velocity gradient, otherwise the tumbling rate can be associated to the rate of change in time of the variance of the angular displacement $\langle \delta\theta^2(t) \rangle$, as we will see in Section 3.4.3.

Based on the physical interpretation of tumbling regarding the trajectories of the unfolded process $\theta(t)$, the tumbling rate can be reinterpreted in terms of stochastic Lagrangian model using statistical mechanics arguments. The unfolded dynamics of the model can be briefly expressed by the following stochastic differential equation,

$$d\theta_t = a(\theta_t)dt + b(\theta_t)dW_t \quad \text{in } \mathbb{R}. \tag{3.44}$$

where W_t is the same Brownian motion introduced in Eq. (3.25) and the coefficients a, b are still given by Eqs. (3.26)-(3.27). In what follows we will make use of the flow-solution of Eq. (3.44): for all $\chi \to \mathbb{R}$, for all $0 \le s \le t$ we introduce the map $(s, \chi) \to \theta(t; \chi, s)$, where $\theta(t; \chi, s)$ denotes the solution of Eq. (3.44) starting from χ as instant of time s.

Here, it is important to remark that the initial condition of the SDE (3.44) is θ_0 and will be specified where necessary for analytical computation. To derive an analytical expression for the tumbling, it is natural to introduce the non-stationary Fokker–Planck equation $\mathscr{P}(\chi, t)$, associated to Eq. (3.44),

$$\partial_t \mathscr{P}(\chi, t) = -\partial_\chi \left[a(\chi) \mathscr{P}(\chi, t), t) \right] + \frac{1}{2} \partial_\chi^2 \left[b^2(\chi) \mathscr{P}(\chi, t) \right]. \tag{3.45}$$

Unfortunately, the solution of Eq. (3.45) is not enough tractable to extract analytically the probability density function $\mathscr{P}$ of the unfolded angle. On the other hand, to make the problem tractable, statistical information can be recovered using the stochastic representation formula. The latter is usually called *Feynman–Kac* representation for the solution of a class of second order linear partial differential equations.

3.4.1 *Feynman–Kac formula for the unfolded dynamics*

Here a general representation on *Feynman–Kac* formula is given, since it will be needed to derive the unfolded statistics for the model. We consider *Kolmogorov backward equation*, which is the *Cauchy problem*,

$$\begin{aligned} \partial_s v(\chi, s) + \mathcal{L} v(\chi, s) &= f(\chi) \quad \text{in } \mathbb{R} \times [0, t] \\ v(\chi, t) &= \phi(\chi) \quad \text{on } \mathbb{R}. \end{aligned} \tag{3.46}$$

Consider the operator $\mathcal{L}$ as the infinitesimal generator related to SDE (3.44)

$$\mathcal{L} = \frac{1}{2} b^2(\chi) \partial_\chi^2 + a(\chi) \partial_\chi \,. \tag{3.47}$$

Under the smoothness assumption of f, ϕ; and recalling a, b to be smooth functions as defined in Eqs. (3.26)-(3.27); with $b^2 > 0$ (see Appendix A.2). The unique solution, $\mathbb{R} \times [0,t] \ni (\chi, s) \mapsto v(\chi, s)$, of Eq. (3.46) is smooth as well and the Itô formula allows to represent the solution as,

$$v(\chi, s) = \langle \phi(\theta(t; \chi, s)) \rangle - \int_s^t \langle f(\theta(r; \chi, s)) \rangle \, dr. \tag{3.48}$$

Our purpose is to derive analytical expression for the complex statistics in the right hand side of Eq. (3.48), by using the *Kolmogorov backward equation* and the fact that the operator $\mathcal{L}$ is the adjoint operator of the stationary Fokker–Planck equation Eq. (3.31) solved by $\mathcal{P}_{st}$. We observe from Eq. (3.48) that

$$\begin{aligned} &\langle \phi(\theta(t; \theta_0, 0)) \rangle - \langle \phi(\theta_0) \rangle - \int_0^t \langle f(\theta(r; \theta_0, 0) \rangle \, dr \\ &= \langle v(\theta_0, 0) - v(\theta_0, t) \rangle = - \int_0^t \frac{\partial v}{\partial s}(\theta_0, s) ds = - \int_0^t \int_{\mathbb{R}} \frac{\partial v}{\partial s}(\chi, s) \mathscr{P}_0(\chi) d\chi ds, \end{aligned} \tag{3.49}$$

The choice of the stationary distribution $\mathcal{P}_{st}$ of the folded angle, as a starting distribution of tumbling dynamics $\mathscr{P}_0$ in Eq. (3.45), allows us to study analytically both the average and the variance of the angular displacement. Since we are interested to look at its asymptotic behaviour, i.e. when t is very large, this particular choice does not impact the final result. Namely, in the long time regime the system completely forgot the information about initial condition showing that no memory effects are introduced in the dynamics (Markovian system). We recall that the stationary Fokker–Planck PDE for $\mathcal{P}_{st}$ in Eq. (3.31) can be rewritten as

$$b^2(\bar{\chi}) \partial_{\bar{\chi}} \mathcal{P}_{st}(\bar{\chi}) = \left[2a(\bar{\chi}) - \partial_{\bar{\chi}} b^2(\bar{\chi}) \right] \mathcal{P}_{st}(\bar{\chi}) + 2\mathcal{J}. \tag{3.50}$$

Thus, computing the integral in Eq. (3.49), with Kolmogorov PDE and integrating by part, as well as using Eq. (3.50), we obtain

$$\begin{aligned} &-\frac{\partial}{\partial s} \int_{-\frac{\pi}{2}}^{\frac{\pi}{2}} v(\chi, s) \mathcal{P}_{st}(\chi) d\chi \\ &\quad = \int_{-\frac{\pi}{2}}^{\frac{\pi}{2}} \left[a(\chi) \partial_\chi v(\chi, s) + \frac{1}{2} b^2(\chi) \partial_\chi^2 v(\chi, s) - f(\chi) \right] \mathcal{P}_{st}(\chi) d\chi \\ &\quad = \int_{-\frac{\pi}{2}}^{\frac{\pi}{2}} \partial_\chi (v(\chi, s)) \left[\mathcal{P}_{st}(\chi) a(\chi) - \frac{1}{2} \partial_\chi \left(\mathcal{P}_{st}(\chi) b^2(\chi) \right) \right] d\chi \\ &\qquad + \frac{1}{2} \int_{-\frac{\pi}{2}}^{\frac{\pi}{2}} \partial_\chi \left[\mathcal{P}_{st}(\chi) b^2(\chi) \partial_\chi (v(\chi, s)) \right] d\chi - \langle f(\bar{\theta}_\infty) \rangle \\ &\quad = - \mathcal{J} \left[v(\tfrac{\pi}{2}, s) - v(-\tfrac{\pi}{2}, s) \right] \\ &\qquad + \frac{1}{2} \mathcal{P}_{st} \left(\tfrac{\pi}{2} \right) b^2 \left(\tfrac{\pi}{2} \right) \left[\partial_\chi v \left(\tfrac{\pi}{2}, s \right) - \partial_\chi v \left(-\tfrac{\pi}{2}, s \right) \right] - \langle f(\bar{\theta}_\infty) \rangle . \end{aligned} \tag{3.51}$$

In the last equality, the periodicity of $\mathcal{P}_{st}(\pi/2) = \mathcal{P}_{st}(-\pi/2)$ and $b(\pi/2, t) = b(-\pi/2, t)$ has been used. We denoted by $\bar{\theta}_\infty$ a random variable of the folded angle distributed according to stationary distribution $\mathcal{P}_{st}$.

The information about $\partial_\chi v(\chi, s)$ can be determined introducing the Feynman–Kac representation for the function $w(\chi, s) = \partial_\chi v(\chi, s)$. Thus, the general form of Kolmogorov backward equation associated to $w(\chi, s)$ reads

$$\begin{aligned} \partial_s w(\chi, s) + \tilde{\mathcal{L}} w(\chi, s) + \partial_\chi (a(\chi)) w(\chi, s) &= f'(\chi) \quad \text{in } \mathbb{R} \times [0, t] \\ w(\chi, t) &= \phi'(\chi) \quad \text{on } \mathbb{R}, \end{aligned} \tag{3.52}$$

with an infinitesimal generator

$$\tilde{\mathcal{L}} = \frac{1}{2} b^2(\chi)\partial_\chi^2 + \left[a(\chi) + \frac{1}{2}\partial_\chi b^2(\chi)\right]\partial_\chi \tag{3.53}$$

related to the flow diffusion $\varrho_t = \varrho(t;\chi,s)$ solving,

$$d\varrho_t = \left[a(\varrho_t) + \frac{1}{2}\partial_\chi b^2(\varrho_t)\right]dt + b(\varrho_t)dW_t, \text{ in } \mathbb{R} \tag{3.54}$$

and leading to the Feynman–Kac representation,

$$\begin{aligned} w(\chi,s) = \langle \phi'(\varrho(t;\chi,s)\exp\left(\textstyle\int_s^t a'\left(\varrho(r;\chi,s)\right)dr\right)\rangle \\ - \int_s^t \langle f'\left(\varrho(r;\chi,s)\right)\exp\left(\textstyle\int_s^r a'\left(\varrho(z;\chi,s)\right)dz\right)\rangle\, dr. \end{aligned} \tag{3.55}$$

Integrating in time Eq. (3.51)

$$\begin{aligned} \langle v(\theta_0,0) - v(\theta_0,t)\rangle = -\mathcal{J}\int_0^t \left[v\left(\tfrac{\pi}{2},s\right) - v\left(-\tfrac{\pi}{2},s\right)\right]ds \\ + \frac{1}{2}\mathcal{P}_{st}\left(\tfrac{\pi}{2}\right) b^2\left(\tfrac{\pi}{2}\right)\int_0^t \left[w\left(\tfrac{\pi}{2},s\right) - w\left(-\tfrac{\pi}{2},s\right)\right]ds - t\,\langle f(\bar{\theta}_\infty)\rangle\,. \end{aligned} \tag{3.56}$$

This last expression is in a general form and will allow to compute analytically, introducing some simplification, the mean and variance of the increment of angular displacement $\delta\theta_t$.

3.4.2 *Average of angular increment displacement*

As said, we are interested in the tumbling rate which is associated to the average angular displacement that, in term of stochastic process, can be expressed as $\delta\theta_t = \theta_t - \theta_0$. So we are looking at the process with respect to the initial condition θ_0. The tumbling rate can be directly identified in the right-hand side of Eq. (3.51), when the Feynman–Kac formula is applied with $\phi(\chi) = \chi$ and $f = 0$. The two contributions in Eq. (3.51) will be analysed separately hereafter. The $\pi/2$-periodicity of the coefficients $a, b(\theta(t;\chi,s)) = a, b(\theta(t;\chi,s) + k\pi/2)$ shall ensure the π-periodicity of the flow solution $(\chi) \mapsto \theta(t;\chi,s)$. Moreover, the uniqueness of the path-wise solution of Eq. (3.44) allows to write,

$$\theta(t;\tfrac{\pi}{2},s) = \theta(t;-\tfrac{\pi}{2},s) + \pi, \tag{3.57}$$

and consequently

$$-\mathcal{J}\int_0^t [v(\tfrac{\pi}{2},s) - v(-\tfrac{\pi}{2},s)]ds = -\mathcal{J}\int_0^t \langle\theta(t;\tfrac{\pi}{2},s)\rangle - \langle\theta(t;-\tfrac{\pi}{2},s)\rangle\, ds = -\pi\mathcal{J}t. \tag{3.58}$$

Moving on the second term in Eq. (3.56), considering the periodicity of the coefficients of ϱ_t in Eq. (3.54) and the fact that $\partial_\chi\phi = 1$, $f = 0$ allows to write,

$$w(\tfrac{\pi}{2},s) - w(-\tfrac{\pi}{2},s) = \langle\exp\left[\textstyle\int_s^t \partial_\theta a(\varrho(t;\tfrac{\pi}{2},r))dr\right]\rangle - \langle\exp\left[\textstyle\int_s^t \partial_\theta a(\varrho(t;-\tfrac{\pi}{2},r))dr\right]\rangle = 0. \tag{3.59}$$

Finally the tumbling rate defined in Eq. (3.43) can be expressed for the model as,

$$\dot{\theta}_\infty \simeq \frac{d}{dt}\langle\delta\theta_t\rangle = -\pi\,\mathcal{J}\,. \tag{3.60}$$

From a physical point of view, this means that the tumbling dynamics in the Lagrangian stochastic model is linear in time with a slope coefficient which is related to the probability flux $\mathcal{J}$ of the stationary density function $\mathcal{P}_{st}$ (Eq. (3.32)).

It is important to recall that the analytical expression (3.60) has been obtained through a particular choice of the initial distribution $\mathscr{P}_0 = \mathcal{P}_{st}$. In the asymptotic behaviour ($t \to \infty$) this choice has no impact on the result, since for any choice of initial condition θ_0 of SDE (3.44) the ergodic theorem applied to the folded orientation angle allows to write,

$$\langle \delta\theta_t \rangle = \int_0^t \langle a(\bar{\theta}_s) \rangle \, ds \simeq \langle a(\bar{\theta}_\infty) \rangle \, t, \tag{3.61}$$

where $\bar{\theta}_\infty \sim \mathcal{P}_{st}$-distributed with respect to a particular choice of the initial condition of the unfolded angle. Furthermore, the property of toroidal diffusion as explained by García-Portugués et al. (2019) has been used. From the integration of Eq. (3.31) in $[-\pi/2, \pi/2]$, we find that $\langle a(\bar{\theta}_\infty) \rangle = -\pi\mathcal{J}$. This confirms the result obtained in Eq. (3.60) using the Feynman–Kac representation and it gives an alternative way to derive the expression of tumbling rate in the stochastic Lagrangian model.

The average value of the angular displacement is shown in Fig. 3.16 (left panel) for the DNS (solid lines) and the stochastic model (dashed lines, for the fixed value of the tuning parameter $a_{\text{int}} = 0.053$), as a function of time for different values of the shear rate. The value of tuning parameter corresponds to the optimal choice to achieve a good agreement for both average and PDF for the unfolded angle $\bar{\theta}$ (as in Fig. 3.12).

The angular displacement in both DNS and model is zero when $\sigma^* = 0$ (absence of flux $\mathcal{J} = 0$) and becomes increasingly negative with $\sigma^* > 0$, since the rods are rotating in average in the clockwise direction by the shear. Asymptotically, looking at the DNS results, one finds that $\langle \delta\theta(t) \rangle \simeq \dot{\theta}_\infty \, t$ where the rotation rate $\dot{\theta}_\infty$ is negative, which confirms the analysis made above for the stochastic model.

Regarding the model behaviour for large values of shear rate, it does not reproduce well the behaviour of the DNS for this particular choice of the tuning parameter $a_{\text{int}} = 0.053$. At the same time, we want to underline that by using the model with a calibration parameter of $a_{\text{int}} = 0.053$ the discrepancy with respect to the DNS is around 20% for large values of σ^*.

In order to better quantify the limit of the model, in Fig. (3.16) (right panel) the measurements of tumbling rate, for different values of a_{int} (lines), are compared with the DNS (markers). To improve the understanding of the model behaviour, we choose to extend the range of values of a_{int} used to analyse the mean and PDF of unfolded angle in Section 3.3. Increasing the value of the calibration parameter, the model starts to be closer to the DNS. Particularly, the value of $a_{\text{int}} = 0.1$ reproduces the DNS result. In DNS, the effect that the tumbling is higher than the model (at least for small values of a_{int} such as $a_{\text{int}} = 0.053$) comes from the fact that the DNS angle trajectories (in Fig. 3.15) resemble Lévy walks.

When the shear rate increases due to a non-trivial trajectories behaviour, the tumbling rate is enhanced, since the rods are strongly moved away from their equilibrium position (i.e., 0 or π).

The effect that in the model the tuning parameter needs to be increased (with respect to the one considered for the folded statistics in Section 3.3) in order to reproduce DNS results, can be explained in the following way. When we consider the unfolded statistics, the effect of diffusion becomes more important than the drift part (not in a trivial way since the diffusion is included in the drift, see Eq. (3.26)). In some sense, the important effect in the model is that the diffusion becomes sufficiently strong, when the shear parameter increases, to bring out the rods from their stable position (equilibrium points, i.e. 0 or π) so that rods tumble.

It is not surprising that the value of the tuning parameter a_{int} does change. Indeed, in the model, the average of the unfolded dynamics $\langle \delta\theta_t \rangle$ has been related to the probability flux $\mathcal{J}$ of the stationary distribution $\mathcal{P}_{st}$ of the folded angle. Conversely, in DNS the fluctuations around

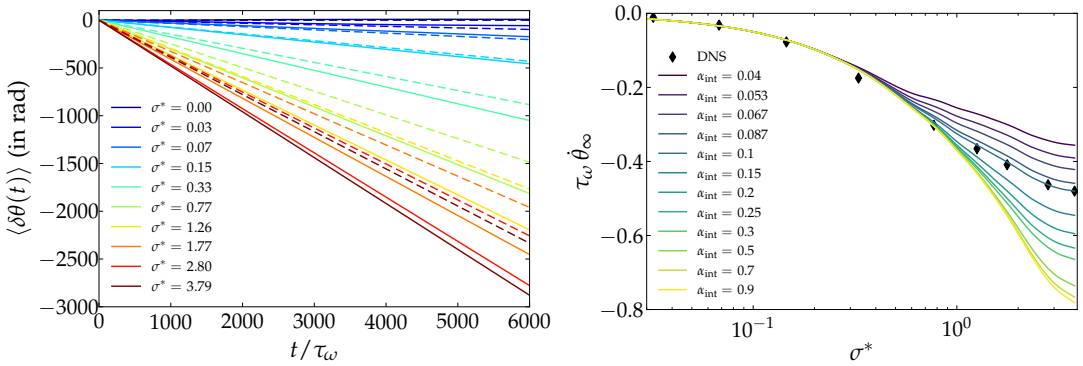

Figure 3.16: Left panel: Average angular displacement of the unfolded angle $\delta\theta(t) = \theta(t) - \theta(0)$ as a function of time showing a linear behaviour $\langle \delta\theta(t) \rangle \simeq \dot{\theta}_\infty t$ at long times. DNS results (lines) and model (dashed lines), choosing $\alpha_{\text{int}} = 0.053$, for different values of shear rate parameter σ^*. Right panel: Asymptotic angular velocity $\dot{\theta}_\infty$ as a function of the shear rate parameter in the DNS (markers) and the model (continuous lines) for different values of α_{int} parameter (in legend).

the peak of the stationary distribution of $\bar{\theta}$ in 0 or π (for large value of σ^*) are independent from the tumbling dynamics. That is, in DNS case the flux of the Fokker-Planck equation is extremely complex and does not appear in divergence form as in the model.

Finally, we can say that changing the value of tuning parameter in this case is although justified since the dynamical behaviour of the folded dynamics in real life can not be directly related to the folded one through $\mathcal{J}$. However, interestingly, the result for the tumbling rate $\dot{\theta}_\infty$ (in Fig. 3.16) can be reproduced by the model just by tuning the parameter which is the same for all σ^*.

3.4.3 *Variance of angular increment displacement*

Here, we investigate the variance of the angular displacement as it has been defined above. A direct approach on the second order moment of angular displacement shows,

$$\langle \theta_t^2 \rangle - \langle \theta_0^2 \rangle = \int_0^t \langle \theta_s a(\bar{\theta}_s) \rangle \, ds + \int_0^t \langle b^2(\bar{\theta}_s) \rangle \, ds. \tag{3.62}$$

The terms a, b are periodic and can be written in term of the folded angle dynamics $\bar{\theta}_s$. The second term of right-hand side is a classical diffusive behaviour and it has an ergodic limit as the time increases compatibly with the $\mathcal{P}_{st}$. Diversely, the first term goes far from the same direct an asymptotic analysis due to the fact that θ_s is not ergodic. This observation motivates the introduction of a Poisson equation and with Feynman–Kac representation in order to derive an analytical expression for the variance of the angular displacement.

The first step in this direction is to consider the variance of the angular displacement in the case where θ_0, the initial condition associated to the SDE (3.44), is distributed according to the stationary distribution of the folded angle given in Eq. (3.31). This allows to identifies $\theta_0 = \bar{\theta}_\infty$ and we are interested in looking into the tumbling dynamics for large t such that

$$\langle \delta\theta_t \rangle - \langle \delta\theta_t \rangle^2 = \langle (\theta_t - \theta_0)^2 \rangle - \left(\langle \theta_t \rangle - \langle \theta_0 \rangle \right)^2. \tag{3.63}$$

In the above expression, the second term is known from Eq. (3.60) as $\left(\langle \theta_t \rangle - \langle \bar{\theta}_\infty \rangle \right)^2 = \pi^2 \mathcal{J}^2 t^2$. The first term is now analysed separately.

For any choice of θ_0 we can write,

$$\begin{aligned}\langle \delta\theta_t^2 \rangle = \left\langle (\theta_t - \theta_0)^2 \right\rangle &= \left\langle \left(\int_0^t a(\bar{\theta}_s) ds + \int_0^t b(\bar{\theta}_s) dW_s \right)^2 \right\rangle \\ &= \left\langle \left(\int_0^t a(\bar{\theta}_s) ds \right)^2 + \int_0^t b^2(\bar{\theta}_s) ds \right\rangle\end{aligned} \tag{3.64}$$

We are interested in $\frac{d}{dt}\langle(\theta_t - \theta_0)^2\rangle$. Considering the first term in Eq. (3.64),

$$\begin{aligned}\frac{d}{dt}\left\langle \left(\int_0^t a(\bar{\theta}_s) ds \right)^2 \right\rangle &= \left\langle \frac{d}{dt} \left(\int_0^t a(\bar{\theta}_s) ds \right)^2 \right\rangle \\ &= 2 \left\langle a(\bar{\theta}_t) \int_0^t a(\bar{\theta}_s) \right\rangle ds = 2 \left\langle \int_0^t a(\bar{\theta}_t)\, a(\bar{\theta}_s) \right\rangle ds \\ &= 2 \left\langle \int_0^t a(\bar{\theta}_0)\, a(\bar{\theta}_s) \right\rangle ds = 2 \left\langle a(\bar{\theta}_0) \int_0^t a(\bar{\theta}_s) \right\rangle ds\end{aligned} \tag{3.65}$$

We consider now ψ_p the solution of the *Poisson equation* associated to the process θ_t on the torus domain $[-\pi/2, \pi/2]$:

$$\begin{aligned}\mathcal{L}\psi_p(\chi) &= a(\chi) - \langle a(\bar{\theta}_\infty) \rangle\,, \quad \text{on } \left(-\tfrac{\pi}{2}, \tfrac{\pi}{2}\right) \\ \psi_p\left(\tfrac{\pi}{2}\right) &= \psi_p\left(-\tfrac{\pi}{2}\right),\end{aligned} \tag{3.66}$$

where $\mathcal{L}$ is the infinitesimal generator introduced in (3.47). We want to remark that all the coefficients of this equation are periodic with periodic derivatives. Thus ψ_p has periodic derivatives, i.e. ψ_p is at least C^1 on the torus. Then, by applying the Itô's lemma to $\psi_p(\bar{\theta}_t)$, we get

$$\int_0^t a(\bar{\theta}_v) dv = t \langle a(\bar{\theta}_\infty) \rangle + \psi_p(\bar{\theta}_t) - \psi_p(\bar{\theta}_0) - \int_0^t \psi_p'(\chi)\, b(\bar{\theta}_v) dW_v \tag{3.67}$$

Next, considering $\bar{\theta}_0$ distributed according to the equilibrium measure $\mathcal{P}_{st}$,

$$\begin{aligned}2 \langle a(\bar{\theta}_0) \int_0^t a(\bar{\theta}_s) ds \rangle &= \left\langle a(\bar{\theta}_0) \left(t \langle a(\bar{\theta}_\infty) \rangle + \psi_p(\bar{\theta}_t) - \psi_p(\bar{\theta}_0) - \int_0^t \psi_p'(\chi)\, b(\bar{\theta}_v) dW_v \right) \right\rangle \\ &= 2\, t\, \langle a(\bar{\theta}_\infty) \rangle^2 + 2 \langle a(\bar{\theta}_0)\, \psi_p(\bar{\theta}_t) \rangle - 2 \langle a(\bar{\theta}_\infty)\, \psi_p(\bar{\theta}_\infty) \rangle\,.\end{aligned} \tag{3.68}$$

Letting the time increasing, for the second term in equation above, we can observe that $2\langle a(\bar{\theta}_0)\, \psi_p(\bar{\theta}_t)\rangle$ becomes decorrelated and Eq. (3.68) reads,

$$2 \langle a(\bar{\theta}_0) \int_0^t a(\bar{\theta}_s) ds \rangle \simeq 2\, t\, \langle a(\bar{\theta}_\infty) \rangle^2 + 2 \langle a(\bar{\theta}_\infty) \rangle \langle \psi_p(\bar{\theta}_\infty) \rangle - 2 \langle a(\bar{\theta}_\infty)\, \psi_p(\bar{\theta}_\infty) \rangle\,. \tag{3.69}$$

Turning to the second contribution of Eq. (3.64) and using the periodicity property of b^2, this term involves only the ergodic process $\bar{\theta}_s$. This allows to compute this term applying the ergodic mean

$$\left\langle \int_0^t b^2(\bar{\theta}_s) ds \right\rangle \simeq \langle b^2(\bar{\theta}_\infty) \rangle\; t. \tag{3.70}$$

At this point, the variance of the angular displacement (Eq. (3.63)), by taking its derivative in time, can be rewritten by simplifying some terms when t is large enough. Indeed, recalling that $-\frac{d}{dt}\left(\langle\theta_t\rangle - \langle\bar{\theta}_\infty\rangle\right)^2 = -2\,\pi^2\mathcal{J}^2 t$ and that the term $2\,t\,\langle a(\bar{\theta}_\infty)\rangle^2 = 2\,\pi^2\mathcal{J}^2 t$ in Eq. (3.69), this leads to have,

$$\frac{d}{dt}\left(\langle \delta\theta_t^2 \rangle - \langle \delta\theta_t \rangle^2 \right) = \langle b^2(\bar{\theta}_\infty) \rangle + 2 \langle a(\bar{\theta}_\infty) \rangle \langle \psi_p(\bar{\theta}_\infty) \rangle - 2 \langle a(\bar{\theta}_\infty)\, \psi_p(\bar{\theta}_\infty) \rangle\,. \tag{3.71}$$

Now, we can rewrite $\langle b^2(\bar{\theta}_\infty)\rangle$ in terms of $\langle \bar{\theta}_\infty a(\bar{\theta}_\infty)\rangle$, from the stationary distribution $\mathcal{P}_{st}$ in Eq. (3.31). Rearranging Eq. (3.50),

$$\begin{aligned} b^2(\bar{\chi})\partial_{\bar{\chi}}\mathcal{P}_{st}(\bar{\chi}) &= \left[2a(\bar{\chi}) - \partial_{\bar{\chi}}b^2(\bar{\chi})\right]\mathcal{P}_{st}(\bar{\chi}) + 2\mathcal{J}. \\ \partial_{\bar{\chi}}\left(b^2(\bar{\chi})\mathcal{P}_{st}(\bar{\chi})\right) &= 2a(\bar{\chi})\mathcal{P}_{st}(\bar{\chi}) + 2\mathcal{J} \end{aligned}$$

Integrating the equation above in $[-\pi/2, \pi/2]$, we get

$$\begin{aligned} \int_{-\frac{\pi}{2}}^{\frac{\pi}{2}} b^2(\bar{\chi})\mathcal{P}_{st}(\bar{\chi})d\bar{\chi} - \pi b^2(\tfrac{\pi}{2})\mathcal{P}_{st}(\tfrac{\pi}{2}) &= \int_{-\frac{\pi}{2}}^{\frac{\pi}{2}} d\bar{\chi}\int_{\frac{\pi}{2}}^{\bar{\chi}} 2a(\bar{\chi})\mathcal{P}_{st}(\bar{\chi})d\bar{\chi} + 2(\bar{\chi}+\tfrac{\pi}{2})\mathcal{J} \\ \langle b^2(\bar{\theta}_\infty)\rangle &= \pi b^2(\tfrac{\pi}{2})\mathcal{P}_{st}(\tfrac{\pi}{2}) + \pi^2\mathcal{J} + \pi\langle a(\bar{\theta}_\infty)\rangle - 2\langle a(\bar{\theta}_\infty)\bar{\theta}_\infty)\rangle. \end{aligned} \tag{3.72}$$

So with $\langle a(\bar{\theta}_\infty)\rangle = -\pi\mathcal{J}$,

$$\langle b^2(\bar{\theta}_\infty)\rangle + 2\langle a(\bar{\theta}_\infty)\bar{\theta}_\infty\rangle = \pi b^2(\tfrac{\pi}{2})\mathcal{P}_{st}(\tfrac{\pi}{2}). \tag{3.73}$$

Replacing this last equality in Eq. (3.71), we get,

$$\begin{aligned} \frac{d}{dt}\left(\langle\delta\theta_t^2\rangle - \langle\delta\theta_t\rangle^2\right) &= \pi b^2(\tfrac{\pi}{2})\mathcal{P}_{st}(\tfrac{\pi}{2}) - 2\langle a(\bar{\theta}_\infty)\bar{\theta}_\infty\rangle \\ &\quad + 2\langle a(\bar{\theta}_\infty)\rangle\langle\psi_p(\bar{\theta}_\infty)\rangle - 2\langle a(\bar{\theta}_\infty)\,\psi_p(\bar{\theta}_\infty)\rangle. \end{aligned} \tag{3.74}$$

Now we can use the *Feynman–Kac* representation associated to the following Poisson equation

$$\begin{aligned} \mathcal{L}\psi(\chi) &= a(\chi) - \langle a(\bar{\theta}_\infty)\rangle, \quad \text{on } \left(-\tfrac{\pi}{2}, \tfrac{\pi}{2}\right) \\ \psi\left(\tfrac{\pi}{2}\right) &= \psi\left(-\tfrac{\pi}{2}\right) = 0, \end{aligned} \tag{3.75}$$

where we have now specified the constant value zero for ψ_p at the boundary. According to Friedman (2010) Vol.1, *Theorem 5.1*, the *Feynman–Kac* formula is

$$\psi(\chi) = -\left\langle \int_0^{\tau_I^\chi} a(\bar{\theta}_s^\chi)ds - \tau_I^\chi\langle a(\theta_\infty)\rangle \right\rangle \tag{3.76}$$

where we have introduced the hitting time $\tau_I^\chi = \inf_{t>0}[|\theta_t^\chi| \geq \pi/2]$, with $I = (-\pi/2, \pi/2)$. This random time represents the first time that the process θ^χ stating at χ, hits the boundaries $-\pi/2$ or $\pi/2$. The difference between ψ and ψ_p is just a constant value and thus

$$2\langle a(\bar{\theta}_\infty)\rangle\langle\psi_p(\bar{\theta}_\infty)\rangle - 2\langle a(\bar{\theta}_\infty)\,\psi_p(\bar{\theta}_\infty)\rangle = 2\langle a(\bar{\theta}_\infty)\rangle\langle\psi(\bar{\theta}_\infty)\rangle - 2\langle a(\bar{\theta}_\infty)\,\psi(\bar{\theta}_\infty)\rangle.$$

By rewriting Eq. (3.76)

$$\psi(\chi) = -\left\langle \int_0^{\tau_I^\chi} a(\bar{\theta}_s^\chi)ds\right\rangle + \langle\tau_I^\chi\rangle\langle a(\bar{\theta}_\infty)\rangle = -\langle\bar{\theta}^\chi_{\tau_I^\chi}|\chi = \bar{\theta}_\infty\rangle + \chi + \langle\tau_I^\chi\rangle\langle a(\bar{\theta}_\infty)\rangle. \tag{3.77}$$

Replacing $\psi(\chi)$ in the last two terms of Eq. (3.74),

$$\begin{aligned} 2\langle a(\bar{\theta}_\infty)\rangle\langle\psi(\bar{\theta}_\infty)\rangle &- 2\langle a(\bar{\theta}_\infty)\psi(\bar{\theta}_\infty)\rangle \\ &= -2\langle a(\bar{\theta}_\infty)\rangle\langle\langle\bar{\theta}^\chi_{\tau_I^\chi}|\chi = \bar{\theta}_\infty\rangle\rangle + 2\langle a(\bar{\theta}_\infty)\langle\bar{\theta}^\chi_{\tau_I^\chi}|\chi = \bar{\theta}_\infty\rangle\rangle \\ &\quad - 2\langle a(\bar{\theta}_\infty)\bar{\theta}_\infty\rangle - 2\langle a(\bar{\theta}_\infty)\rangle\langle a(\bar{\theta}_\infty)\langle\tau_I^{\bar{\theta}_\infty}\rangle\rangle \\ &\quad + 2\langle a(\bar{\theta}_\infty)\rangle\langle\bar{\theta}_\infty\rangle + 2\langle a(\bar{\theta}_\infty)\rangle^2\langle\tau_I^{\bar{\theta}_\infty}\rangle. \end{aligned} \tag{3.78}$$

Coming back to Eq. (3.74), we get

$$\begin{aligned}\frac{d}{dt}\left(\langle\delta\theta_t^2\rangle-\langle\delta\theta_t\rangle^2\right)=&\pi b^2(\tfrac{\pi}{2})\mathcal{P}_{st}(\tfrac{\pi}{2})+2\langle a(\bar{\theta}_\infty)\rangle\langle\bar{\theta}_\infty\rangle-4\langle a(\bar{\theta}_\infty)\bar{\theta}_\infty\rangle\\&-2\langle a(\bar{\theta}_\infty)\rangle\langle a(\bar{\theta}_\infty)\langle\tau_I^{\bar{\theta}_\infty}\rangle\rangle+2\langle a(\bar{\theta}_\infty)\rangle^2\langle\tau_I^{\bar{\theta}_\infty}\rangle\\&-2\langle a(\bar{\theta}_\infty)\rangle\langle\bar{\theta}^{\bar{\theta}_\infty}_{\tau_I^{\bar{\theta}_\infty}}\rangle+2\langle a(\bar{\theta}_\infty)\langle\bar{\theta}^{\chi}_{\tau_I^{\chi}}|\chi=\bar{\theta}_\infty\rangle\rangle\,,\end{aligned}\tag{3.79}$$

that, by replacing $\langle a(\bar{\theta}_\infty)\rangle=\pi\mathcal{J}$ and $\langle a(\bar{\theta}_\infty)\bar{\theta}_\infty\rangle$ from Eq. (3.73), becomes

$$\begin{aligned}\frac{d}{dt}\left(\langle\delta\theta_t^2\rangle-\langle\delta\theta_t\rangle^2\right)=&-\pi b^2(\tfrac{\pi}{2})\mathcal{P}_{st}(\tfrac{\pi}{2})+2\langle b^2(\bar{\theta}_\infty)\rangle-2\pi\mathcal{J}\langle\bar{\theta}_\infty\rangle\\&-2\langle a(\bar{\theta}_\infty)\rangle\langle a(\bar{\theta}_\infty)\langle\tau_I^{\bar{\theta}_\infty}\rangle\rangle+2\langle a(\bar{\theta}_\infty)\rangle^2\langle\tau_I^{\bar{\theta}_\infty}\rangle\\&-2\langle a(\bar{\theta}_\infty)\rangle\langle\bar{\theta}^{\bar{\theta}_\infty}_{\tau_I^{\bar{\theta}_\infty}}\rangle+2\langle a(\bar{\theta}_\infty)\langle\bar{\theta}^{\chi}_{\tau_I^{\chi}}|\chi=\bar{\theta}_\infty\rangle\rangle\,.\end{aligned}\tag{3.80}$$

This analytical expression should represent the estimation of the diffusion coefficient

$$\mathcal{D}_\sigma=\frac{d}{dt}\left(\langle\delta\theta_t^2\rangle-\langle\delta\theta_t\rangle^2\right),$$

corresponding to the tumbling diffusive behaviour. In DNS, this diffusive coefficients is asymptotically re-established by measuring the long time variance of the angular displacement. Before to compare $\mathcal{D}_\sigma$ with DNS results, some simplifications can be discussed in order to compute Eq. (3.80).

A first approach consists in focusing on the first three terms in Eq. (3.80). They are easy to evaluate since they depend only on the knowledge of the stationary distribution $\mathcal{P}_{st}$ in Eq. (3.32). Conversely the other terms associated to the hitting time at the boundary of the domain are more complex to compute, as they can not directly provided by the simple knowledge of the stationary distribution $\mathcal{P}_{st}$. We remark that in the case of $\sigma^*=0$ and by choosing a parametrization of $\mathcal{C}^{\text{iso}}_{ijkl}$ as in Eq. (3.38), where $a=0$ and b is constant we have a right prediction on the diffusion coefficient. For this reason, a first approximation in order to estimate the diffusion coefficient $\mathcal{D}_\sigma$ is to neglect the terms involving the hitting time, such that,

$$\mathcal{D}^{\text{I}}_\sigma=-\pi b^2(\tfrac{\pi}{2})\mathcal{P}_{st}(\tfrac{\pi}{2})+2\langle b^2(\bar{\theta}_\infty)\rangle-2\pi\mathcal{J}\langle\bar{\theta}_\infty\rangle\,,\tag{3.81}$$

where $\mathcal{D}^{\text{I}}_\sigma$ constitutes our first approach in the estimation of the diffusion coefficient. In this case, we expect that this approximation should work in the limit of σ^* small.

Alternatively, a different estimation of Eq. (3.80) can be introduced by going a bit far on the manipulation of the terms that involves the hitting time. When σ^* is large, we can assume that the instantaneous rotation is always in the same sense with large probability, and under the imposed shear that is negative. So starting at point χ, we can evaluate that $\langle\bar{\theta}_{\tau^\chi_\psi}|\chi=\bar{\theta}_\infty\rangle=-\pi/2$, and the mean rotation velocity is $\dot{\theta}_\infty\simeq-\pi\,\mathcal{J}$. This leads to estimate the mean hitting time as,

$$\langle\tau_I^{\chi}\rangle=\frac{\chi+\pi/2}{\pi\,\mathcal{J}}\quad\text{and}\quad\langle\tau_I^{\bar{\theta}_\infty}\rangle=\frac{\langle\bar{\theta}_\infty\rangle+\pi/2}{\pi\,\mathcal{J}}.\tag{3.82}$$

Thus the following term in Eq. (3.80),

$$-2\langle a(\bar{\theta}_\infty)\rangle\langle\bar{\theta}^{\chi}_{\tau_I^{\chi}}|\chi=\bar{\theta}_\infty\rangle+2\langle a(\bar{\theta}_\infty)\langle\bar{\theta}^{\chi}_{\tau_I^{\chi}}|\chi=\bar{\theta}_\infty\rangle\rangle=0\,,$$

and Eq. (3.80) can be simplified by considering $\langle a(\bar{\theta}_\infty)\rangle = -\pi\mathcal{J}$ and Eq. (3.73),

$$\begin{aligned}\frac{d}{dt}\left(\langle\delta\theta_t^2\rangle - \langle\delta\theta_t\rangle^2\right) &= -\pi b^2(\tfrac{\pi}{2})\mathcal{P}_{st}(\tfrac{\pi}{2}) + 2\langle b^2(\bar{\theta}_\infty)\rangle - 2\pi\mathcal{J}\langle\bar{\theta}_\infty\rangle \\ &\quad + 2\pi\mathcal{J}\langle a(\bar{\theta}_\infty)\frac{\bar{\theta}_\infty}{\pi\mathcal{J}}\rangle + 2(-\pi\mathcal{J})^2\frac{\langle\bar{\theta}_\infty\rangle}{\pi\mathcal{J}} \\ &= \langle b^2(\bar{\theta}_\infty)\rangle\,.\end{aligned} \tag{3.83}$$

This means that a second evaluation on the diffusion coefficient $\mathcal{D}_\sigma$ gives

$$\mathcal{D}_\sigma^{\mathrm{II}} = \langle b^2(\bar{\theta}_\infty)\rangle\,, \tag{3.84}$$

constituting our second approach in its estimation.

The above derivation of $\mathcal{D}_\sigma^{\mathrm{II}}$ is based on heuristic arguments. We want to remark here that the function ψ admits an analytical solution in the same spirit of the solution of $\mathcal{P}_{st}$ in Eq. (3.32). We are pursuing the formal derivation of $\mathcal{D}_\sigma^{\mathrm{II}}$ by employing this analytical form. Moreover, the fact of considering σ^* large to derive expression (3.84) is in line with the aim of the model, whose goal is to reproduce DNS results for large values of the shear rate parameter. Hereafter we will first show the results for the DNS, and then we will compare it to the two different approximations $\mathcal{D}_\sigma^{\mathrm{I}}$ and $\mathcal{D}_\sigma^{\mathrm{II}}$.

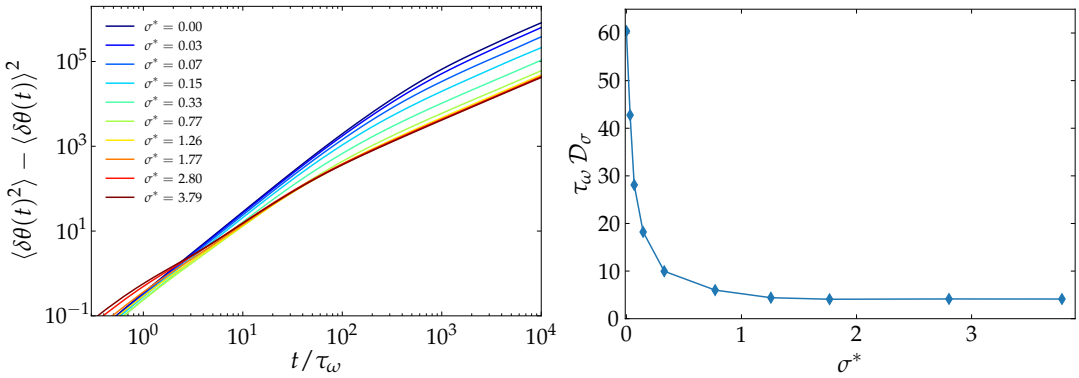

Figure 3.17: Left panel: Variance of the angular increment $\delta\theta(t)$ as a function of time showing in the DNS measurement. Right panel: Measurements of diffusion coefficient $\mathcal{D}_\sigma$ in the diffusive regime $t/\tau_\omega \in [2.0\ 10^3, 1.0\ 10^4]$ as a function of σ^* in DNS.

Figure 3.17 (left panel) shows the DNS measurements for the variance of the angular displacement $\delta\theta(t)$ as a function of time. After a ballistic regime at very small time, there is a transition zone at intermediate time where the behaviour of the system is super-diffusive but without a clear emergence of stable regime. At much longer times, a diffusive behaviour is asymptotically recovered. The elapsed time to reach the diffusive regime depends on the shear rate parameter. In fact as σ^* increases, the intermediate time to reach the diffusive behaviour decreases. The reliance on the shear rate can be explained by considering that small values of σ^* coincide with very long Lagrangian correlations of the velocity gradient compared to larger value of σ^*. In general, in the diffusive regime, the behaviour of the variance of angular displacement is described by $\langle\delta\theta^2(t)\rangle - \langle\delta\theta(t)\rangle^2 = \mathcal{D}_\sigma\, t$. Left panel of Fig. 3.17 shows the DNS measurement of the diffusion coefficient $\mathcal{D}_\sigma$, within the range $t/\tau_\omega \in [2.0\ 10^3, 1.0\ 10^4]$ as function of the shear rate σ^*. As the shear rate increases, the diffusion coefficient becomes smaller due to the presence of the shear that tends to deplete the structures within the flow. Furthermore, $\mathcal{D}_\sigma$, for the last three values of σ^*, becomes constant. This saturation could be originated by the effect of finite domain. Indeed, as pointed out in Paragraph 3.3.1 (Box size

effect) there is a limit in performing the DNS for large values of the shear rate while keeping the box domain constant. That is, when the value of σ is too strong and the size of the box is maintained constant, the elongated structures induced by the shear become all parallels to the imposed direction of the shear (see Fig. 3.14, snapshots of the vorticity structures appear as stripes) and are of the order of the box length L_x. This could produce the saturation effects, impacting the measurements that we had analysed.

Still, this is not completely clear, and in order to shed light on such behaviour, one needs to perform others simulations increasing both the value of the shear rate and, at the same time, the size of the computational domain L_x. This could confirm or infirm the saturation that so far we are observing.

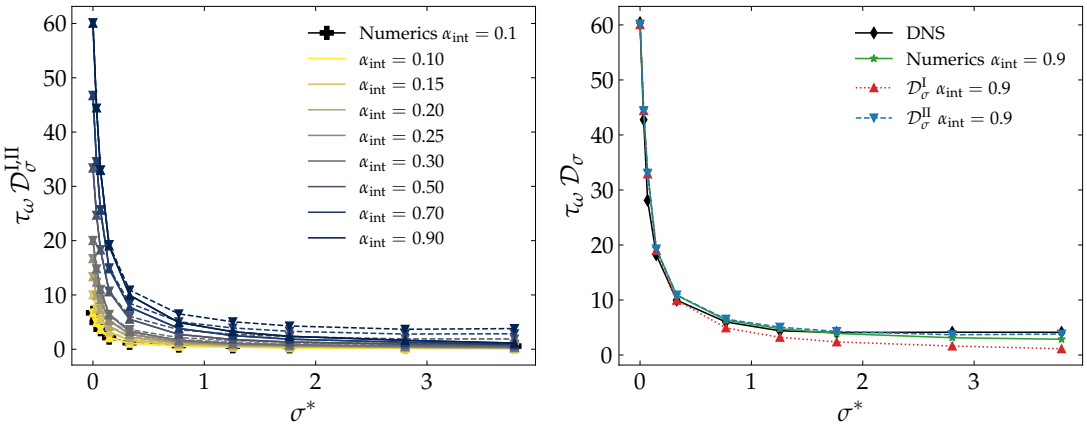

Figure 3.18: Left panel: Measurements of diffusion coefficient $\mathcal{D}_\sigma^{\mathrm{I}}$ in Eq.(3.81) (continuous line with upper triangular markers) and $\mathcal{D}_\sigma^{\mathrm{II}}$ in Eq.(3.84) (dotted line with lower triangular markers) for different values of the tuning parameter α_{int} (as in legend). In black cross marked line corresponds to the model result by integrating numerically Eq. (3.44) for the tuning parameter $\alpha_{\mathrm{int}} = 0.1$. Right panel: Measurement of the diffusion coefficient $\mathcal{D}_\sigma$: in DNS (in black diamond line), in the model according to Eq. (3.81) (in red upper triangles marker dotted line), in the model according to Eq. (3.81) (in blue lower triangles marker dashed line), and in the model result by integrating numerically Eq. (3.44) (in green starred marker line), for the tuning parameter $\alpha_{\mathrm{int}} = 0.9$, as a function of σ^*. The numerical integration for the model has been performed using an Euler–Maruyama scheme with an integration time-step $\Delta t = 5 \cdot 10^{-4}$ and with a final time $T = 1000$.

COMPARISON BETWEEN MODEL AND DNS RESULTS The analytical result of diffusion coefficient $\mathcal{D}_\sigma^{\mathrm{I}}$ in Eq. (3.81) (continuous line with upper triangular markers) and $\mathcal{D}_\sigma^{\mathrm{II}}$ in Eq.(3.84) (dotted line with lower triangular markers) are shown in Fig. 3.18 (left panel) for different values of α_{int} (in legend). In this case the two approaches match for small values of σ^* and for any values of α_{int}. As soon as the shear rate parameter increases, the term estimation of $\mathcal{D}_\sigma^{\mathrm{II}}$ becomes larger than the $\mathcal{D}_\sigma^{\mathrm{I}}$, which means that the terms related to the hitting time has an important weight in the estimation of the diffusion coefficients.

To confirm the validity of the analytical expressions (3.81) and (3.84), a direct numerical integration of Eq. (3.44) (using an Euler–Maruyama scheme) for $\alpha_{\mathrm{int}} = 0.1$ has been performed. This result matches with the analytical prediction when $\sigma^* \leq 1.25$ for both $\mathcal{D}_\sigma^{\mathrm{I}}$ and $\mathcal{D}_\sigma^{\mathrm{II}}$, and for larger values a small discrepancy arises, we have checked the behaviour even if in Fig. 3.18 (black line crosses) is not directly visible. It is also true that from the direct numerical integration some error bar in measuring the derivative in time of the variance of $\delta\theta_t$ should be expected.

Another important consideration is the dependence on α_{int} in both of two approaches . Indeed, the general idea all along this chapter was to keep constant the tuning parameter α_{int} as function of σ^*, even if it has an impact on the behaviour of $\mathcal{D}_\sigma^{\text{I}}$ and $\mathcal{D}_\sigma^{\text{II}}$.

As we can notice, the model for $\alpha_{\text{int}} = 0.1$, does not reproduce the DNS result (see right panel of Fig. 3.18). As soon as α_{int} increases, the model becomes closer and closer to DNS result (see right panel of Fig. 3.18). Figure 3.18 (right panel) shows the comparison of the diffusion coefficient $\mathcal{D}_\sigma$ in DNS case compared with the $\mathcal{D}_\sigma^{\text{I}}$, $\mathcal{D}_\sigma^{\text{II}}$ and numerical integration of Eq. (3.44), having fixed $\alpha_{\text{int}} = 0.9$.

Moreover, to better understand the analytical expression (3.80), a direct numerical integration of Eq. (3.44) has been performed for $\alpha_{\text{int}} = 0.9$. In this case, the analytical prediction follow the same trend of DNS and we find also a good agreement, for small value of σ^*, for both $\mathcal{D}_\sigma^{\text{I}}$ and $\mathcal{D}_\sigma^{\text{II}}$. Conversely, for $\sigma^* \geq 0.32$, the analytical expression $\mathcal{D}_\sigma^{\text{II}}$ in (3.84) has a better agreement, as expected, than $\mathcal{D}_\sigma^{\text{I}}$ when compared with DNS result. In the first analytical approach Eq. (3.81), the model tends to underestimates the diffusion coefficient which means that some important effects are inscribed in the estimation of the terms related to the hitting time in Eq. (3.80). Interestingly, the numerical integration of the model and $\mathcal{D}_\sigma^{\text{II}}$ match very well between them and, as well with DNS. This may suggests that $\mathcal{D}_\sigma^{\text{II}}$ in Eq. (3.84) is a good approximation for the diffusion coefficient of for the variance of the angular displacement.

Another point worthy of discussion, concerns the good choice of $\alpha_{\text{int}} = 0.9$ to reproduce the DNS result. Actually, this value is larger than the one used to mimic the statistics of the mean angular displacement (right panel in Fig. 3.16). The effect to increase the value of α_{int} is justified since the PDF of $\delta\theta$ (in Fig. 3.19) shows stretched-exponential tails in the diffusive regime. This means that the diffusion in the model has to be increased in order to replicate the large fluctuations embedded in the complex DNS behaviour.

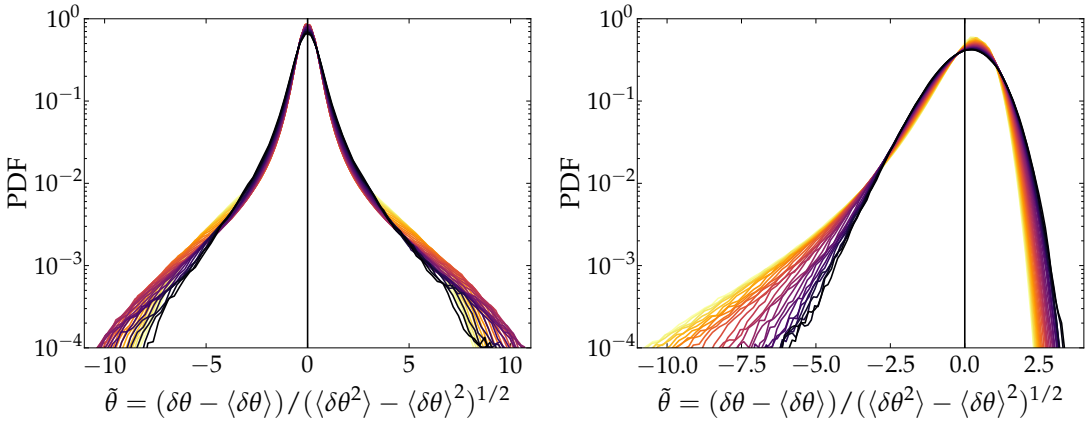

Figure 3.19: Probability density function (PDF) of the angular increment $\delta\theta(t) = \theta(t) - \theta(0)$ centred and rescaled to unit variance for $\sigma^* = 0$ (left panel) and $\sigma^* = 2.6$ (right panel). The different curves correspond to different time lags logarithmically spaced between $t = 80\,\tau_\omega$ and $t = 6000\,\tau_\omega$ (from light yellow to dark violet).

To finish this overview, we have plotted in Fig. 3.19 the probability density function of the increment $\delta\theta(t)$ at different times for $\sigma^* = 0$ (left panel) and $\sigma^* = 2.8$ (right panel) computed in DNS case. Here, the distribution have been centred and rescaled to unit variance. At first glance, one observes strong qualitative differences between these two cases. The presence of shear completely depletes fluctuations at positive values, as already observed for the vorticity. The different curves correspond to different time lags, logarithmically spaced between $t = 80\,\tau_\omega$ and $t = 6000\,\tau_\omega$ (from light yellow to dark violet). As the time increases, the tails of the distribution for both $\sigma^* = 0$ (left panel) and $\sigma^* = 2.8$ (right panel) tend to shrink, being this

behaviour most noticeable in the presence of shear. Indeed, it seems that as time increases the dark lines tend to a more Gaussian behaviour.

Another observation is that the presence of stretched-exponential tails would indicate the angle experiencing a Lévy walk, as observed the trajectories in Fig. 3.15. Moreover, the PDF confirms the complex dynamics in the DNS case, underlying the limit of the model in reproducing these intricate behaviours. Despite the limits of the model and its dependence on a tuning parameter, when the anisotropic effects are introduced, model results are very close to the DNS.

3.5 CONCLUSIONS

We have studied the dynamics and statistics of the like-rod particle placed in an homogeneous turbulent shear flow. In the framework of a velocity flow model consisting of a stationary part and a delta-correlated chaotic part, we have obtained several analytical results by considering the Lagrangian stochastic model of a rod. Furthermore, to assess the applicability conditions and the limitations of our stochastic model, direct numerical simulations have been performed. The range of validity of the model has been defined by means of the dimensionless Kubo number $Ku \ll 1$. Moreover, the model has been developed considering the anisotropy of the velocity gradient correlations within the homogeneous turbulent shear flow.

Firstly, the stationary angular distribution was discussed in detail both for the DNS and model case. We obtained an explicit expression for the stationary probability distribution of the folded angle $\bar{\theta}$. Moreover, the behaviour of this distribution depends on the shear rate parameter σ^* and coincides with the DNS results, having introduced a tuning parameter α_{int} for the velocity gradient correlations. Secondly, the orientation dynamics of the rod has shown the importance of considering the anisotropic correlations within the model, in order to better reproduce the DNS measurements.

In the presence of mean shear the tumbling dynamics of a rod consists of aperiodic transitions between two unstable states: the one aligned with the direction of the shear and that anti-aligned with it. When a fluctuation takes the rod away from the aligned or anti-aligned states, and moves it into the unstable region of the flow, the mean shear makes the rod flip. In this framework, an alternative definition to measure the tumbling rate has been proposed, such that future experimental works could take advantage of it. It consists in counting the total number of turns that the unfolded angle is making and regarding to its long time asymptotic behaviour. In particular, the derivative of the long-time behaviour of the average angular displacement $\langle \delta\theta(t) \rangle$ has been identified as the quantity that allows to have an alternative definition of tumbling rate. The analytical expression of such quantity has been computed and compared with DNS, resulting in good agreement. Additionally, we have shown that the tumbling rate can be associated to the probability flux of the stationary distribution of the unfolded angle dynamics. This led to make an equivalent view-point of what Wilkinson and Mehlig (2003) did in another context in order to define the rate of coagulation of suspended particles eventually coagulated (caustic formation).

Moreover, the trajectories of the angular displacement $\delta\theta(t)$ are a combination of diffusion with long-range excursions, that resemble to mimic the behaviour of Lévy walks. In this respect, a future perspective could be to model the fluctuations of the velocity gradient by using an α-stable process, in an attempt to get a more realistic description of the complex dynamics observed in DNS. α-stable processes belong to the family of Lévy ones, and are relatively straightforward to simulate. However, the use of such processes involves the introduction of additional parameters that need to be calibrated, adding some level of complexity.

Lastly, the variance of angular displacement has been measured in DNS, revealing that the diffusive behaviour at long time strongly depends on the shear rate parameter. In the diffusive

regime an asymptotic analysis allows to derive the diffusion coefficient of the model. When this is compared with the DNS one, a limitation of the model emerges. Indeed, this statistic is strongly affected by the non-Gaussian behaviour of the real measurements which are not taken into account in the model. Nevertheless, in our view, the latter provides an open perspective, in which the anisotropic behaviour on the velocity gradient correlation is taken into account, and a possible extension to the case of non-Gaussian statistics could be the subject of new investigations as anticipated above.

4 NUMERICAL SCHEME FOR THE ORIENTATION OF NON-SPHERICAL PARTICLES

Outline. In this chapter we present an extension of the stochastic Lagrangian model, developed in Chapter 3 for the orientation of non-spherical particle, to the three dimensional case. This model will be coupled with the stochastic classical hybrid Eulerian/Lagrangian for the description of the dispersed phase. Moreover, an alternative definition of the rotational modes of a non-spherical particle in three dimensions will be introduced, in the same spirit of Chapter 3. We propose and analyse a semi-implicit splitting numerical method for the non-linear stochastic differential equation (SDE) present in the model (for which globally Lipschitz condition fails); our goal is to preserve the geometric features hidden in this system and to obtain convergent schemes. The analysis will be followed by the application to a semi-real case, considering the non-spherical particles embedded in a homogeneous shear flow.

4.1 INTRODUCTION

Investigating the dynamics of non-spherical particles suspended in turbulent flows is fundamental in making advances in several engineering and environmental applications such as clouds in the atmosphere, plankton dynamics in the ocean, combustion systems and paper-making, to name a few. A modern exhaustive review on the subject, including models used to describe non-spherical particles motion, alongside with numerical and experimental methods for measuring particle dynamics, has been provided by Voth and Soldati (2017).

A standard approach which can be used for simulations of millions of small particles, is the point-particle approach (Kuerten (2016)). These particles are much smaller than the Kolmogorov length scale η_K, and the velocity gradient can be assumed spatially uniform (smooth) since below this scale viscosity regularises the velocity fluctuations. Besides, in this framework, the Eulerian/Lagrange (Stock (1996); Eaton (2009); Soldati and Marchioli (2009)) approach is often used to investigate the particle motion in flow. While the Eulerian approach is adopted for the turbulence field, the non-spherical particles are treated in the Lagrangian framework. This is the approach considered in our study.

4.1.1 *From micro to macro approach*

A direct numerical simulation (DNS) (Fan and Ahmadi (1995); Marchioli et al. (2010)) is possible, and remains a unique computational tool that provides informations about a number of quantities currently inaccessible in laboratory, and constitutes a valuable asset in understating turbulence phenomena. In such simulations, the motion of wide range of eddies, from physical systems, down to Kolmogorov dissipation length scale, is explicitly accounted for. In such case, the orientation dynamics has been studied in homogeneous isotropic turbulence (HIT) (Shin and Koch (2005); Pumir and Wilkinson (2011); Parsa et al. (2012); Chevillard and Meneveau (2013); Byron et al. (2015)), as well as experimentally (Bernstein and Shapiro (1994); Newsom and Bruce (1998); Ni et al. (2015)). At the same time, studies of anisotropic particles in inhomogeneous turbulent flow, for example in a turbulent channel flow (Zhang et al. (2001);

Mortensen et al. (2008); Marchioli et al. (2010); Marchioli and Soldati (2013); Zhao et al. (2015)) have been motivated by their particular relevance for industrial applications.

However, the complexity of non-spherical particle suspended in a turbulent flow has limited the application of advanced engineering techniques, as computational fluid dynamics, to the design and optimization of the various unit operation and processes, resulting in lower product quality and efficiency. Application of these techniques requires the development of reduced physical models for anisotropic particles within turbulent flow, that can be implemented into predictive industrial computational tools. Indeed, performing DNS of typical industrial problems is computationally very expensive or even sometimes unfeasible. Thus, in the case of large number of particles and turbulent flows at high Reynolds numbers, as well as in the presence of complex geometries, the number of degrees of freedom is huge and one has to resort to a contracted probabilistic description. In this case, the fluid phase is described by a small set of statistical mean fields, such as Reynolds Averaged Navier–Stokes Simulations (RANS), or large-eddy simulations (LES) (Pope (2001)).

On the other hand, the dispersed phase is directly described by a large number of particles which are individually tracked by a set of equations describing their dynamical behaviour. Time evolution of the variables of interest is described by stochastic differential equations (SDEs), the so-called Langevin equations, and has been extensively analysed by Minier and Peirano (2001). The study of the orientational and rotational motion of non-spherical particles using mean-field/PDF (probability density function) approaches has received less attention than DNS. For example, the problem has been studied by Chen et al. (2016) using an LES, where a model for the sub-grid scale (SGS) was introduced by means of an SDE for the velocity gradient tensor, and results have been obtained for the HIT.

One of the purposes of this chapter is to introduce a three-dimensional formulation of the stochastic Lagrangian model presented in Chapter 3, for the orientation of non-spherical particles, which can be added to the transport stochastic model of the dispersed phase. The flow is assumed to be sufficiently diluted that the effects of the particles on the flow can be neglected. In addition, Jeffery (1922) approach has been considered, where particles are small inertialess tracers with a size smaller than the Kolmogorov length scale η_K but sufficiently large to neglect Brownian motion (molecular diffusion). It is worth to underline, as pointed out by Minier et al. (2001), the multi-scale character of the problem : the Kolmogorov time-scale τ_η, the Lagrangian integral time-scale of the fluid T_L, and the integration time-scale Δt. The first two are physical characteristic time-scales, whereas Δt represents the 'observation' time-scale. The latter, such as that used in industrial codes, impacts the choice of the model.

Another point of interest is the rotational behaviour of an axisymmetric particle, actively investigated in HIT (Parsa et al. (2012); Gustavsson et al. (2014); Marcus et al. (2014); Byron et al. (2015)) and in turbulent channel flow (Zhao et al. (2015); Zhao and Andersson (2016); Zhao et al. (2019)) using DNS. In particular, the rate of change of tumbling, which denotes the orientational dynamics of the symmetry axis of the particle, and of spinning, which indicates the rotation of the particle around its own symmetry axis, has been analysed. Conversely to these previous studies, in DNS framework, the stochastic model for the orientation is described by an SDE that is nowhere differentiable in time, so that alternative definitions of both, tumbling, and spinning rate are introduced.

4.1.2 *Numerical challenge*

The accuracy on predicting the orientation of non-spherical particles in this framework depends on two ingredients: the Lagrangian stochastic model for the orientation, and the numerical algorithm. The purpose of the orientation model is to describe the physics as accurately as possible (within purposes/hypotheses of the model), with the resulting computation being

economically feasible. On the other hand, accurate numerical algorithms are required to solve the modelled SDE. Both of these factors affect the accuracy of the numerical prediction of the orientation of non-spherical particles. From the numerical perspective, the time step, to avoid increasing the computational time should be the same for the integration of mean-field and SDE, imposed externally by the algorithm that solves the mean-field equations for the fluid. This implies that there is no possibility to control the time step when integrating the SDE for the model orientation.

Besides the 3D extension of the model, another question we want to tackle here is 'What is a suitable numerical scheme for large integration time steps that can be used for the SDE associated to the model, without damaging the statistical properties of the orientation?' Answering this question leads to a better understanding of the behaviour of numerical errors (in weak and strong sense) of the scheme adopted for the SDE, and of the validity of the integration scheme in the industrial computation setting (large number of particles, large integration step-size). In this framework, developing efficient and accurate numerical tools is highly valuable for improving the performance of industrial codes, ensuring the release of highly-efficient computational schemes. Specifically, the Lagrangian stochastic model for the orientation has been implemented in the Lagrangian module of *Code_Saturne*, that is a free, open-source software developed and released by Électricité de France (EDF) to solve computational fluid dynamics applications.

As said, for practical computations, the orientation model is interfaced with mean-field/PDF transport models. The fluid field consists of a set of partial differential equations (PDEs) describing the dynamics of mean quantities (Markatos (1986); Launder (1990); Wilcox et al. (1998)) and a set of SDEs which describes the variables of interests for the discrete particles (Peirano et al. (2006)). In this approach, the numerical solution is obtained by using a hybrid method (Muradoglu et al. (2001); Peirano et al. (2006)) where the mean fluid properties are computed by numerically solving the mean field equation with classical finite difference or finite volume methods (Jones (1994)), whereas the properties of particles are determined by solving the SDEs (Pope (1995); Peirano et al. (2006)).

The development of an efficient, stable and accurate numerical scheme faces two main difficulties. The first one arises from the nature of stochastic models: SDEs do not obey the rules of ordinary differential equation (ODE) and one has to deal with the theory of stochastic integrals. The second one is related to the mathematical model of complex physical processes and its constraints.

Numerical schemes for SDEs are iterative methods where trajectories of the solution are computed at discrete time steps. These schemes are now abundant and their convergence is classified according to their type, i.e. the path-wise approximation (strong sense) or the approximation to the probability distribution (weak sense), and order of convergence (Pagés (2018)).

In this context, we are interested on both, the statistics of the particle orientation and rotation (which are connected to the study of the weak convergence), and on the behaviour of the stochastic trajectories (linked to the study of the strong convergence), due to the complexity of the model. In particular, the turbulent fluctuations of the symmetric and antisymmetric part of the velocity gradient are modelled by Brownian motions where the correlation tensor of the velocity gradient has been considered anisotropic (see, e. g., Chapter 3). This implies that is relevant to ensure that the characteristic features of trajectories are faithfully resolved to construct a strongly convergent approximation scheme. Particularly, the strong approximation may show the influence of certain parameters (e. g., the different shape of the particles or different time scales in turbulence) and it can lead to understand the consequence of certain interactions among components of the orientation vectors, by having introduced some anisotropies within the fluctuating part of the velocity gradient. Moreover, the orientation vector $\boldsymbol{p}$ is of unitary

norm, that is the modelled SDE for the orientation lives on a sphere, implying that the direct simulation of the trajectories needs to reproduce accurately their motion on this curved surface. Thus, both, weak and strong solutions (Pagés (2018)) for the SDE of orientation are studied.

Traditionally, there are two fundamentally different algorithmic approaches to solve numerically complex physical processes, considered in discrete form: (i) a fully coupling approach where governing equations are solved as a single, usually very complicated system; (ii) a decoupling approach in which governing equations are decoupled in simpler sub-problems and are solved as simpler tasks. The operator splitting methods (Blanes et al. (2008)) belong to the second type, and are used to solve complex physical models of different nature, especially in geophysical and environmental physics. These methods were originally designed to reduce the computational difficulties by decomposing delicate differential equations, of both, deterministic, and stochastic nature, into simpler solvable equations. Interested readers can find more general details in the overview papers of Strang (1968); Marchuk (1968).

When dealing with SDEs, decomposition methods require particular attention due to the presence of the stochastic integral in the Itô or Stratonovich formulation. In addition, those methods have been mostly explored in the case of non-globally Lipschitz diffusion coefficients (see, e. g., Higham et al. (2002); Mattingly et al. (2002)), due to their effectiveness in presence of superlinearly growing coefficients. Indeed, when the coefficients of an SDE are globally Lipschitz continuous, then standard results (e. g., Pagés (2018)) show convergence of the Euler–Maruyama approximation in the strong and numerically weak sense to the exact solution of the SDE. Conversely, as studied by Hutzenthaler et al. (2011), for a large class of SDEs with non-globally Lipschitz continuous coefficients (in both drift and diffusion part), the Euler–Maruyama approximation converges neither in the strong mean-square sense nor in the weak sense to the exact solution at a finite time point. This requires to pay particular attention on the choice of a suitable numerical scheme, since the orientation equation that we are going to focus on, presents difficulties coming from the non-globally Lipschitz diffusion coefficient similar to what has been explored by Hutzenthaler et al. (2011).

In this work, we propose to apply a splitting method for the approximation of the Lagrangian stochastic model for the orientation, where the SDE is appropriately decomposed in different contributions to obtain numerical solutions with less computational complexity.

Then, each sub-part of the splitting requires a numerical discretisation to generate paths of the SDE as much computationally efficient as possible. Thus, the construction of explicit or semi-implicit schemes which are capable to maintain the properties of the complex physical process for time steps as large as possible is, here, of fundamental relevance. This leads to an important issue related to the SDE that describes the orientation of a non-spherical particle. The orientation vector is of unitary norm, that is numerically we have to deal with the preservation of structural properties of the SDE, which is well-established in the context of ODE, by means of Geometric numerical integrators, (Hairer et al. (2006)) but less explored for its stochastic counterpart (Piggott and Solo (2016)). In classical setting of SDE, evolving without preserving structural properties (geometrical constraints), there is a vast literature on the weak and strongly convergent schemes, such as Euler–Maruyama, Milstein or high order Itô-Taylor approximation schemes; nevertheless they could fail in preserving structural properties.

Particular attention is paid in developing a numerical scheme for each sub-part of the splitting, in order to meet all the requirements. Furthermore, an accurate analysis on the numerical error both, in weak and strong sense, is provided for each sub-part. Then, for each sub-part of the splitting, a first order Euler–Maruyama scheme has been considered since the choice of a splitting technique introduces an additional source of error coming from the composition operator of the splitting.

Statistical error of the Monte Carlo scales as $\sqrt{N_p}$, where N_p is the number of particles. Due to the slow convergence of the Monte Carlo particle method, most likely the statistical error

dominates other numerical errors, including the time-stepping error (when it becomes small). Hence, using high-order accurate SDE schemes in this context, only increases the complexity of the schemes, without helping to reduce the overall numerical error.

To determine the formal order of accuracy and convergence of the numerical scheme, the exact solution of the problem (for the weak error), or an accurate trajectory estimate (for the strong error), is required to provide a reference for evaluating the numerical error . In the weak error analysis, for some cases, the exact solution to the problem may be obtained with simplification of the problem. In our case, the exact solution to the problem is derived assuming the HIT case, where the mean field contribution is set to zero. This choice is justified since we are mainly interested on the behaviour of the stochastic part of the numerical scheme. Conversely, the deterministic part of the splitting method, coming from the mean-field contribution, is much better known, e. g., Press et al. (1986), so that only a brief sketch of the implementation will be considered.

The study of the numerical error of the Monte Carlo, is computationally demanding. A large number of particles are required in the Monte Carlo simulation to make the statistical error negligible compared to the other numerical errors. In order to study the convergence, in weak and strong sense, of the SDE scheme with respect to time, we have performed simulations in parallel via OpenMPI. Besides, the numerical tests have been implemented on a customised code, specifically designed to make numerical analysis affordable.

Ultimately, long-time behaviours of SDEs are also a notable concern in stochastic processes (e. g., Khasminskii (2011)). The dynamical properties of SDEs have been largely investigated, including stochastic stability (Mao (2007); Khasminskii (2011)) and ergodicity (Hairer (2005)), among the others. The SDE that we consider lives in $SO(3)$, thus there exists an invariant measure, i.e. the distribution of the process converges to a unique limit for any starting initial condition. This is a reason for the study of long-time behaviour, since it allows to investigate whether the discretisation of the SDE preserves or not such a property. In real applications this is an important key-point, since the initial value is negligible and usually should not impact the observed phenomena. Moreover, in an ergodic system time average along trajectories and ensemble average across trajectories coincide. Indeed, such property can be exploited on computing statistical observables, evaluating them on a single path simulated over a long time horizon instead of relaying on a large amount of trajectories. Numerical methods are quite sensitive in preserving long time behaviour; for instance, we refer to Roberts and Tweedie (1996); Mattingly et al. (2002). In particular, we show that the constructed splitting algorithm along with a suitable numerical approximation for each of its sub-parts, asymptotically preserves the ergodicity and moments are bounded.

4.1.3 *Main contributions*

The aim of this chapter is resumed in the following five points, recollecting the main contributions that we brought:

(i) The model presented in Chapter 3 is extended to a non-spherical particle of arbitrary axisymmetric shape, described by a single shape parameter, Λ. Furthermore, assumptions are discussed, that have been introduced to reduce model complexity and to build a test-case where an analytical solution of the moments exists and can be used to numerically investigate the weak convergence.

(ii) The SDE which describes the orientation of non-spherical particles does not allow to compute the derivative in time of the process, that implies to find a new formulation for the rotation statistics, i.e. tumbling and spinning rate, for the model.

(iii) Considering a splitting algorithm and introducing a novel approximation technique, we construct a semi-implicit Euler–Maruyama scheme that preserves the unitary norm of the orientation vector for a specific sub-part of the splitting. For the other sub-parts, classical methods for the ODE and SDE are considered and discussed. Moreover, we show that the stochastic sub-parts of the splitting converge weakly and strongly with order Δt and $\sqrt{\Delta t}$, respectively. Then the study of convergence of the splitting is extended by composing the two stochastic sub-equations in the HIT case, where the mean field contributions are set to zero. When the splitting scheme is applied, the weak and strong convergence rate match that of classical Euler–Maruyama method (Pagés (2018)).

(iv) The long-time behaviour is analysed, showing that the constructed splitting method well reproduces the invariant distribution in HIT case. This result is used to compare analytical and numerical results of tumbling and spinning rate in their new formulations.

(v) A representative test case, in a more realistic applicative setting, has been considered, in which a mean field part is accounted through a mean homogeneous shear flow. Here, the numerical strong convergence of the decomposition method and the long-time behaviour are studied revealing the robustness of the numerical scheme.

The rest of the work is organised as follows. In Section 4.2, we briefly recall hybrid Lagrangian stochastic model for the fluid velocity which is in general implemented in an industrial code (in our case *Code_Saturne*), in order to furnish a general setting in which the orientation model is implemented. In Section 4.3, we introduce the Lagrangian stochastic model for the orientation and the rotational statistics associated to the model. In Section 4.4, the splitting method and the numerical schemes of different sub-parts are presented, followed by the discussion of strong and weak numerical convergence. In addition, the homogeneous isotropic turbulence case is tested and its long time behaviour, including tumbling and spinning statistics, analysed. In Section 4.5, the splitting scheme is tested for an homogeneous shear flow, including its strong numerical convergence and its long time behaviour. Conclusions are reported in Section 4.6.

4.2 LAGRANGIAN STOCHASTIC MODEL FOR THE FLUID VELOCITY

The Lagrangian stochastic model for the orientation has been implemented in an industrial CFD code (*Code_Saturne*) and here, the general context of its applicative framework is briefly presented. Stochastic modelling approaches have become increasingly used for the study of polydispersed two-phase flow. These approaches are referred to as PDF (Probability Density Function) methods (Peirano et al. (2006)), where turbulent closure is achieved through a modelled transport equation for the joint PDF of some variables, which constitute the state vector of the process. Moreover, among these approaches, a complete description of polydispersed two-phase flow is represented by a hybrid Moments/PDF method which gathers two different points of view, and two different levels of information. The fluid phase is approached by the classical Eulerian moment method, limited to the first two moments in RANS or to the filtered field in LES, numerically obtained by solving PDEs on a grid, whereas the dynamics of the dispersed phase is the one-point PDF, directly simulated by a stochastic process solving the SDEs for the time evolution of the particle state vector (Peirano et al. (2006)). In this approach, describing particle dynamics in high Reynolds number turbulent flow, the standard particle state vector, with inertia, contains particle location and velocity, as well as the velocity of the fluid seen by the particle, i.e. $\boldsymbol{Z} = (\mathbf{X}_p, \boldsymbol{u}_p, \boldsymbol{u}_s)$, as presented by Peirano et al. (2006). The choice is valid for inertial spherical particles. Furthermore, when other phenomena need to be accounted for, the particle state vector is naturally extended to include the relevant variables attached to each particle.
The general form, for a spherical inertial particle (when only drag forces act on particles), of

the state-of-the-art of Langevin model (Minier (2016)) where the equation of the velocity of the fluid seen comes from an extension of the *generalised Langevin model* (GLM) (Pope (2001)) for the fluid particles, takes the form,

$$dX_{p,i} = u_{p,i}\, dt \tag{4.1}$$

$$du_{p,i} = \frac{1}{\tau_p}\left(u_{s,i} - u_{p,i}\right) dt \tag{4.2}$$

$$du_{s,i} = -\frac{1}{\rho_f}\frac{\partial \langle P_f \rangle}{\partial x_i} dt + \left(\langle u_{p,j} \rangle - \langle u_{f,j} \rangle\right) \frac{\partial \langle u_{f,i} \rangle}{\partial x_j} dt + G^*_{ij}\left(u_{s,j} - \langle u_{f,j} \rangle\right) dt + B_{s,ij}\, d\widetilde{W}_j(t), \tag{4.3}$$

where $\widetilde{W}_j(t)$ is a vector of independent Wiener processes. The following model involves conditional means such as for example $\langle \boldsymbol{u}_p(t)|\boldsymbol{x}\rangle$, $\langle \boldsymbol{u}_f(t)|\boldsymbol{x}\rangle$, which means that all the mean field quantities within the model need to be evaluated at time t for the particle at position $\boldsymbol{x} = \mathbf{X}_p(t)$. The matrix G^*_{ij} is build from the matrix G_{ij} of the GLM (Pope (2001)) and is given by $G^*_{ij} = -(1/2 + 3/4\, C_0)(\varepsilon/k)\, H_{ij}$ where C_0 is a constant, k is the fluid turbulent kinetic energy and ε is the mean dissipation rate of the turbulent kinetic energy. The matrix H_{ij} accounts for the crossing-trajectories effect and contains the Csanady factors which stand for the ratio between the timescale of the fluid particle velocities T_L and the timescale of the fluid velocity seen by discrete particles. The general diffusion coefficients matrix $B_{s,ij}$ can be found in Minier (2016), as well as more others details on Eqs. (5.4)-(5.6).

In this work, we consider anisotropic inertialess particles since from a modelling perspective they represent a more complex case to address. This comes from the fact that anisotropic tracer particles are responsive to the intricate turbulence behaviour, in contrast to the case of inertial ones, that do not mimic all these features, reacting smoothly to turbulence.

In perspective, the extension of the model to anisotropic inertial particles is interesting and implies the additional work of including the particle relaxation time τ_p in the Jeffery's equation. We would underline that the numerical scheme, hereafter developed can be adapted to the inertial case since it deals with the general numerical problem of orientation that remains the same for both, inertialess and inertial particles.

When anisotropic inertialess particles are considered, the fibre state vector is supplemented by the particle orientation vector $\boldsymbol{p}$. In this case, particles consist of fluid tracers by meaning that particle velocity tends towards fluid velocity, getting a relevant fibre state vector $\boldsymbol{Z} = (\mathbf{X}_f, \boldsymbol{u}_f, \boldsymbol{p})$. The Langevin model in Eqs. (4.1), (5.5) and (5.6), using some simplification detailed in Minier (2016), in the particle tracer limit of vanishing inertia (i.e. in this case $\boldsymbol{u}_s = \boldsymbol{u}_f$), as explained in (Chibbaro and Minier (2011)), reverts continuously to the Simplified Langevin Model (SLM) developed by Pope (1994), becoming

$$dX_{f,i} = u_{f,i}\, dt \tag{4.4}$$

$$du_{f,i} = -\frac{1}{\rho_f}\frac{\partial \langle P_f \rangle}{\partial x_i} dt - \frac{1}{T_L}\left(u_{f,i} - \langle u_{f,i} \rangle\right) dt + \sqrt{C_0 \varepsilon}\, d\widetilde{W}_i(t). \tag{4.5}$$

The Lagrangian time scale of the velocity correlation is defined by $T_L = \frac{1}{(\frac{1}{2}+\frac{3}{4}C_0)}\frac{k}{\varepsilon}$ with the other quantities detailed in Minier et al. (2004); Peirano et al. (2006). In the above Langevin model which has been reduced for the position and velocity of the fluid seen Eqs. (4.4)-(4.5), the fluid mean velocity field $\langle u_{f,i} \rangle$, the turbulent kinetic energy k, the mean dissipation rate ε and the mean pressure gradient are provided by an Eulerian solver. In this case, for the two-phase calculation performed with Moment/PDF approach, the time step can be further constrained by the fluid flow computation. From now on, the discussion will be focused on the SDE that models the orientation disregarding the external framework.

4.3 LAGRANGIAN STOCHASTIC MODEL FOR THE ORIENTATION

An axisymmetric ellipsoid, i.e. a spheroid, is the simplest shape commonly adopted to closely represent non-spherical particles, where the shape of a spheroid is easily parametrised by the aspect ratio λ, as shown in Fig. 2.1 of Chapter 2). Aspect ratio is defined as the ratio between the symmetry axis and the two equal axes. Moreover, we consider a small spheroidal tracer particle whose size is smaller than the Kolmogorov length scale η_K, so that the local flow around the particle can be considered to be inertia-free and Stokes flow solutions can be used to relate the rotational dynamics of the particle to the local velocity gradient tensor.

In this section, we briefly recall the Jeffery's equation presented in Chapter 2 that has been largely used to investigate the orientation and rotation in DNS context. Then, the Lagrangian stochastic model for the orientation of a rod-like particle developed in Chapter 3, is extended to spheroidal particle. In addition, the model is required to be coherent with the considered transport equations, Eqs. (4.4)-(4.5), and the associated numerical scheme for the orientation has to be transparent, i.e. it does not introduce numerical constraints on the modelled transport part of the system in Eqs. (4.4)-(4.5). Ultimately, the rotation statistics of the model is discussed to clarify the link on what has been already investigated in DNS (Parsa et al. (2012)).

4.3.1 *Deterministic equation for the orientation*

The problem was tackled by Jeffery (1922) who considered a spheroidal tracer particle that has a centre of mass velocity matching the fluid velocity at the particle position $d\mathbf{X}(t)/dt = \boldsymbol{u}(\mathbf{X}(t), t)$, where $\mathbf{X}(t)$ is the Lagrangian position at the centre of mass of the particle, and $\boldsymbol{u}(\mathbf{X}(t), t)$ is the fluid velocity at the particle position. The orientation $\boldsymbol{p}$ of spheroidal rigid particles is described, in terms of the particle shape parameter Λ, by the Jeffery's equation (Jeffery (1922)), that we recall to be,

$$\frac{dp_i}{dt} = O_{ij}\, p_j + \Lambda \left(S_{ij}\, p_j - p_i\, p_k\, S_{kl}\, p_l \right), \quad \Lambda = \frac{\lambda^2 - 1}{\lambda^2 + 1}, \tag{4.6}$$

where $S_{ij} = (A_{ij} + A_{ji})/2$ is the rate-of-strain tensor, and $O_{ij} = (A_{ij} - A_{ji})/2$ is the rate-of-rotation tensor which are the symmetric and antisymmetric part of the velocity gradient tensor along the Lagrangian trajectory.

In a turbulent flow, a small spheroidal particle rotates in response to the velocity gradient along its Lagrangian trajectory and Eq. (4.6) results to be fully characterised in terms of this latter. The velocity gradient tensor $A_{ij}(t) = \partial u_i / \partial x_j(t)$ fluctuates and is dominated by the small-scale motions of the order of the Kolmogorov scale η_K. Its fluctuating part results similar in many different turbulent flows and it has been extensively studied by Meneveau (2011). Indeed, the dynamics of spheroidal particle in turbulence is strictly related to a better understanding of the Lagrangian velocity gradient. For this purpose, the complex particle angular dynamics has been investigated in DNS by studying the alignment of $\boldsymbol{p}$ with respect to the eigenvectors of the rotation rate O_{ij} and the strain rate S_{ij} (Pumir and Wilkinson (2011)). Furthermore, it is important to underline that this feature is the fundamental basis for developing a model for the orientation (Chevillard and Meneveau (2013)). DNS is still the most common method and an important tool for analysing the role played by the velocity gradient tensor on the orientation and rotation of the particles, as argued in Chapter 2, in HIT (Shin and Koch (2005); Pumir and Wilkinson (2011); Parsa et al. (2012); Chevillard and Meneveau (2013); Byron et al. (2015)), or in a turbulent channel flow (Mortensen et al. (2008); Marchioli et al. (2010); Marchioli and Soldati (2013); Challabotla et al. (2015a); Zhao and Andersson (2016)).

Following the presentation given in Chapter 2, the orientation of a spheroid, characterised by the shape parameter Λ, can be described by a linear ODE representing a generalisation

of Eq. (4.8) to any shape, where the long-time dynamics is determined by the eigenvalues and eigenvectors of the matrix $\boldsymbol{O} + \Lambda \boldsymbol{S}$ (Ni et al. (2014)). Moreover, it is still satisfied for an incompressible flow $\mathrm{Tr}(\boldsymbol{O} + \Lambda \boldsymbol{S}) = 0$ since $\mathrm{Tr}(\boldsymbol{A}) = 0$. Bretherton (1962) realised that we may alternatively model the orientation of the particle with any vector $\boldsymbol{q}$ which obeys the same linear terms, but without compensating for any elongation:

$$\frac{dq_i}{dt} = \left(O_{ij} + \Lambda S_{ij}\right) q_j, \tag{4.7}$$

defining $p_i = q_i / \|\boldsymbol{q}\|$, where p_i is the solution of Eq. (4.6). Owing to the common linear terms in Eq. (4.6) and (4.7), the vector $\boldsymbol{q}$ will have the same angular dynamics as $\boldsymbol{p}$. In addition, $\boldsymbol{q}$ may be stretched and compressed by the strain S_{ij}. However, since we are only interested in the angular degrees of freedom, we can at any instant recover $\boldsymbol{p}$ by normalising $\boldsymbol{q}$ to unit length.

Also, from a numerical perspective, in DNS Eq. (4.6) is integrated along the particle trajectory on a time-lapse of a multiple of Kolmogorov time scale using an Adams-Bashforth second order in time scheme or following the methodology proposed by Fan and Ahmadi (1995). The use of these higher order integration schemes comes primarily to the presence of non-linear terms in Eq. (4.6) and by the deterministic nature of the orientation equation, i.e. it does not present much numerical difficulties since well known classical schemes are used (Press et al. (1986)).

4.3.2 *Stochastic model for the orientation*

Despite the accuracy and completeness of informations provided by the DNS, it will not be handy to design large scale systems at practical Reynolds numbers for industrial applications. Indeed, in practical applications it is necessary to resort to a mesoscopic or macroscopic description of the phenomena to make the problem affordable.

Several Lagrangian stochastic models for the velocity gradient tensor, which have found several applications in the mean-field/PDF framework, have been proposed in literature (e. g., Girimaji and Pope (1990); Chevillard and Meneveau (2006); Pumir and Wilkinson (2011) and presented in Chapter 2. In fact, many practical situations require a more detailed representation of the finer scale properties of the velocity gradient tensor. Relevant examples include rotation and orientation dynamics (Pumir and Wilkinson (2011); Chevillard and Meneveau (2013)), or polymer stretching-relaxation dynamics (Balkovsky and Fouxon (1999); Chertkov (2000); Procaccia et al. (2008)). The stochastic modelling techniques for the velocity gradient tensor, for example, have been coupled to LES to provide small-scale information along trajectories (e. g., Chen et al. (2016); Johnson and Meneveau (2018)). In this way, the effect of large-scale features captured in LES is transmitted to the small scale dynamics. The work of Chen et al. (2016) represents one of the first attempts to study the orientation of anisotropic particles, by coupling an Ornstein–Uhlenbeck model for the velocity gradient tensor to an LES, in isotropic homogeneous turbulence. In the same context, Johnson and Meneveau (2018) studied the deformation of droplets in a turbulent channel flow introducing a more refined model for the velocity gradient tensor (Johnson and Meneveau (2016)). However, these works represent attempts in including the velocity gradient statistics which have not received much attention in the modelling context.

In Chapter 3, the Lagrangian stochastic model for the orientation of a rod-like particle has been presented. We recall that the model considers a linear companion,

$$dr_i = \langle A_{ij} \rangle \, r_j \, dt + \beta_{imj} \, r_j \circ dw_t^m, \quad p_i = \frac{r_i}{\|\boldsymbol{r}\|}. \tag{4.8}$$

where $\circ$ corresponds to the integral in Stratonovich form and $\|\cdot\|$ is the Euclidean norm. The closure of the model has been obtained by assuming that the velocity gradient fluctuations

$A'_{ij} = A_{ij} - \langle A_{ij} \rangle$ are Gaussian and short correlated in time. In particular, the diffusion tensor in expression (3.23) has been expressed as,

$$\beta_{imj}\beta_{kml} = 2\,\mathcal{C}^{\text{eff}}_{ijkl}, \tag{4.9}$$

where $\mathcal{C}^{\text{eff}}_{ijkl}$ represents the effective diffusion tensor in expression (3.20). Moreover, two different limits have been assumed: when the observation time of the dynamics is much larger than the integral correlation time ($\tau_{\text{I}} = \max(\tau_{\text{I}}^{ijkl})$), i.e. $\Delta t \gg \tau_{\text{I}}$, and when $\Delta t \ll \tau_\eta$, i.e. the observation time is smaller than the Kolmogorov time scale τ_η. The latter corresponds to the typical turnover time of the velocity gradient fluctuations. Then, the Kubo number has been defined $Ku = \tau_{\text{I}}/\tau_\eta \ll 1$ giving the working hypothesis of the model.

The Lagrangian stochastic model for the orientation can be recovered using Eq. (4.8), by considering that the symmetric and antisymmetric part of the velocity gradient tensor play a different role as in the Jeffery's equation (4.6), since the symmetric part is driven by the shape parameter Λ. Therefore, rewriting the linear Eq. (4.8) in terms of any vector $\boldsymbol{q}$ as in Eq. (4.7), leads to

$$dq_i(t) = \left(\langle O_{ij}\rangle + \Lambda\,\langle S_{ij}\rangle\right)\, q_j\, dt + \left(\beta^a_{imj} + \Lambda\,\beta^s_{imj}\right)\, q_j \circ d\mathrm{w}^m_t, \tag{4.10}$$

$$p_i = \frac{q_i}{\|\boldsymbol{q}\|}, \tag{4.11}$$

where the orientation $\boldsymbol{p}$, as we will show in the following, can be derived by using Itô's Lemma. Equation (4.10) is expressed in the Stratonovich sense ($\circ$) and $d\mathrm{w}^m_t$ ($m = 1, \dots 9$) is a vector of nine-dimensional Wiener process whose components are independent, standard one-dimensional Wiener processes. The fluctuations contribution are expressed in terms of symmetric and antisymmetric tensor (using the superscript s, a for anti- and symmetric part) $\beta^s_{imj} = (\beta_{imj} + \beta_{jmi})/2$, $\beta^a_{imj} = (\beta_{imj} - \beta_{jmi})/2$, respectively.

In this case we consider extrinsic coordinates, so that we can well mimic the deterministic dynamics and take into account the physics of the problem. This choice adds some advantages from the numerical point of view, since intrinsic coordinates would introduce singularities and cause instabilities.

4.3.2.1 *Model assumptions and parametrisations*

In general, the integral correlation time τ_{I}^{ijkl} in Eq. (4.9), and consequently $\mathcal{C}^{\text{eff}}_{ijkl}$, could be measured by DNS data, providing the spatial dependence of the diffusion tensor among coordinates of Eq. (4.10). Moreover, its form is not known in advance as for the two dimensional case analysed in Chapter 2.

Here, we restrict ourselves to consider the case where there is no spatial dependence on the integral correlation time τ_{I}^{ijkl}. This assumption is firstly motivated by the fact that we are interested to develop and investigate a suitable numerical scheme, thus we aim to simplify as much as possible the model to compute most of the results analytically. Secondly, even if the hypothesis is restrictive for the general model, one of the postulates of turbulent theory is that at small scales, the statistical properties of turbulence should be universal, at least for infinite Reynolds numbers. This hypothesis is explicitly made by the Kolmogorov theory ('K41') (Frisch (1995)), which has been assumed in a number of phenomenological models (Nelkin (1994)). Because of the postulated universality at small scales, one expects that the velocity gradient tensor has the highest possible symmetry, in particular, it can be considered homogeneous and isotropic.

We anticipate that the numerical approximation scheme associated to the SDE for the orientation is not constrained to a particular choice of the correlation tensor of the velocity

gradient fluctuations. Indeed, its numerical adaption can be extended to other choices of the tensor that depend exclusively on the physical model. However, the isotropic case presents some advantages: firstly, some analytical solutions can be derived by allowing a fair comparison both with numerical approximations and with previous existing results (e. g., Parsa et al. (2012); Byron et al. (2015)); secondly, the numerical scheme can be analysed in more detail by having a direct control on the role played by each term in Eq. (4.17), that we will define below.

Under homogeneous and isotropic assumptions, we can rewrite Eq. (4.9) as,

$$\beta_{imj}\beta_{kml} = 2\,\tau_1\,\mathcal{C}_{ijkl}(0), \tag{4.12}$$

by having considered the approximation made in expression (3.19) and where the tensor $\mathcal{C}_{ijkl}(0) = \langle A'_{ij}(0)A'_{kl}(0)\rangle$ is homogeneous and isotropic. This strongly simplifies the expression of the tensor since it can be expressed in terms of the Kronecker δ-tensor, and symmetry imposes that, for a fourth-order isotropic tensor:

$$\mathcal{C}_{ijkl} = c_1\delta_{ik}\delta_{jl} + c_2\delta_{ij}\delta_{kl} + c_3\delta_{il}\delta_{jk}. \tag{4.13}$$

We use the Einstein convention of summation of repeated indices throughout.

The coefficients are derived by imposing that the correlation tensor of the velocity gradient fluctuations $\langle A'_{ij}(0)A'_{kl}(0)\rangle = \langle \partial_j u'_i \partial_l u'_k\rangle$ satisfies incompressibility (trace-free), homogeneity, and isotropy (Pumir (2017)).

More specifically, incompressibility imposes that $\mathcal{C}_{iikl}$, related to $\langle A'_{ii}A'_{kl}\rangle = 0$, satisfy $c_1 + 3c_2 + c_3 = 0$. In addition, the homogeneity imposes $\mathcal{C}_{ijji} = 0$ (related to $\langle A'_{ij}A'_{ji}\rangle = 0$), which leads to: $c_1 + c_2 + 3c_3 = 0$. Last, the dissipation of turbulent kinetic energy is equal to $\mathcal{C}_{ijij} = \varepsilon/\nu$ (related to $\nu\,\langle A'_{ij}A'_{ij}\rangle = \varepsilon$), which gives, $3c_1 + c_2 + c_3 = \varepsilon/(3\nu)$. This leads to the explicit expression for one point correlation of the velocity gradient fluctuations,

$$\mathcal{C}_{ijkl}(0) = \frac{\varepsilon}{30\nu}(4\delta_{ik}\delta_{jl} - \delta_{ij}\delta_{kl} - \delta_{il}\delta_{jk}). \tag{4.14}$$

The second order moment of the velocity gradient tensor fluctuation is therefore expressed in terms of only one dimensional quantity: the correlation time scale of the velocity gradient tensor. It is defined by $\varepsilon/\nu = \tau_\eta^{-2}$ where ε is the turbulent energy dissipation rate, and ν is the kinematic viscosity of the fluid. Finally Eq. (4.12) is recovered,

$$\beta_{imj}\beta_{kml} = 2\,D\,Ku(\langle A_{ij}\rangle)\,(4\delta_{ik}\delta_{jl} - \delta_{ij}\delta_{kl} - \delta_{il}\delta_{jk}), \tag{4.15}$$

where $D = 1/(30\tau_\eta)$ and $Ku = \tau_1/\tau_\eta$.

The Stratonovich formulation of Eq. (4.10) is not very suitable to make computations and develop a numerical scheme, thereby we will take advantage from the Itô formulation. Applying the conversion rule from Stratonovich to Itô integral, as reported in Appendix B.1, Eq. (4.10) becomes

$$dq_i = \left(\langle O_{ij}\rangle + \Lambda\,\langle S_{ij}\rangle + 5D\,Ku(\Lambda^2 - 1)\delta_{ij}\right)\,q_j\,dt + \left(\beta^a_{imj} + \Lambda\,\beta^s_{imj}\right)\,q_j\,dw^m_t. \tag{4.16}$$

The Lagrangian stochastic model for the orientation $\boldsymbol{p}$ can be obtained using the Itô's Lemma on the renormalisation function $\boldsymbol{q} \mapsto \boldsymbol{p} = F(\boldsymbol{q})$ with $p_i = F_i(\boldsymbol{q}) = q_i/\|\boldsymbol{q}\|$ getting, as presented in Appendix B.2,

$$\begin{aligned} dp_i = {} & \langle O_{il}\rangle\,p_l dt + \Lambda\left(\langle S_{il}\rangle - p_i p_j\,\langle S_{jl}\rangle\right)\,p_l dt \\ & - \frac{\nu_s}{2}\Lambda^2 p_i dt + \nu_s\Lambda\left(dW^s_{il} - p_i p_j dW^s_{jl}\right)\,p_l - \frac{\nu_a}{2}p_i dt + \nu_a dW^a_{il}\,p_l, \end{aligned} \tag{4.17}$$

or in the Stratonovich (∂) form,

$$\begin{aligned} dp_i = &\left(\langle O_{il}\rangle + \Lambda \langle S_{il}\rangle\right) p_l dt - \Lambda p_i p_j \langle S_{jl}\rangle p_l dt \\ &+ \left(\nu_a \partial \mathrm{W}^a_{il} + \nu_s \Lambda \partial \mathrm{W}^s_{il}\right) p_l - \nu_s \Lambda p_i p_j \partial \mathrm{W}^s_{jl} p_l, \end{aligned} \tag{4.18}$$

where $\nu_s = \sqrt{6\,D\,Ku}$ and $\nu_a = \sqrt{10\,D\,Ku}$ (with $D = 1/(30\tau_\eta)$) contain the scaling parameters. We have used the matrix notation for the Wiener process $\mathrm{W}^{il}_t = \mathrm{w}^{3(i-1)+l}_t$, that is the Wiener vector w^m_t has been expressed in terms of a 3 by 3 matrix using the same nine scalar Wiener processes as outlined in 2 in Appendix B.1. In addition, the Wiener matrix has been decomposed in its symmetric and antisymmetric part (using the superscript a, s for the anti- and symmetric part) $\mathrm{W}^s_{il} = (\mathrm{W}^{il}_t + \mathrm{W}^{li}_t)/2$ and $\mathrm{W}^a_{il} = (\mathrm{W}^{il}_t - \mathrm{W}^{li}_t)/2$ respectively. Finally, Eq. (4.17) results to be the stochastic version of Jeffery's equation (4.6). Consequently, this last equation preserves the same structure of the deterministic one, where the dynamics is driven by two main contributions, the mean-field and the Gaussian fluctuating part.

In the following, we will consider a probability space and therefore the expectation operator $\mathbb{E}[\cdot]$ that comes with the set of Brownian motions previously introduced in Eq. (4.17). We will still denotes the ensemble average $\langle\cdot\rangle$.

PROPERTIES AND REMARKS ON THE SDE MODEL Equation (4.17) is presented adopting an extrinsic coordinate system (Cartesian coordinates), since we do not want to loose the physical description of the problem in the equation. Indeed, considering extrinsic coordinates provides a direct interpretation of the role of the Brownian symmetric and antisymmetric matrices with respect to the symmetric and antisymmetric part of the velocity gradient tensor in the deterministic Jeffery's equation (Eq. (4.6)). It is important to remark that, when switching to an intrinsic description, the physical interpretation of the problem could become much harder, and some singularities are introduced which numerically should be avoided.

To create a link with the two dimensional case in Chapter 3, we would remind that an intrinsic description has been used in that case to reduce the difficulties and to study the problem analytically. However, the 2D problem represents a simplified case since the intrinsic description leads to a scalar equation: that would never be the case in the three dimensional setting.

Here, in addition, the extrinsic description is associated to a numerical scheme implemented in a CFD code; this is more flexible with respect to an intrinsic one, since it allows a further enrichment of the physical model by maintaining the same structure of the numerical scheme under consideration. The discussion about the choice of extrinsic and intrinsic coordinates is brought to attention due also to the nature of Eq. (4.17): in fact, its solution evolves on the manifold $SO(3)$. In the literature, many authors investigated how to formulate SDEs on manifolds.

One option is to work extrinsically and to consider only manifolds embedded in $\mathbb{R}^n$, that implies defining SDEs in the Cartesian space and then confine the solutions to the manifold. Another approach is to use an interpretation of SDEs on manifolds where the existence of solutions is defined intrinsically. A survey of various approaches to understand SDEs on manifolds has been given by Armstrong et al. (2018).

Moreover, these two approaches are strictly related to the convention used for the SDEs, i.e. Itô (e. g., Eq. (4.17)) or Stratonovich (e. g., Eq. (4.18)). In general, since Stratonovich and Itô calculus are just on two-coordinate systems, one would expect to be able to work using both conventions interchangeably. Often, in modelling physics and engineering systems, Stratonovich calculus is chosen, as shown in Chapter 3). On the other hand, the Itô integral has a number of good probabilistic properties and is used because more handling from a numerical point of view.

4.3.3 *Spinning and tumbling rates in the stochastic model*

The preferential orientation of non-spherical particles has profound implications for the particle rotation statistics. As detailed in Chapter 2, the rotational dynamics of spheroids in turbulent flows is related to the temporal evolution of a unit vector $\boldsymbol{p}(t)$, which can be also expressed in terms of the total angular velocity of the particle $\boldsymbol{\Omega} = \boldsymbol{\omega}/2 + \Lambda \boldsymbol{p} \times \boldsymbol{S}\boldsymbol{p}$, such that the Jeffery's equation (4.6) can be rewritten as $d\boldsymbol{p}/dt = \boldsymbol{\Omega} \times \boldsymbol{p}$.

In the Lagrangian stochastic model for the orientation, Eq. (4.17), due to the presence of stochastic integrals, the particle angular velocity $\boldsymbol{\Omega}$ is not properly defined. This requires to introduce a suitable statistics to describe the spinning and tumbling rates for the stochastic model. More precisely, we identify the angular displacement vector associated to the particle angular velocity $\boldsymbol{\Omega}\, dt = \partial\boldsymbol{\phi}$ (in Stratonovich formulation) as the measurement that properly characterises the tumbling and spinning statistics. Equation (4.18) in terms of rotational dynamics can be rewritten as

$$d\boldsymbol{p} = \partial\boldsymbol{\phi} \times \boldsymbol{p}, \tag{4.19}$$

and its Itô form (Eq. (4.17)),

$$d\boldsymbol{p} = d\boldsymbol{\phi} \times \boldsymbol{p} - \frac{1}{2}(\nu_a^2 + \Lambda\nu_s^2)\boldsymbol{p}\, dt. \tag{4.20}$$

Here the angular increment $d\boldsymbol{\phi}$ associated to the particle angular velocity can be identified discarding the Itô-Stratonovich transformation term since it does not provide any contribution to the rotational dynamics,

$$d\boldsymbol{\phi} = \frac{1}{2}\langle\boldsymbol{\omega}\rangle\, dt + \Lambda(\boldsymbol{p} \times \langle\boldsymbol{S}\rangle\, \boldsymbol{p})dt + \frac{\nu_a}{2} d\mathbf{w}^a + \nu_s \Lambda\, \boldsymbol{p} \times d\mathbf{W}^s \boldsymbol{p}. \tag{4.21}$$

The mean antisymmetric part of the velocity gradient tensor has been rewritten as $\langle\boldsymbol{O}\rangle\, \boldsymbol{p} = (\langle\boldsymbol{\omega}\rangle \times \boldsymbol{p})/2$, where $\langle\boldsymbol{\omega}\rangle$ is the mean vorticity vector. Analogously, the fluctuating part becomes $d\mathbf{W}^a\, \boldsymbol{p} = (d\mathbf{w}^a \times \boldsymbol{p})/2$, where we have identified the increment of the vorticity vector fluctuation in terms of antisymmetric matrix $\mathbf{W}^a$, as $\mathbf{w}^a = 2(\mathbf{W}^a_{32}, \mathbf{W}^a_{13}, \mathbf{W}^a_{21})^\intercal$.

Similarly to the presentation of the tumbling and spinning rate given above for the deterministic case (Byron et al. (2015)), we can define the orthogonal and parallel projection of the angular increment $d\boldsymbol{\phi}$ on $\boldsymbol{p}$ (a sketch is given in Fig. 4.1) as,

$$\boldsymbol{\phi}_{\perp p}(t) = \boldsymbol{\phi}_{\perp p}(0) + \int_0^t \boldsymbol{p} \times (d\boldsymbol{\phi} \times \boldsymbol{p})\,, \tag{4.22}$$

$$\boldsymbol{\phi}_{\parallel p}(t) = \boldsymbol{\phi}_{\parallel p}(0) + \int_0^t \boldsymbol{p} \cdot d\boldsymbol{\phi}. \tag{4.23}$$

We remark that the term $\boldsymbol{p} \times (d\boldsymbol{\phi} \times \boldsymbol{p}) = d\boldsymbol{\phi} \times \boldsymbol{p}$ since the Stratonovich term is zero when we take the cross product with $\boldsymbol{p}$.

Going a bit further in the computation, i.e. replacing Eq. (4.21) in Eq. (4.22) and (4.23) respectively, we get

$$\begin{aligned}\boldsymbol{\phi}_{\perp p}(t) = \boldsymbol{\phi}_{\perp p}(0) &+ \int_0^t \left[\frac{1}{2}(\mathbb{1} - \boldsymbol{p}\boldsymbol{p}^\intercal)\,\langle\boldsymbol{\omega}\rangle + \Lambda \boldsymbol{p} \times \langle\boldsymbol{S}\rangle\, \boldsymbol{p}\right] ds \\ &+ \int_0^t \left[\frac{\nu_a}{2}(\mathbb{1} - \boldsymbol{p}\boldsymbol{p}^\intercal) d\mathbf{w}^a + \nu_s \Lambda \boldsymbol{p} \times d\mathbf{W}^s \boldsymbol{p}\right],\end{aligned} \tag{4.24}$$

$$\boldsymbol{\phi}_{\parallel p}(t) = \boldsymbol{\phi}_{\parallel p}(0) + \frac{1}{2}\int_0^t \boldsymbol{p} \cdot \langle\boldsymbol{\omega}\rangle\, ds + \frac{\nu_a}{2}\int_0^t \boldsymbol{p} \cdot d\mathbf{w}^a, \tag{4.25}$$

where $\mathbb{1}$ is the identity matrix.

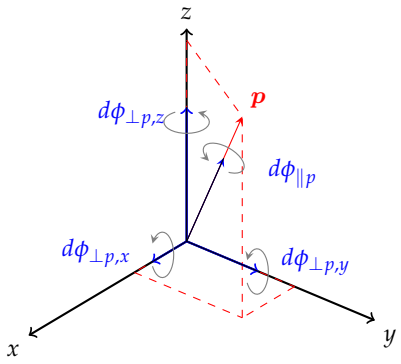

Figure 4.1: Sketch of angular increment in the Lagrangian stochastic model in Eq. (4.21). The total angular increment $d\phi$ has been decomposed in tumbling $d\phi_{\perp p}$ and spinning $d\phi_{\parallel p}$ components in Eq. (4.22) and (4.23) respectively. The latter has been projected along Cartesian axis.

Independently to the type of flow that we are considering (i.e. homogeneous isotropic, homogeneous shear or wall bounded turbulent flow), the rotational dynamics of the spheroidal particle can be characterised by the mean and variance of the tumbling and spinning quantities defined for the stochastic model.

In terms of averages, the tumble and spinning motion can be identified by the norm of the mean of the orthogonal $\phi_{\perp p}$ and parallel projection $\phi_{\parallel p}$, respectively,

$$\widehat{\Phi}_{\perp p}(t) = \frac{d}{dt} \left\| \mathbb{E}\left[\phi_{\perp p}(t)\right] \right\|, \tag{4.26}$$

$$\widehat{\Phi}_{\parallel p}(t) = \frac{d}{dt} \mathbb{E}\left[\phi_{\parallel p}(t)\right], \tag{4.27}$$

The mean of the parallel projection $\phi_{\parallel p}$ at the equilibrium state goes to zero, since the SDE (4.17) for the orientation behaves in average as its deterministic counterpart, Eq. (4.6), which contains only even terms, given the symmetry $\boldsymbol{p} \to -\boldsymbol{p}$. Computing the norm of the mean of the orthogonal $\phi_{\perp p}$ and parallel projection $\phi_{\parallel p}$ is interesting to have a control on the behaviour of the variances as we can see hereafter.

In equivalent manner, the second observable associated to the tumbling and spinning rate is the variance of the norm of the orthogonal and parallel projection. These two quantities can be expressed as,

$$\Phi_{\perp p}(t) = \frac{d}{dt} \left[\mathbb{E}\left\|\phi_{\perp p}(t)\right\|^2 - \left\| \mathbb{E}\left[\phi_{\perp p}(t)\right] \right\|^2 \right], \tag{4.28}$$

$$\Phi_{\parallel p}(t) = \frac{d}{dt} \left[\mathbb{E}\left[\phi^2_{\parallel p}(t)\right] - \mathbb{E}\left[\phi_{\parallel p}(t)\right]^2 \right] \tag{4.29}$$

We draw the attention on the definitions given in Eqs. (4.26), (4.28) and (4.29), since they represent the extension to the 3D case of the mean and variance of the angular displacement defined in Chapter 3 for the 2D case. Indeed, these quantities fully characterize the modes of rotation in 3D for the Lagrangian stochastic model, Eq. (4.17), and they can be analysed for different types of flows. Interestingly, these statistics are not easy to handle since are not ergodic, representing a challenging case of study from a numerical point of view.

4.3.3.1 *Tumbling and spinning in homogeneous isotropic turbulence*

The first test case consists in deriving and investigating the analytical formulation of tumbling and spinning rates for the stochastic model in HIT. In this case, the mean contribution of the velocity gradient tensor is zero and Eq. (4.17) becomes,

$$\begin{aligned}
dp_1 &= -\frac{1}{2}\left(\nu_s^2\Lambda^2+\nu_a^2\right)p_1dt+\left(\nu_a d\mathrm{W}_{1l}^a+\nu_s\Lambda d\mathrm{W}_{1l}^s\right)p_l-\nu_s\Lambda p_1p_j d\mathrm{W}_{jl}^s p_l\\
dp_2 &= -\frac{1}{2}\left(\nu_s^2\Lambda^2+\nu_a^2\right)p_2dt+\left(\nu_a d\mathrm{W}_{2l}^a+\nu_s\Lambda d\mathrm{W}_{2l}^s\right)p_l-\nu_s\Lambda p_2p_j dW_{jl}^s p_l\\
dp_3 &= -\frac{1}{2}\left(\nu_s^2\Lambda^2+\nu_a^2\right)p_3dt+\left(\nu_a d\mathrm{W}_{3l}^a+\nu_s\Lambda d\mathrm{W}_{3l}^s\right)p_l-\nu_s\Lambda p_3p_j d\mathrm{W}_{jl}^s p_l.
\end{aligned} \tag{4.30}$$

It is important to notice that the set of equations above, when they are not coupled with the Lagrangian transport models, makes the stochastic model for $\boldsymbol{p}_t$ reversible in time due to the presence of Brownian motions. In fact, the forward and backward Kolmogorov operators are self-adjoint.

This 'time reversibility' is directly related to a change of $|\Lambda| \to -|\Lambda|$ in Eq. 4.30 which implies that rod-like particles ($\Lambda > 0$) have the same statistical behaviour of disk-like particles ($\Lambda < 0$). This is an important difference with respect to Eq. (4.6) studied in DNS, where the turbulence breaks time reversal invariance.

In Eq. 4.30 the mean contribution of the velocity gradient tensor is zero which means that the Eq. (4.28) and (4.29) are reduced to compute the averaged squared values. By considering Eq. (4.22), having used Eq. (4.21), we get

$$\begin{aligned}
\Phi_{\perp p}^{\mathrm{hit}} &= \frac{d}{dt}\mathbb{E}\left\|\phi_{\perp p}(t)\right\|^2\\
&= \frac{d}{dt}\mathbb{E}\left\|\int_0^t\left[\frac{\nu_a}{2}(\mathbb{1}-\boldsymbol{p}\boldsymbol{p}^{\intercal})d\mathbf{w}^a+\nu_s\Lambda\boldsymbol{p}\times d\mathbf{W}^s\boldsymbol{p}\right]\right\|^2\\
&= \frac{d}{dt}\mathbb{E}\left[\int_0^t \nu_a^2+\nu_s^2\Lambda^2 dt\right] = \nu_a^2+\nu_s^2\Lambda^2,
\end{aligned} \tag{4.31}$$

where the Itô isometry has been applied to compute the stochastic integral (detailed computation is presented in Appendix B.3).

Applying the same considerations, the spinning rate can be obtained by using Eq. (4.21) in Eq. (4.23),

$$\begin{aligned}
\Phi_{\parallel p}^{\mathrm{hit}} &= \frac{d}{dt}\mathbb{E}\left[\phi_{\parallel p}(t)\right]^2 = \frac{d}{dt}\mathbb{E}\left[\frac{\nu_a}{2}\int_0^t \boldsymbol{p}\cdot d\mathbf{w}^a\right]^2\\
&= \frac{d}{dt}\mathbb{E}\left[\int_0^t \frac{\nu_a^2}{2}dt\right] = \frac{\nu_a^2}{2}.
\end{aligned} \tag{4.32}$$

These analytical results are constant in time.

Further, replacing the definitions of $\Lambda = (\lambda^2-1)/(\lambda^2+1)$, $\nu_s = \sqrt{6\,D\,Ku}$ and $\nu_a = \sqrt{10\,D\,Ku}$ with $D = 1/(30\tau_\eta)$ in Eq. (4.31) and (4.32), we get,

$$\Phi_{\perp p}^{\mathrm{hit}} = \frac{Ku}{3\tau_\eta}+\frac{Ku}{5\tau_\eta}\left(\frac{\lambda^2-1}{\lambda^2+1}\right)^2, \tag{4.33}$$

$$\Phi_{\parallel p}^{\mathrm{hit}} = \frac{Ku}{6\tau_\eta}. \tag{4.34}$$

Similar qualitatively result for Eq. (4.33) has been obtained by Parsa et al. (2012) using different arguments. In particular, they assume the independency between the velocity gradient tensor

$\boldsymbol{A}$ and the orientation $\boldsymbol{p}$ for a randomly oriented spheroidal particle. Even if the statistics are different from those derived by Parsa et al. (2012), in our opinion the results are qualitatively comparable. Moreover, both statistics are restricted to the observation of the tumbling and spinning dynamics in the diffusive regime (long-time limit of the phenomena). Interestingly, the behaviour of rod- and disk-like particles in Eq. (4.33) and (4.34) is the same, which comes from time reversibility. Conversely, in turbulence time irreversibility is present leading to a different behaviour between rod- and disk-like particles as presented in Fig. 2.4 of Chapter 2.

4.3.3.2 *Tumbling and spinning in homogeneous shear flow*

A second test case for the derivation of tumbling and spinning statistics can be built by considering a turbulent homogeneous shear flow (HSF). Indeed, HSF is statistically homogeneous, i.e. turbulence statistics are invariant under spatial translations and therefore simpler than wall-bounded turbulence, such as a turbulent channel flow. This implies that is still possible to derive some analytical solutions about statistics. Despite the simplicity, HSF remains physically relevant since it owns several common features with more general wall-bounded flows. Moreover, it represents a good framework to test the numerical scheme since it does not add too much difficulties coming from the mean part contribution in Eq. (4.17).

In the HSF case, the flow is characterised by mean profiles of the velocity components $\langle u_x \rangle = \sigma y$, $\langle u_y \rangle = \langle u_z \rangle = 0$, where x is the streamwise direction, y is the cross-terms coordinate along which the mean velocity varies, and σ is a constant mean shear rate, $\sigma = d\langle u_x \rangle / dy$. This means that the mean contribution of the velocity gradient can be written as,

$$\langle A_{ij} \rangle = \begin{pmatrix} 0 & \sigma & 0 \\ 0 & 0 & 0 \\ 0 & 0 & 0 \end{pmatrix} = \langle S_{ij} \rangle + \langle O_{ij} \rangle = \frac{1}{2} \begin{pmatrix} 0 & \sigma & 0 \\ \sigma & 0 & 0 \\ 0 & 0 & 0 \end{pmatrix} + \frac{1}{2} \begin{pmatrix} 0 & \sigma & 0 \\ -\sigma & 0 & 0 \\ 0 & 0 & 0 \end{pmatrix}, \tag{4.35}$$

For this particular choice of the mean shear, Eq. (4.17) becomes,

$$\begin{aligned} dp_1 =& \frac{\sigma}{2}(\Lambda+1)p_2 dt - \sigma\Lambda p_1^2 p_2 dt - \frac{1}{2}\left(\nu_s^2\Lambda^2 + \nu_a^2\right) p_1 dt \\ &+ \left(\nu_a d\mathrm{W}_{1l}^a + \nu_s\Lambda d\mathrm{W}_{1l}^s\right) p_l - \nu_s\Lambda p_1 p_j d\mathrm{W}_{jl}^s p_l, \\ dp_2 =& \frac{\sigma}{2}(\Lambda-1)p_1 dt - \sigma\Lambda p_2^2 p_1 dt - \frac{1}{2}\left(\nu_s^2\Lambda^2 + \nu_a^2\right) p_2 dt \\ &+ \left(\nu_a d\mathrm{W}_{2l}^a + \nu_s\Lambda d\mathrm{W}_{2l}^s\right) p_l - \nu_s\Lambda p_2 p_j d\mathrm{W}_{jl}^s p_l, \\ dp_3 =& -\sigma\Lambda p_1 p_3 p_2 dt - \frac{1}{2}\left(\nu_s^2\Lambda^2 + \nu_a^2\right) p_3 dt \\ &+ \left(\nu_a d\mathrm{W}_{3l}^a + \nu_s\Lambda d\mathrm{W}_{3l}^s\right) p_l - \nu_s\Lambda p_3 p_j d\mathrm{W}_{jl}^s p_l. \end{aligned} \tag{4.36}$$

The equations above have the coefficients that are constant in time both in drift and diffusion part. Further, the stochastic orientation vector $\boldsymbol{p}_t$ lives on a sphere so that the process is ergodic, converging towards an equilibrium measure. This represents an important property that will be used, hereafter, to derive some semi-analytical forms about tumbling and spinning statistics.

In the presence of mean velocity gradients we can compute the norm of the mean of the orthogonal projection $\phi_{\perp p}$, according to Eq. (4.26),

$$\widehat{\Phi}_{\perp p}^{\mathrm{hsf}}(t) = \frac{d}{dt}\left\| \mathbb{E}\left[\int_0^t \boldsymbol{g}^{\perp}(\boldsymbol{p}_s) ds \right] \right\|, \quad \text{with} \quad \boldsymbol{g}^{\perp}(\boldsymbol{p}_s) = \frac{\sigma}{2} \begin{pmatrix} -(\Lambda-1)p_1 p_3 \\ (\Lambda+1)p_2 p_3 \\ (\Lambda-1)p_1^2 - (\Lambda+1)p_2^2 \end{pmatrix}, \tag{4.37}$$

where we have explicitly computed $\boldsymbol{g}^{\perp}(\boldsymbol{p}(t)) = (\mathbb{1} - \boldsymbol{p}\boldsymbol{p}^{\intercal})\langle\boldsymbol{\omega}\rangle/2 + \Lambda\boldsymbol{p}\times\langle\boldsymbol{S}\rangle\boldsymbol{p}$, that corresponds to the drift part of Eq. (4.24).

Regarding the variance of the norm of the orthogonal projection in Eq. (4.28), this can be rewritten by superimposing the contribution of mean shear and that coming from the fluctuations, the latter already computed in the HIT case, leading to,

$$\Phi^{\mathrm{hsf}}_{\perp p}(t) = \frac{d}{dt}\left[\mathbb{E}\left\|\int_0^t \boldsymbol{g}^{\perp}(\boldsymbol{p}_s)ds\right\|^2 - \left\|\mathbb{E}\left[\int_0^t \boldsymbol{g}^{\perp}(\boldsymbol{p}_s)ds\right]\right\|^2\right] + \Phi^{\mathrm{hit}}_{\perp p}. \tag{4.38}$$

Similarly, the same analysis can be performed for the parallel projection $\phi_{\parallel p}$. The scalar quantity associated to the spinning that differs from zero is the norm squared since, as said, the expectation $\mathbb{E}[\phi_{\parallel p}]$ is always zero by the symmetry $\boldsymbol{p}\to-\boldsymbol{p}$, and it can be written as,

$$\Phi^{\mathrm{hsf}}_{\parallel p}(t) = \frac{d}{dt}\mathbb{E}\left\|\int_0^t g^{\parallel}(\boldsymbol{p}_s)ds\right\|^2 + \Phi^{\mathrm{hit}}_{\parallel p}, \quad \text{with} \quad g^{\parallel}(\boldsymbol{p}_s) = \frac{\sigma}{2}p_3, \tag{4.39}$$

where we have explicitly computed $g^{\parallel}(\boldsymbol{p}_s) = \boldsymbol{p}\cdot\langle\boldsymbol{\omega}\rangle/2$, that corresponds to the drift part of Eq. (4.25).

We now derive the semi-analytical forms (using ergodicity assumption) to compare with numerical results for the quantities introduced above, i.e. the mean quantity $\widehat{\Phi}^{\mathrm{hsf}}_{\perp p}(t)$, as well as the variance $\Phi^{\mathrm{hsf}}_{\parallel p}(t)$ and $\Phi^{\mathrm{hsf}}_{\parallel p}(t)$, respectively. Equation (4.37) can be strongly simplified if we consider the long time behaviour, by applying the ergodicity assumption. Under this hypothesis we get,

$$\begin{aligned}
\widehat{\Phi}^{\mathrm{hsf}}_{\perp p_\infty} &= \lim_{t\to\infty}\frac{d}{dt}\left(\left\|\mathbb{E}\left[\int_0^t \boldsymbol{g}^{\perp}(\boldsymbol{p}_s)ds\right]\right\|^2\right)^{-\frac{1}{2}} \\
&= \lim_{t\to\infty}\left(\sum_{i=1}^{3}\mathbb{E}\left[\int_0^t g_i^{\perp}(\boldsymbol{p}_s)ds\right]^2\right)^{-\frac{1}{2}}\left(\sum_{i=1}^{3}\mathbb{E}\left[\int_0^t g_i^{\perp}(\boldsymbol{p}_s)ds\right]\mathbb{E}\left[g_i^{\perp}(\boldsymbol{p}_t)\right]\right) \\
&= \left(\sum_{i=1}^{3}\mathbb{E}\left[g_i^{\perp}(\boldsymbol{p}_\infty)\right]^2 t^2\right)^{-\frac{1}{2}}\left(\sum_{i=1}^{3}\mathbb{E}\left[g_i^{\perp}(\boldsymbol{p}_\infty)\right]^2 t\right) = \left(\sum_{i=1}^{3}\mathbb{E}\left[g_i^{\perp}(\boldsymbol{p}_\infty)\right]^2\right)^{\frac{1}{2}}
\end{aligned} \tag{4.40}$$

Equivalently for Eq. (4.38), after an initial time t_0, the process reaches a stationary state, i.e. allowing to considering a time lag $\tau = |t_0 - s|$. In this way, we can write,

$$\begin{aligned}
\Phi^{\mathrm{hsf}}_{\perp p_\infty} &= \lim_{t\to\infty}\frac{d}{dt}\sum_{i=1}^{3}\mathbb{E}\left[\left(\int_0^t g_i^{\perp}(\boldsymbol{p}_s)\right)^2 ds\right] - \frac{d}{dt}\sum_{i=1}^{3}\mathbb{E}\left[\int_0^t g_i^{\perp}(\boldsymbol{p}_s)ds\right]^2 + \Phi^{\mathrm{hit}}_{\perp p} \\
&= \lim_{t\to\infty} 2\sum_{i=1}^{3}\mathbb{E}\left[\int_0^t g_i^{\perp}(\boldsymbol{p}_s)g_i^{\perp}(\boldsymbol{p}_t)ds\right] - 2\sum_{i=1}^{3}\int_0^t \mathbb{E}\left[g_i^{\perp}(\boldsymbol{p}_s)\right]\mathbb{E}\left[g_i^{\perp}(\boldsymbol{p}_t)s\right]ds + \Phi^{\mathrm{hit}}_{\perp p} \\
&= \lim_{t\to\infty} 2\sum_{i=1}^{3}\int_{t_0}^{t}\mathcal{R}_{g_i^{\perp}}(\tau)d\tau + \Phi^{\mathrm{hit}}_{\perp p} = 2\sum_{i=1}^{3}\int_{t_0}^{\infty}\mathcal{R}_{g_i^{\perp}}(\tau)d\tau + \Phi^{\mathrm{hit}}_{\perp p},
\end{aligned} \tag{4.41}$$

where the stationarity measure has been used to define

$$\mathcal{R}_{g_i^{\perp}}(\tau) = \mathbb{E}\left[g_i^{\perp}(\boldsymbol{p}_{t_0})g_i^{\perp}(\boldsymbol{p}_{t_0+\tau})\right] - \mathbb{E}\left[g_i^{\perp}(\boldsymbol{p}_{t_0})\right]\mathbb{E}\left[g_i^{\perp}(\boldsymbol{p}_{t_0+\tau})\right]. \tag{4.42}$$

In analogy with the presentation made for the tumbling, a semi-analytical expression for the norm squared of the parallel projection $\phi_{\parallel p}$ is given by,

$$\Phi^{\mathrm{hsf}}_{\parallel p_\infty} = \int_{t_0}^{\infty}\mathbb{E}\left[g^{\parallel}(\boldsymbol{p}_{t_0})g^{\parallel}(\boldsymbol{p}_{t_0+\tau})\right]d\tau + \Phi^{\mathrm{hit}}_{\parallel p}. \tag{4.43}$$

Finally, these semi-analytical expressions (4.40), (4.41) and (4.43) will be used as diagnostic tool for the numerical scheme. For clarity we list their final results below,

$$\widehat{\Phi}^{\text{hsf}}_{\perp p_\infty} = \left(\sum_{i=1}^{3} \mathbb{E}\left[g_i^{\perp}(\boldsymbol{p}_\infty) \right]^2 \right)^{\frac{1}{2}}, \tag{4.44}$$

$$\Phi^{\text{hsf}}_{\perp p_\infty} = 2 \sum_{i=1}^{3} \int_{t_0}^{\infty} \mathcal{R}_{g_i^{\perp}}(\tau) d\tau + \Phi^{\text{hit}}_{\perp p}, \tag{4.45}$$

$$\Phi^{\text{hsf}}_{\parallel p_\infty} = \int_{t_0}^{\infty} \mathbb{E}\left[g^{\parallel}(\boldsymbol{p}_{t_0}) g^{\parallel}(\boldsymbol{p}_{t_0+\tau}) \right] d\tau + \Phi^{\text{hit}}_{\parallel p}. \tag{4.46}$$

Interestingly, Eq. (4.44) can be easily computed by evaluating the moments $\mathbb{E}[g_i^{\perp}]$ in the long time limit ($\boldsymbol{p}_\infty$) where Eq. (4.17) is stationary in time, and all moments do not depend on time. Conversely, Eq. (4.45) and (4.46) correspond to compute the time correlations of each contribution $g_i^{\perp}$ or $g_i^{\parallel}$, which is numerically much harder than just evaluate the moments in the stationary state as for the case of Eq. (4.44).

4.4 NUMERICAL SCHEME

In this section we develop a numerical method for weak and strong solutions of SDE (4.17). We would like first to remark that finding a numerical solution to an SDE, as (4.17), is a much harder problem than considering an ODE, such as the deterministic counterpart, Eq. (4.6). In general, all the well developed high-order ODEs schemes degrade to low-order accuracy when applied to Itô SDE and, even worse, they can lead to inconsistent schemes because most ODE schemes violate the non-anticipatory property of Itô SDEs. The numerical solution of SDEs is a broad research area. In general, SDEs are difficult to solve analytically and many attempts have been made to develop efficient numerical methods, as in Mao (2007); Pagés (2018).

Equation (4.17) has to be treated carefully since its solution is a vector in $\mathbb{R}^3$ which represents an orientation of unitary norm. The unit length is preserved by the presence of the non-linear terms, both in the drift and in the stochastic contributions. In particular, the solution evolves in the manifold $SO(3)$, and this underlines the geometric character of SDE (4.17). As mentioned in paragraph 4.3.2.1, for such kind of systems both, Stratonovich and Itô formulations are possible, having their advantages and drawbacks.

Several integration schemes have been developed for Itô and Stratonovich formulations, as for example Itô SDE schemes (Klauder and Petersen (1985); Greiner et al. (1988); Milstein (1994); Platen (1995); Mackevičius and Navikas (2001); Pagés (2018)), and Stratonovich SDE schemes (Burrage and Tian (2002); Tian and Burrage (2002); Rößler (2009)). In this work, the Itô convention will be adopted since in general is very convenient in the development of numerical schemes for SDEs. However, the employment of these two formulations for the splitting scheme that we will develop do not present a numerical issue.

In order to preserve the unit norm all along the simulation we have to deal with the discretisation of non-linear terms, not only in the drift part but also in the stochastic one, which adds more drawbacks from a numerical point of view.

In fact, for a large class of SDEs with non-globally Lipschitz continuous coefficients in both drift and diffusion part (similar to our case), it has been proved that the Euler–Maruyama scheme does not converge neither in the strong mean-square sense nor in the numerically weak sense to the exact solution at a finite time point, as discussed in Hutzenthaler et al. (2011)). This requires to pay particular attention on the choice of the numerical scheme.

Moreover, as said before, the solution evolves on the manifold $SO(3)$; this underlines a significant issue whether or not this geometric feature of SDE (4.17) is preserved, especially for

long time simulations, which is as important as in the deterministic case (Hairer et al. (2006)). Numerically, preserving the norm, is a delicate point since the numerical solution tends to drift off the manifold and the accuracy of the solution strongly depends on the time step.

As said, employing a classical Euler–Maruyama discretisation scheme without paying attention to the time step used, implies that the resulting numerical trajectories leave the manifold instantly, often leading to wrong estimate and to non-convergence. In order to avoid such failures, discretisation schemes that preserve the manifold structure have been studied. Such algorithms are known as *geometric integrators* (Hairer et al. (2006)). We would like to remark that the preservation of manifold structure can also result in computational efficiency gains. A larger step size may be sufficient to obtain a given level of accuracy when compared to what might have been expected from non-geometric considerations, with the added bonus of geometry preservation (Faltinsen et al. (2001)).

Many geometric integrators for SDEs are based on their well understood deterministic counter-parts, but key difficulties often arise in their extension to the stochastic setting; the area of convergence analysis for stochastic geometric integrators is a recent research field. An exhaustive presentation of the geometric SDE integrators can be found in Piggott (2016).

In general, there are two types of numerical methods for differential equations and their stochastic counterpart on manifolds: the first consists in numerical methods whose solutions automatically stay on the manifold (intrinsically); for example, Lie group methods such as the Crouch–Grossman method (Crouch and Grossman (1993)), the constrained Runge–Kutta method (Munthe-Kaas (1998); Carbonell et al. (2005)), the Magnus expansion method or variations thereof (Burrage and Burrage (1999); Blanes et al. (2009); Marjanovic et al. (2015)), the spectral element method Li et al. (2018a), and the stochastic Lie group integrators (Malham and Wiese (2008)) can maintain the numerical solutions on the correct Lie groups. The second kind of numerical methods is designed to stay on the correct manifolds by using some constraints explicitly (extrinsically), such as the discrete gradient methods (McLachlan et al. (1999); Li et al. (2018b)), the averaged vector field methods (Quispel and McLaren (2008); Cai et al. (2018)) and the projection methods (Hairer et al. (2006); Zhou et al. (2016)). All these studies have been developed according to specific types of SDEs. For our problem we want to adopt a pragmatic approach to solve the three dimensional SDE (4.17), by adopting the quaternions dynamics. In general, quaternions have been largely used to solve the deterministic problem (Zhao and Van Wachem (2013b)) of the orientation on a sphere, nonetheless, in our knowledge, their adaptation to SDEs is limited to few studies (Piggott (2016)).

Another difficulty relies on the coupling between the orientation model and the mean field, solved by CFD methods; in particular, the coupling is done by means of the mean symmetric and antisymmetric velocity gradients $\langle \boldsymbol{O} \rangle$ and $\langle \boldsymbol{S} \rangle$. They evolve on a discrete grid in space and time. This implies that there is no possibility to control the time step when integrating the SDE since it is imposed by the mean contribution; thus, the choice of a suitable numerical scheme to integrate the SDE (4.17) is also constrained by stability issues. This motivates the question: 'For which choice of the time step does the numerical method reproduce the characteristics of the model?'. This naturally brings up the discussion about the approach to adopt in terms of choice of an explicit or implicit method in time.

Efforts have been made to develop explicit and implicit numerical methods for solving SDEs, as reported in the overviews Mao (2007); Pagés (2018)). We refer to *explicit* method, if it is explicit both in deterministic and stochastic components. Otherwise, if both deterministic and stochastic components are implicit, a numerical integrator is then called *implicit* method. Not much work has been done to introduce an *implicit* numerical integrator of SDEs; as an example, we refer to Kloeden and Platen (1992). Explicit SDE schemes are usually used for simplicity and efficiency, while implicit schemes can achieve better convergence and stability, when compared to the explicit ones, and they have no constraints related to the time step. Other

methods mix explicit and implicit discretisation, by considering implicit drift components and explicit stochastic (i.e. diffusion) contributions (Milstein (1994)). We can refer to such methods as *semi-implicit* (or *drift-implicit*) since the introduction of implicitness is restricted to the deterministic terms.

In this approach the goal is to improve stability properties with respect to a pure explicit method; Saito and Mitsui (1996) proposes various schemes showing stability analyses. Other techniques exist, we can mention Burrage and Tian (2001), which propose a method that is a combination of the semi-implicit Euler method and the implicit Euler method, called 'the composite Euler method', or Milstein et al. (1998) that constructs 'the balanced implicit method' by introducing modified implicit coefficients to both the deterministic and stochastic components of the explicit Euler method, based on a splitting technique.

As mentioned before, the choice of an *explicit* Euler–Maruyama discretisation would suit the case of globally Lipschitz coefficients, which is not our case; we will have to pay attention to the complexity of the SDE under study in order to understand which choice has to be preferred. It will turn out that, after sub-dividing the problem, we will evaluate the choice of both, *explicit* and *semi-implicit*.

The development of a numerical scheme for the SDE (4.17) involves the complexity of the problem as well. There are two fundamentally different algorithm approaches: either a fully coupling approach, for which the governing equations are solved as single system (usually very complicated), or the decoupling approach, for which the equations are decoupled in simpler sub-problems and are solved as simpler tasks.

The latter includes the splitting methods that were originally designed to reduce the computational difficulties by decomposing delicate deterministic differential equations into simpler solvable ones: the general details are exposed in the overview papers of Strang (1968); Marchuk (1968); McLachlan and Quispel (2002). In a second moment, they were applied also to stochastic problems Petersen (1998); Shardlow (2003). Methodologically, splitting methods are numerical solvers that belong to the class of the decomposition methods. These methods have been applied in various fields, in computational fluid dynamics (Hundsdorfer and Verwer (2013); Sheng (1989)), particle tracking with collisions (Dullweber et al. (1997); Hairer et al. (2006); Chin and Geiser (2011)) and multi-scale problems (Weinan et al. (2003); Abdulle et al. (2012)).

Splitting methods are characterised by fast implementation, thanks to separation into simpler computable parts, accuracy, obtained via higher order splitting schemes or adaptive splitting schemes, and flexibility, important for adapting the method to modifications of a physical model, e. g., time-, spatial-dependency, non-linearity of stochastic operators. In particular, the time step is imposed by the mean field PDF approach, and it may be large; thus, stability with respect to large time steps is an issue that we need to take into account.

Specifically to the analysis of SDEs, the split-step backward Euler (SSBE) method has been studied by Higham et al. (2002); Mattingly et al. (2002). In order to improve numerical stability of the SSBE method, based on the work of Mattingly et al. (2002), the split-step method has been introduced by Ding et al. (2010), and split-step backward balanced Milstein methods by Wang and Liu (2009).

4.4.1 *Splitting scheme*

Our proposed method appropriately splits the different contributions coming from Eq. (4.17) and it applies a suitable numerical integration (explicit or semi-implicit as detailed hereafter) for each resulting part, in order to obtain a stable numerical solution with reduced computational complexity. To achieve all this, a split-step-forward method is chosen. The orientation dynamics in Eq. (4.17) is characterised by a geometric structure where the orientation dynamics changes under the action of the velocity gradient tensor by the averages of stretching and rotation

contributions. Equation (4.17) can be decomposed for the splitting algorithm in four separate processes:

- a drift term that represents the mean stretching ($\mathbb{MS}$), given by the symmetric part of the mean velocity gradient;
- a drift term that represents the mean rotation ($\mathbb{MR}$), given by the antisymmetric part of the mean velocity gradient;
- a stochastic term that represents the Brownian stretching ($\mathbb{BS}$), given by the symmetric Wiener matrix;
- a stochastic term that represents the Brownian rotation ($\mathbb{BR}$), given by the antisymmetric Wiener matrix.

They are:

$$\mathbb{MS}: \quad \frac{d\boldsymbol{p}_s(t)}{dt} = \Lambda\left(\langle \boldsymbol{S}\rangle \boldsymbol{p}_s - \boldsymbol{p}_s\boldsymbol{p}_s^{\intercal}\langle \boldsymbol{S}\rangle \boldsymbol{p}_s\right) \tag{4.47}$$

$$\mathbb{MR}: \quad \frac{d\boldsymbol{p}_a(t)}{dt} = \langle \boldsymbol{O}\rangle \boldsymbol{p}_a(t) \tag{4.48}$$

$$\mathbb{BS}: \quad d\boldsymbol{p}_{bs}(t) = -\frac{\nu_s^2}{2}\Lambda^2\boldsymbol{p}_{bs}dt + \nu_s\Lambda\left(d\mathbf{W}^s\,\boldsymbol{p}_{bs} - \boldsymbol{p}_{bs}\boldsymbol{p}_{bs}^{\intercal}\,d\mathbf{W}^s\,\boldsymbol{p}_{bs}\right) \tag{4.49}$$

$$\mathbb{BR}: \quad d\boldsymbol{p}_{ba}(t) = -\frac{\nu_a^2}{2}\boldsymbol{p}_{ba}dt + \nu_a\boldsymbol{p}_{ba}d\mathbf{W}^a. \tag{4.50}$$

All these sub-parts are characterised by having a unitary norm $\|\boldsymbol{p}\| = 1$ and the subscripts (s, a, bs, ba) denote the symmetric, antisymmetric, Brownian symmetric and Brownian antisymmetric parts, respectively. The original Cauchy problem related to Eq. (4.17) is solved in $[0, T]$ with initial condition $\boldsymbol{p}_0 = \boldsymbol{p}(t = 0)$. When applying time integration, we consider one step-size $\Delta t > 0$ and we decompose the interval $[0, T]$ into sub-intervals $[t_k, t_{k+1}]$ with $t_{k+1} = t_k + \Delta t$ and $k = 0, \ldots, N-1$; on each sub-interval $[t_k, t_{k+1}]$ we solve sequentially the four sub-problems to obtain $\tilde{\boldsymbol{p}}_{k+1} \approx \boldsymbol{p}(t_{k+1})$.

As said, the idea behind the splitting approach is to split Eq. (4.17) into explicitly solvable subequations, and to apply a proper composition of the resulting solutions. A standard procedure is to use a Lie–Trotter composition (Trotter (1959)) or, less common, the Strang composition (Strang (1968)), both of them being analysed by Tubikanec et al. (2020).

Here, a first-order splitting method using the Lie–Trotter composition is employed,

$$\tilde{\boldsymbol{p}}(t_{k+1}) = (\mathcal{L}_{ba} \circ \mathcal{L}_{bs} \circ \mathcal{L}_a \circ \mathcal{L}_s)\tilde{\boldsymbol{p}}(t_k), \tag{4.51}$$

where $\mathcal{L}_s$, $\mathcal{L}_a$, $\mathcal{L}_{bs}$, $\mathcal{L}_{ba}$ denotes the operators associated to Eqs. (4.47), (4.48), (4.49) and (4.50) respectively. The different sub-problems are connected via the initial conditions:

$$\begin{cases} \tilde{\boldsymbol{p}}_s(t_{k+1}) = \mathcal{L}_s(\tilde{\boldsymbol{p}}_s(t_k), t_k, t_{k+1}) & \text{with } \tilde{\boldsymbol{p}}_s(t_k) = \tilde{\boldsymbol{p}}(t_k), \\ \tilde{\boldsymbol{p}}_a(t_{k+1}) = \mathcal{L}_a(\tilde{\boldsymbol{p}}_a(t_k), t_k, t_{k+1}) & \text{with } \tilde{\boldsymbol{p}}_a(t_k) = \tilde{\boldsymbol{p}}_s(t_{k+1}), \\ \tilde{\boldsymbol{p}}_{bs}(t_{k+1}) = \mathcal{L}_{bs}(\tilde{\boldsymbol{p}}_{bs}(t_k), \mathbf{W}^s(t_k, t_{k+1}), t_k, t_{k+1}) & \text{with } \tilde{\boldsymbol{p}}_{bs}(t_k) = \tilde{\boldsymbol{p}}_a(t_{k+1}), \\ \tilde{\boldsymbol{p}}_{ba}(t_{k+1}) = \mathcal{L}_{ba}(\tilde{\boldsymbol{p}}_{ba}(t_k), \mathbf{W}^a(t_k, t_{k+1}), t_k, t_{k+1}) & \text{with } \tilde{\boldsymbol{p}}_{ba}(t_k) = \tilde{\boldsymbol{p}}_{bs}(t_{k+1}), \end{cases} \tag{4.52}$$

and the approximation at the next iteration time step is restored by $\tilde{\boldsymbol{p}}(t_{k+1}) = \tilde{\boldsymbol{p}}_{ba}(t_{k+1})$. In this approach the original problem (4.17) is replaced by the sub-problems Eq. (4.52) on the

sub-intervals $t \in [t_k, t_{k+1}]$. As detailed in Eq. (4.52), the four Eqs. (4.47)-(4.50) are advanced in order (𝕄𝕊, 𝕄ℝ, 𝔹𝕊, 𝔹ℝ) with each one taking one full time step at once and the result is integrated at first order accuracy.

In the deterministic case, where ODEs are involved, the change of the original problem with sub-problems usually results in some error, called *local splitting error*. If the operators (with coefficients constant in time) involved in the splitting are commutative, the method is exact; conversely, i.e. if they do not commute, the induced error is of order Δt. In general, in Eq. (4.52), a local splitting error is produced by the non-commutative character of the operators $\mathcal{L}_a$ and $\mathcal{L}_{bs}$.

Here we want to remark that numerically Eq. (4.22) and (4.23) for the tumbling and spinning respectively, can be directly discretised in $[0, T]$ with time step Δt and $t_{k+1} = t_k + \Delta t$ as,

$$\tilde{\phi}_{\perp p,k+1} = \tilde{\phi}_{\perp p,k} + \tilde{\boldsymbol{p}}_k \times \tilde{\boldsymbol{p}}_{k+1}\,, \tag{4.53}$$

$$\tilde{\phi}_{\parallel p,k+1} = \tilde{\phi}_{\parallel p,k} + \frac{1}{2}\tilde{\boldsymbol{p}}_k \cdot \langle \boldsymbol{\omega} \rangle\, \Delta t + \frac{\nu_a}{2}\tilde{\boldsymbol{p}}_k \cdot \Delta \mathbf{w}^a_k, \tag{4.54}$$

which results to be numerically an easier task compared to choose a suitable numerical integration scheme for the SDE (4.21).

Remark 1 (On the Brownian tensor reduction) The model is developed by introducing $9d$-Brownian vector $\mathbf{w}$ or equivalently a the 3×3 Brownian matrix $\mathbf{W}$, with $W^{ij} = w^{3(i-1)+j}$ (see Remark 2). Considering then the stochastic stretching and rotation parts in the orientation decomposition, we can observe that *(i)* $\mathbf{W}^s$, considering alone, can be reduced to a $6d$-Brownian vector, *(ii)* $\mathbf{W}^a$, considering alone, can be reduced to a $3d$-Brownian vector, *(iii)* $\mathbf{W}^s$ and $\mathbf{W}^a$ are just uncorrelated, not independent.

The reduction/simplification of the Brownian vector from 9 to 6 or 3 (through the Lévy theorem identification that transform the SDE without transforming the law of the solution) is then possible, for instance for the weak error analysis purpose of each separate sub-equations of stochastic stretching and rotation.

Considering specifically the Brownian rotation part, we can also transform the equation in a more intrinsic way and work with the $2d$ Brownian motion on the sphere, having the Laplace-Beltrami operator as infinitesimal generator on the unit sphere.

But the algorithm needs to be performed with its 9 Brownian components to preserve the correct correlation structure of the noise part form a sub-part of the splitting to another. In particular, this is mandatory if the model is applied to compute some unfolded quantities such as ϕ, $\phi_{\perp p}$ and $\phi_{\parallel p}$. The dynamics of these latter relies on the triplet $(\boldsymbol{p}, \mathbf{W}^s, \mathbf{W}^a)$ as it is shown in SDE (4.22)-(4.23) and force $\boldsymbol{p}$ to be computed with the dependent Brownians $(\mathbf{W}^s, \mathbf{W}^a)$.

4.4.2 *Error criteria*

Following Pagés (2018), we introduce the definitions of strong and weak convergence. In this context, the weak convergence is appropriate to guarantee the accuracy of the particle orientation and rotation rate statistics and also to ensure that spurious numerical integration errors do not affect the results or can be taken under control in real applications. Equally important is the study of the strong convergence due to the intricate behaviour of the trajectories within the model. In fact, the model involves the diffusion tensor that, in general, could be much more intricate than the isotropic structure here considered. For these reasons, both strong and weak convergence errors will be analysed in the numerical results.

We consider the solution $\boldsymbol{p}(T)$ of the SDE (4.17) after time T from the deterministic initial condition $\boldsymbol{p}(0) = \boldsymbol{p}_0$. This can be written as the Itô integral of Eq. (4.17) in a more general compact form,

$$\boldsymbol{p}(T) = \boldsymbol{p}_0 + \int_0^T \boldsymbol{D}(\boldsymbol{p}(t))dt + \int_0^T \boldsymbol{B}(\boldsymbol{p}(t))d\mathbf{W}_t \tag{4.55}$$

where $\boldsymbol{D}(\boldsymbol{p}(t))$ and $\boldsymbol{B}(\boldsymbol{p}(t))$ are the drift and diffusion coefficients, respectively. Then, a numerical approximate solution to $\boldsymbol{p}(T)$, denoted by $\bar{\boldsymbol{p}}(T)$, is obtained by approximately integrating Eq. (4.17) in a sequence of time steps of size Δt. The numerical approximation $\bar{\boldsymbol{p}}(T)$ can be obtained by using increments of Wiener processes; and, for the scheme to be consistent, $\bar{\boldsymbol{p}}(T)$ must converge to $\boldsymbol{p}(T)$ as Δt tends to zero.

Strong convergence. The numerical scheme, for $\boldsymbol{p}(T) \in L^2(\Omega)$, is deemed to be *strong* β-order accurate if the error

$$\mathcal{E}\mathrm{rr}^{\mathrm{s}}(p_i) = \left(\mathbb{E}\sup_{0\leq t\leq T}|p_i(t) - \bar{p}_i(t)|^2\right)^{\frac{1}{2}} \leq C^{\mathrm{s}}(T)(\Delta t)^{\beta} \tag{4.56}$$

for some constant C^{s} which may depend on T but is independent from Δt. For instance, in the case of Euler–Maruyama scheme, we get a strong convergence of order $\beta = 1/2$. We would like to remark that, with respect to the classical definition of mean-square convergence, we strengthen the condition by adding the supremum over $t \in [0, T]$. In the following, we will be interested not only in the strong convergence of $\boldsymbol{p}$, but also in the processes $\phi_{\perp p}$ (Eq. (4.22)) and $\phi_{\parallel p}$ (Eq. (4.23)) defined in Section 4.3.3 to compute the statistic tumbling and spinning for the stochastic model. The main reason to analyse the strong convergence of these two processes is that we do not have access to an analytical prediction of them. In this case, an analogous definition of Eq. (4.56) is employed for $\mathcal{E}\mathrm{rr}^{\mathrm{s}}(\phi_{\perp p})$ and $\mathcal{E}\mathrm{rr}^{\mathrm{s}}(\phi_{\parallel p})$ for these two processes.

Weak convergence. In the case of weak convergence, it is meaningful to consider the convergence of $\boldsymbol{p}(T)$ and $\bar{\boldsymbol{p}}(T)$ in distribution. Such convergence is analysed in terms of expectation $\mathbb{E}[f(\boldsymbol{p}(T))]$ of a sufficiently smooth test function f. For f the minimal constraint is that the expectation is well defined, and in our case since the process $\boldsymbol{p}_t$ is bounded, smoothness is the only condition. Thus, the numerical scheme is deemed to be weak β-order accurate if the error,

$$\mathcal{E}\mathrm{rr}^{\mathrm{w}}(f) = |\mathbb{E}[f(\boldsymbol{p}(T))] - \mathbb{E}[f(\bar{\boldsymbol{p}}(T))]| \leq C^{\mathrm{w}}(T)(\Delta t)^{\beta} \tag{4.57}$$

for some constant C^{w} which may depend on T but is independent from Δt. For instance, in the case of Euler–Maruyama scheme, we get a weak of convergence of order $\beta = 1$.

A possible amelioration for some future perspectives, on the study of the weak error, can be the employment of the Richardson–Romberg extrapolation (Pagés (2018)), a sequence acceleration method used to improve the rate of convergence of a sequence of estimates. In particular, it does not add any additional numerical complexity and at the same time increases the order of convergence.

4.4.2.1 *Splitting scheme: a step by step error evaluation*

The presentation of numerical convergence is structured as follows: we present a suitable numerical scheme for both the Brownian rotation sub-step (𝔹ℝ) and for the Brownian stretching sub-step (𝔹𝕊) of the splitting; then the strong and weak convergence will be analysed. In particular, for the Brownian stretching (𝔹𝕊), two different discretisation schemes are introduced and compared. Finally, the strong and weak convergence for the splitting algorithm will be

tested in the HIT where the contributions coming from the mean field in Eq. (4.17) are set to zero.

To demonstrate the convergence of the schemes under study, the exact solution (or an accurate estimate of it) is required. In the following, for the strong convergence, we compare the numerical solution to an approximation of the exact one computed, at a suitable refined time step, whereas, for the weak convergence, an expression of the exact solution is provided.

In particular, the expression of the exact solution for weak convergence is obtained by a simplification of Eq. (4.17), in the HIT case. This assumption allows to derive analytical expressions for first, second and third moments of the orientation $\boldsymbol{p}$,which are used as test functions in Eq. (4.57). They are derived applying the Itô's Lemma to Eq. (4.17), as reported in Appendix B.4, getting

$$\mathbb{E}[p_i](t) = \mathbb{E}[p_i](0)e^{-\frac{c}{2}t} \tag{4.58}$$

$$\mathbb{E}[p_i p_j](t) = \mathbb{E}[p_i p_j](0)e^{-\frac{3c}{2}t} \tag{4.59}$$

$$\mathbb{E}[p_i^2](t) = \mathbb{E}[p_i^2](0)e^{-\frac{3}{2}ct} + \frac{1}{3}\left(1 - e^{-\frac{3}{2}ct}\right) \tag{4.60}$$

$$\mathbb{E}[p_i^3](t) = e^{-3ct}\left(\mathbb{E}[p_i^3](0) - \frac{3}{5}\mathbb{E}[p_i](0)\right) + \frac{3}{5}\mathbb{E}[p_i](0)e^{-\frac{c}{2}t} \tag{4.61}$$

where the constant c takes different values with respect to the sub-equation considered:

$$c = \begin{cases} \Lambda^2\nu_s^2 & \text{for } (\mathbb{BS}) & \text{Eq. (4.49)} \\ \nu_a^2 & \text{for } (\mathbb{BR}) & \text{Eq. (4.50)} \\ \Lambda^2\nu_s^2 + \nu_a^2 & \text{for } (\mathbb{BS}) + (\mathbb{BR}) & \text{Eq. (4.49)} + \text{(4.50)} \end{cases} \tag{4.62}$$

where we recall that $\nu_s = \sqrt{Ku/(5\tau_\eta)}$ and $\nu_a = \sqrt{Ku/(3\tau_\eta)}$.

As mentioned above, the convergence tests are performed in the case of HIT flow, that is Eq. (4.48)-(4.47) for $\mathbb{MS}$ and $\mathbb{MR}$ are not taken into account. This choice has been made since we are mainly interested to analyse the weak and strong error related to the stochastic part of the splitting algorithm scheme. In fact, the deterministic part has been widely studied in literature, unlike the stochastic one where the investigation remains limited. Moreover the constant c is always positive and for $t \to \infty$ the results in Eq. (4.58) to (4.61) are compatible with the uniform distribution on a sphere:

$$\rho(p_1, p_2, p_3) = \rho(\boldsymbol{p}) = \frac{1}{(2\pi)^{3/2}} \exp\left(-\frac{\|\boldsymbol{p}\|^2}{2}\right) \tag{4.63}$$

4.4.2.2 *Numerical parameters*

In the following we list the numerical parameters used to study the strong and weak convergence. The case of rod-like particles with a shape parameter $\Lambda = 1$ in Eq. (4.17) has been considered. Each test case is integrated on $t \in [0, T]$ for different time steps $\Delta t = 2^{-h}$, with $h = 1, \dots, 12$. For the strong error evaluation the reference trajectory is computed with $h = 13$, which has been denoted as $\mathrm{ref}(\Delta t) = 2^{-13}$. The final time $T = 0.5$ is the same for all choices, in order to show the asymptotic convergence with respect to the time step Δt. We perform the convergence test for each simulation trial using the same number of particles $N_p = 5 \cdot 10^8$, and for the weak convergence an empirical estimator is introduced, by repeating the trials independently $N_e = 10$. A total of four different values of the characteristic time scale parameter $\tau_\eta = 0.01, 0.1, 1, 10$ are considered, fixing the Kubo number $Ku = 1$ (Eq. (4.17)). In this way we aim to estimate the influence of τ_η both on weak and strong convergence. Moreover, two

different choices of initial conditions have been used: $\boldsymbol{p}_a^0 = (1,0,0)$ and $\boldsymbol{p}_b^0 = (1,1,1)/\sqrt{3}$; this is done in order to observe the order of convergence for all moments, since they might be zero for a particular choice of the initial condition. For instance, this is the case of $\boldsymbol{p}_a^0$ for Eq. (4.59).

Numerically the strong error that we are going to evaluate becomes,

$$\mathcal{E}\mathrm{rr}^{\mathrm{s}}(p_i) = \left(\frac{1}{N_p} \sum_{n=1}^{N_p} \sup_{k\in[0,K],T=K\Delta t} \left| \bar{p}_{i,k\Delta t}^{n,\mathrm{ref}(\Delta t)} - \bar{p}_{i,k\Delta t}^{n} \right|^2 \right)^{\frac{1}{2}}. \tag{4.64}$$

The same definition is applied for processes $\phi_{\perp p}$ and $\phi_{\parallel p}$, respectively. The numerical weak error is evaluated as,

$$\mathcal{E}\mathrm{rr}^{\mathrm{w}}(f) = \frac{1}{N_e} \sum_{m=1}^{N_e} \left| \mathbb{E}[f(\boldsymbol{p}(T))]^{\mathrm{exact}} - \frac{1}{N_p} \sum_{n=1}^{N_p} [f(\bar{\boldsymbol{p}}_n(T))] \right|_m. \tag{4.65}$$

This is a general formula for a generic test function f; in our case the expressions of the exact solutions are obtained by replacing $f(\boldsymbol{p})$ with p_i, $p_i p_j$ and p_i^3 and applying Eq. (4.58) to (4.61).

4.4.3 *Discretisation of the Brownian Rotation*

In this section, we are interested in the sub-part of the splitting scheme represented by Eq. (4.50), that we recall to be,

$$d\boldsymbol{p}_{ba}(t) = -\frac{\nu_a^2}{2}\boldsymbol{p}_{ba}dt + \nu_a d\mathbf{W}^a \boldsymbol{p}_{ba},$$

where we remark that $\boldsymbol{p}_{ba}$ is a unitary vector, i.e. $\|\boldsymbol{p}_{ba}\| = 1$. This equation is linear, i.e. globally Lipschitz, so *a priori* an Euler–Maruyama scheme should converge in this context. However, in this equation there is the additional geometric constraint of unitary norm that numerically is not preserved. In other words, we can say that Eq. (4.50) contains a singularity that is visible when a change from Cartesian to spherical coordinates is applied (the latter is singular in one of the two angles).

Equation (4.50) represents a Brownian motion on a sphere (Van Den Berg and Lewis (1985)) and can be rewritten in the Stratonovich formulation (∂) as,

$$d\boldsymbol{p}_{ba}(t) = \frac{\nu_a}{2}\, \partial\mathbf{w}^a \times \boldsymbol{p}_{ba}; \tag{4.66}$$

where the vector $\mathbf{w}^a = 2(\mathbf{W}_{32}^a, \mathbf{W}_{13}^a, \mathbf{W}_{21}^a)^\intercal = (W_8 - W_6, W_3 - W_7, W_4 - W_2)^\intercal$ has been used as in Section 4.3.3 to bring up the cross product ($\times$). This means that Eq. (4.66) can be interpret as a rotational kinematics equation for the vector $\boldsymbol{p}_{ba}$ induced by the angular increment $\partial\mathbf{w}^a$.

Diffusion processes on a curved surface, usually a sphere, in a three dimensional Euclidean space $\mathbb{R}^3$ arise in several contexts. For example, at cellular level, diffusion is an important mode for the transport of biological substances such as lipids or proteins (Krishna et al. (2000); Faraudo (2002); Sbalzarini et al. (2006)). Alternatively, spherical diffusion occurs on a wide range of different scales, from micro to macro, such as in swimming of bacteria motion (Li et al. (2008)), spin dynamics Antoine et al. (1991), polymer systems (Snook (2006)) and global migration patterns of marine mammals Brillinger (2012).

While diffusion in Euclidean space has been extensively studied, both analytically and numerically (Wax (1954); Gould et al. (1996)), there have been fewer studies of diffusion on curved surfaces. Often Monte Carlo simulation algorithms for such models on curved spaces are constructed using approximate tangent plane methods, which are accurate only for very small time steps, which makes algorithms computationally expensive. Algorithms allowing simulation over larger time steps are hence of particular interest for our purposes. To cite

other previous works, some algorithms are based on an approximation of transition density of Brownian motion on the sphere (Nissfolk et al. (2003); Carlsson et al. (2010b)), others studies include the diffusion of Brownian particles on the surface of a sphere using the distribution of solid angles (Krishna et al. (2000); Brillinger (2012)). Mijatović et al. (2018) develops an algorithm for increments of Brownian motion on an sphere of arbitrary dimension based on Wright–Fisher diffusion. On the other hand, there is a relatively underdeveloped literature on the analysis and verification of strong and weak convergence of numerical schemes for SDEs on manifold with respect to those evolving without geometric constraints. To cite an example, the strong convergence of SDEs evolving in $SO(n)$ have been studied by Piggott and Solo (2016) using geometric SDE integrators based on the exponential Euler–Maruyama scheme.

Direct approach for Brownian rotation scheme. In order to underline the limit and difficulties beyond the development of a suitable numerical scheme to solve Eq. (4.50), here we present what we will call 'direct scheme' approach by discretizing Eq. (4.50) using a semi-implicit Euler–Maruyama scheme. An issue related to the discretisation of Eq. (4.50), is the preservation of the unitary norm: in fact, at each time step the solution has to be re-normalized; if the norm tends to zero, singularities are introduced. In this case the employment of such numerical scheme presents some limits that we try to underline in Section 4.4.3.2, after having presented an alternative numerical strategy using quaternions.

Starting with an initial condition $\widehat{\boldsymbol{p}}_{ba,0}$ such that $\|\widehat{\boldsymbol{p}}_{ba,0}\| = 1$, the discretised version of Eq. (4.50) in $[0, T]$, with time step Δt and $t_{k+1} = t_k + \Delta t$, reads:

$$\begin{aligned}
\tilde{p}_{ba(1),k+1} &= \left[\widehat{p}_{ba(1),k} + \frac{\nu_a}{2}\left(\Delta \mathrm{w}^a_{2,k}\,\widehat{p}_{ba(3),k} - \Delta \mathrm{w}^a_{3,k}\,\widehat{p}_{ba(2),k}\right)\right]\frac{1}{1+\frac{\nu_a^2}{2}\Delta t} \\
\tilde{p}_{ba(2),k+1} &= \left[\widehat{p}_{ba(2),k} + \frac{\nu_a}{2}\left(\Delta \mathrm{w}^a_{3,k}\,\widehat{p}_{ba(1),k} - \Delta \mathrm{w}^a_{1,k}\,\widehat{p}_{ba(3),k}\right)\right]\frac{1}{1+\frac{\nu_a^2}{2}\Delta t} \\
\tilde{p}_{ba(3),k+1} &= \left[\widehat{p}_{ba(3),k} + \frac{\nu_a}{2}\left(\Delta \mathrm{w}^a_{1,k}\,\widehat{p}_{ba(2),k} - \Delta \mathrm{w}^a_{2,k}\,\widehat{p}_{ba(1),k}\right)\right]\frac{1}{1+\frac{\nu_a^2}{2}\Delta t},
\end{aligned} \tag{4.67}$$

where at each time step we re-normalize and obtain $\widehat{\boldsymbol{p}}_{ba,k+1} = \tilde{\boldsymbol{p}}_{ba,k+1}/\|\tilde{\boldsymbol{p}}_{ba,k+1}\|$. We remark that the norm of $\tilde{\boldsymbol{p}}_{ba,k+1}$ can tend to zero, that could give problems in terms of convergence, by introducing a singularity in the numerical scheme.

Moreover, the error regarding norm convergence, as detailed in Appendix B.5, reads:

$$\mathbb{E}\|\tilde{\boldsymbol{p}}_{ba,k+1}\|^2 = 1 - \frac{\nu_a^4}{4}\Delta t^2 + \mathcal{O}(\Delta t^3) \tag{4.68}$$

So, at least for the mean, the norm of the 'direct scheme' is not preserved and, as we will show later, this error, regarding just the norm, converges with same rate than the one obtained by the scheme in Eq. (4.87) that use quaternions to solve the Brownian rotation. However, the constant factor in front of Δt^2 in Eq. (4.68), is much larger than the one found evaluating the norm of the quaternions in Eq. (4.88). This difference already could give some insight in preferring the quaternion scheme at least for large time step size. In Fig. 4.2, we plot the strong error as a function of the time step Δt, for different values of τ_η; in particular, Fig. 4.2a shows the behaviour of the strong error for the first component $p_{ba,1}$ (for simplicity, since all the components act in the same manner), in Fig. 4.2b we plot the first component of the vector $\phi_{\perp p_{ba}}$ (for the same reason) and in Fig. 4.2c the scalar $\phi_{\parallel p_{ba}}$, as defined by Eq. (4.53) and (4.54). We choose as initial condition for the particle orientation $\boldsymbol{p}_a^0 = (1, 0, 0)$. Looking at Fig. 4.2, the direct scheme converges with a strong rate of order $1/2$. We remark that for different choices

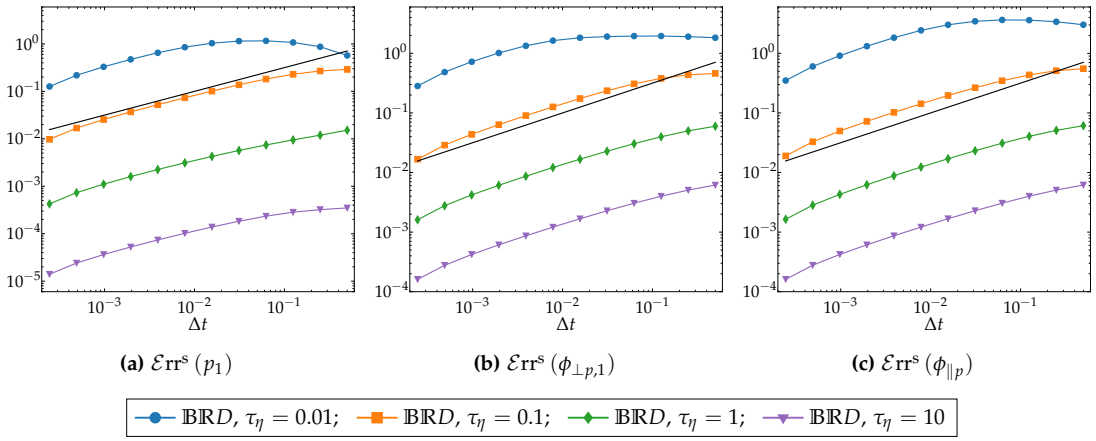

Figure 4.2: Stochastic rotation sub-step through the 'direct scheme' ($\mathbb{BRD}$): Strong error ($\mathcal{E}\mathrm{rr}^{\mathrm{s}}$) of the numerical scheme in Eq. (4.67) against the time step Δt for different values of τ_η. In (a) the first component of $\boldsymbol{p}_{ba}$, (b) the first component $\phi_{\perp p_{ba}}$ of tumbling and (c) the spinning $\phi_{\parallel p_{ba}}$. Black line indicates the slope 1/2; the initial condition of particle orientation is $\boldsymbol{p}_a^0 = (1,0,0)$.

of τ_η the magnitude of the error changes; in fact, for $\tau_\eta = 10$ (i.e., a small diffusion coefficient, $\nu_a \approx \sqrt{1/\tau_\eta}$), we get a better error than for $\tau_\eta = 0.01$. Finally, we would like to remark that the study of strong error is extremely sensitive to the trajectory that needs to stay on manifold (a sphere in our case). Indeed, if the gap with respect to the reference trajectory becomes large this has a huge impact on strong convergence, that, in our case, is emphasised by taking the supremum as in Eq. (4.64).

Moving to consider the weak error as a function of Δt, as shown in Fig. 4.3, we can observe that the behaviour of the weak error strongly depends on the parameter τ_η. In Fig. 4.3a the first component of the moment $\mathbb{E}[\boldsymbol{p}_{ba}]$ converges with a slope 1 as expected by the employment of first order Euler–Maruyama scheme, choosing as initial condition for particle orientation $\boldsymbol{p}_a^0 = (1,0,0)$. The same behaviour is observed for the higher moments $\mathbb{E}[p_{ba,1}^2]$, $\mathbb{E}[p_{ba,1}^3]$ in Fig. 4.3b and 4.3c respectively. In order to show the weak convergence of the cross moment $\mathbb{E}[p_{ba,1}p_{ba,2}]$, presented in Fig. 4.3d, the initial condition has been fixed to $\boldsymbol{p}_b^0 = (1,1,1)/\sqrt{3}$. In fact, by choosing the initial condition $\boldsymbol{p}_a^0 = (1,0,0)$, the cross moments are identically zero (Eq. (4.59)), which means that we are evaluating only the Monte Carlo error of the performing test.

The magnitude of the weak error is strongly impacted by the amplitude of diffusion coefficient $\nu_a \approx \sqrt{1/\tau_\eta}$. In terms of error, the scheme reacts in a special manner for the critical value of $\tau_\eta = 0.01$. We would expect that the error convergence for $\tau_\eta = 0.01$ (blue line) would have been above the error convergence for $\tau_\eta = 0.1$ (orange line), which is not the case. A possible explanation is that the analytical solution overcomes the machine precision since we need to compute an exponential of a very small number; for instance, considering the exact solution for $\mathbb{E}[p_{ba,1}^2]$ (Eq. (4.60)) leads to the evaluation of $\sim \exp(-50)$. This brings some numerical drawbacks since we are computing an error which is very close to zero. Moreover, this behaviour is more amplified in even moments with respect to odd ones, as Eqs. (4.58)-(4.61) show, for the same reason. A special case is represented by the convergence of $\mathbb{E}[p_{ba,1}p_{ba,2}]$ for $\tau_\eta = 10$, where the magnitude of the error is of the same order of Monte Carlo using as initial condition $\boldsymbol{p}_b^0$. In order to observe the convergence of order 1 the number of particles N_p should be significantly increased. We want to underline that this effect will be noticeable for all numerical convergence tests performed in this Chapter.

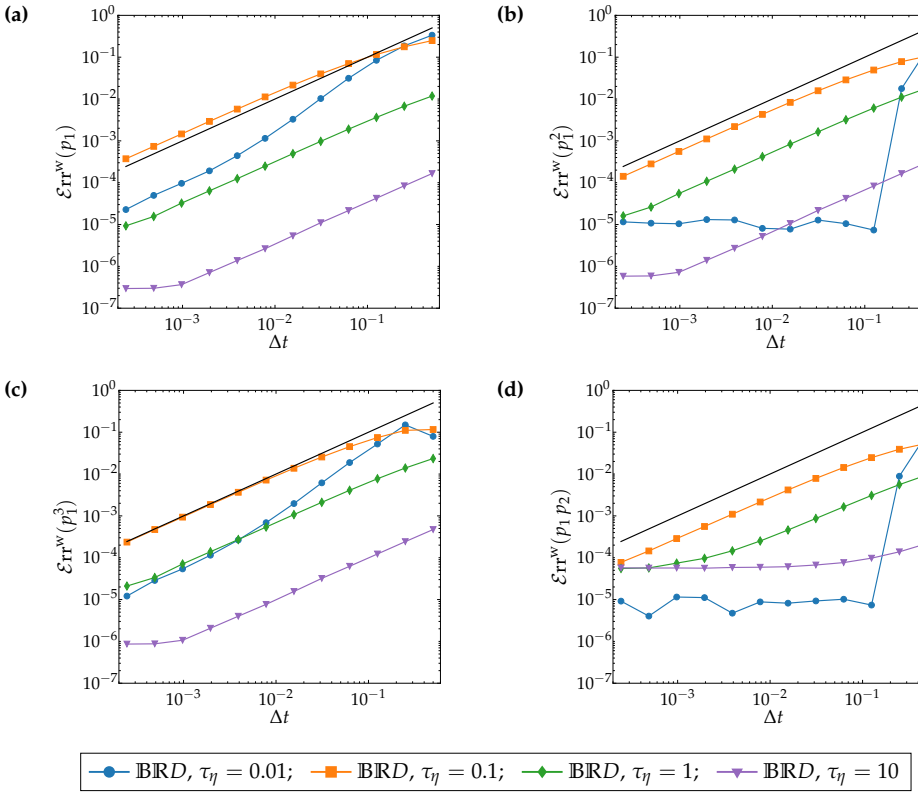

Figure 4.3: Weak error ($\mathcal{E}\mathrm{rr}^{\mathrm{w}}$) for the stochastic rotation sub-step through a direct scheme ($\mathbb{BIR}D$) in Eq. (4.67) against the time step Δt for different values of τ_η. In (a), (b), and (c) the first three moments of the first component $p_{ba,1}$ for an initial condition of particle orientation $\boldsymbol{p}_a^0 = (1,0,0)$. In (d) the second cross moment $p_{ba,1}p_{ba,2}$ is shown using a different initial condition $\boldsymbol{p}_b^0 = (1,1,1)/\sqrt{3}$. Black line indicates the slope 1.

From the study of strong and weak error shown above the employment of a semi-implicit Euler–Maruyama scheme in Eq. (4.67) seems to be reasonable and very direct to implement. Nevertheless, it hides some limits that are not straight away evident by just observing the convergence of the renormalised vector $\widehat{\boldsymbol{p}}_{ba,k+1} = \tilde{\boldsymbol{p}}_{ba,k+1}/\|\tilde{\boldsymbol{p}}_{ba,k+1}\|$. Indeed, some issue are strictly related to non-renormalised vector and $\tilde{\boldsymbol{p}}_{ba,k+1}$, as well as by observing the marginal probability density function of the components of $\boldsymbol{p}$. In particular, these issues are empathised for small values of τ_η, i.e. large value of the diffusion coefficient, and taking large time step Δt. They will be briefly discussed in Section 4.4.3.2, after the presentation of an alternative numerical strategy to solve the Brownian rotation.

We are going to anticipate that the case shown above motivates the construction of a numerical scheme that lives on a sphere in order to get better performance on the rotational motion. This problem has been solved in the deterministic case by introducing the quaternion dynamics. In our case, since we are working with an SDE, additional work to adapt the quaternions to the stochastic case is required.

A further advantage of introducing quaternions is characterised by the study of inertial particles. When, the interest is to consider the dispersion of a large numbers of rigid inertial non-spherical which are moved according to their inertia and to hydrodynamic drag and rotate according to hydrodynamic torque, the most common and convenient way is to compute rotational properties of particles in body frame and, then transform them into world space. In general, this implies that the time integration of the rotation operator, to transform vector and

tensor variables between the different frameworks is addressed by using unit quaternion (Zhao and Van Wachem (2013b)). This could suggest that in the development of a stochastic model for the translation and rotation of non-spherical inertial fibres a suitable numerical scheme that use quaternion dynamics could be necessary. Another interesting application which involves the numerical integration of stochastic quaternions is the Brownian Dynamics of rigid particles of arbitrary shape, where the torque of the body can be written in terms of the unit quaternions describing its orientation (Delong et al. (2015)).

ROTATION IN $SO(3)$ We now introduce basic concepts about rotation properties in $SO(3)$ and the quaternion dynamics, which will be useful in the following to define our numerical scheme. The integration of rotation for a given angular velocity is often required in practice. The application areas include many disciplines such as navigation in aerospace technologies, robotics, computer graphics or classical dynamics of rigid bodies, to name a few. In general, the deterministic motion of rigid bodies include translation and rotation. In contrast to translational motion where the motion is formed by addition of incremental displacements, rotations combine in the form of products of the incremental rotations matrices. Thus, efficient and accurate integration of rotation is still actively investigated, especially nowadays that ever increasing computational power allows for larger systems to be considered, which requires numerical integration schemes that are both, accurate and not too much computationally expensive.

In the kinematics of rotational motion several different approaches are available to describe the rotation between two different frames, and in general the best approach depends specifically on the problem. In particular, the translation and rotation motion of a non-spherical rigid particle can be determined in two Cartesian coordinates: in body space (Lagrangian framework), where the origin of the Cartesian coordinates is fixed at the particle mass centre and the axis of coordinates rotates along with the particle, and in the world space (Eulerian framework), where the coordinates are fixed in the origin of the initial Cartesian reference frame. The most commonly used method to describe the rotational motion are rotation matrices, Euler angles and unit Quaternions (Diebel (2006)).

The special orthonormal group $SO(3) = \{\mathscr{R} \in \mathbb{R}^{3\times 3} \,|\, \mathscr{R}^T\mathscr{R} = \mathbb{1} \text{ and } \det(\mathscr{R}) = 1\}$ (where $\mathbb{1}$ indicates the identity matrix), the set of rotation matrices is often viewed as the most convenient representation because the rotation operation is simply a matrix-vector multiplication, and the matrix columns form an orthonormal basis. A vector $\boldsymbol{v}$ transforms from one coordinates system to another by the application of the rotation matrix as,

$$\boldsymbol{v}' = \mathscr{R}\boldsymbol{v} \tag{4.69}$$

where $\boldsymbol{v}'$ represents the rotated counterpart of $\boldsymbol{v}$. Further, given an angular velocity vector ω expressed, for example, in the body frame, the time derivative of the rotation matrix is given by

$$\frac{d\mathscr{R}}{dt} = \mathscr{R}\,[\boldsymbol{\omega}]_\times, \tag{4.70}$$

where $[\,]_\times$ denotes the antisymmetric 3×3 matrix of the form

$$[\boldsymbol{\omega}]_\times = \begin{pmatrix} 0 & -\omega_3 & \omega_2 \\ \omega_3 & 0 & -\omega_1 \\ -\omega_2 & \omega_1 & 0 \end{pmatrix}. \tag{4.71}$$

Direct numerical integration of the differential equation (4.70) with standard integration routines, such as explicit Runge–Kutta methods, does not preserve the structure of $SO(3)$. The

column of $\mathscr{R}$ becomes non-orthogonal and even non-unit length due to the truncation and round-off error of the numerical integration at every time step. These errors can be reduced by using high-order methods with small time step over a short integration time, but performing integration over long times becomes difficult. The problem of maintaining the structure $SO(3)$ is an example of a wider class of problems addressed by the geometrical numerical integration method (Budd and Piggott (2003)). For the rotation problem, higher order exponential methods can be employed (Andrle and Crassidis (2013)) but are hard to derive and to implement.

Another approach makes use of Euler angles to represent three composed axis rotations by mapping the rigid particle in the body space to the world space. Computationally, this method guarantees $\mathscr{R}$ is orthonormal, even if these angles involve a combination of sin and cos functions, which are non linear. On the other hand, this representation contains singularities, i.e. there are some orientations giving rise to the loss of one degree of freedom, when two of three axis are rotating into a parallel configuration (also called the Gimbal lock problem). This method works in applications involving one or two dimensional rotations, but for a general 3D rotation it turns out to be most often not suitable.

Since all three-parameter representations suffer from singularities, unit quaternions can be employed (four-parameter representation) in order to avoid these problems. Quaternions were introduced by Hamilton (1844) and reviewed in Sola (2017)). A quaternion is defined by,

$$\mathfrak{q} = \mathfrak{q}_0 + \mathfrak{q}_1\hat{e}_1 + \mathfrak{q}_2\hat{e}_2 + \mathfrak{q}_3\hat{e}_3 \tag{4.72}$$

where $\mathfrak{q}_0$, $\mathfrak{q}_1$, $\mathfrak{q}_2$, $\mathfrak{q}_3$ are real numbers and $\hat{e}_i$ are unit vectors directed along the x, y and z axis respectively. Quaternions can be also written as a real number and a vector,

$$\mathfrak{q} = (\mathfrak{q}_0, \mathbf{q}). \tag{4.73}$$

The conjugate and the norm of a quaternion are defined respectively as,

$$\mathfrak{q}^* = \mathfrak{q}_0 - \mathfrak{q}_1\hat{e}_1 - \mathfrak{q}_2\hat{e}_2 - \mathfrak{q}_3\hat{e}_3 \tag{4.74}$$

$$\|\mathfrak{q}\| = \sqrt{\mathfrak{q}^*\mathfrak{q}} = \sqrt{\mathfrak{q}_0^2 + \mathfrak{q}_1^2 + \mathfrak{q}_2^2 + \mathfrak{q}_3^2}. \tag{4.75}$$

A unit quaternion is defined as a quaternion of unitary norm $\|\mathfrak{q}\| = 1$, which implies $\mathfrak{q}^* = \mathfrak{q}^{-1}$ having defined $\mathfrak{q}^{-1} = \mathfrak{q}^*/\|\mathfrak{q}\|$.

In general, dealing with the numerical integration in quaternions implies that the time integration of the rotation is addressed using unit quaternions (other methods exists using non-unit quaternion (Rucker (2018)). After the time step, the corresponding rotation matrix is computed from quaternions and used to determine the orientation in the rotated configuration by Eq. (4.69). This requires the inverse relationship between rotation matrices and unit quaternions. The rotation matrix corresponding to the unit quaternion is given by,

$$\mathscr{R} = \left(\hat{\mathfrak{q}}_0^2 - \hat{\mathbf{q}}^\intercal\hat{\mathbf{q}}\right)\mathbb{1} + 2\hat{\mathbf{q}}\hat{\mathbf{q}}^\intercal + 2\mathfrak{q}_0[\hat{\mathbf{q}}]_\times, \quad \hat{\mathfrak{q}} = \frac{\mathfrak{q}}{\|\mathfrak{q}\|}. \tag{4.76}$$

Equation (4.69) expresses the transformation of a vector by a rotation matrix and is equivalent to,

$$\boldsymbol{v}' = \mathfrak{q}\boldsymbol{v}\mathfrak{q}^{-1} = \mathscr{R}\boldsymbol{v} \tag{4.77}$$

Thus, the quaternion dynamics is first solved to determine the rotation matrix and subsequently $\mathscr{R}$ is applied to $\boldsymbol{v}$ to compute the vector in the rotated framework. However, other methods exist to directly compute the vector in the rotated framework without the necessity of determining the corresponding rotation matrix (e. g., Zhao and Van Wachem (2013b)).

Equation (4.70) can be solved by using the unit quaternions. Indeed, the time derivative of the unit quaternion is determined by the angular velocity vector $\boldsymbol{\omega}$ as,

$$\frac{d\mathfrak{q}}{dt} = \frac{1}{2}\boldsymbol{F}_{\mathfrak{q}}(\boldsymbol{\omega})\ \mathfrak{q} \tag{4.78}$$

where

$$\boldsymbol{F}_{\mathfrak{q}}(\boldsymbol{\omega}) = \begin{pmatrix} 0 & -\boldsymbol{\omega}^{\mathsf{T}} \\ \boldsymbol{\omega}^{\mathsf{T}} & [\boldsymbol{\omega}]_{\times} \end{pmatrix} = \begin{pmatrix} 0 & -\omega_1 & -\omega_2 & -\omega_3 \\ \omega_1 & 0 & \omega_3 & -\omega_2 \\ \omega_2 & -\omega_3 & 0 & \omega_1 \\ \omega_3 & \omega_2 & -\omega_1 & 0 \end{pmatrix}. \tag{4.79}$$

In order to preserve the constraint of a unit quaternion, the new quaternion solved by Eq. (4.78) requires a re-normalisation after each integration time step.

Several algorithms have been developed to integrate unit quaternions to represent rotations. Some of them are based on the Taylor expansion of Eq. (4.78). The Euler method is the most simple algorithm, however the re-normalisation procedure brings numerical errors, including the relatively large truncation error of the first-order Euler scheme. To reduce these errors, other schemes, based on the Taylor expansion, have been developed such as the leap-frog method (Walton and Braun (1993)), the second order Adam–Bashforth method (Mortensen et al. (2008)), the Runge–Kutta method (Press et al. (1986)) and the scalar factor method (Kleppmann (2007)).

As said, the numerical integration of a Brownian motion in $SO(3)$ results to be a much harder problem than the deterministic counterpart presented above. Moreover, a simple discretisation scheme to integrate Eq. (4.50) leads to a significant error or, even worst, it does not converge, as we have shown in Fig. 4.2. In order to derive a better integration method for this part of the splitting algorithm we can introduce unit quaternions to represent the stochastic rotation. The main steps consist in solving the rotation kinematics in the unit quaternion space and then using the solutions to reconstruct the matrix that rotates the vector $\boldsymbol{p}_a$ in the new configuration.

Compared to the deterministic case, where the integration of unit quaternion is performed on the angular velocity $\boldsymbol{\omega}$, in the stochastic case we have to work with angular increments represented by the Wiener vector $\partial\mathbf{w}^a$ in Eq. (4.66). This leads to an analogous formulation for the time derivative of unit quaternions (4.78) in the stochastic case,

$$\frac{d\mathfrak{q}}{dt} = \frac{\nu_a}{4}\boldsymbol{F}_{\mathfrak{q}}(\partial\mathbf{w}^a)\ \mathfrak{q} \tag{4.80}$$

where the matrix $\boldsymbol{F}_{\mathfrak{q}}(\partial\mathbf{w}^a)$ depends on the Wiener vector $\partial\mathbf{w}^a$ in the Stratonovich form (∂) and has the same structure of the matrix (4.79). Equation (4.80) can be rewritten in a different way to appear as a classical SDE,

$$d\mathfrak{q} = \frac{\nu_a}{4}\ \boldsymbol{\mathcal{Q}}(\mathfrak{q}) \circ d\mathbf{w}^a, \tag{4.81}$$

where $\boldsymbol{\mathcal{Q}}$ is the diffusion matrix,

$$\boldsymbol{\mathcal{Q}} = \begin{pmatrix} -\mathfrak{q}_1 & -\mathfrak{q}_2 & -\mathfrak{q}_3 \\ \mathfrak{q}_0 & -\mathfrak{q}_3 & \mathfrak{q}_2 \\ \mathfrak{q}_3 & \mathfrak{q}_0 & -\mathfrak{q}_1 \\ -\mathfrak{q}_2 & \mathfrak{q}_1 & \mathfrak{q}_0 \end{pmatrix}. \tag{4.82}$$

The Stratonovich ($\circ$) formulation has been adopted to preserve the properties of unit quaternions. To derive the SDE (4.81) in the Itô form, we can apply the classical transformation

between these two stochastic integral (with the observation that $\mathbf{w}^a$ has the form of $\sqrt{2}\times$ 3d-standard Brownian motion), such as the Itô formulation of Eq. (4.81) which is given by,

$$d\mathfrak{q}_i = \frac{\nu_a^2}{16}\sum_{j=0}^{3}\sum_{k=1}^{3}\mathcal{Q}_{jk}\frac{\partial \mathcal{Q}_{ik}}{\partial \mathfrak{q}_j}dt + \frac{\nu_a}{4}\mathcal{Q}_{ik}(\mathfrak{q})d\mathrm{w}_k^a = -\frac{3}{16}\nu_a^2\mathfrak{q}_i dt + \frac{\nu_a}{4}\mathcal{Q}_{ik}(\mathfrak{q})d\mathrm{w}_k^a. \tag{4.83}$$

The strategy presented above to solve a Brownian rotation in $SO(3)$ using unit quaternions is very general and can be applied in other contexts involving Brownian motion on a sphere, as well (Antoine et al. (1991); Krishna et al. (2000); Brillinger (2012)).

Equation (4.50) is a sub-part of a splitting algorithm, which means that we are interested in tracking the increment of rotations produced by the angular increment $d\mathbf{w}^a$. In this case, the employment of unit quaternions to reconstruct the rotation matrix corresponds to compute the incremental rotation associated to the Brownian rotation step of the algorithm. Indeed, the solution of Eq. (4.81) in time can be computed with respect to a fixed reference axis $\mathfrak{q}^{\mathrm{fix}}$ that can be arbitrarily chosen since we are interested in the incremental rotation matrix. Then, the orientation in the rotated framework, equivalent to Eq. (4.69), is given by,

$$\boldsymbol{p}_{ba}(t+\Delta t) = \mathscr{R}^{\Delta t}(\mathfrak{q})\boldsymbol{p}_{ba}(t), \tag{4.84}$$

where the rotation matrix is given by Eq. (4.76).

4.4.3.1 *Numerical scheme*

Numerically Eq. (4.83) has been discretised using a semi-implicit Euler–Maruyama scheme. Moreover, the reference frame has been fixed to $\mathfrak{q}^{\mathrm{fix}}$. The discretised version of Eq. (4.83) in $[0,T]$ with time step Δt and $t_{k+1} = t_k + \Delta t$, reads:

$$\begin{aligned}
\tilde{\mathfrak{q}}_{0,k+1} &= \big[\tilde{\mathfrak{q}}_{0,k} + \frac{\nu_a}{4}\big(-\tilde{\mathfrak{q}}_{1,k}\,\Delta\mathrm{w}_{1,k}^a - \tilde{\mathfrak{q}}_{2,k}\,\Delta\mathrm{w}_{2,k}^a - \tilde{\mathfrak{q}}_{3,k}\,\Delta\mathrm{w}_{3,k}^a\big)\big]\frac{1}{1+\frac{3}{16}\nu_a^2\Delta t}\\
\tilde{\mathfrak{q}}_{1,k+1} &= \big[\tilde{\mathfrak{q}}_{1,k} + \frac{\nu_a}{4}\big(\tilde{\mathfrak{q}}_{0,k}\,\Delta\mathrm{w}_{1,k}^a - \tilde{\mathfrak{q}}_{3,k}\,\Delta\mathrm{w}_{2,k}^a + \tilde{\mathfrak{q}}_{2,k}\,\Delta\mathrm{w}_{3,k}^a\big)\big]\frac{1}{1+\frac{3}{16}\nu_a^2\Delta t}\\
\tilde{\mathfrak{q}}_{2,k+1} &= \big[\tilde{\mathfrak{q}}_{2,k} + \frac{\nu_a}{4}\big(\tilde{\mathfrak{q}}_{3,k}\,\Delta\mathrm{w}_{1,k}^a + \tilde{\mathfrak{q}}_{0,k}\,\Delta\mathrm{w}_{2,k}^a - \tilde{\mathfrak{q}}_{1,k}\,\Delta\mathrm{w}_{3,k}^a\big)\big]\frac{1}{1+\frac{3}{16}\nu_a^2\Delta t}\\
\tilde{\mathfrak{q}}_{3,k+1} &= \big[\tilde{\mathfrak{q}}_{3,k} + \frac{\nu_a}{4}\big(-\tilde{\mathfrak{q}}_{2,k}\,\Delta\mathrm{w}_{1,k}^a + \tilde{\mathfrak{q}}_{1,k}\,\Delta\mathrm{w}_{2,k}^a + \tilde{\mathfrak{q}}_{0,k}\,\Delta\mathrm{w}_{3,k}^a\big)\big]\frac{1}{1+\frac{3}{16}\nu_a^2\Delta t}.
\end{aligned} \tag{4.85}$$

In order to preserve the unit constraint, the quaternion $\tilde{\mathfrak{q}}_{k+1}$ requires to be re-normalized at each time step,

$$\hat{\mathfrak{q}}_{k+1} = \frac{\tilde{\mathfrak{q}}_{k+1}}{\|\tilde{\mathfrak{q}}_{k+1}\|}. \tag{4.86}$$

In addition, we are going to fix in time $\tilde{\mathfrak{q}}_k = \mathfrak{q}^{\mathrm{fix}}$, since the solution of Eq. (4.85) involves an increment of the rotation. As said, the choice of fixing a reference quaternion is totally free: the simplest one consists of selecting the unitary quaternion $\mathfrak{q}^{\mathrm{fix}} = (1,0,0,0)$.

Furthermore, for this choice, the form of Eq. (4.85) is strongly simplified, leading to, rewriting in vector form in terms quaternion increments,

$$\begin{aligned}
&\big(\Delta\tilde{\mathfrak{q}}_{0,k+1};\,\Delta\tilde{\mathfrak{q}}_{1,k+1};\Delta\tilde{\mathfrak{q}}_{2,k+1};\,\Delta\tilde{\mathfrak{q}}_{3,k+1};\,\Delta\tilde{\mathfrak{q}}_{4,k+1}\big)^{\mathsf{T}}\\
&\qquad = \Big(1;\,\frac{\nu_a}{4}\Delta\mathrm{w}_{1,k}^a;\,\frac{\nu_a}{4}\Delta\mathrm{w}_{2,k}^a;\,\frac{\nu_a}{4}\Delta\mathrm{w}_{3,k}^a\Big)^{\mathsf{T}}\frac{1}{1+\frac{3}{16}\nu_a^2\Delta t}
\end{aligned} \tag{4.87}$$

In order to preserve the unit constraint, the quaternion $\Delta\tilde{\mathfrak{q}}_{k+1}$ requires re-normalisation at each time step, $\Delta\hat{\mathfrak{q}}_{k+1} = \Delta\tilde{\mathfrak{q}}_{k+1}/\|\Delta\tilde{\mathfrak{q}}_{k+1}\|$.

Moreover, as we did for the direct scheme, the error regarding norm convergence, as detailed in Appendix B.5, in this case reads:

$$\mathbb{E}\|\Delta\tilde{\mathfrak{q}}_{k+1}\|^2 = 1 - \left(\frac{3}{16}\right)^2 \nu_a^4\,\Delta t^2 + \mathcal{O}(\Delta t^3), \tag{4.88}$$

where the error converges with $\approx \Delta t^2$, and with a constant factor which is smaller than that found using a the direct schemes in expression (4.68).

After solving Eq. (4.87) and re-normalising at each time step, the rotation matrix (4.76) is computed and the orientation vector is updated as:

$$\widehat{\boldsymbol{p}}_{ba,k+1} = \mathscr{R}^{\Delta t}(\Delta\hat{\mathfrak{q}}_{k+1})\tilde{\boldsymbol{p}}_{ba,k}. \tag{4.89}$$

where in this case at each time step the updated orientation vector it is already normalized, i.e. $\|\widehat{\boldsymbol{p}}_{ba,k+1}\| = 1$.

The scheme presented above converges in strong and weak sense. We show in Fig. 4.4 the strong error as a function of the time step Δt, for different values of τ_η; in particular, Fig. 4.4a shows the behaviour of the first component $p_{ba,1}$ (for simplicity, since all the components act in the same manner), in Fig. 4.4b we plot the first component of the vector $\phi_{\perp p_{ba},1}$ (for the same reason) and in Fig. 4.4c the scalar quantity $\phi_{\parallel p_{ba}}$. The three quantities converge in a strong sense but with an error that is driven by the amplitude of the diffusion coefficient ($\nu_a \approx \sqrt{1/\tau_\eta}$). In particular, the error decreases proportionally to $1/\tau_\eta$. As we can observe in the results, the value $\tau_\eta = 0.01$ represents a limit-case for which the SDE becomes difficult to solve.

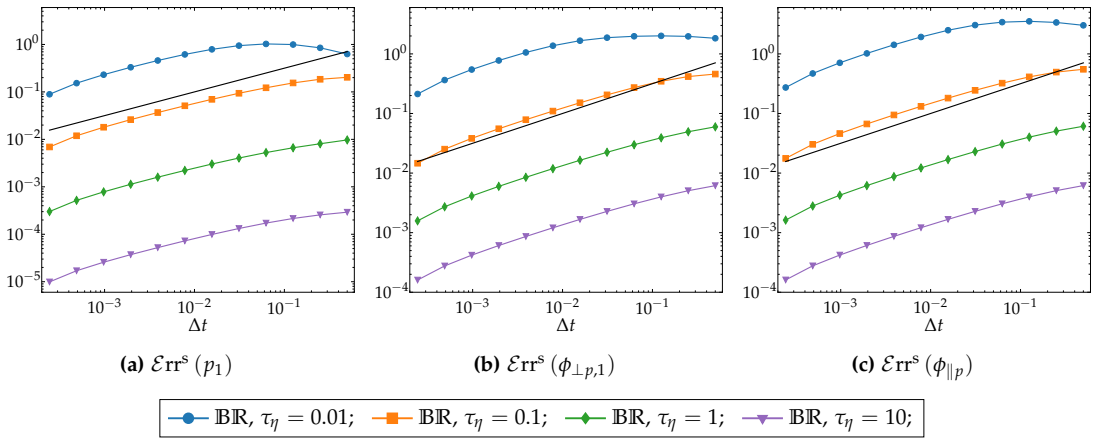

Figure 4.4: Stochastic rotation sub-step ($\mathbb{BR}$): Strong error ($\mathcal{E}\mathrm{rr}^{\mathrm{s}}$) of the numerical scheme in Eq. (4.89) against the time step Δt for different values of τ_η. In (a) the first component of $\boldsymbol{p}_{ba}$, (b) the first component $\phi_{\perp p_{ba}}$ of tumbling and (c) the spinning $\phi_{\parallel p_{ba}}$. Black line indicates the slope 1/2; and the initial condition of particle orientation is $\boldsymbol{p}_a^0 = (1,0,0)$.

Moving to consider the weak error as a function of Δt as shown in Fig. 4.5, we can observe that the behaviour of the weak error strongly depends on the parameter τ_η. In Fig. 4.5a the first component of the moment $\mathbb{E}[\boldsymbol{p}_{ba}]$ converges with a slope 1 as expected by the employment of first order Euler–Maruyama scheme, choosing as initial condition for particle orientation $\boldsymbol{p}_a^0 = (1,0,0)$. The same behaviour is observed for the higher moments $\mathbb{E}[p_{ba,1}^2]$, $\mathbb{E}[p_{ba,1}^3]$ in

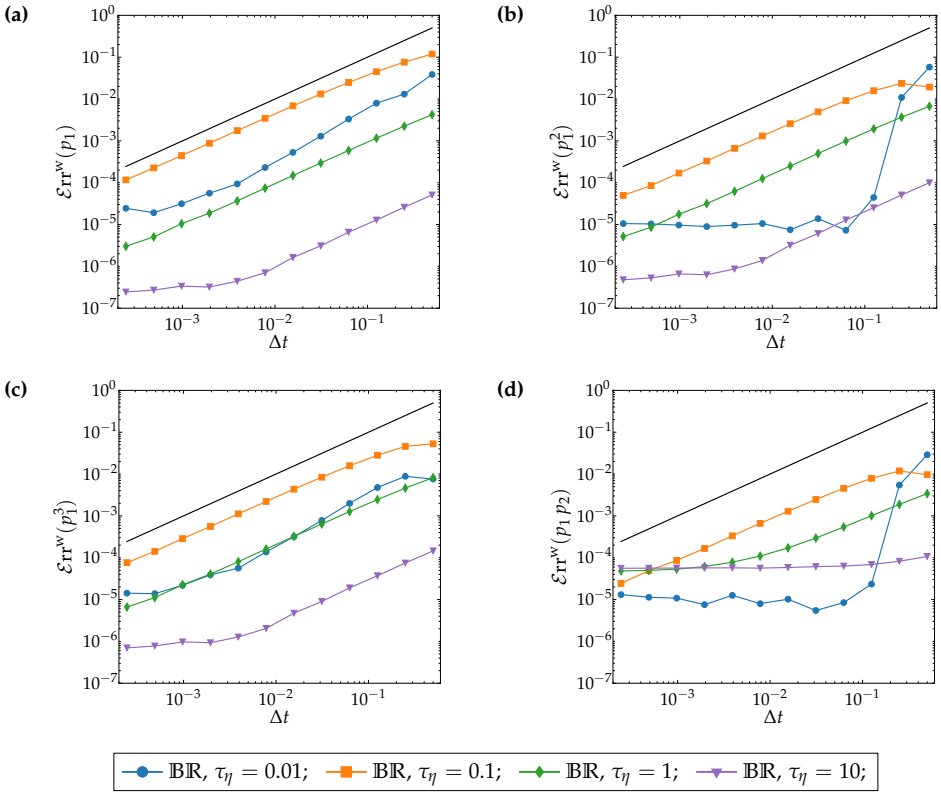

Figure 4.5: Weak error ($\mathcal{E}\mathrm{rr}^{\mathrm{w}}$) for the stochastic rotation sub-step ($\mathbb{BR}$) in Eq. (4.89) against the time step Δt for different values of τ_η. In (a), (b), and (c) the first three moments of the first component $p_{ba,1}$ for an initial condition of particle orientation $\boldsymbol{p}_a^0 = (1,0,0)$. In (d) the second cross moment $p_{ba,1}p_{ba,2}$ is shown using a different initial condition $\boldsymbol{p}_b^0 = (1,1,1)/\sqrt{3}$. Black line indicates the slope 1.

Fig. 4.5b and 4.5c respectively. In order to show the weak convergence of the cross moment $\mathbb{E}[p_{ba,1}p_{ba,2}]$, presented in Fig. 4.5d, the initial condition has been fixed to $\boldsymbol{p}_b^0 = (1,1,1)/\sqrt{3}$. In fact, by choosing the initial condition $\boldsymbol{p}_a^0 = (1,0,0)$, the cross moments are identically zero (Eq. (4.59)), which means that we are evaluating only the Monte Carlo error of the performing test.

As mentioned before, there is a strong impact from the amplitude of diffusion coefficient $\nu_a \approx \sqrt{1/\tau_\eta}$. In terms of error, the scheme reacts in a special manner for the critical value of $\tau_\eta = 0.01$. We would expect that the error convergence for $\tau_\eta = 0.01$ (blue line) would have been above the error convergence for $\tau_\eta = 0.1$ (orange line), which is not the case. A possible explanation is that the analytical solution overcomes the machine precision since we need to compute an exponential of a very small number; for instance, considering the exact solution for $\mathbb{E}[p_{ba,1}^2]$ (Eq. (4.60)) leads to the evaluation of $\sim \exp(-50)$. This brings some numerical drawbacks since we are computing an error which is very close to zero. Moreover, this behaviour is more amplified in even moments with respect to odd ones, as Eqs. (4.58)-(4.61) show, for the same reason.

A perspective, in order to better understand this behaviour is the investigation of the variance of the weak error that would shed light on these results.

4.4.3.2 *Remarks about 'Direct' and Quaternion scheme*

The strong and weak numerical convergence for the 'direct' scheme in Eq. (4.67) and the quaternion scheme in Eq. (4.89) seems to be very similar both in order of convergence and magnitude of the error. The quaternion scheme perform slightly better that the direct scheme, regarding the magnitude of the weak error for $\tau_\eta = 0.01$ and large Δt

Indeed, the performance and any possible distinction of the direct scheme with respect to the employment of more sophisticated quaternions dynamics should not be limited to the observation of strong and weak convergence of each component of the unitary vector $\boldsymbol{p}$ and consequently to the projected quantities $\phi_{\perp p_{ba}}$, $\phi_{\parallel p_{ba}}$. In fact, the renormalization step, in some sense, could mask some important differences between these to schemes.

In order to empathised the better performance of quaternions against a direct discretisation of Eq. (4.67), it is important to evaluate the sensibility of these two schemes to perform the rotation before the renormalisation step. This consists to compute the symmetric path-wise quantity $\mathbb{E}[\max_{0\leq t\leq T}(1-\|\tilde{\boldsymbol{n}}(t)\|)^2]$, where the vector $\tilde{\boldsymbol{n}}$ with $\|\tilde{\boldsymbol{n}}\| \neq 1$, corresponds to $\tilde{\boldsymbol{p}}_{ba,k+1}$ for the direct scheme in Eq. (4.67) and $\hat{\mathfrak{q}}_{k+1}$ to quaternions scheme in Eq. (4.85), respectively. The path-wise error with respect to the unitary norm is shown in Fig. 4.6 (left panel), choosing a final time $T = 10$, as a function of time step Δt. For the choice of $\tau_\eta = 0.01$ (i.e., a small diffusion coefficient, $\nu_a \approx \sqrt{1/\tau_\eta}$) and sufficiently large time step $\Delta t \leq 0.03$ the error for the direct scheme is one order of magnitude grater that the quaternion scheme, that shed the light of one advantages in using quaternions. Even better case, in terms of magnitude of the error, is represented by choosing $\tau_\eta = 0.1$, where the quaternion scheme converges for all values of Δt considered. This shows that the rotation performed with the quaternion scheme introduces a small error before the renormalization step.

Finally, in order to confirm the rate of convergence found in the analytical expression (4.68) and (4.88), we show the $\mathbb{E}[(1-\|\tilde{\boldsymbol{n}}(t)\|)^2]$ in Fig. 4.6 (right panel), where the slope of black line is 2.

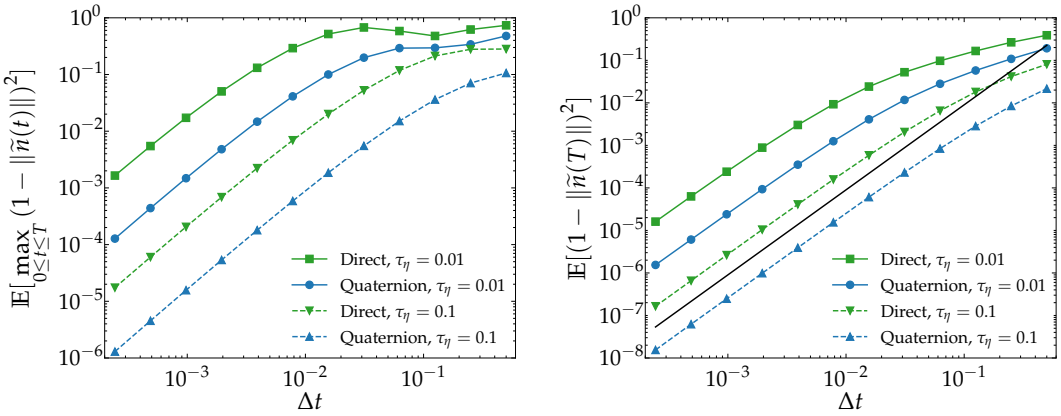

Figure 4.6: Left panel: Path-wise error for the norm of the non-normalised vector $\tilde{\boldsymbol{n}}$ against the time step Δt for different values of τ_η. The vector $\tilde{\boldsymbol{n}}$ with $\|\hat{\boldsymbol{n}}\| \neq 1$, corresponds to $\tilde{\boldsymbol{p}}_{ba,k+1}$ for the direct scheme in Eq. (4.67) and $\hat{\mathfrak{q}}_{k+1}$ to quaternions scheme in Eq. (4.85), respectively. Right panel: Mean error convergence against the time step Δt for different values of τ_η. Simulation performed with an initial condition a $\boldsymbol{p}_a^0 = (1,0,0)$, number of particles $N_p = 10^6$, time step $\Delta t = 2^{-h}$ with $h = 1,\ldots,12$, final time $T = 10$ and time scale parameter $\tau_\eta = 0.01, 0.1$. Black line indicates the slope 2.

The investigation of the scheme at long-time behaviour it is not enough discriminant for these two schemes since they converges naturally on the uniform measure on the sphere. Therefore, another important aspect, it is the behaviour of the marginal probability density functions $\mathcal{P}(p_i)$

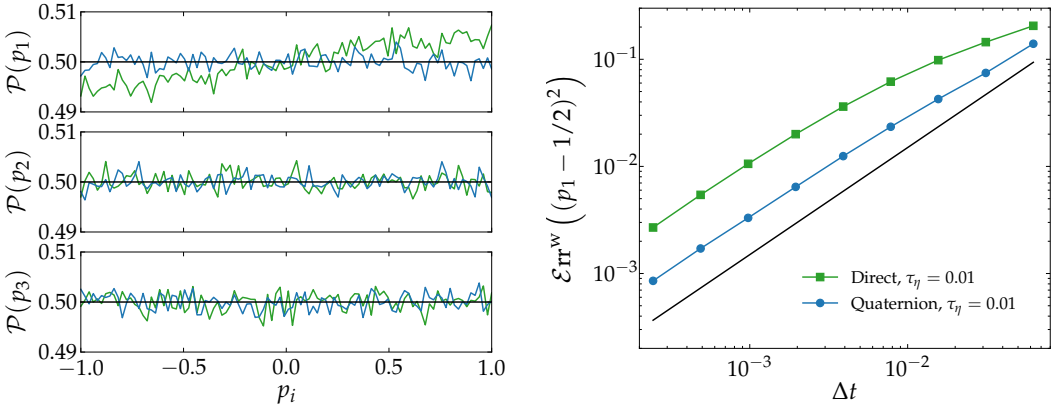

Figure 4.7: Left panel: Marginal probability density function $\mathcal{P}(p_i)$ for the direct and quaternion scheme. Black lines the three marginal distributions at the stationary state have the same value $\mathcal{P}(p_1) = \mathcal{P}(p_2) = \mathcal{P}(p_3) = 1/2$. Simulation performed with an initial condition a $\boldsymbol{p}_a^0 = (1,0,0)$, number of particles $N_p = 10^6$, time step $\Delta t = 0.1$, final time $T = 0.1$ and time scale parameter $\tau_\eta = 0.01$. Right panel: Weak error for the test function $f = (p_1 - 1/2)^2$ as a function of Δt. Simulation performed with an initial condition a $\boldsymbol{p}_a^0 = (1,0,0)$, number of particles $N_p = 10^6$, time step $\Delta t = 2^{-h}$ with $h = 4,\ldots,12$, final time $T = 0.0625$ and time scale parameter $\tau_\eta = 0.01$. Black line indicates the slope 1.

in the short time. In the case of uniform rotation on a sphere, the three marginal distribution at the stationary state have the same value $\mathcal{P}(p_1) = \mathcal{P}(p_2) = \mathcal{P}(p_3) = 1/2$. Figure 4.7 (left panel) shows the marginal distributions at final time $T = 0.1$ starting from an initial condition $\boldsymbol{p}_a^0 = (1,0,0)$ and $\tau_\eta = 0.01$. The direct scheme holds for long time the memory about the initial condition, and as a result the $\mathcal{P}(p_1)$ is not uniform being asymmetric. Conversely, the scheme, which operates using quaternions, well reproduces the uniform stationary distribution $1/2$. This feature could be interesting when the study of the orientation stochastic model it is no longer in the framework of HIT flows, but in unstationary regimes. To underline the difference, observed in the marginals distributions, the weak error for the test function $f = (p_1 - 1/2)^2$ is shown in Fig.4.7 (right panel) for a final time $T = 0.0625$ and $\tau_\eta = 0.01$. The magnitude of the weak error for the direct scheme is four times larger than the quaternion scheme.

4.4.4 *Discretisation of the Brownian Stretching*

Here we will analyse the orientation given by the symmetric part of the velocity gradient fluctuations Eq. (4.49), that we recall to be,

$$d\boldsymbol{p}_{bs}(t) = -\frac{\nu_s^2}{2}\Lambda^2 \boldsymbol{p}_{bs} dt + \nu_s \Lambda \left(d\mathbf{W}^s \, \boldsymbol{p}_{bs} - \boldsymbol{p}_{bs} \boldsymbol{p}_{bs}^{\mathsf{T}} \, d\mathbf{W}^s \, \boldsymbol{p}_{bs} \right).$$

Equation (4.49) is a sub-part of the splitting algorithm and requires the design of a numerical scheme. In the continuous case the unitary norm is intrinsically preserved by the non-linear term $\boldsymbol{p}_{bs}\boldsymbol{p}_{bs}^{\mathsf{T}} \, d\mathbf{W}^s \, \boldsymbol{p}_{bs}$; on the other hand this constraint is never satisfied in the discretised version since this term requires to be explicitly solved. Moreover, the presence of non-linearities in the diffusion part introduces a further difficulty related *a priori* to the non-globally Lipschitz diffusion coefficient as investigated by Bossy et al. (2021) and references therein.

The three components of the Eq. (4.49) are rewritten as,

$$
\begin{aligned}
dp_{bs,1} =& -\frac{\nu_s^2}{2}\Lambda^2 p_{bs,1}dt + \frac{\nu_s}{2}\Lambda\Big[2p_{bs,1}(1-p_{bs,1}^2)dW_1 - 2p_{bs,1}p_{bs,2}^2 dW_5 - 2p_{bs,1}p_{bs,3}^2 dW_9 \\
&+ p_{bs,2}(1-2p_{bs,1}^2)(dW_2+dW_4) + p_{bs,3}(1-2p_{bs,1}^2)(dW_3+dW_7) \\
&- 2p_{bs,1}p_{bs,2}p_{bs,3}(dW_6+dW_8)\Big] \\
dp_{bs,2} =& -\frac{\nu_s^2}{2}\Lambda^2 p_{bs,2}dt + \frac{\nu_s}{2}\Lambda\Big[2p_{bs,2}(1-p_{bs,2}^2)dW_5 - 2p_{bs,2}p_{bs,1}^2 dW_1 - 2p_{bs,2}p_{bs,3}^2 dW_9 \\
&+ p_{bs,1}(1-2p_{bs,2}^2)(dW_2+dW_4) + p_{bs,3}(1-2p_{bs,2}^2)(dW_6+dW_8) \\
&- 2p_{bs,1}p_{bs,2}p_{bs,3}(dW_3+dW_7)\Big] \\
dp_{bs,3} =& -\frac{\nu_s^2}{2}\Lambda^2 p_{bs,3}dt + \frac{\nu_s}{2}\Lambda\Big[2p_{bs,3}(1-p_{bs,3}^2)dW_9 - 2p_{bs,3}p_{bs,1}^2 dW_1 - 2p_{bs,3}p_{bs,2}^2 dW_5 \\
&+ p_{bs,1}(1-2p_{bs,3}^2)(dW_3+dW_7) + p_{bs,2}(1-2p_{bs,3}^2)(dW_6+dW_8) \\
&- 2p_{bs,1}p_{bs,2}p_{bs,3}(dW_2+dW_4)\Big]
\end{aligned}
\tag{4.90}
$$

An alternative approach to describe the orientation in Eq. (4.49) is to consider the linear evolution of Eq. (B.8), equivalent to Eq. (4.16), but rewritten in terms of Wiener matrix $\mathbf{W}_t$, and the subsequent re-normalisation, to preserve the unitary norm. We recall that Eq. (B.8) involves both the symmetric and the antisymmetric contributions; for this sub-part of the splitting scheme, we are interested only on the symmetric part of the velocity gradient fluctuations.

Isolating the symmetric contribution from Eq. (B.8), we have

$$
d\boldsymbol{q}_{bs} = \frac{5}{6}\nu_s^2\Lambda^2\boldsymbol{q}_{bs}dt - \frac{\nu_s}{3}\Lambda\mathrm{Tr}(d\mathbf{W})\boldsymbol{q}_{bs} + \nu_s\Lambda d\mathbf{W}^s\boldsymbol{q}_{bs}, \tag{4.91}
$$

Rewritten in components,

$$
\begin{aligned}
dq_{bs,1} =& \frac{5}{6}\nu_s^2\Lambda^2 q_{bs,1} - \frac{\nu_s}{3}\Lambda q_{bs,1}\left(dW_1+dW_5+dW_9\right) \\
&+ \frac{\nu_s}{2}\Lambda\left(2q_{bs,1}dW_1 + q_{bs,2}(dW_2+dW_4) + q_{bs,3}(dW_3+dW_7)\right) \\
dq_{bs,2} =& \frac{5}{6}\nu_s^2\Lambda^2 q_{bs,2} - \frac{\nu_s}{3}\Lambda q_{bs,2}\left(dW_1+dW_5+dW_9\right) \\
&+ \frac{\nu_s}{2}\Lambda\left(q_{bs,1}(dW_2+dW_4) + 2q_{bs,2}dW_5 + q_{bs,3}(dW_6+dW_8)\right) \\
dq_{bs,3} =& \frac{5}{6}\nu_s^2\Lambda^2 q_{bs,3} - \frac{\nu_s}{3}\Lambda q_{bs,3}\left(dW_1+dW_5+dW_9\right) \\
&+ \frac{\nu_s}{2}\Lambda\left(q_{bs,1}(dW_3+dW_7) + q_{bs,2}(dW_6+dW_8) + 2q_{bs,3}dW_9\right).
\end{aligned}
\tag{4.92}
$$

The orientation is given by coupling Eq. (4.91) with the normalisation $\boldsymbol{p}_{bs}(t) = \boldsymbol{q}_{bs}(t)/\|\boldsymbol{q}_{bs}(t)\|$. For numerical stability reason, we anticipate that Eq. (4.91) requires the employment of an explicit scheme in order to prevent the appearance of singularities coming from the positive sign in the drift term. Indeed, the mean reverting term in Eq. (4.91) and (4.49) have opposite sign; this suggests that a semi-implicit scheme is not indicated for the discretisation of Eq. (4.91).

4.4.4.1 *Numerical scheme*

Two different numerical schemes are investigated for Eq. (4.90) and (4.92). Numerically, a semi-implicit Euler–Maruyama scheme has been used to discretise Eq. (4.90). In this case, starting with an initial condition $\widehat{\boldsymbol{p}}_{bs,0}$ such that $\|\widehat{\boldsymbol{p}}_{bs,0}\| = 1$, the discretised version of Eq. (4.90) in $[0, T]$ with time step Δt and $t_{k+1} = t_k + \Delta t$, reads:

$$
\begin{aligned}
\tilde{p}_{bs(1),k+1} = &\Big[\widehat{p}_{bs(1),k} \\
&+ \frac{\nu_s}{2}\Lambda\big[2\widehat{p}_{bs(1),k}(1-\widehat{p}^2_{bs(1),k})\Delta W_{1,k} - 2\widehat{p}_{bs(1),k}\widehat{p}^2_{bs(2),k}\Delta W_{5,k} - 2\widehat{p}_{bs(1),k}\widehat{p}^2_{bs(3),k}\Delta W_{9,k} \\
&+ \widehat{p}_{bs(2),k}(1-2\widehat{p}^2_{bs(1),k})(\Delta W_{2,k}+\Delta W_{4,k}) + \widehat{p}_{bs(3),k}(1-2\widehat{p}^2_{bs(1),k})(\Delta W_{3,k}+\Delta W_{7,k}) \\
&- 2\widehat{p}_{bs(1),k}\widehat{p}_{bs(2),k}\widehat{p}_{bs(3),k}(\Delta W_{6,k}+\Delta W_{8,k})\big]\Big]\frac{1}{1+\frac{\nu_s^2}{2}\Lambda^2\Delta t} \\
\tilde{p}_{bs(2),k+1} = &\Big[\widehat{p}_{bs(2),k} \\
&+ \frac{\nu_s}{2}\Lambda\Big[2\widehat{p}_{bs(2),k}(1-\widehat{p}^2_{bs(2),k})\Delta W_{5,k} - 2\widehat{p}_{bs(2),k}\widehat{p}^2_{bs(1),k}\Delta W_{1,k} - 2\widehat{p}_{bs(2),k}\widehat{p}^2_{bs(3),k}\Delta W_{9,k} \\
&+ \widehat{p}_{bs(1),k}(1-2\widehat{p}^2_{bs(2),k})(\Delta W_{2,k}+\Delta W_{4,k}) + \widehat{p}_{bs(3),k}(1-2\widehat{p}^2_{bs(2),k})(\Delta W_{6,k}+\Delta W_{8,k}) \\
&- 2\widehat{p}_{bs(1),k}\widehat{p}_{bs(2),k}\widehat{p}_{bs(3),k}(\Delta W_{3,k}+\Delta W_{7,k})\Big]\Big]\frac{1}{1+\frac{\nu_s^2}{2}\Lambda^2\Delta t} \\
\tilde{p}_{bs(3),k+1} = &\Big[\widehat{p}_{bs(3),k} \\
&+ \frac{\nu_s}{2}\Lambda\Big[2\widehat{p}_{bs(3),k}(1-\widehat{p}^2_{bs(3),k})\Delta W_{9,k} - 2\widehat{p}_{bs(3),k}\widehat{p}^2_{bs1}\Delta W_{1,k} - 2\widehat{p}_{bs(3),k}\widehat{p}^2_{bs(2),k}\Delta W_{5,k} \\
&+ \widehat{p}_{bs(1),k}(1-2\widehat{p}^2_{bs(3),k})(\Delta W_{3,k}+\Delta W_{7,k}) + \widehat{p}_{bs(2),k}(1-2\widehat{p}^2_{bs(3),k})(\Delta W_{6,k}+\Delta W_{8,k}) \\
&- 2\widehat{p}_{bs(1),k}\widehat{p}_{bs(2),k}\widehat{p}_{bs(3),k}(\Delta W_{2,k}+\Delta W_{4,k})\Big]\Big]\frac{1}{1+\frac{\nu_s^2}{2}\Lambda^2\Delta t},
\end{aligned}
\tag{4.93}
$$

where at each time step we re-normalize and obtain $\widehat{\boldsymbol{p}}_{bs,k+1} = \tilde{\boldsymbol{p}}_{bs,k+1}/\|\tilde{\boldsymbol{p}}_{bs,k+1}\|$.

As detailed in Appendix B.5, for this scheme we have:

$$
\mathbb{E}\|\tilde{\boldsymbol{p}}_{bs,k+1}\|^2 = 1 - \frac{\nu_s^4}{4}\Lambda^4\Delta t^2 + \mathcal{O}(\Delta t^3). \tag{4.94}
$$

This error converges with the same order of expression (4.88) for the quaternion.

Numerically, an explicit Euler–Maruyama scheme has been used to discretise Eq (4.91). By considering as initial condition $\widehat{\boldsymbol{q}}_{bs,0}$ such that $\|\widehat{\boldsymbol{q}}_{bs,0}\| = 1$, the discretised version of Eq. (4.91) in $[0, T]$ with time step Δt and $t_{k+1} = t_k + \Delta t$, reads:

$$
\begin{aligned}
\tilde{q}_{bs(1),k+1} &= \left(1+\frac{5}{6}\nu_s\Lambda^2\Delta t\right)\widehat{q}_{bs(1),k} - \frac{\nu_s}{3}\Lambda\widehat{q}_{bs(1),k}\left(\Delta W_{1,k}+\Delta W_{5,k}+\Delta W_{9,k}\right) \\
&\quad + \frac{\nu_s}{2}\Lambda\left[2\widehat{q}_{bs(1),k}\Delta W_{1,k} + \widehat{q}_{bs(2),k}(\Delta W_{2,k}+\Delta W_{4,k}) + \widehat{q}_{bs(3),k}(\Delta W_{3,k}+\Delta W_{7,k})\right] \\
\tilde{q}_{bs(2),k+1} &= \left(1+\frac{5}{6}\nu_s\Lambda^2\Delta t\right)\widehat{q}_{bs(2),k} - \frac{\nu_s}{3}\Lambda\widehat{q}_{bs(2),k}\left(\Delta W_{1,k}+\Delta W_{5,k}+\Delta W_{9,k}\right) \\
&\quad + \frac{\nu_s}{2}\Lambda\left[\widehat{q}_{bs(1),k}(\Delta W_{2,k}+\Delta W_{4,k}) + 2\widehat{q}_{bs(2),k}\Delta W_{5,k} + \widehat{q}_{bs(3),k}(\Delta W_{6,k}+\Delta W_{8,k})\right] \\
\tilde{q}_{bs(3),k+1} &= \left(1+\frac{5}{6}\nu_s\Lambda^2\Delta t\right)\widehat{q}_{bs(3),k} - \frac{\nu_s}{3}\Lambda\widehat{q}_{bs(3),k}\left(\Delta W_{1,k}+\Delta W_{5,k}+\Delta W_{9,k}\right) \\
&\quad + \frac{\nu_s}{2}\Lambda\left[\widehat{q}_{bs(1),t_k}(\Delta W_{3,k}+\Delta W_{7,k}) + \widehat{q}_{bs(2),k}(\Delta W_{6,k}+\Delta W_{8,k}) + 2\widehat{q}_{bs(3),k}\Delta W_{9,k}\right]
\end{aligned}
\tag{4.95}
$$

and the orientation will be as $\widehat{\boldsymbol{p}}_{bs,k+1} = \tilde{\boldsymbol{q}}_{bs,k+1}/\|\tilde{\boldsymbol{q}}_{bs,k+1}\| = \widehat{\boldsymbol{q}}_{bs,k+1}$.

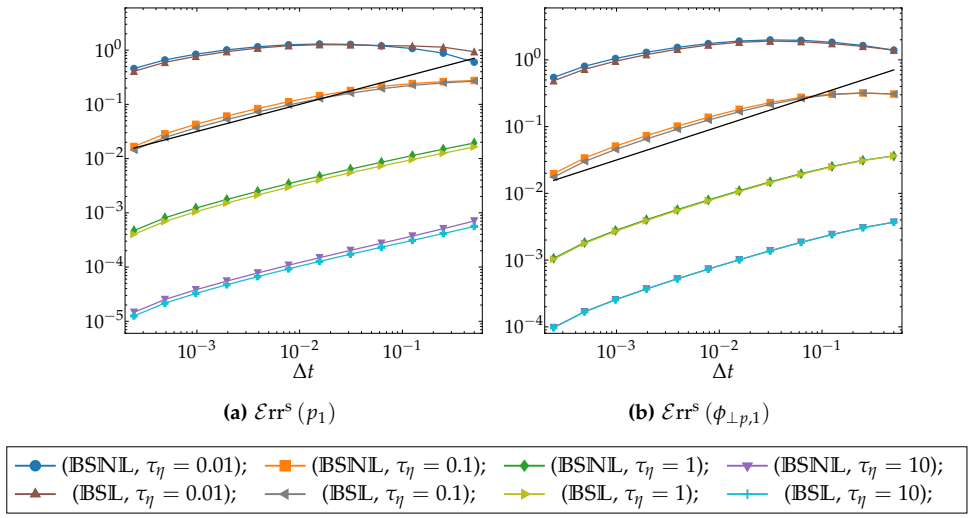

(a) $\mathcal{E}\mathrm{rr}^{\mathrm{s}}(p_1)$ **(b)** $\mathcal{E}\mathrm{rr}^{\mathrm{s}}(\phi_{\perp p,1})$

Figure 4.8: Stochastic stretching sub-step (BS): Strong error ($\mathcal{E}\mathrm{rr}^{\mathrm{s}}$) of the numerical scheme in Eq. (4.93) (BSNL) and Eq. (4.95) (BSL) against the time step Δt for different values of τ_η. In (a) the first component of $\boldsymbol{p}_{bs}$, (b) the first component of the vector $\boldsymbol{\phi}_{\perp p_{bs}}$ of tumbling. Black line indicates the slope 1/2; and the initial condition of particle orientation is $\boldsymbol{p}_a^0 = (1,0,0)$.

Figure 4.8 shows the strong error for the schemes Eq. (4.93) and (4.95) as a function of the time step Δt, for different values of τ_η. The two schemes have the same behaviour for the first component $p_{bs,1}$ and $\phi_{\perp p_{bs},1}$, as shown in Fig. 4.8a and 4.8b respectively. Furthermore, the order of convergence for the values of $\tau_\eta = 0.1, 1, 10$ is 1 following the prediction of the classical Euler–Maruyama scheme. Conversely, the value of $\tau_\eta = 0.01$ highlights the limit of the scheme for these particular choices of Δt. Indeed, for this value of τ_η the SDE (4.49) becomes stiff and the time step Δt needs to be adapted to this particular choice of time scale parameter. Here we remark that the stretching part does not contribute to spin the particles around its symmetric axis as can be seen from Eq. (4.23), i.e. $\phi_{\parallel p_{bs}} = 0$.

The weak error as a function of Δt is shown in Fig. 4.9; we can observe that the behaviour of the two schemes is the same, as shown for the strong error, with an order of convergence for the weak error of 1. The first component of the moment $\mathbb{E}[\boldsymbol{p}_{bs}]$ is visible in Fig. 4.9a for the initial condition of particle orientation $\boldsymbol{p}_a^0 = (1,0,0)$: we can observe a strong dependence on the τ_η parameter. Moreover, for $\Delta t > 0.01$ the behaviour of the two schemes results to be slightly different for $\tau_\eta = 0.01$. The same behaviour is observed for the higher moments $\mathbb{E}[p_{bs,1}^2]$, $\mathbb{E}[p_{bs,1}^3]$ in Fig. 4.9b and 4.9c respectively. In order to show the weak convergence of the cross moment $\mathbb{E}[p_{bs,1}p_{bs,2}]$, shown in Fig. 4.9d, the initial condition has been fixed to $\boldsymbol{p}_b^0 = (1,1,1)/\sqrt{3}$.

As remarked for the weak convergence of the Brownian rotation part (Fig. 4.5), we still notice a strong influence of the amplitude of the diffusion coefficient $\nu_s \approx \sqrt{1/\tau_\eta}$. However, in this case, a less marked effect on computing the exponential of very small numbers is present with respect to the previous results; in fact, considering the exact solution for $\mathbb{E}[p_{bs,1}^2]$ (Eq. (4.60)), leads to the evaluation of $\sim \exp(-15)$ instead of $\sim \exp(-50)$, as remarked in the previous case. A special case is represented by the convergence of $\mathbb{E}[p_{bs,1}p_{bs,2}]$ for $\tau_\eta = 10$, where the magnitude of the error is of the same order of Monte Carlo using as initial condition $\boldsymbol{p}_b^0$, and to observe the convergence of order 1 the number of particles N_p should be significantly increased.

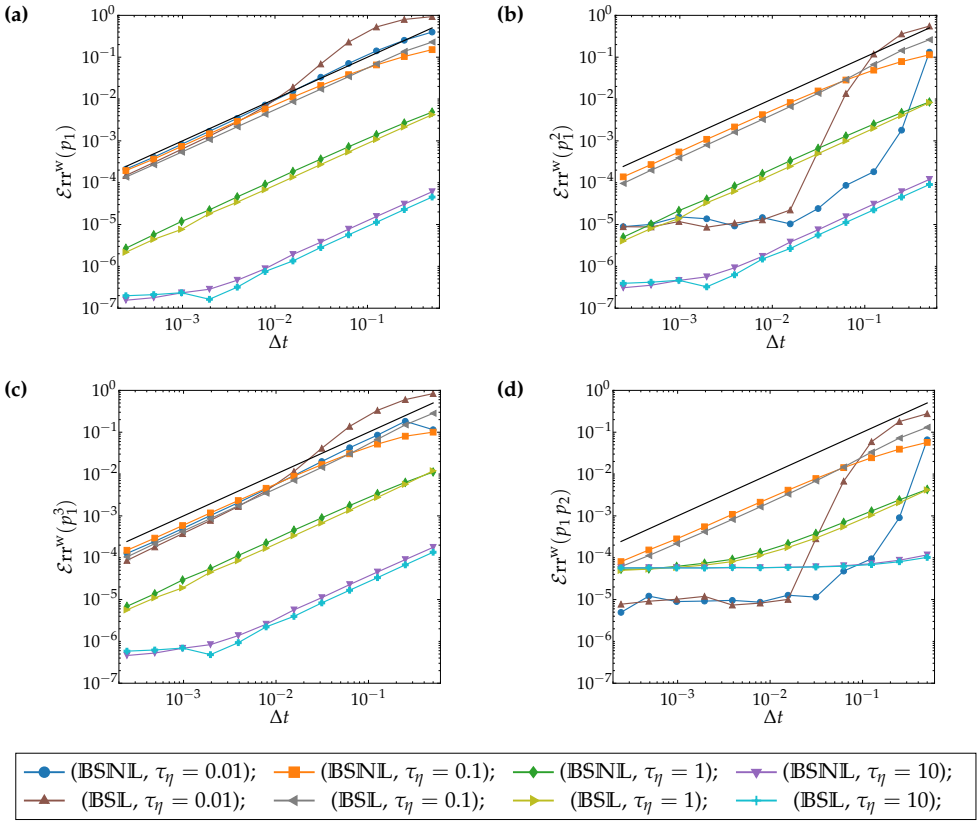

Figure 4.9: Stochastic stretching sub-step (𝔹𝕊): Weak error ($\mathcal{E}\mathrm{rr}^{\mathrm{w}}$) of the numerical scheme in Eq. (4.93) (𝔹𝕊ℕ𝕃) and Eq. (4.95) (𝔹𝕊𝕃) against the time step Δt for different values of τ_η. In (a), (b), and (c) the first three moments of the first component $\boldsymbol{p}_{bs}$ for an initial condition of particle orientation $\boldsymbol{p}_a^0 = (1,0,0)$. In (d) the second cross moment $p_{bs,1}p_{bs,2}$ is shown using a different initial condition $\boldsymbol{p}_b^0 = (1,1,1)/\sqrt{3}$. Black line indicates the slope 1.

4.4.5 *Splitting scheme for HIT*

In the previous Sections 4.4.3 and 4.4.4 a suitable numerical scheme for Brownian rotation and stretching sub-parts of the splitting, and the analysis of weak and strong convergence have been presented.

The scope of this section is to investigate the accuracy of the splitting algorithm in a strong and weak sense using the Lie–Trotter composition in Eq. (4.52), in the case of HIT, where the mean contribution is set to zero, i.e. $\mathcal{L}_s$ and $\mathcal{L}_a$ are not present. This simplification of the original problem is fully justified since the analytical solution for moments in Eqs. (4.58)-(4.61) can be used to study exactly the weak convergence without resorting to a method of manufactured numerical solution. Furthermore, we are mainly interested on the numerical behaviour of the stochastic contribution in Eq. (4.17) which results to be much more delicate to treat numerically compared to its deterministic counterpart. Setting to zero the mean part in Eq. (4.52) and expliciting the operators $\mathcal{L}_{bs}$ and $\mathcal{L}_{ba}$, the splitting algorithm reads,

$$\begin{cases} d\boldsymbol{p}_{bs}(t) = -\dfrac{\nu_s^2}{2}\Lambda^2\boldsymbol{p}_{bs}dt + \nu_s\Lambda\left(d\mathbf{W}^s\,\boldsymbol{p}_{bs} - \boldsymbol{p}_{bs}\boldsymbol{p}_{bs}^{\mathsf{T}}\,d\mathbf{W}^s\,\boldsymbol{p}_{bs}\right) & \text{with } \boldsymbol{p}_{bs}(t_k) = \boldsymbol{p}(t_k), \\ d\boldsymbol{p}_{ba}(t) = -\dfrac{\nu_a^2}{2}\boldsymbol{p}_{ba}dt + \nu_a\boldsymbol{p}_{ba}d\mathbf{W}^a. & \text{with } \boldsymbol{p}_{ba}(t_k) = \boldsymbol{p}_{bs}(t_{k+1}); \end{cases} \tag{4.96}$$

then the solution at later time steps is given by $\boldsymbol{p}(t_{k+1}) = \boldsymbol{p}_{ba}(t_{k+1})$. The order of advancement of the two schemes is the one presented in Eq. (4.96). Early preliminary tests showed that the results in time of the moments by changing the order of operations, i.e. performing first the Brownian rotation and then the Brownian stretching, do not affect final results. For sake of clarity, in this study the strong and weak convergence by changing the order of operations has not been analysed. We argue that the covariance matrix computed by commuting the matrices $\mathbf{W}^s$ and $\mathbf{W}^a$ is always zero due to the intrinsic structure of the symmetric and antisymmetric construction of the matrix $\boldsymbol{W}$, which could explain the insensitivity under the change of the order of the operations.

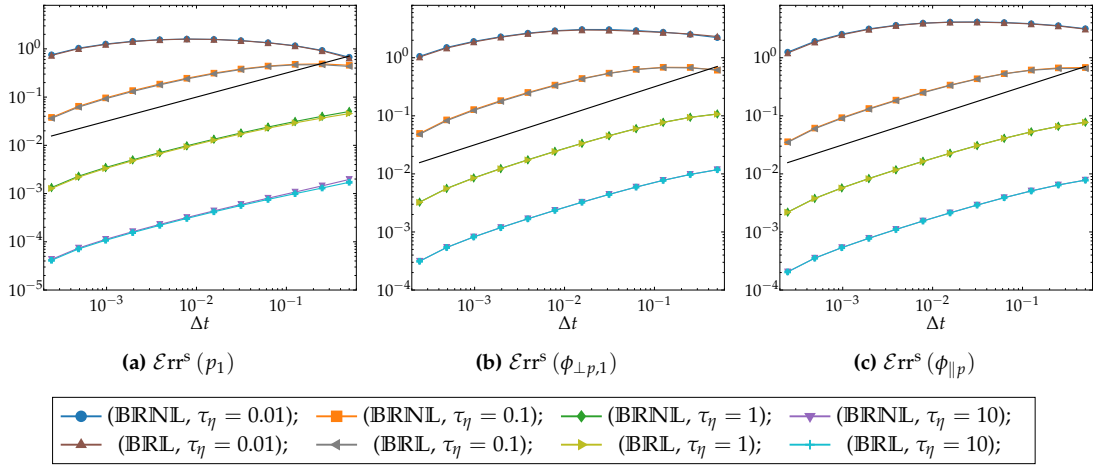

(a) $\mathcal{E}\mathrm{rr}^{\mathrm{s}}(p_1)$ **(b)** $\mathcal{E}\mathrm{rr}^{\mathrm{s}}(\phi_{\perp p,1})$ **(c)** $\mathcal{E}\mathrm{rr}^{\mathrm{s}}(\phi_{\parallel p})$

Figure 4.10: Splitting scheme in HIT: Strong error ($\mathcal{E}\mathrm{rr}^{\mathrm{s}}$) of the splitting algorithm Eq. (4.96) using the numerical scheme in Eq. (4.93) followed by Eq. (4.89) (BRNL) and Eq. (4.95) followed by Eq. (4.89) (BRL), against the time step Δt for different values of τ_η. In (a) the first component of $\boldsymbol{p}$, (b) the first component $\phi_{\perp p}$ of tumbling and (c) the spinning $\phi_{\parallel p}$. Black line indicates the slope 1/2; and the initial condition of particle orientation is $\boldsymbol{p}_a^0 = (1, 0, 0)$.

In the following, we analyse both strong and weak convergence for two different discretisations of Eq. (4.96) obtained by:

- BRNL, i.e. Eq. (4.93) followed by Eq. (4.89);
- BRL, i.e. Eq. (4.95) followed by Eq. (4.89).

Figure 4.10 shows the strong error for the three quantities p_1, $\phi_{\perp p,1}$ and $\phi_{\parallel p}$ against Δt for different values of τ_η, in Fig. 4.10a, 4.10b and 4.10c respectively. The order of convergence is 1/2, confirming that the composition of operators in this case obeys to the convergence of the two sub-parts of the splitting algorithm. It is interesting to notice that the stretching sub-part is dominant with respect to the rotation; this can be explained considering that the stretching sub-part produces higher values of the strong error with respect to the rotation sub-part. Furthermore, we observe that BRNL and BRL have the same behaviour.

The weak error as a function of the time step Δt, for different values of τ_η is presented in Fig. 4.11. The behaviour of the weak error of the moments is equivalent to that observed in the sub-part of the splitting with an order of convergence of 1. The results of $\mathbb{E}[p_1]$, $\mathbb{E}[p_1^2]$ and $\mathbb{E}[p_1^3]$ has been obtained with an initial condition $\boldsymbol{p}_a^0 = (1, 0, 0)$, and are shown in Fig. 4.11a, 4.11b, and 4.11c respectively. Alternatively, the initial condition $\boldsymbol{p}_b^0 = (1, 1, 1)/\sqrt{3}$ has been used to show the order of convergence of $\mathbb{E}[p_1 p_2]$ in Fig. 4.11d. Moreover, the magnitude of the weak error for various moments are much closer to the one produced in the stretching sub-part

compared to the rotation part. This indicates that the stretching contribution is dominant as for the strong convergence, which suggests that the numerical method used in the stretching sub-part should be refined to obtain better error results.

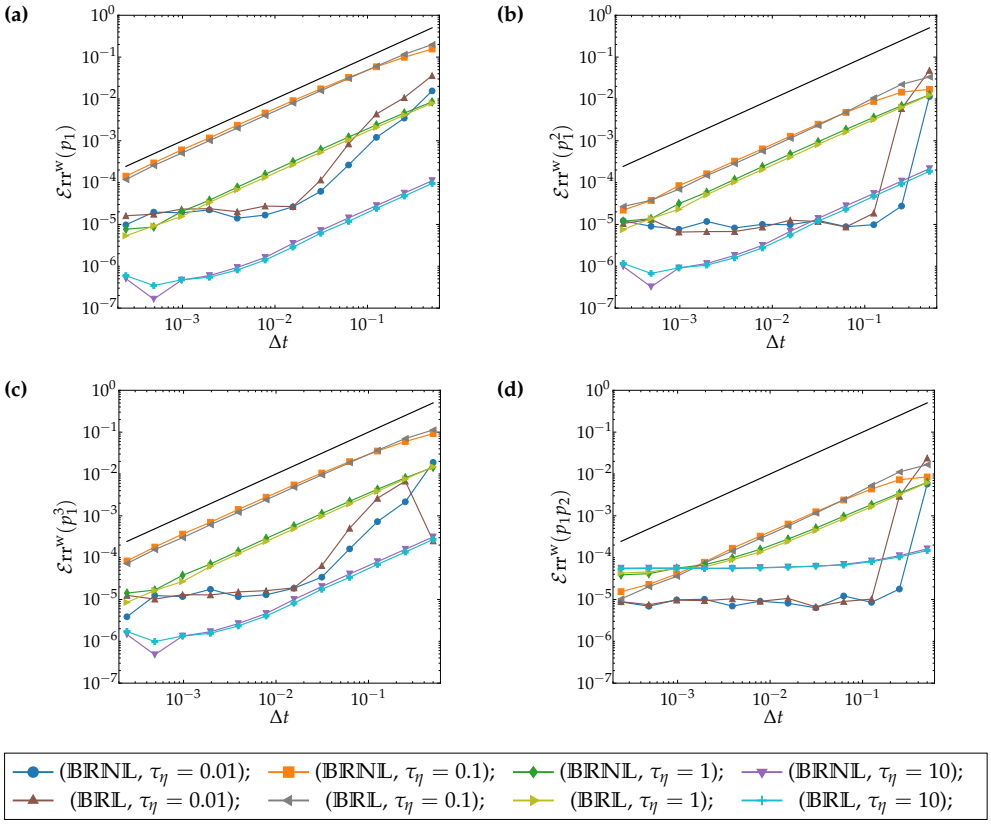

Figure 4.11: Splitting scheme in HIT: Weak error ($\mathcal{E}\mathrm{rr}^{\mathrm{w}}$) of the splitting algorithm Eq. (4.96) using the numerical scheme in Eq. (4.93) followed by Eq. (4.89) ($\mathbb{BRNL}$) and Eq. (4.95) followed by Eq. (4.89) ($\mathbb{BRL}$), against the time step Δt for different values of τ_η. In (a), (b), and (c) the first three moments of the first component $\boldsymbol{p}_{bs}$ for an initial condition of particle orientation $\boldsymbol{p}_a^0 = (1,0,0)$. In (d) the second cross moment $p_{bs,1}p_{bs,2}$ is shown using a different initial condition $\boldsymbol{p}_b^0 = (1,1,1)/\sqrt{3}$. Black line indicates the slope 1.

4.4.5.1 *Long time behaviour*

Here we study the asymptotic behaviour of the spitting scheme in HIT Eq. (4.96), using the first declination, i.e. performing the scheme in Eq. (4.93) followed by Eq. (4.89). The asymptotic convergence in real applications is very important in order to evaluate the evolution of the system for an elapsed simulation time which is in general very long. Moreover, in an ergodic system there is a coincidence between time average along trajectories and ensemble average across trajectories. Indeed, such property can be exploited on computing statistical observables of the process evaluating them from a single path simulated over a long time horizon instead of relaying on a large amount of trajectories. For this purpose, the marginal probability distribution function (PDF) expressed in spherical coordinates is analysed and compared with analytical results. Then, the numerical evaluation of the tumbling and spinning rate in Eq. (4.53) and (4.54) are compared with the analytical results in Eq. (4.33) and (4.34).

For a randomly orientated particle, as in HIT case, simple analytical expressions for the marginals PDFs in spherical coordinates are given by,

$$\mathcal{P}_\phi(\varphi) = \frac{1}{2}\sin(\varphi), \tag{4.97}$$

$$\mathcal{P}_\theta(\vartheta) = \frac{1}{2\pi}, \tag{4.98}$$

where the transformation from Cartesian coordinates (p_1, p_2, p_3) to spherical coordinates with unitary radius $(1, \vartheta, \varphi)$ is given by,

$$\varphi = \arccos\left(p_3/\|\boldsymbol{p}\|\right), \quad \vartheta = \arctan\left(p_2/p_1\right), \tag{4.99}$$

with $0 \leq \varphi \leq \pi$ and $0 \leq \vartheta \leq 2\pi$. Figure 4.12 shows the evolution in time of the numerical

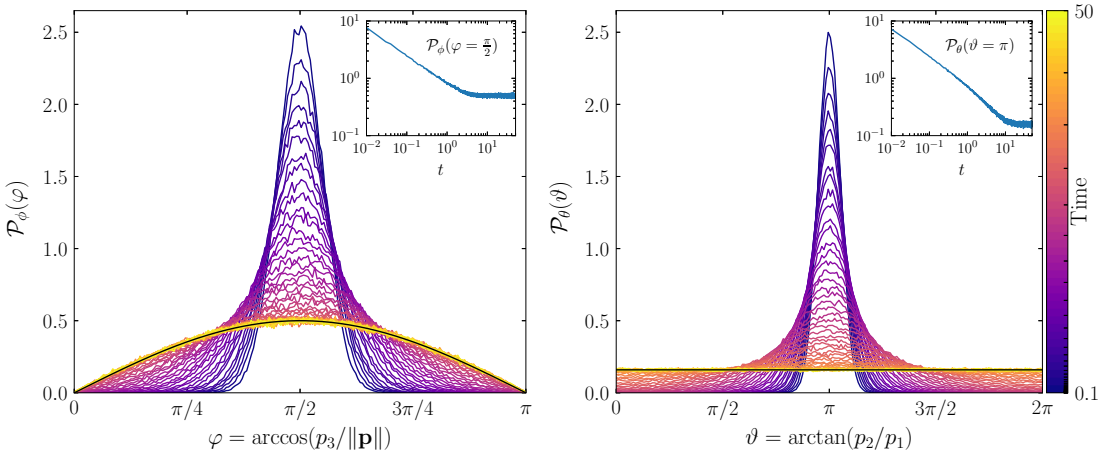

Figure 4.12: Evolution in time of marginal PDF computed numerically for the angles φ (left panel) and ϑ (right panel) in HIT case. The different curves correspond to different instant of time logarithmically spaced between $t \in [0.1, 50]$ starting from a deterministic initial condition $\boldsymbol{p}_a^0 = (1, 0, 0)$. In black line the analytical result of Eq. (4.97) (left panel) and Eq. (4.98) (right panel). Simulation performed with a number of particles $N_p = 10^5$, time step $\Delta t = 10^{-2}$, final time $T = 50$, time scale parameter $\tau_\eta = 1$ and a shape parameter $\Lambda = 1$. Inset: the values of the PDF in $\pi/2$, i.e. $\mathcal{P}_\phi(\varphi = \pi/2)$ at different instant of time $t \in [0.01, 50]$ are displayed in log-log plot for the angle φ (inset left panel). Equivalently, the values of the PDF in π, i.e. $\mathcal{P}_\theta(\vartheta = \pi)$, in time are reported for the angle ϑ (inset right panel).

results for $\mathcal{P}_\phi(\varphi)$ (left panel) and $\mathcal{P}_\theta(\vartheta)$ (right panel) starting from an initial condition $\boldsymbol{p}_a^0 = (1, 0, 0)$. The different curves indicate different instants of time and are logarithmically spaced $t \in [0.1, 50]$. As time increases, the numerical results collapse on the analytical curves (in black line). This confirms that the numerical scheme is able to converge toward the analytical PDF and for long time it remains stable. Moreover, the convergence of the PDF towards the invariant measure for the two marginal PDFs is exponentially fast as shown in the inset of Fig. 4.12 for φ (inset left panel) and ϑ (inset right panel). This last result suggests that the numerical method developed is geometrically ergodic (i.e. converges exponentially fast), which is an high-valuable characteristic that can be take in advantage in real applications.

Tumbling and Spinning

We want to use the long time behaviour as discussed above, to evaluate the tumbling and spinning rate for the stochastic Lagrangian model of orientation (Eq. (4.17)), which has been

defined in Section 4.3.3. In particular, for the HIT case, in Eq. (4.33) and (4.34), the derivative in time of the average value of the norm squared of $\phi_{\perp p}$ and $\phi_{\parallel p}$ has been computed analytically (Section 4.3.3.1).

Therefore, it is important to evaluate if the numerical scheme developed is able to reproduce these statistics. As we already know from the convergence analysis, the processes associated to these quantities converge in strong sense, but nevertheless the uncertainties of these statistics in long time behaviour remain an open question. Numerically Eq. (4.33) and (4.34) have been computed as follow,

$$\widetilde{\Phi}_{\perp p} = \frac{1}{T - t_0} \left[\frac{1}{N_p} \sum_n \left\| \tilde{\phi}^{(n)}_{\perp p}(T) \right\|^2 - \frac{1}{N_p} \sum_n \left\| \tilde{\phi}^{(n)}_{\perp p}(t_0) \right\|^2 \right], \tag{4.100}$$

$$\widetilde{\Phi}_{\parallel p} = \frac{1}{T - t_0} \left[\frac{1}{N_p} \sum_n \left(\tilde{\phi}^{(n)}_{\parallel p}(T) \right)^2 - \frac{1}{N_p} \sum_n \left(\tilde{\phi}^{(n)}_{\parallel p}(t_0) \right)^2 \right], \tag{4.101}$$

where the numerical solution of $\tilde{\phi}_{\perp p}$ and $\tilde{\phi}_{\parallel p}$ is given by Eq. (4.53) and (4.54), respectively.

In this case the numerical simulations are performed varying the particle aspect ratios λ or the shape parameter Λ. The numerical parameters used are: the number of particles $N_p = 10^5$, the time step $\Delta t = 10^{-3}$, the final time $T = 1000$, the time scale parameter $\tau_\eta = 1$. Moreover, we are using as initial condition a uniform distribution on a sphere. Regarding the final time T, we would like to underline that it is 2000 times bigger with respect to the one fixed for the convergence study ($T = 0.5$); this highlights the robustness and stability with respect to long times. The time scale parameter $\tau_\eta = 1$ has been selected from the convergence study as intermediate value. The initial and final time were fixed at $t_0 = 10$, $T = 1000$, verifying that t_0 is large enough and all the moments are well converged and stationary in time.

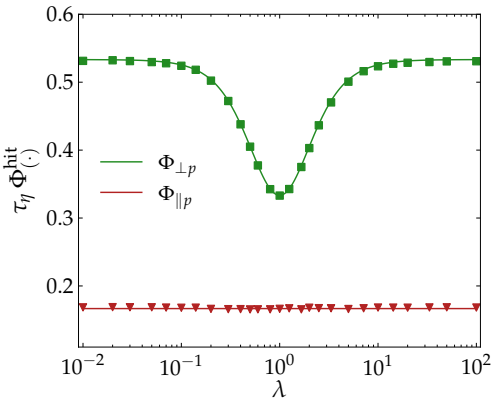

Figure 4.13: Analytical tumbling rate Eq. (4.33) (green line) and spinning rate Eq. (4.34) as a function of the particle aspect ratio λ for the HIT case. Markers show results of numerical simulations of Eq.(4.100) and (4.101). Simulations are performed with a number of particles $N_p = 10^5$, time step $\Delta t = 10^{-3}$, final time $T = 1000$, time scale parameter $\tau_\eta = 1$ and using as initial condition a uniform distribution on a sphere.

Figure 4.13 shows the comparison between the analytical (solid lines) and numerical (markers) results for the tumbling rate $\Phi^{\text{hit}}_{\perp p}$ and spinning rate $\Phi^{\text{hit}}_{\parallel p}$ as a function of the particle aspect ratio λ. These two results match with the analytic expressions, with the deviations between analytical (lines) and numerical (markers) reported in Table 4.2 for $\sigma = 0$, confirming that the stochastic part of the numerical scheme is able to reproduce these statistics for long time simulations. Moreover, this shed light on the discretisation used (Eq. (4.53) and (4.54))

to compute these quantities, which is a practical simple tool to evaluate the tumbling and spinning in the stochastic model, without adding other numerical difficulties.

4.5 NUMERICAL TEST WITH MEAN SHEAR

In this section, the proposed splitting scheme for the SDE (4.17) is illustrated in an homogeneous shear flow case (HSF), introduced in Section 4.3.3.2. In presence of a mean velocity gradient, the splitting scheme corresponds to Eq. (4.52), with the four elementary operators. Expressing them in their extended form, we have

$$\begin{cases} \dfrac{d\boldsymbol{p}_s(t)}{dt} = \Lambda\left(\langle \boldsymbol{S}\rangle \boldsymbol{p}_s - \boldsymbol{p}_s\boldsymbol{p}_s^{\intercal}\langle \boldsymbol{S}\rangle \boldsymbol{p}_s\right) & \text{with } \boldsymbol{p}_s(t_k) = \boldsymbol{p}(t_k), \\ \dfrac{d\boldsymbol{p}_a(t)}{dt} = \langle \boldsymbol{O}\rangle \boldsymbol{p}_a(t) & \text{with } \boldsymbol{p}_a(t_k) = \boldsymbol{p}_s(t_{k+1}), \\ d\boldsymbol{p}_{bs}(t) = -\dfrac{\nu_s^2}{2}\Lambda^2\boldsymbol{p}_{bs}dt + \nu_s\Lambda\left(d\mathbf{W}^s\,\boldsymbol{p}_{bs} - \boldsymbol{p}_{bs}\boldsymbol{p}_{bs}^{\intercal}\,d\mathbf{W}^s\,\boldsymbol{p}_{bs}\right) & \text{with } \boldsymbol{p}_{bs}(t_k) = \boldsymbol{p}_a(t_{k+1}), \\ d\boldsymbol{p}_{ba}(t) = -\dfrac{\nu_a^2}{2}\boldsymbol{p}_{ba}dt + \nu_a\boldsymbol{p}_{ba}d\mathbf{W}^a. & \text{with } \boldsymbol{p}_{ba}(t_k) = \boldsymbol{p}_{bs}(t_{k+1}), \end{cases} \tag{4.102}$$

where the solution at the next iteration time step is restored by $\boldsymbol{p}(t_{k+1}) = \boldsymbol{p}_{ba}(t_{k+1})$. The first two sub-parts of the splitting are deterministic, involving only the mean velocity gradient that has been split in its symmetric and antisymmetric contributions. We recall that the matrices $\langle \boldsymbol{S}\rangle$ and $\langle \boldsymbol{O}\rangle$, defined in Eq. (4.35), are constant in time.

The mean stretching (MS) sub-step of the splitting, i.e. Eq. (4.47), is composed by the symmetric part of the mean velocity gradient tensor $\langle \boldsymbol{S}\rangle$. This first sub-step in Eq. (4.102), as the stochastic counterpart, consists in a linear part that stretches the vector $\boldsymbol{p}$ modifying both its orientation and unitary norm; the latter is preserved by the non-linear term. A suitable numerical solution for this sub-part can be achieved employing classical numerical methods for the ODE, such as exponential method through a diagonalisation procedure or high-order Runge–Kutta methods. Specifically, for this numerical test, a fourth-order Runge–Kutta (RK4) method has been implemented to solve this sub-part of the splitting.

The second sub-step in Eq. (4.102), corresponds to the mean rotation (MR) sub-step of the splitting, i.e. Eq. (4.48). This sub-part involves the antisymmetric part of the mean velocity gradient tensor $\langle \boldsymbol{O}\rangle$, that purely rotates the vector $\boldsymbol{p}$ in a new position by preserving its unitary norm.

The presence of the antisymmetric matrix $\langle \boldsymbol{O}\rangle$ (constant in time) allows to directly solve the rotation dynamics of this sub-part of the splitting, by reconstructing the rotation matrix $\mathscr{R}$ (where its properties have been discussed in Section 4.4.3). Let us consider the mean angular velocity $\langle \boldsymbol{\omega}\rangle$, identified by the relation $\langle \boldsymbol{O}\rangle\ \boldsymbol{p} = (\langle \boldsymbol{\omega}\rangle \times \boldsymbol{p})/2$; then the rotation vector $\boldsymbol{\zeta} = \langle \boldsymbol{\omega}\rangle\,\Delta t$ encodes the increment of rotation over the period of time Δt. In this way the solution of the deterministic rotation sub-part is obtained by the exponential map (Celledoni and Owren (2003)) which is given by the Rodriguez formula (Bottasso and Borri (1998)),

$$\mathscr{R} = \mathbb{1} + \frac{\sin(\|\boldsymbol{\zeta}\|)}{\|\boldsymbol{\zeta}\|}\,[\boldsymbol{\zeta}]_\times + \frac{1-\cos(\|\boldsymbol{\zeta}\|)}{\|\boldsymbol{\zeta}\|^2}\,[\boldsymbol{\zeta}]_\times^2, \tag{4.103}$$

where $[\boldsymbol{\zeta}]_\times$ is the antisymmetric matrix associated to the rotation vector $\boldsymbol{\zeta}$, as in Eq. (4.71). Then, the orientation in the rotated framework, between two instant of times is given by,

$$\boldsymbol{p}_a(t+\Delta t) = \mathscr{R}^{\Delta t}(\boldsymbol{\zeta})\,\boldsymbol{p}_a(t). \tag{4.104}$$

The aim of this section is to study the behaviour of the splitting scheme relative to the stochastic part presented in Section 4.4.5, in the presence of a mean velocity gradient. This

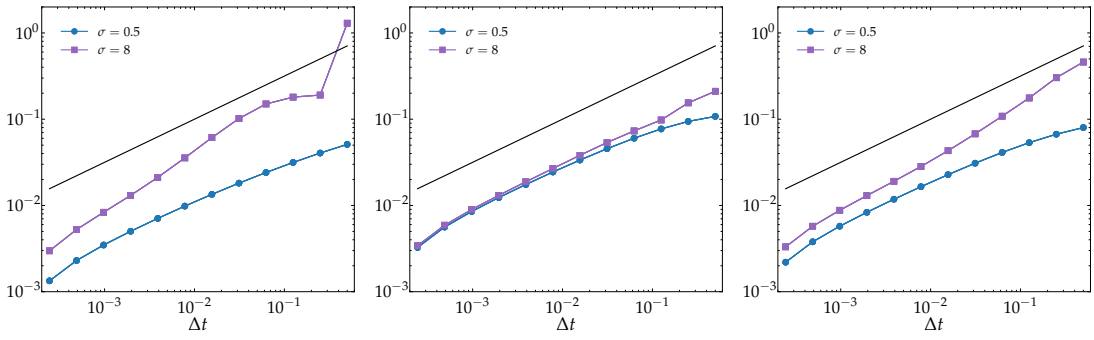

(a) $\mathcal{E}\mathrm{rr}^{\mathrm{s}}(p_1)$ **(b)** $\mathcal{E}\mathrm{rr}^{\mathrm{s}}(\phi_{\perp p,1})$ **(c)** $\mathcal{E}\mathrm{rr}^{\mathrm{s}}(\phi_{\parallel p})$

Figure 4.14: Splitting scheme in HSF: Strong error ($\mathcal{E}\mathrm{rr}^{\mathrm{s}}$) of the splitting algorithm Eq. (4.102) using RK4 for the mean stretching in Eq. (4.47) (𝕄𝕊) and the Rodriguez formula for the mean rotation Eq. (4.48) (𝕄ℝ); followed by the stochastic part Eq. (4.96) using numerical scheme (𝔹ℝℕ𝕃) (for $\tau_\eta = 1$) against the time step Δt for two different values of shear parameter σ. In (a) the first component of $\boldsymbol{p}$, (b) the first component $\boldsymbol{\phi}_{\perp p}$ of tumbling and (c) the spinning $\phi_{\parallel p}$. Black line indicates the slope $1/2$; the initial condition of particle orientation is $\boldsymbol{p}_a^0 = (1, 0, 0)$.

means that we are not directly focused on the convergence analysis as done before, but rather to test the coupling between the stochastic and deterministic part. Moreover, this case introduces additional difficulties because of the presence of deterministic terms. Indeed, an exact solution for the moments is no longer accessible; from a numerical point of view additional parameters, such as the shear rate σ, affect the convergence error. Here, we restrict ourself to testing the strong error convergence by fixing $\tau_\eta = 1$ (with the amplitude diffusion coefficient $\nu_s, \nu_a \approx \sqrt{1/\tau_\eta}$) and considering two different values of the shear rate $\sigma = 0.5, 8$ for $\langle \boldsymbol{S} \rangle$ and $\langle \boldsymbol{O} \rangle$, defined in Eq. (4.35).

Figure 4.14 shows the strong error as a function of the time step Δt for the two values of σ. The deterministic sub-parts Eq. (4.47) (𝕄𝕊) and Eq. (4.48) (𝕄ℝ) are implemented as described above and are followed by their stochastic counterparts using the numerical scheme (𝔹ℝℕ𝕃) in Eq. (4.96). The first component p_1 (p_2, p_3 have the same behaviour) is shown in Fig. 4.14a, where the strong error converges with a slope slightly greater than $1/2$ when $\Delta t < 10^{-2}$ for both values of σ. This could be explained by the presence of high order schemes for the mean stretching (𝕄𝕊), and an exact solution for the mean rotation (𝕄ℝ); it means that the splitting scheme marginally mixes the different orders of convergence.

The magnitude of the error strongly depends on the values of the shear rate, but does not deviate significantly from the ones observed for the strong convergence in HIT case (Section 4.4.5), when Δt becomes sufficiently small. Same observations can be done for $\phi_{\perp p,1}$ of tumbling and spinning $\phi_{\parallel p}$ in Fig. 4.14b and 4.14c, respectively. For this two quantities the magnitude of the error does not increase significantly moving from $\sigma = 0.5$ to $\sigma = 8$.

4.5.1 *Long time behaviour*

Analogously on what we did in Section 4.4.5.1, the asymptotic behaviour is hereafter analysed. The marginal probability distribution function (PDF) expressed in spherical coordinates has been studied. In this case, an analytical solution for the stationary marginals PDFs of φ and ϑ is not available and only numerical results are reported.

Figure 4.15 shows the evolution in time of the numerical results for $\mathcal{P}_\phi(\varphi)$ (left panel) and $\mathcal{P}_\theta(\vartheta)$ (right panel) starting from an initial condition $\boldsymbol{p}_a^0 = (1, 0, 0)$. The different curves indicate

different instants of time and are logarithmically spaced $t \in [0.1, 50]$. As time increases, the numerical results approach the same value (from violet to yellow lines). Compared to the HIT case, where the orientation is uniformly distributed on a sphere, the presence of a mean shear rate tends to align the vector $\boldsymbol{p}$ along its direction which corresponds to $\varphi = \pi/2$ and $\vartheta = 0, \pi, 2\pi$. These two results confirm that the numerical scheme converges toward a unique invariant measure. Moreover, the convergence towards the invariant measure for the two marginal PDFs is exponentially fast as shown in the inset of Fig. 4.15 for φ (inset left panel) and ϑ (inset right panel).

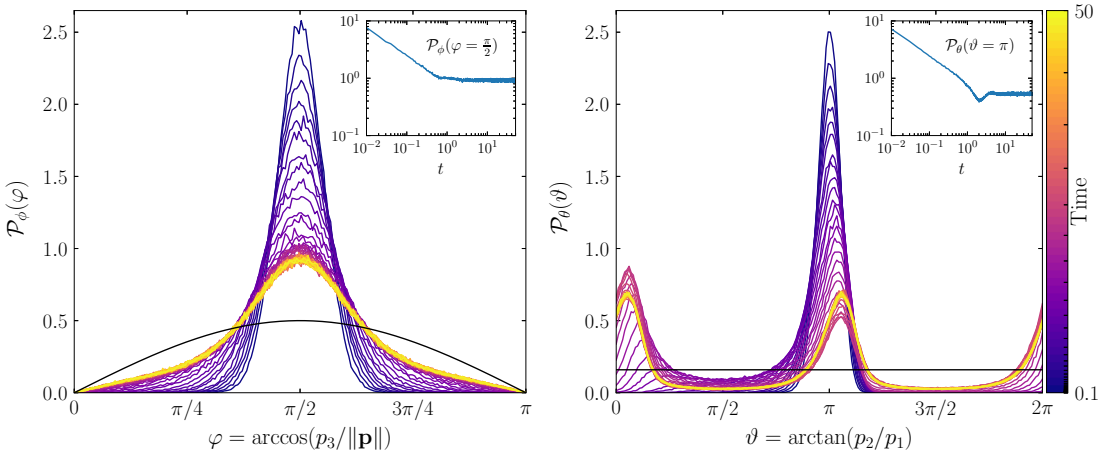

Figure 4.15: Evolution in time of marginal PDF computed numerically for the angles φ (left panel) and ϑ (right panel). The different curves correspond to different instant of time logarithmically spaced between $t \in [0.1, 50]$ starting from a deterministic initial condition $\boldsymbol{p}_a^0 = (1, 0, 0)$. In black line the analytical result of Eq. (4.97) (left panel) and Eq. (4.98) (right panel). Simulation is performed with a number of particles $N_p = 10^5$, time step $\Delta t = 10^{-2}$, final time $T = 50$, time scale parameter $\tau_\eta = 1$ and a shape parameter $\Lambda = 1$. Inset: the values of the PDF in $\pi/2$, i.e. $\mathcal{P}_\phi(\varphi = \pi/2)$ at different instants of time $t \in [0.01, 50]$ are presented in log-log plot for the angle φ (inset left panel). Equivalently, the values of the PDF in π, i.e. $\mathcal{P}_\theta(\vartheta = \pi)$, in time are reported for the angle ϑ (inset right panel).

Tumbling and Spinning

Inherent to the asymptotic behaviour of the numerical scheme, it is interesting to compute numerically the norm of the orthogonal projection $\widehat{\Phi}_{\perp p}$ in Eq. (4.26), and of the parallel projection $\widehat{\Phi}_{\parallel p}$ in Eq. (4.27), that we recall has to be zero. These two quantities, numerically, are evaluated as,

$$\widehat{\tilde{\Phi}}_{\perp p}^{\text{hsf}} = \frac{1}{T - t_0} \left[\frac{1}{N_p} \sum_n \left\| \tilde{\phi}_{\perp p}^{(n)}(T) \right\| - \frac{1}{N_p} \sum_n \left\| \tilde{\phi}_{\perp p}^{(n)}(t_0) \right\| \right], \tag{4.105}$$

$$\widehat{\tilde{\Phi}}_{\parallel p}^{\text{hsf}} = \frac{1}{T - t_0} \left[\frac{1}{N_p} \sum_n \left(\tilde{\phi}_{\parallel p}^{(n)}(T) \right) - \frac{1}{N_p} \sum_n \left(\tilde{\phi}_{\parallel p}^{(n)}(t_0) \right) \right], \tag{4.106}$$

where the numerical solution of $\tilde{\phi}_{\perp p}$ and $\tilde{\phi}_{\parallel p}$ is given by Eq. (4.53) and (4.54), respectively.

Due to the lack of analytical results, $\widehat{\tilde{\Phi}}^{\text{hsf}}_{\perp p}$ is compared with its semi-analytical form in Eq. (4.44), that we recall here to be,

$$\widehat{\Phi}^{\text{hsf}}_{\perp p_\infty} = \left(\sum_{i=1}^{3} \mathbb{E}\left[g_i^{\perp}(\boldsymbol{p}_\infty) \right]^2 \right)^{\frac{1}{2}} \quad \text{with } \boldsymbol{g}^{\perp}(\boldsymbol{p}_s) = \frac{\sigma}{2} \begin{pmatrix} -(\Lambda-1)p_1 p_3 \\ (\Lambda+1)p_2 p_3 \\ (\Lambda-1)p_1^2 - (\Lambda+1)p_2^2 \end{pmatrix}.$$

The numerical parameters are the same used in the HIT case. Concerning $\widehat{\Phi}^{\text{hsf}}_{\parallel p}$, it should always be zero (Section 4.3.3.2).

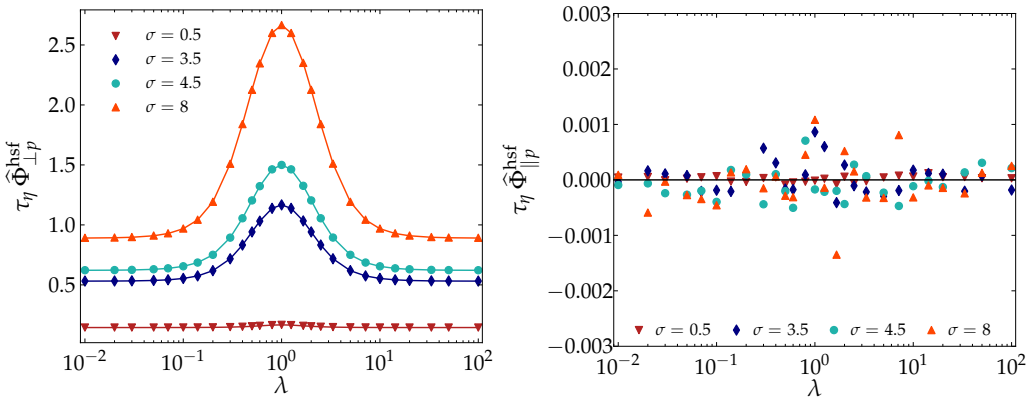

Figure 4.16: The mean tumbling rate Eq. (4.26) and spinning rate Eq. (4.27) as a function of the particle aspect ratio λ in HSF for different values of the shear rate parameter σ (as in legend). Markers show results of numerical simulations of Eq. (4.106) and (4.105). Semi-analytical Eq. (4.44) (lines in left panel) and analytical result $\widehat{\Phi}_{\parallel p} = 0$ (black line in left panel). Simulations are performed with a number of particles $N_p = 10^5$, time step $\Delta t = 10^{-3}$, final time $T = 1000$, time scale parameter $\tau_\eta = 1$ and using as initial condition a uniform distribution on a sphere.

Figure 4.16 shows numerical results (in markers) as a function of particle aspect ratio λ of Eq. (4.105) (left panel) and Eq. (4.106) (right panel), which are compared to semi-analytical Eq. (4.44) (in lines) and zero (black line), respectively. Four different values of the shear rate parameter σ are used (in legend). Both $\widehat{\tilde{\Phi}}_{\perp p}$ and $\widehat{\tilde{\Phi}}_{\parallel p}$ evaluated numerically match with their semi-analytical/analytical values, with the deviations between semi-analytical (lines) and numerical (markers) reported in Table 4.1. The maximum of the error between these two approaches can be observed in the right panel of Fig. 4.16 (for the left panel the behaviour is the same); it passes from order 2×10^{-3} for $\sigma = 8$ to 10^{-4} for $\sigma = 0.5$. Thus, the error values increase with σ, which is reasonable compared to strong convergence results.

As we did for the HIT case, we consider the variance of the norm of $\phi_{\perp p}$ and $\phi_{\parallel p}$, that is $\tilde{\Phi}_{\perp p}$ and $\tilde{\Phi}_{\parallel p}$ in Eq. (4.28) and (4.29), respectively. We compare the numerical approximations given by Eq (4.100) and (4.101) with the semi-analytical definitions in Eq. (4.45) and (4.39), that we recall to be,

$$\Phi^{\text{hsf}}_{\perp p_\infty} \simeq 2 \sum_{i=1}^{3} \int_{t_0}^{\infty} \mathcal{R}_{g_i^{\perp}}(\tau) d\tau + \Phi^{\text{hit}}_{\perp p},$$

$$\text{with } \mathcal{R}_{g_i^{\perp}}(\tau) = \mathbb{E}\left[g_i^{\perp}(\boldsymbol{p}_{t_0}) g_i^{\perp}(\boldsymbol{p}_{t_0+\tau}) \right] - \mathbb{E}\left[g_i^{\perp}(\boldsymbol{p}_{t_0}) \right] \mathbb{E}\left[g_i^{\perp}(\boldsymbol{p}_{t_0+\tau}) \right].$$

$$\Phi^{\text{hsf}}_{\parallel p}(t) = \int_{t_0}^{\infty} \mathbb{E}\left[g^{\parallel}(\boldsymbol{p}_{t_0}) g^{\parallel}(\boldsymbol{p}_{t_0+\tau}) \right] d\tau + \Phi^{\text{hit}}_{\parallel p}. \quad \text{with} \quad g^{\parallel}(\boldsymbol{p}_s) = \frac{\sigma}{2} p_3.$$

Error of mean $\widehat{\Phi}_{\perp p}$ and $\widehat{\Phi}_{\parallel p}$										
λ		0.01	0.07	0.4	0.6	1.0	1.66	2.5	14.28	100.0
$\sigma = 0.5$	$\widehat{\mathcal{E}}^{\text{hsf}}_{\perp p}$	0.000025	0.000013	0.000008	0.000048	0.000038	0.000044	0.000035	0.000055	0.000038
	$\widehat{\mathcal{E}}^{\text{hsf}}_{\parallel p}$	0.000089	0.000104	0.000051	0.000018	0.000041	0.000080	0.000059	0.000007	0.000053
$\sigma = 3.5$	$\widehat{\mathcal{E}}^{\text{hsf}}_{\perp p}$	0.000935	0.000916	0.000259	0.000086	0.000036	0.000076	0.000312	0.000872	0.000908
	$\widehat{\mathcal{E}}^{\text{hsf}}_{\parallel p}$	0.000060	0.000125	0.000127	0.000080	0.000023	0.000376	0.000147	0.000255	0.000087
$\sigma = 4.5$	$\widehat{\mathcal{E}}^{\text{hsf}}_{\perp p}$	0.001411	0.001376	0.000383	0.000098	0.000051	0.000161	0.000414	0.001361	0.001409
	$\widehat{\mathcal{E}}^{\text{hsf}}_{\parallel p}$	0.000376	0.000092	0.000119	0.000280	0.000111	0.000024	0.000301	0.000344	0.000086
$\sigma = 8$	$\widehat{\mathcal{E}}^{\text{hsf}}_{\perp p}$	0.003592	0.003407	0.000784	0.000179	0.000043	0.000185	0.000804	0.003449	0.003621
	$\widehat{\mathcal{E}}^{\text{hsf}}_{\parallel p}$	0.000276	0.000127	0.000630	0.000850	0.002023	0.001144	0.000011	0.000055	0.000630

Table 4.1: Values of the errors $\widehat{\mathcal{E}}^{\text{hsf}}_{\perp p} = \left|\widehat{\tilde{\Phi}}^{\text{hsf}}_{\perp p} - \widehat{\Phi}^{\text{hsf}}_{\perp p_\infty}\right|$ and $\widehat{\mathcal{E}}^{\text{hsf}}_{\parallel p} = \left|\widehat{\tilde{\Phi}}^{\text{hsf}}_{\parallel p} - \widehat{\Phi}^{\text{hsf}}_{\parallel p_\infty}\right|$ of mean tumbling and spinning rate in the model $\widehat{\Phi}_{\perp p}$ (Eq. (4.26)), $\widehat{\Phi}_{\parallel p}$ (Eq. (4.27)), for some values of λ. These values are relative to the deviation between markers and continuous lines in Fig. 4.16.

Figure 4.17 represents numerical results (in markers) and semi-analytical solutions (in lines) as a function of the particle aspect ratio λ for different values of the shear rate σ (in legend). We present the variance of the tumbling rate (Eq. (4.38)) in the right panel, and the spinning rate (Eq. (4.39)) in left panel. We observe that the spinning (in right panel) results are in a good agreement for all values of the particle aspect ratio λ, with the deviations between semi-analytical (lines) and numerical (markers) reported in Table 4.2. In addition, the maximum relative error is given by spherical particles ($\lambda = 1$) which is $\approx 0.5\%$. This shows that the unfolded statistic of spinning rate in the stochastic model is well reproduced by the numerical splitting scheme.

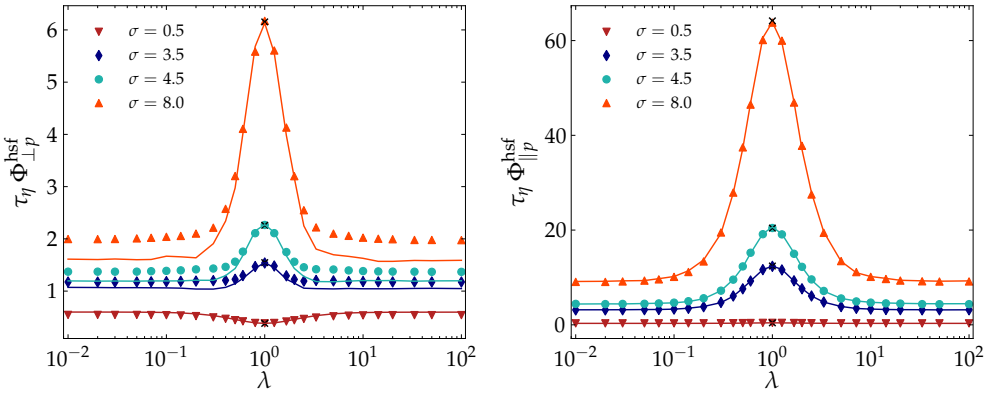

Figure 4.17: The variance of tumbling rate Eq. (4.28) and spinning rate Eq. (4.29) as a function of the particle aspect ratio λ in HSF for different values of the shear rate parameter σ (as in legend). Markers show results of numerical simulations computed according to Eq.(4.100) and (4.101) in HSF. Moreover, black cross markers are the analytical results obtained for the case of sphere ($\lambda = 1$) (in Appendix B.6). Semi-analytical tumbling rate in Eq. (4.45) (lines in left panel) and semi-analytical spinning rate in Eq. (4.46) (lines in right panel) are reported. Simulations are performed with a number of particles $N_p = 10^5$, time step $\Delta t = 10^{-3}$, final time $T = 1000$, time scale parameter $\tau_\eta = 1$ and using as initial condition a uniform distribution on a sphere.

Left panel of Fig. 4.17 shows the comparison between numerical and semi-analytical results of the tumbling rate in the stochastic model as a function of λ. For small values of λ a good agreement is found, also compared to the exact solution for $\lambda = 1$ (details are presented in Appendix B.6), which is shown in the black crosses markers. Moreover, we notice that the results differ for the flattest disks ($\lambda \ll 1$) and equivalently for long rods ($\lambda \gg 1$), in particular for large values of σ. The error between these two approaches is reported in Table 4.2.

A possible source of error could be the computation of the semi-analytical results for the tumbling; in fact, it leads to evaluate integral correlations of several components, such as $\mathcal{R}_{p_1p_3}(\tau)$,$\mathcal{R}_{p_2p_3}(\tau)$, $\mathcal{R}_{p_1^2}(\tau)$, $\mathcal{R}_{p_2^2}(\tau)$ and $\mathcal{R}_{p_1p_2}(\tau)$). It is a numerically difficult task, more difficult than computing directly $\tilde{\Phi}_{\perp p}$. Other difficulties come from the fact that for the spinning we compute only a second order moment, while for the tumbling fourth order moments are considered. In addition, the spinning only involves p_3, conversely the tumbling gathers the contributions of all components of $\boldsymbol{p}$. We would remark that, in the presence of shear, the SDE that describes the orientation (Eq. (4.36)) shows a simpler structure for component p_3 than for the other two components.

We are still searching a clear explanation for the error associated to the tumbling; in perspective, other methods of analysis can be used to compute this correlation, different with respect to Monte Carlo evaluation.

Error of variance $\Phi_{\perp p}$ and $\Phi_{\parallel p}$										
λ		0.01	0.07	0.4	0.6	1.0	1.66	2.5	14.28	100.0
$\sigma = 0$	$\mathcal{E}^{\text{hit}}_{\perp p}$	0.001857	0.001541	0.000227	0.000182	0.000279	0.001906	0.001692	0.002248	0.002379
	$\mathcal{E}^{\text{hit}}_{\parallel p}$	0.001786	0.001481	0.000821	0.001128	0.000367	0.001117	0.000616	0.001456	0.001549
$\sigma = 0.5$	$\mathcal{E}^{\text{hsf}}_{\perp p}$	0.054828	0.053699	0.023996	0.007241	0.000137	0.009160	0.025728	0.055718	0.057170
	$\mathcal{E}^{\text{hsf}}_{\parallel p}$	0.000749	0.001883	0.001235	0.001244	0.003162	0.002228	0.001604	0.000300	0.000650
$\sigma = 3.5$	$\mathcal{E}^{\text{hsf}}_{\perp p}$	0.103256	0.114694	0.134366	0.054659	0.008298	0.064419	0.136334	0.132703	0.126056
	$\mathcal{E}^{\text{hsf}}_{\parallel p}$	0.020740	0.005817	0.043774	0.000481	0.039395	0.077273	0.008652	0.004965	0.005912
$\sigma = 4.5$	$\mathcal{E}^{\text{hsf}}_{\perp p}$	0.176494	0.185755	0.168004	0.071884	0.006968	0.070441	0.176106	0.177326	0.170685
	$\mathcal{E}^{\text{hsf}}_{\parallel p}$	0.030356	0.033789	0.027787	0.118855	0.193280	0.168652	0.145102	0.090144	0.094814
$\sigma = 8$	$\mathcal{E}^{\text{hsf}}_{\perp p}$	0.384828	0.415358	0.234539	0.090977	0.043472	0.151385	0.299867	0.433211	0.386030
	$\mathcal{E}^{\text{hsf}}_{\parallel p}$	0.079306	0.145548	0.099135	0.371444	0.103639	0.104940	0.382177	0.130605	0.117721

Table 4.2: Values of error $\mathcal{E}^{\text{hsf}}_{\perp p} = \left|\tilde{\Phi}^{\text{hsf}}_{\perp p} - \Phi^{\text{hsf}}_{\perp p_\infty}\right|$ and $\mathcal{E}^{\text{hsf}}_{\parallel p} = \left|\tilde{\Phi}^{\text{hsf}}_{\parallel p} - \Phi^{\text{hsf}}_{\parallel p_\infty}\right|$, of the variance of tumbling and spinning rate in the model $\Phi_{\perp p}$ (Eq. (4.28)) and $\Phi_{\parallel p}$ (Eq. (4.29)), for some values of λ. Moreover, on first line is reported the HIT case ($\sigma = 0$) (in Fig. 4.13) computed with respect analytical results in Eq. (4.33) and (4.34), for tumbling and spinning rate, respectively. These values are relative to the deviation between markers and continuous lines in Fig. 4.17.

4.6 CONCLUSIONS

We studied the orientation and rotation dynamics of non-spherical tracer particles in a turbulent flow in the context of stochastic modelling, also referred as PDF approach. In the first part of the work, we have proposed a Lagrangian stochastic model for the three dimensional case, able to describe the orientation of non-spherical particles. This model has been coupled to classical hybrid Eulerian/Lagrangian stochastic methods, obtaining a complete system for the dynamics of non-spherical tracer particles in a turbulent flow. The 'classical' definitions, used in DNS, of

tumbling and spinning rate, associated to the rotation dynamics of non-spherical particles, are not accessible by the stochastic model. However, a different notion of these two statistics has been introduced.

In the second part of the work, we constructed and analysed a semi-implicit splitting numerical method for the non-linear stochastic differential equation (SDE) proposed in the model. Classical Euler–Maruyama method commonly fails to converge with optimal rate, or eventually diverges, when coefficients have not bounded first derivative (i.e., globally Lipschitz condition fails), which is the case of the SDE under study. Another key point is that the numerical scheme is not constrained by the assumptions of the model, and stay insensitive to the particular choice of tensor correlations introduced. The semi-implicit splitting numerical method includes four different sub-parts: the first two are related to the deterministic stretching and rotation contribution of the mean velocity gradient; the others two are represented by the stochastic Brownian stretching and Brownian rotation contribution for the velocity gradient fluctuations. In particular, a semi-implicit Euler–Maruyama for the Brownian rotation sub-part has been developed by adapting the deterministic quaternion dynamics to the stochastic case. This allowed to find a convergent scheme avoiding to introduce more intricate numerical methods.

In overall, the semi-implicit splitting method has been proved to be mean-square convergent of order $1/2$ and weakly convergent of order 1. Moreover, we showed that, in contrast with classical Euler–Maruyama type methods, the proposed splitting method is able to preserve the geometric features of the SDE under study (namely, the constraint to lie on a manifold $SO(3)$). This makes our scheme applicable at reasonable computational costs. Further, we pointed out that our method is stable on long times, which is an high-valuable feature for real applications. The statistics of tumbling and spinning rate were well numerically reproduced when compared to the analytical solution in homogeneous isotropic turbulence.

In the last part of the work, the numerical scheme was analysed in a semi-real case, by considering the non-spherical particles embedded in a homogeneous shear flow. This last case confirmed the effectiveness of the numerical scheme for the study of the model in other turbulent flows, such as a turbulent channel flow, as we discuss in the Chapter 5.

As a perspective, the numerical splitting scheme could be adapted to treat also inertial particles, since it deals with the general numerical problem of the orientation, that remains the same for both inertialess and inertial particles. Therefore, the extension of the model to anisotropic inertial particles is interesting and implies the additional work of including the particle relaxation time τ_p in the Jeffery's equation.

5 ORIENTATION IN A CHANNEL FLOW

Outline. In the following chapter the orientational and rotational behaviour of inertialess spheroidal particles in a turbulent channel is investigated by coupling the orientation stochastic Lagrangian model to an hybrid Eulerian/Lagrangian PDF method. The proposed model and its numerical scheme discussed in Chapter 4 have been implemented in an industrial CFD code (*Code_Saturne*) and detailed comparisons of the orientation statistics with DNS are carried out. Indeed, this last part of the work represents the bridge between two different issues of the modelling: the first concerns whether and to which extent the model is able to reproduce features of the 'reality'; the second is about its numerical implementation within an industrial code. Moreover, to better understand the capability and limit of the model, a detailed investigation has been performed using the mean-field information by filtering the DNS dataset, which can be treated as a 'perfect' RANS. Finally, the characterisation of tumbling and spinning motion within the model is discussed in terms of the statistics introduced in Chapter 4, while the classical deterministic definitions of the motions is employed for presenting results from DNS.

5.1 INTRODUCTION

The dynamics of solid particles suspended in a wall-bounded turbulent flow is important in order to understand the hydrodynamics of solid suspensions. In particular, here, the interest is on the prediction of flow-induced alignment and rotation of non-spherical particles in a turbulent suspension which is of interest in many areas of science and engineering, as well as in many practical applications. Particles asphericity impacts on the fundamental properties of turbulence and on the rheological properties of suspensions, being relevant in applications ranging from the dispersion of plastic micro-particles, to the distribution of cellulose fibres in the paper and pulp industry, to the motion of red blood cells travelling through blood vessels, and ice-crystal dynamics in clouds, to name a few.

In this work, we focus the discussion to small inertialess rigid fibres, with a size smaller than the Kolmogorov length scale η_K, such that point-particle approach can be applied, assuming dilute conditions and additionally, neglecting the feedback on the flow. Moreover, the dynamics of non-spherical particles is studied by approximating the actual particle shape as an axisymmetric ellipsoid, i.e., either prolate (rod-like) or oblate (disk-like) spheroids (Fig. 2.1 in Chapter 2).

Following growing interest in the subject, physical modelling and different numerical approaches have been used to study the motion of non-spherical particles in various flow fields, with an extensive literature having been produced, as reviewed by Voth and Soldati (2017). Previous studies have revealed the dynamics of inertialess spheroidal particles in homogeneous isotropic turbulence (HIT) both, using direct numerical simulations (DNS) (Shin and Koch (2005); Pumir and Wilkinson (2011); Chevillard and Meneveau (2013); Gustavsson et al. (2014); Ni et al. (2014); Byron et al. (2015)), and also experimental investigations (Parsa et al. (2012); Marcus et al. (2014); Ni et al. (2015)). These have shown that particles preferentially align with respect to fluid vorticity and strain, which causes particle rotation to differ from that of spherical fluid particles. Specifically, rods tend to align their symmetry axis with the local

fluid vorticity vector, which leads particles to preferentially rotate around their symmetric axis (Parsa et al. (2012)). Conversely, disks align their long axes with the local fluid vorticity, leading to minimal rotations about their symmetry axis (Byron et al. (2015)).

These results represent a special case, however, since lack of mean shear distinguishes HIT from most of the turbulent flows found in practice. This motivates the study of particles in turbulent channel flows, that represent an interesting case for particle motion, since the flow changes among qualitatively different states while increasing distance from the channel wall. In the bulk region of the channel, where the vorticity field is nearly isotropic, particles orient almost randomly (Andersson et al. (2015)), while the alignment near the channel walls crucially depends on the aspect ratio. Disk-like particles strongly align their symmetry axis $\boldsymbol{p}$ in the wall-normal direction, whereas rod-like tracer particles align parallel with the wall, mostly in the streamwise direction (Challabotla et al. (2015b)). The strong preferential orientation of non-spherical particles reduces the mean particle rotation below that for spheres, which is equal to the mean fluid rotation. In spite of the substantial reduction of mean angular velocity of tracers with high aspect ratio, enhanced fluctuations of the streamwise component of the angular velocity has been observed by Challabotla et al. (2015b).

Zhao et al. (2015) showed the existence of two qualitatively different modes of inertialess spheroids rotation in channel-flow turbulence. Just as in HIT (Parsa et al. (2012); Byron et al. (2015)), rods preferentially spin and disks tumble in the central region ('centre mode'). In the near-wall region, however, both tumbling and spinning are suppressed while increasing asphericity ('wall mode'). Spheroidal particles in 'centre mode' are nearly randomly oriented in the channel centre, where the mean shear vanishes and the vorticity field is almost isotropic. The local fluid vorticity vector $\boldsymbol{\omega}$ and the orientation vector of rod-like particles $\boldsymbol{p}$ are both preferentially aligned in the strongest Lagrangian stretching direction, while disk-like particles orient in the Lagrangian compression direction, which is perpendicular to the fluid vorticity vector (Ni et al. (2014); Zhao and Andersson (2016)). The shape-dependent particle rotational behaviour is therefore caused by how a spheroidal particle orients itself relatively to the local fluid vorticity. In 'wall mode', rod- and disk-like spheroids are preferentially aligned in the Lagrangian stretching (streamwise) direction and the Lagrangian compression (wall-normal) direction, respectively. The rotational behaviour is strongly affected by the mean shear (i.e. anisotropic fluid vorticity), and is therefore qualitatively consistent with a spheroid rotation in uniform shear flow, following the so-called Jeffery orbits (Challabotla et al. (2015b); Voth (2015)).

The role of deterministic factors, i.e. the mean shear and vorticity anisotropy, on the orientational behaviour of spheroidal particles has been studied by a direct simulated turbulent Couette–Poisueille flow (Yang et al. (2018)). This flow was used to achieve a better understanding of spheroidal particle rotation in sheared turbulence by exploring the different mechanisms that identify the rotation in the centre and near the wall, namely the anisotropy of the particle orientation and fluid shear. These are the two main factors influencing the particle rotational behaviour. It has been found that in the centre region the mean shear has practically no influence on the particle orientations. In the wall region, however, mean shear plays a role in particle rotation whenever particles are preferentially oriented. Furthermore, findings on the orientation and rotation behaviour near the high shear wall show an almost undistinguishable behaviour on respect to previous studies in the turbulent channel flows (Zhao et al. (2015)).

Considering the relevance of the problem for industrial processes, models that reach an acceptable compromise between simplicity and accuracy are needed. In all the above mentioned works, the turbulent flow field is treated as a continuous phase, and simulated in the Eulerian frame using a direct numerical simulation (DNS). Discrete particles interact with the flow eddies and are solved by Lagrangian particle tracking. DNS may be regarded as a numerical experiment providing the most promising way to reproduce features of turbulence up to

the smallest Kolmogorov scale, giving access to a complete picture. Nonetheless, DNS is computationally expensive and not designed to handle suspensions of a large number of small finite-size particles in complex geometries or high Reynolds number, as often met in engineering systems. To overcome the noted shortfalls of DNS methods, turbulence models are still necessary to describe the motion of particles in turbulent flow. Within this framework, a Lagrangian stochastic method predicting particle-laden turbulence (also referred to as PDF method, e. g., Minier (2016)) is adopted. The influence of the underlying turbulent fluid is represented by a stochastic model of the particle equation of motion. However, adopting a stochastic closure for the fluid seen by the particle would yield a velocity field where the velocity gradients would be unavailable.

Many micro-physical processes such as, orientation and rotation of fibres, deformation of bubbles and polymers dynamics strongly depend on the velocity gradient tensor, which is dominated by the turbulent structure in viscous range. Recently, the modelling challenge on how to reproduce a detailed dynamics of small scale properties of turbulence that are not accessible by using Reynold Averaged Navier-Stokes Simulations (RANS) or Large Eddy Simulations (LES) has been investigated by Chen et al. (2016); Johnson and Meneveau (2018). These authors introduced a method for coupling existing stochastic models for the velocity gradient tensor with coarse-grained fluid simulations (see Section 2.5 in Chapter 2). However, this problem have not received much attention in the modelling context and, while their method is tailored for small scales, other approaches have to be envisaged depending on the physics scale of interest.

In this work, the orientation and rotation of spheroidal particle is studied by using the stochastic Lagrangian model for the orientation developed in Chapters 3-4. The observation timescale Δt was assumed to be longer than the characteristic timescale of the velocity gradient seen by the particle, such that gradients can be regarded as fast processes and removed from the particle state vector. The model and the numerical scheme presented in Chapters 4 constitute the basis for the study of an applicative prototype of inhomogeneous anisotropic flow. Our model for particle orientation has been coupled with an hybrid Euler-Lagrangian stochastic transport. In particular, we have investigated the turbulent channel flow for which DNS were available thanks to the work of co-authors in Campana et al..

More specifically, the results on the orientation and rotation statistics are analysed in three different cases. Firstly, a DNS dataset of turbulent channel flow (provided by simulations performed by co-authors in Campana et al.) is used as experimental results for judging the performance of the model. Secondly, in order to provide insight into the accuracy of the stochastic Lagrangian orientation model, isolated from hybrid stochastic Eulerian/Lagrangian (with RANS), an *a priori* case is constructed by filtering the DNS dataset (A-DNS), which can be treated as 'perfect' RANS results. Lastly, the next case consists of running the hybrid RANS case using the CFD code (*Code_Saturne*) (provided by simulations performed by co-authors in Campana et al.) with no input from the DNS, which provides relevant results on the performance of the model in real industrial test case simulations. The comparison of the *a priori* (A-DNS) case with the DNS results will be explored in most details. This choice is made to highlight the contribution provided by the model itself, as well as to understand its intrinsic limit for reproducing orientation and rotation statistics.

The results obtained both for the orientation and for rotation statistics in A-DNS and RANS-type simulations are used for a preliminary investigation performed with a stochastic Lagrangian model of particle orientation. In this respect, proposing a model directly on the orientation represents, in our view, a more difficult task than exploring Jeffery's equation coupled with the stochastic Lagrangian model for the velocity gradient since the deterministic rotation statistics used in DNS are no longer applicable.

The work is organised as follows. The three different methodologies for the fluid and particle motion, as well as brief recalls on the stochastic Lagrangian model for the orientation and the underlying assumptions, are presented in Section 5.2. Results about the variance of the orientation vector $\boldsymbol{p}$ conditioned on the wall normal direction y^+ for the rod- and disk-like particles in DNS, A-DNS and RANS cases are discussed in Section 5.3. In Section 5.4 the rotation rate statistics are firstly presented for the DNS case and then for the model, using the alternative definition of the rotation modes introduced in Chapter 4. Conclusions are provided in Section 5.5.

5.2 METHODOLOGY

We consider the motion of inertialess spheroidal particles smaller than the Kolmogorov length scale in a fully developed turbulent channel flow. The particle concentration is very diluted, so that one-way coupling from fluid to particles is assumed, and collisions between particles are neglected. In this section, the governing equations for turbulent flow in the DNS, filtered DNS (A-DNS) and mean-field/PDF approach (Peirano et al. (2006)) are presented.

5.2.1 *DNS method*

The turbulent channel flow of a dilute suspension is computed by DNS in Eulerian framework. The fluid motion is considered governed by the incompressible Navier–Stokes equations,

$$\frac{\partial u_i}{\partial t} + u_j \frac{\partial u_i}{\partial x_j} = -\frac{\partial P}{\partial x_i} + \nu \frac{\partial^2 u_i}{\partial x_j^2}, \quad \frac{\partial u_j}{\partial x_j} = 0, \tag{5.1}$$

with a kinematic viscosity ν, where $\boldsymbol{u}(\boldsymbol{x},t)$ and $P(\boldsymbol{x},t)$ are the velocity and pressure field (divided by density), respectively. In the following, the channel is sufficiently long and has a sufficiently high-aspect-ratio, that the flow is homogeneous in the streamwise x and spanwise z directions; the only direction of inhomogeneity is the wall-normal y direction. A friction Reynolds number is defined as $Re_\tau = u_\tau h/\nu$, based on the channel half-height h and a friction velocity

$$u_\tau = \sqrt{-\frac{h}{\rho}\frac{d\left\langle P_\mathrm{w}\right\rangle}{dx}} = \sqrt{\frac{\tau_\mathrm{w}}{\rho}} \tag{5.2}$$

where $d\left\langle P_\mathrm{w}\right\rangle/dx$ is the mean pressure gradient in the streamwise direction (externally applied pressure gradient that drives the flow in the channel) and $\tau_\mathrm{w} = -h\, d\left\langle P_\mathrm{w}\right\rangle/dx$ is the wall shear stress. Hereafter, the superscript '+' denotes the normalisation by viscous scale for velocity (u_τ), length ($\delta_\nu = u_\tau/\nu$) and time ($\tau_\nu = \nu/u_\tau^2$). Such quantities are given in wall (or viscous) units.

The Lagrangian point-particle approach is used to describe the dynamics of small inertialess particles. These tracer-particles passively follow the translational motion of the local fluid, with a rotational motion determined by the Jeffery's equation (Jeffery (1922)), that we recall to be,

$$\frac{dp_i}{dt} = O_{ij}p_j + \Lambda\left(S_{ij}p_j - p_i p_k S_{kl} p_l\right), \tag{5.3}$$

where O_{ij} and S_{ij} are the antisymmetric and symmetric parts of the fluid velocity gradient A_{ij} along tracer trajectories. The shape parameter $\Lambda = (\lambda^2-1)/(\lambda^2+1)$ is related to the aspect ratio λ of the ellipsoid, defined as the ratio between the length of the symmetry axis and that of two equal axis (see Fig. 2.1).

5.2.1.1 *Simulation set up*

The spheroids are suspended in a channel flow whose dynamics is integrated by the open-source spectral code *Channelfow 2.0* developed at EPFL (https://www.channelflow.ch). The DNS has been performed by co-authors in Campana et al.. The chosen domain size is $4\pi h \times 2h \times 4\pi h/3$ and simulations are performed using a de-aliased spectral code (Fourier-Chebyshev) with 192^3 collocation points. Time marching is done by a variable step-size, third-order semi-implicit backward differentiation formula (SBDF3) with a time step regularly adjusted to satisfy the CFL condition and capped to $\Delta t_{\max}$. The flow is maintained in a statistical steady state by imposing a constant bulk velocity. The resulting Reynolds number is $Re_\tau \approx 395$. A summary of the numerical parameters is shown in Table 5.1.

h	L_x	L_z	N_x	N_y	N_z	Δx^+	$\Delta t_{\max}$	U_b	ν	τ_w	Re_τ
1	4π	$4\pi/3$	192	193	192	25.9	0.01	0.835	$1.25\,10^{-4}$	$2.44\,10^{-3}$	395

Table 5.1: Parameters of the numerical simulation: channel half-width h; domain sizes in the streamwise (L_x) and spanwise (L_z) directions; resolutions N_x, N_y and N_z; step size Δx^+ in the streamwise direction (in wall units); capped value $\Delta t_{\max}$ of the adaptative time step; bulk velocity U_b; kinematic viscosity ν; wall shear stress $\tau_w = \nu\,\partial_y U(0)$; friction Reynolds number $Re_\tau = \sqrt{\tau_w}\,h/\nu$.

Particle trajectories (positions and orientations) are integrated using a second-order Adams–Bashforth scheme. Evaluating the fluid velocity at the particle location requires a high-order scheme to avoid spurious oscillations (Choi et al. (2004); Hinsberg, van et al. (2013)). As advocated by Stelzenmuller et al. (2017), we did not use a costly full spectral interpolation but rather a third-order Hermite cubic interpolation which requires evaluating the second-order derivatives of the fluid velocities at every time step. In order to evaluate the fluid velocity gradient, several schemes (trilinear, truncated Hermite, full Hermite) have been tested in the case of rods ($\Lambda = 1$). To assess such a choice, the particles tumbling rate $\langle \|d\boldsymbol{p}/dt\|^2 \rangle$ and their spinning rate $(1/4)\,\langle |\boldsymbol{p}\cdot\boldsymbol{\omega}|^2 \rangle$, where $\boldsymbol{\omega} = \nabla \times \boldsymbol{u}$ denotes the fluid vorticity at the particles position, have been measured. Up to statistical errors, no significant differences have been observed, advocating in favour of the cost-efficient trilinear interpolation that is used in the sequel.

Figure 5.1 shows the instantaneous vorticity amplitude (top) and the simultaneous orientation of rods (down) in a slice along the x and y directions. One clearly sees that close to the walls, the rods are preferentially aligned with the mean flow direction. In addition, one guesses that their orientation tends to follow the streamlines associated to detachment events.

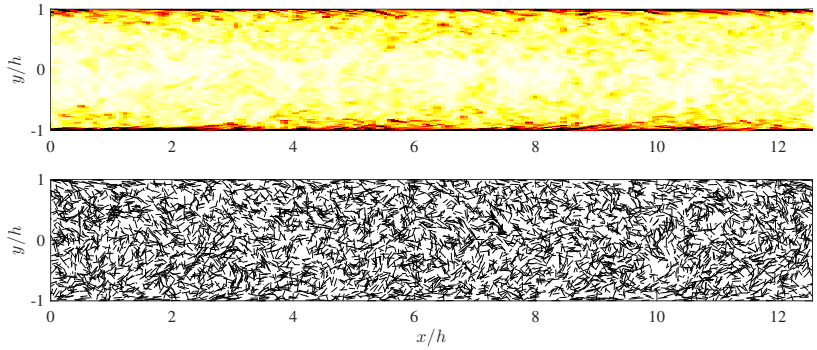

Figure 5.1: Top: instantaneous amplitude of the vorticity field in the $z = 0$ plane (white: low values, dark red: high values). Down: orientation of rods at the same instant of time for tracers located in the slice $0 < z < 0.025$.

The results of Eulerian-averaged velocity profile and Reynolds stress components for the DNS are shown in left and right panel of Fig. 5.2, respectively. The mean streamwise velocity profile $U(y) = \langle u_x \rangle$ shows the expected log-law behaviour $U^+(y^+) = (1/\kappa)\log y^+ + b$ at $y^+ \gtrsim 20$, with the extracted Von Kármán constant $\kappa = 0.384$ and $b = 4.17$, as obtained from the experimental measurements of Samie et al. (2018). The velocity variances (right panel) clearly reproduce the measurements in DNS or experiments (e. g., Pope (2001); Samie et al. (2018)).

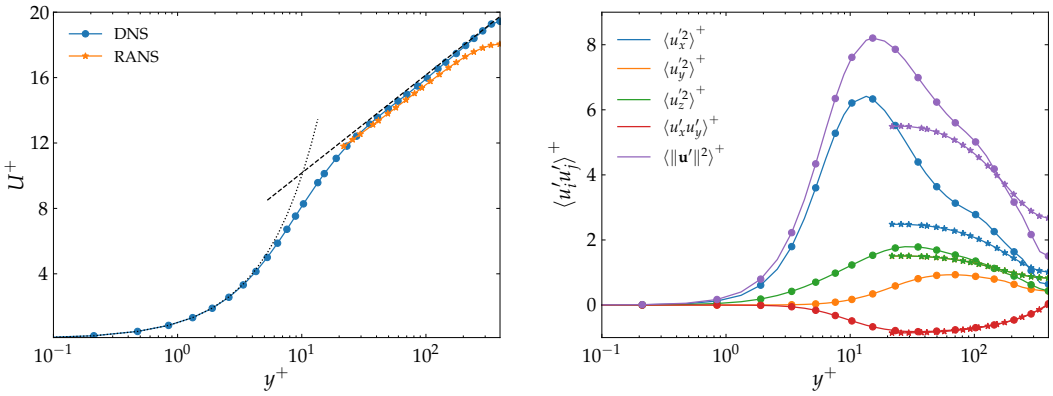

Figure 5.2: Left panel: Mean velocity profile $U(y) = \langle u_y \rangle$ (in wall units). The two dashed lines denote the linear viscous boundary layer $U^+(y^+) = y^+$ at $y^+ \lesssim 5$ and the turbulent log layer $U^+(y^+) = (1/0.384)\log(y^+) + 4.17$ at $y^+ \gtrsim 20$. Right panel: Reynolds stress components as a function of the wall-normal coordinate y^+. The DNS results are in lines with circle markers and RANS in lines with starred markers.

5.2.1.2 *A-DNS case*

For the *a priori* test case (A-DNS), every 200 time steps of DNS, 450 snapshots of the velocity gradient tensor has been averaged and the results stored on a uniform grid of 193 cells in wall-normal direction with $y^+ \approx 4$ for the first point away from the wall. Moreover, the trajectories computed from the fully resolved DNS dataset have been filtered in time with the same resolution above, and a total number of 450 snapshots stored. We anticipate that for this test case the orientation model for the spheroids (Eq. (5.12)) was disjointed from the hybrid Eulerian/Lagrangian solver and stand-alone integrated by using the numerical splitting scheme proposed in Chapter 4.

5.2.2 *Hybrid PDF method*

In two-phase flow modelling, various methods can be followed. Here, we consider a hybrid Eulerian-Lagrangian PDF approach (Minier et al. (2001)). The continuous phase is described by a classical Eulerian momentum approach, i.e. the fluid phase is represented by RANS equations (Pope (2001)). On the other hand, the particle phase is solved with a PDF approach, where the instantaneous exact equations are replaced with a set of modelled instantaneous equations. In general, for inertial spherical particles, the modelled equations for the particle velocity ($\boldsymbol{u}_p$) and the velocity of the fluid seen by the particle ($\boldsymbol{u}_s$), are the Langevin equations, that is a set of stochastic differential equations (SDEs). Then, particles are characterised by a particle state vector $\boldsymbol{Z} = (\mathbf{X}_p, \boldsymbol{u}_p, \boldsymbol{u}_s)$, being $\mathbf{X}_p$ the particle position, whose study is detailed in Minier

(2016). We recall from Chapter 4 that the general form of the state-of-the-art Langevin model (Minier (2016)) takes the form,

$$dX_{p,i} = u_{p,i}\, dt \tag{5.4}$$

$$du_{p,i} = \frac{1}{\tau_p}\left(u_{s,i} - u_{p,i}\right) dt \tag{5.5}$$

$$du_{s,i} = -\frac{1}{\rho_f}\frac{\partial \langle P_f \rangle}{\partial x_i} dt + \left(\langle u_{p,j} \rangle - \langle u_{f,j} \rangle\right) \frac{\partial \langle u_{f,i} \rangle}{\partial x_j} dt + G^*_{ij}\left(u_{s,j} - \langle u_{f,j} \rangle\right) dt + B_{s,ij}\, d\widetilde{W}_j(t), \tag{5.6}$$

where $\widetilde{W}_j(t)$ is a vector of independent Wiener processes. We anticipate that this Brownian vector is independent from that one introduced within the model for the orientation (Eq. (5.12)). The matrix is given by $G^*_{ij} = -(1/2 + 3/4\, C_0)(\varepsilon/k)\, H_{ij}$ where C_0 is a constant, k is the fluid turbulent kinetic energy and ε is the mean dissipation rate of the turbulent kinetic energy. The matrix H_{ij} accounts for the crossing-trajectories effect. The general diffusion coefficients matrix $B_{s,ij}$, as well as more others details on Eqs. (5.4)-(5.6) can be found in Minier (2016).

Compared to the case of inertial spherical particles presented above, here, in the presence of non-spherical inertialess particles, a fundamental aspect is the choice of the fibre state vector. Firstly, by considering (spheroidal) tracer particles, the models Eqs. (5.4), (5.5) and (5.6), using some simplification detailed in Minier (2016), need to be taken in the limit of vanishing inertia ($\tau_p \to 0$), that corresponds to consider the particle velocity tending towards the fluid velocity, i.e. in this case $\boldsymbol{u}_s = \boldsymbol{u}_f$. In this limit the modelled equations become (Chibbaro and Minier (2011)),

$$dX_{f,i} = u_{f,i} dt \tag{5.7}$$

$$du_{f,i} = -\frac{1}{\rho_f}\frac{\partial \langle P_f \rangle}{\partial x_i}\, dt - \frac{1}{T_L}\left(u_{f,i} - \langle u_{f,i} \rangle\right) dt + \sqrt{C_0 \varepsilon}\, d\widetilde{W}_i(t) \tag{5.8}$$

where T_L represents the Lagrangian time scale of the velocity correlation and is defined by $T_L = \frac{1}{(\frac{1}{2}+\frac{3}{4}C_0)}\frac{k}{\varepsilon}$ and the other quantities are defined precisely in Minier et al. (2004); Peirano et al. (2006). This model corresponds to the Simplified Langevin Model (SLM, Pope (1994)). In the above Langevin model, which has been reduced for the position and velocity of the fluid Eqs. (5.7)-(5.8), the fluid mean velocity field $\langle u_{f,i} \rangle$, the turbulent kinetic energy k, the mean dissipation rate $\langle \varepsilon \rangle$ and the mean pressure gradient, are provided by an Eulerian solver. In this case, for the two-phase calculation performed with Moment/PDF (or Eulerian/Lagrangian) approach, the time step can be further constrained by the fluid flow computation.

5.2.2.1 *Lagrangian stochastic model for the orientation*

Fibre modelling can be cast into the framework of microscopic, mesoscopic and macroscopic approaches. The stochastic (or mesoscopic) description brings the gap between DNS studies (microscopic) and averaged rheological relations (macroscopic). In this regard, presenting a stochastic Lagrangian model for the orientation of spheroidal tracer particle requires a brief discussion on how the fibre state vector can be defined.

Studying the orientational and rotational motion using Jeffery's equation (5.3) along a Lagrangian trajectory, requires knowledge of the velocity gradient, evaluated at the particle position, which means the fibre state vector is $\boldsymbol{Z} = (\mathbf{X}_f, \boldsymbol{u}_f, \boldsymbol{p}, \boldsymbol{A}_f)$, where $\boldsymbol{A}_f$ is the fluid velocity gradient along the Lagrangian trajectory. With respect to spherical particles, the fibre state vector is supplemented by particle orientation $\boldsymbol{p}$ and the fluid velocity gradient. This, from a modelling point of view, represents the fine-scale properties of the flow, that needs to be modelled.

Moreover, it should be noted that adopting a stochastic closure for the velocity of the fluid seen, which typically involves a Wiener process with uncorrelated, independent increments and continuous trajectories, nowhere differentiable, would yield no information on the velocity gradient. In fact, any knowledge about velocity increments in space as in DNS, are lost in the stochastic Lagrangian trajectories. Therefore, a stochastic Lagrangian model for the velocity gradient tensor seen by the particles was introduced (Chin and Geiser (2011); Chevillard and Meneveau (2013); Johnson and Meneveau (2018)), to include informations about the detailed dynamics of small scale turbulence.

However, small scale quantities are extremely complex to model. In addition, the model developed in Chapter 4 has been designed for an observation time Δt, larger than the Lagrangian correlation integral time of the velocity gradient τ_{I}. This implies that A_{ij} along the particle trajectory can be regarded as a fast process, such that the fibre state vector is reduced to $\boldsymbol{Z} = (\mathbf{X}_f, \boldsymbol{u}_f, \boldsymbol{p})$ and the coarse-grained information about A_{ij} is embedded in the SDE for $\boldsymbol{p}$.

Recalling from Section 4.3 (in Chapter 4), the stochastic model for the orientation of spheroidal particles has been introduced using the vector $\boldsymbol{q}$, which obeys the same linear terms in Eq. (5.3), but without compensating for any elongation, so that:

$$dq_i(t) = \left(\langle O_{ij}\rangle + \Lambda \langle S_{ij}\rangle\right) q_j\, dt + \left(\beta^a_{imj} + \Lambda\, \beta^s_{imj}\right) q_j \circ d\mathrm{w}^m_t, \quad p_i = \frac{q_i}{\|\boldsymbol{q}\|}, \tag{5.9}$$

where the orientation $\boldsymbol{p}$ is obtained by re-normalizing the vector $\boldsymbol{q}$. Equation (5.9) is expressed in the Stratonovich sense ($\circ$) and $d\mathrm{w}^m_t$ ($m = 1, \dots 9$) is a vector of a nine-dimensional Wiener process whose components are independent, standard, one-dimensional Wiener processes. The fluctuations contribution are expressed in terms of symmetric and antisymmetric tensors $\beta^s_{imj} = (\beta_{imj} + \beta_{jmi})/2$, $\beta^a_{imj} = (\beta_{imj} - \beta_{jmi})/2$, respectively.

Then, the closure of the model has been obtained assuming the velocity gradient fluctuations $A'_{ij} = A_{ij} - \langle A_{ij}\rangle$ Gaussian and short-correlated in time. In particular, the diffusion tensor in expression (3.23) has been expressed as,

$$\beta_{imj}\beta_{kml} = 2\,\mathcal{C}^{\mathrm{eff}}_{ijkl}, \tag{5.10}$$

where $\mathcal{C}^{\mathrm{eff}}_{ijkl}$ represents the effective diffusion tensor in expression (3.20). Furthermore, two different limits have been assumed: when the observation time of the dynamics is much larger than the integral correlation time ($\tau_{\mathrm{I}} = \max(\tau_{\mathrm{I}}^{ijkl})$), i.e. $\Delta t \gg \tau_{\mathrm{I}}$, and when $\Delta t \ll \tau_\eta$, i.e. the observation time is smaller than the Kolmogorov time scale τ_η, corresponding to the typical turnover time of the velocity gradient fluctuations. Then, the Kubo number has been defined $Ku = \tau_{\mathrm{I}}/\tau_\eta \ll 1$ giving the working hypothesis of the model.

5.2.2.2 *Model assumptions*

The modification induced by the mean shear on the velocity gradient correlation tensor, is far more intricate than the case of HIT flow, which can be fully analysed in terms of only one dimensional quantity ε/τ_η. As discussed in Chapter 3, in the presence of shear, the effective diffusion tensor $\mathcal{C}^{\mathrm{eff}}_{ijkl}$ fairly reproduced the the statistics for the orientation of a rod part. Indeed, this means, as we have seen, that the integral Lagrangian correlation time strongly depends on its different components τ_{I}^{ijkl}, and for an inhomogeneous flow, it depends also on the distance from the wall (y^+). For this reason, hereafter, a brief discussion on the behaviour of the integral Lagrangian correlation time τ_{I}^{ijkl} is presented.

Figure 5.3 (right panel) shows the integral Lagrangian autocorrelation time τ_{I}^{ijij} as a function of y^+. The overall behaviour of the integral time of the velocity gradient tensor tends to increase moving toward the centre of the channel. However, it strongly depends on the components. As

we can see, as an example, the component 1212 (orange line in lower triangular markers) is non monotonic with a minimum at $y^+ \approx 10$. This is the most important contribution, representing the component related to $\partial_y u'_x$, which expresses the inhomogeneous direction.

Another interesting quantity is constituted by the measurement of Ku^{ijkl} (in this case we report in the inset only the $ijij$ components), versus the distance from the wall. We can notice that the Kubo parameter changes with y^+: its variation, considering the set of components, is not extremely large, except for the 1212 and 1313. Therefore, we can consider its value fairly constant as a function of y^+, and varies, depending on the component, between 1.5 and 5. The already complex behaviour of τ_I^{ijkl} in the 2D homogeneous shear flow (Chapter 3) becomes even more intricate in a turbulent channel due to the effects of shear and inhomogeneity.

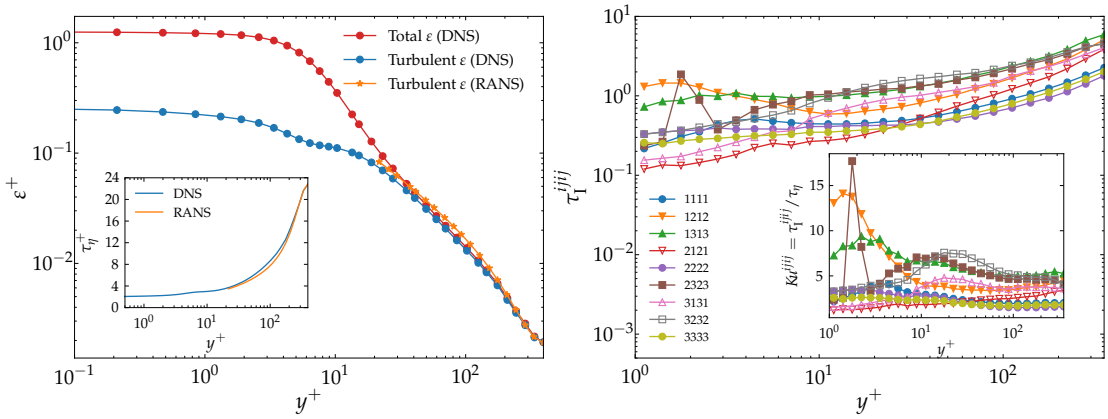

Figure 5.3: Left panel: Averaged kinetic energy dissipation $\varepsilon = 2\nu \langle S_{ij} S_{ij} \rangle$ as a function of y^+, where $\boldsymbol{S}$ denotes the symmetric part of the velocity gradient. Both the full dissipation (using $\boldsymbol{S}$) and the turbulent dissipation (using $\boldsymbol{S}'$) are represented in DNS and RANS case. In inset the Kolmogorov time scale $\tau_\eta = \sqrt{\nu/\varepsilon}$, in viscous units, is reported for both DNS and RANS as a function of y^+. Right panel: DNS measurements of the integral correlation time τ_I^{ijij} (autocorrelation components) as a function of the distance from the wall. In inset the measurements of Kubo parameter $Ku^{ijij} = \tau_I^{ijij}/\tau_\eta$ as a function of y^+.

Due to this intricate picture, in order to investigate the orientation model, the same assumptions discussed in Chapter 4 have been used for the correlation of β_{imj}. Recalling that the correlation tensor of the velocity gradient fluctuations $C_{ijkl}(0) = \langle A'_{ij}(0) A'_{kl}(0) \rangle$ was considered homogeneous, isotropic and satisfying incompressibility condition, we have

$$\beta_{imj}\beta_{kml} = 2\, D\, Ku(\langle A'_{ij} \rangle, y^+)\, (4\delta_{ik}\delta_{jl} - \delta_{ij}\delta_{kl} - \delta_{il}\delta_{jk}), \tag{5.11}$$

where $D = 1/(30\tau_\eta)$ and Ku as previously discussed is taken as a scalar quantity with a possible dependence on y^+. The outcome of considering isotropic fluctuations within the model for the orientation coincides to treat the Kubo number as a tuning parameter.

Under this hypothesis, the Lagrangian stochastic model for the orientation $\boldsymbol{p}$ was obtained using the Itô's Lemma on the renormalisation function $\boldsymbol{q} \mapsto \boldsymbol{p} = F(\boldsymbol{q})$ with $p_i = F_i(\boldsymbol{q}) = q_i/\|\boldsymbol{q}\|$. From Section 4.3 we recall the equation to be,

$$\begin{aligned} dp_i = {} & \langle O_{il} \rangle\, p_l dt + \Lambda \left(\langle S_{il} \rangle - p_i p_j \langle S_{jl} \rangle \right) p_l dt \\ & - \frac{\nu_s}{2} \Lambda^2 p_i dt + \nu_s \Lambda \left(dW^s_{il} - p_i p_j dW^s_{jl} \right) p_l - \frac{\nu_a}{2} p_i dt + \nu_a dW^a_{il} p_l, \end{aligned} \tag{5.12}$$

where $\nu_s = \sqrt{6\, D\, Ku}$ and $\nu_a = \sqrt{10\, D\, Ku}$ (with $D = 1/(30\tau_\eta)$) contain the scaling parameters. We have used the matrix notation for the Wiener process $W^{il}_t = w^{3(i-1)+l}_t$, that is the Wiener

vector w_t^m has been expressed in terms of 3 by 3 matrix using the same nine scalar Wiener process (Section 4.3). In addition, the Wiener matrix has been decomposed in its symmetric and antisymmetric part $\mathrm{W}_{il}^s = (\mathrm{W}_t^{il} + \mathrm{W}_t^{li})/2$ and $\mathrm{W}_{il}^a = (\mathrm{W}_t^{il} - \mathrm{W}_t^{li})/2$ respectively. Finally, Eq. (5.12) results to be the stochastic version of Jeffery's equation (5.3).

As said, the fluctuating part of the model depends on the ratio $Ku(y^+)/\tau_\eta(y^+)$. Several tests have been performed in order to find a good value of the ratio $Ku(y^+)/\tau_\eta(y^+)$ which gives comparable results, when fitting the variance of the orientation $\langle p_i^2|y^+\rangle$ (no sum on i), as we will present in Section 5.3. Interestingly, it turns out that the best agreement is obtained by fixing $Ku = 1$, and taking the value of τ_η in the bulk of the channel, so that this ratio for the model is taken constant all along the channel, i.e. we have a value of $1/\tau_\eta^{\mathrm{bulk}}$ that drives the diffusive part of the orientation model. A first explanation for this result can be given by considering that Ku^{ijkl}, as observed above, shows a very weak dependence along the channel. On the other hand, it is not clear why the best choice corresponds in fixing the value of $\tau_\eta^{\mathrm{bulk}}$ in the centre of the channel. From preliminary tests we obtained that using the value of $\tau_\eta(y^+)$ as in inset of Fig. 5.3 (right panel), the variance of the orientation vector $\boldsymbol{p}$ remained randomly oriented for all the shape parameters across the channel. This means that the diffusion term in the model is stronger than the mean velocity gradient contribution.

Finally, these tests have been performed in the case of the A-DNS set-up, and then, the same configuration has been used to assess how the model performs when coupled with RANS. Indeed, both turbulence dissipation, and consequently $\tau_\eta^{\mathrm{bulk}}$ results for the RANS are in perfect agreement with DNS measurements, as shown in Fig. 5.3 (left panel). This ensures that the fluctuating part of the model in A-DNS and RANS cases are the same, leading to the conclusion that any difference that we will experience by observing both orientation and rotation statistics can be attributed to other contributions, such as mean velocity gradient, and/or the trajectories behaviour, but not to the stochastic part of the orientation model in Eq. (5.12).

In general, the integral correlation time τ_{I}^{ijkl} in Eq. (5.10), measured from DNS data, could provide the spatial dependence of the diffusion tensor within the coordinates of Eq. (5.9). We notice, as a perspective, that an effective correlation tensor could be tailored by applying a sort of homogenization between the components of the integral time correlation τ_{I}^{ijkl}, in order to provide some information about anisotropic fluctuations of the velocity gradient, that are completely discarded when isotropic and homogeneous assumptions are made.

5.2.2.3 *Simulation set up*

In the hybrid Lagrangian-Eulerian PDF approach, the first step is to evaluate the mean field fluid variable which is included in the Lagrangian model Eqs. (5.7)-(5.8). The channel flow has been solved on an infinite one dimensional rectangular box of size $x = 0.05$, $y = 1$ and $z = 0.05$. The domain is discretised with 1 cell along the streamwise direction and 100 cells along y direction. Periodic boundary conditions are imposed along the x and z directions while a symmetry condition is imposed along $y = 1$ and a wall condition is imposed on the bottom surface $zy = 0$. The flow is numerically computed using *Code_Saturne* (developed by Électricité de France), assuming that the flow is incompressible and by imposing a streamwise pressure gradient corresponding to a given friction velocity. The properties of the turbulent steady flow are obtained using a LRR-IP $R_{ij} - \varepsilon$ model (Launder et al. (1975)) with a Rotta constant $C_0 = 3.5$ (i.e. $C_R = 1 + 1.5\,C_0 = 6.25$). The diffusion model used in the fluid simulation is the isotropic model of Shir, while the wall function model corresponds to the two-scale log wall function model implemented in *Code_Saturne*. The fluid viscosity is set to $\nu = 0.0025$, so that the flow Reynolds number based on near-wall scales is $Re_\tau = 395$.

Spheroidal particles are tracked within this turbulent flow using the Lagrangian module in *Code_Saturne*. The orientation model for the spheroids (Eq. (5.12)) is integrated by using the

numerical splitting scheme developed in Chapter 4. Particles are initially injected uniformly in the domain and uniformly oriented. As for the fluid case, periodic boundary conditions are imposed along the x- and z-direction while a symmetry is imposed for $y = 1$. A wall boundary condition is applied for particles crossing the internal face at $y^+ \approx 20$.

Another difficulty arises here for the boundary condition that has to be applied for spheroid orientations. More precisely, we cannot resort to the use of a simplified model where the orientation of a spheroid is fixed to a given value after the boundary condition is applied. This is indeed not consistent with the measurements made using DNS simulations: the spheroids coming from the region below $y^+ \approx 20$ display a range of possible orientations. This distribution of orientation strongly depends on the aspect ratio of the spheroids : spherical particles have a uniform distribution, while rods have a higher probability to be aligned along the streamwise direction and disks have a higher tendency to align along the wall normal direction. These measurements show that the boundary conditions for spheroid orientation have non-trivial distributions of orientations.

In order to study the orientation, different kinds of boundary conditions on the orientation were applied. Some preliminary tests have been performed by modifying the boundary condition on the orientation of spheroids using data available from the DNS measurements. The idea was to resort the orientation distribution which gives a higher probability to be aligned with the x-direction as the aspect ratio nears $\Lambda = 1$ (rods), and a higher probability to be aligned with the y-direction as the aspect ratio nears $\Lambda = -1$ (disks). Preliminary results did not show significant improvements on the model capability to reproduce the orientation statistics. Moreover, imposing the orientation distribution (at $y^+ \approx 20$) coming from DNS measurements is not properly in the spirit of modelling, which would limit as much as possible external inputs. Interestingly, as we will briefly discuss later, using such kind of near-wall information for the orientation can introduce an irreversibility within the model.

The RANS results provide a quite accurate description of the mean velocity profile within the first part of the log-layer, as shown in Fig. 5.2 (right panel). However, the bulk velocity appears to be underestimated. Considering the Reynolds stress profiles globally in Fig. 5.2 (left panel), they are different from DNS data, except for the component $\langle u'_x u'_y \rangle$, where they match perfectly. A good agreement is found also for $\langle u'_z \rangle$.

It should be noted that the aim of using RANS is not meant to evaluate its goodness with respect to DNS, but to provide a preliminary test of the orientation model in an industrial CFD code. Moreover, in the context of hybrid Eulerian/Lagrangian PDF methods, it is not necessarily true that the improvement in the prediction of the fluid mean velocity $\langle u_{f,i} \rangle$ leads to an improvement in the overall predictivity of the model. In this respect, is interesting to understand for the velocity of the fluid seen $u_{f,i}$, whether Eq. (5.8) is coherent with the fluid phase description provided by the Eulerian solver. Indeed, when hybrid Eulerian/Lagrangian methods are used on particle simulations, a consistency issue could arise between Eulerian and Lagrangian solvers. The inconsistency is the so called spurious drift effect (Minier and Peirano (2001)) that is recurrent in many Lagrangian stochastic models. In particular, it refers to the limit case of particle tracers, where the Lagrangian mean velocity field directly extracted from the Langevin model must be equal to that coming from the turbulence model chosen in the Eulerian solver.

In our case, this is a key point since we have to simulate the behaviour of inertialess particles. The Langevin model implemented in *Code_Saturne* is consistent in the tracer limit by construction, and is thus free from spurious drifts. However, this model showed some limits in accounting for the presence of near-wall instantaneous coherent structures, restricting the analysis of the orientation results to $y^+ \gtrsim 20$.

In perspective, others hybrid methods (Chibbaro and Minier (2008)) can be considered. In particular for the prediction of coherent structures, which are relevant when studying

particle dynamics near the walls. A better estimate of average fluid quantities can arise from improvements in Langevin equations, provided that possible inconsistency errors are faced.

5.3 ORIENTATION RESULTS

Inertialess particles are transported by local fluid, regardless of their shape. The shape parameter Λ (or equivalently the aspect ratio λ) has a strong impact on the particle orientation and rotation dynamics as shown in the snapshot (from DNS) of Fig. 5.4, where the orientation of rod-like particles differs from that of disk-like particles. Inertialess particles are uniformly

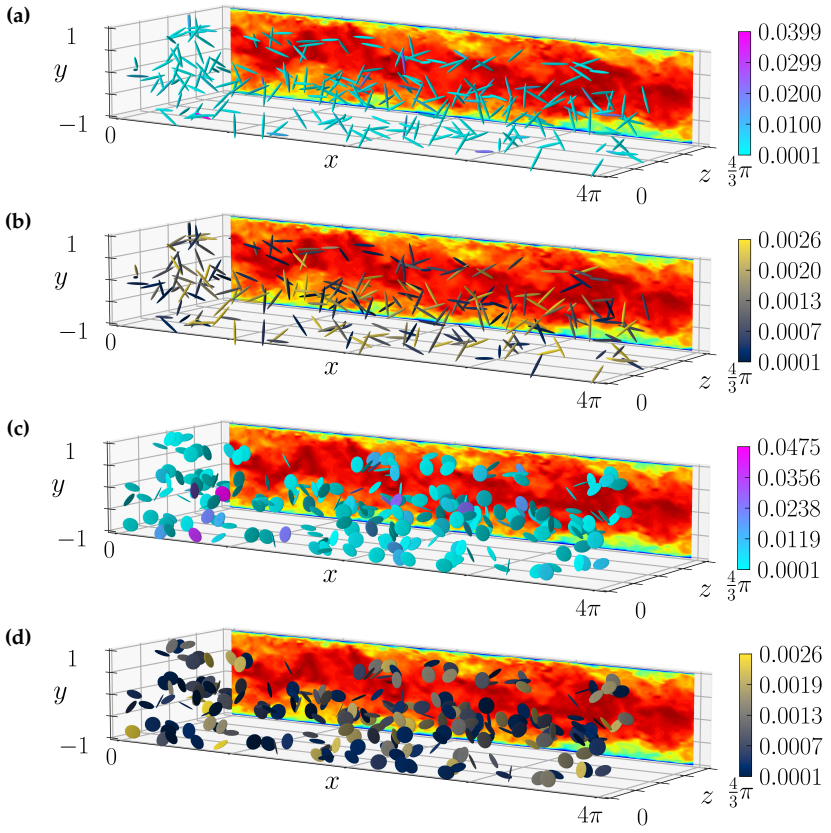

Figure 5.4: Instantaneous distribution of prolate particles with shape parameter in DNS: $\Lambda = 0.95$ in (a)-(b) and oblate particles with shape parameter $\Lambda = -0.95$ in (c)-(d). The shape reflects the particle orientation and colour-coding indicates the tumbling rate in (a) and and the spinning rate in (b) of prolate particles; and the tumbling rate in (c) and the spinning rate in (d), of oblate particles, in viscous units. The background contour represents instantaneous streamwise velocity of fluid in $x - y$ plane.

distributed in space all across the channel. In the bulk region of the channel, spheroids are randomly oriented since turbulence is nearly homogeneous and isotropic. Far from the core region of the channel, the shape of the particles determines the preferential orientation of spheroids. Particularly, in the near wall region, rods particles ($\Lambda = 0.95$ in Fig. 5.4a or 5.4b) are strongly aligned in the streamwise direction, while disks ($\Lambda = -0.95$ in Fig. 5.4c or 5.4d) show a preferential orientation of their symmetric axis $\boldsymbol{p}$ in the wall-normal direction. This behaviour is in line with previous works that consider almost two regions of the channel flow: a region near the centre and a region near the wall of the channel (Challabotla et al. (2015b); Yang et al. (2018); Jie et al. (2019)).

We anticipate that the different behaviour of the preferential orientation in various regions of the channel, impacts also the two contributions to particle rotation, i.e. tumbling and spinning. The colour coding in Fig. 5.4 reveals the different behaviour of tumbling, in Fig. 5.4a, and spinning, in Fig. 5.4b for rod-like particles, and analogously for disk-like particles in Fig. 5.4c and Fig. 5.4d.

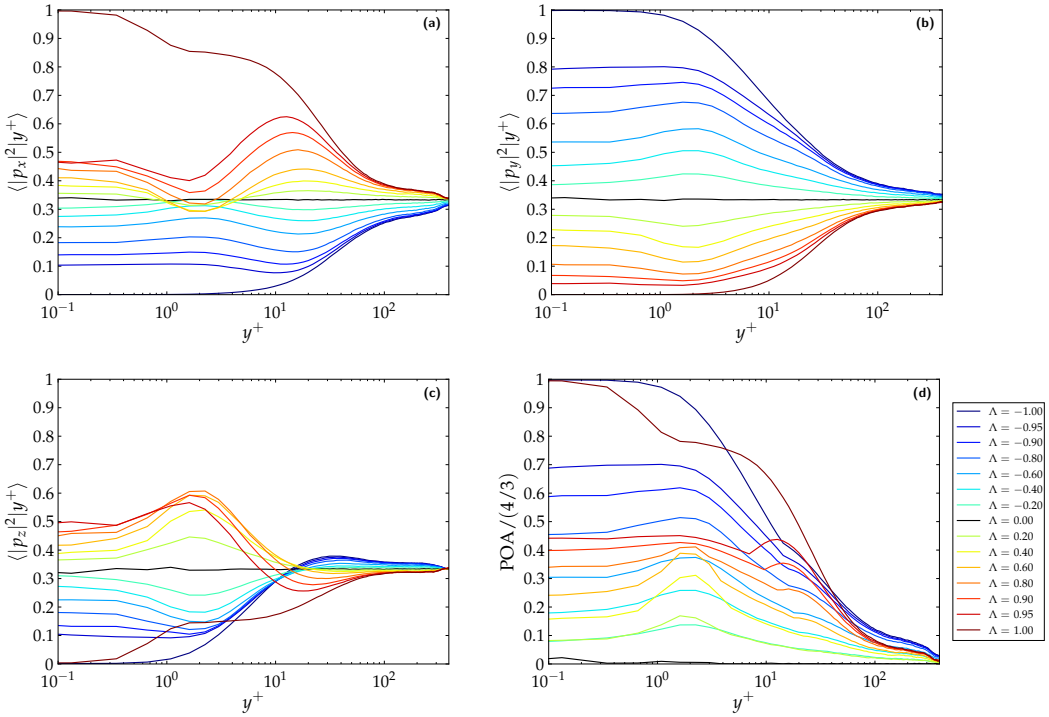

Figure 5.5: Mean-squared components of the orientation vector $\boldsymbol{p}$, in DNS, as a function of the distance y^+ to the boundary for different values of the shape parameter Λ as labelled. In (a) streamwise, (b) wall-normal and (c) spanwise directions, respectively. In (d) scalar measure of particle orientation anisotropy POA $= |\langle |p_x|^2|y^+\rangle - 1/3| + |\langle |p_y|^2|y^+\rangle - 1/3| + |\langle |p_z|^2|y^+\rangle - 1/3|$ renormalised to its maximum value $(4/3)$.

The squared average components, in DNS, of the orientation vector $\boldsymbol{p}$ are shown in Fig. 5.5a for the streamwise, in Fig. 5.5b for the wall-normal, and in Fig. 5.5c for the spanwise component, each time as a function of the distance from the wall, for the entire range of the shape parameter, from $\Lambda = -1$ to $\Lambda = 1$ (in legend). Prolate particles are oriented, noticeably, differently from oblate particles, across the viscous sub-layer and buffer-layer $y^+ \approx 30$. Spherical particles are always randomly oriented all along the wall-normal direction, with a squared averaged equal to $1/3$. It can be observed from Fig. 5.5b that the preferential orientation, moving from oblate to prolate particles, varies monotonically. Moreover, longer rods in the viscous sub-layer $y^+ < 5$ become perfectly aligned with the mean shear, and very flat disks perfectly align perpendicular to the flow direction. Indeed in this region the presence of the mean shear is dominant, such that the alignment reaches a constant value which is different for each Λ. More intricate variations are visible along streamwise direction in Fig. 5.5a. The alignment in the streamwise direction, for $\Lambda = 1$ and $\Lambda = -1$, confirms the behaviour of spheroids in the wall-normal direction. A less clear picture is given by the range of values with finite aspect ratio. In this case, the behaviour of the alignment above the log-layer is no longer monotonic, showing a qualitatively different orientation of prolate particles with respect to the oblate ones. In fact, the alignment of prolate particles increases from the centre of the channel up

to $y^+ \approx 10$, to subsequently decrease in the buffer region, reaching a minimum within the viscous sub-layer. This behaviour is less marked in the case of oblate particles.

The mechanism could be explained by the presence of coherent structures within the channel flow. In wall-bounded turbulence the flow can be described as a collection of interacting coherent structures that greatly contribute to the flow dynamics. The existence of extreme stress events near the wall of the turbulent channel are referred to 'sweeps' and 'ejections', in accord with a common terminology, and have been linked to the action of quasi-streamwise vortices (Polanco (2019)). These are elongated vortical structures almost aligned with the streamwise coordinate, but slightly tilted in the wall-normal direction. The quasi-streamwise vortices are typically found in the buffer-layer and their average diameter is of 40 viscous units, that is, comparable to the size of the buffer region. Away from the buffer layer, the most significant coherent motions are hairpin vortices. These are formed by pairs of quasi-streamwise vortices that lift up from the wall and merge forming a loop (Marusic and Adrian (2010)). Hence quasi-streamwise vortices are often the legs of hairpin vortices, and represent their extension into the inner region of the flow (Adrian (2007)). The head of a hairpin vortex is typically located above $y^+ \approx 100$. The presence of these structures can explain the particular behaviour of the orientation within the buffer-layer and in the emitting zone of viscous sub-layer.

This picture of intricate structures leads to a non-trivial preferential particle alignment in anisotropic turbulence with both, vorticity, and Lagrangian stretching direction of the velocity gradient tensor, as investigated by Zhao and Andersson (2016), and could explain the aforementioned findings about particle orientation. Finally, the behaviour of streamwise and wall-normal components is directly reflected along spanwise direction in Fig. 5.5c, since the sum of the squared average components must stay unitary. Regarding the behaviour in the bulk region of the channel, $\langle |p_x|^2 | y^+ \rangle \approx \langle |p_y|^2 | y^+ \rangle \approx \langle |p_z|^2 | y^+ \rangle \approx 1/3$, irrespective of the particle shape. This confirms that both, prolate and oblate particles tend to orient themself randomly in the almost isotropic homogeneous vorticity field.

A measurement of the anisotropy of the orientation is shown in Fig. 5.5d, where the particle orientation anisotropy (POA) renormalised, measures the deviation from the random distribution 1/3. Oblate particles present much more departure from isotropy than prolate shapes, especially above the buffer layer. This is a direct consequence of the particular behaviour of the squared average of the orientation vector for the streamwise components. Further, the deviation from random distribution between oblate and prolate particles tends to decrease when $|\Lambda|$ becomes small. Earlier, the particle orientation anisotropy has been investigated in Couette–Poiseuille flow by Yang et al. (2018), observing almost the same behaviour for the half-height of the domain considered in their investigation.

The mean squared orientation results for the model in the *a priori* (A-DNS) test case, are shown in Fig. 5.6. All results are presented for $y^+ \gtrsim 4$, since the stochastic model was not designed to reproduce the features above the viscous sub-layer. Indeed, particles below this threshold are no longer resolved by the classical stochastic hybrid Eulerian/Lagrangian PDF method. The overall results show that a fairly good agreement is obtained between model prediction and DNS data for $y^+ \gtrsim 30$, in particular for prolate particles (upper triangles).

The orientation of both, oblate and prolate particles in the model for the wall-normal component, in Fig. 5.6b, slightly overestimates the DNS (continuous lines) in the log-layer region. Moreover, the model above this region, for small values of $|\Lambda|$, tends to reach a constant value approaching channel walls. The trend of the curves for each Λ all along y^+, moderately deviates from DNS, with a slope of the first derivative (with respect to y^+) which is less pronounced in the model than in DNS. This can be related to the presence of anisotropy fluctuations all along the channel in the DNS case, particularly approaching the channel wall. Conversely, the model considered an isotropic correlation tensor for the velocity gradient fluctuations. Indeed, as we have presented in Chapter 3, including this additional feature in

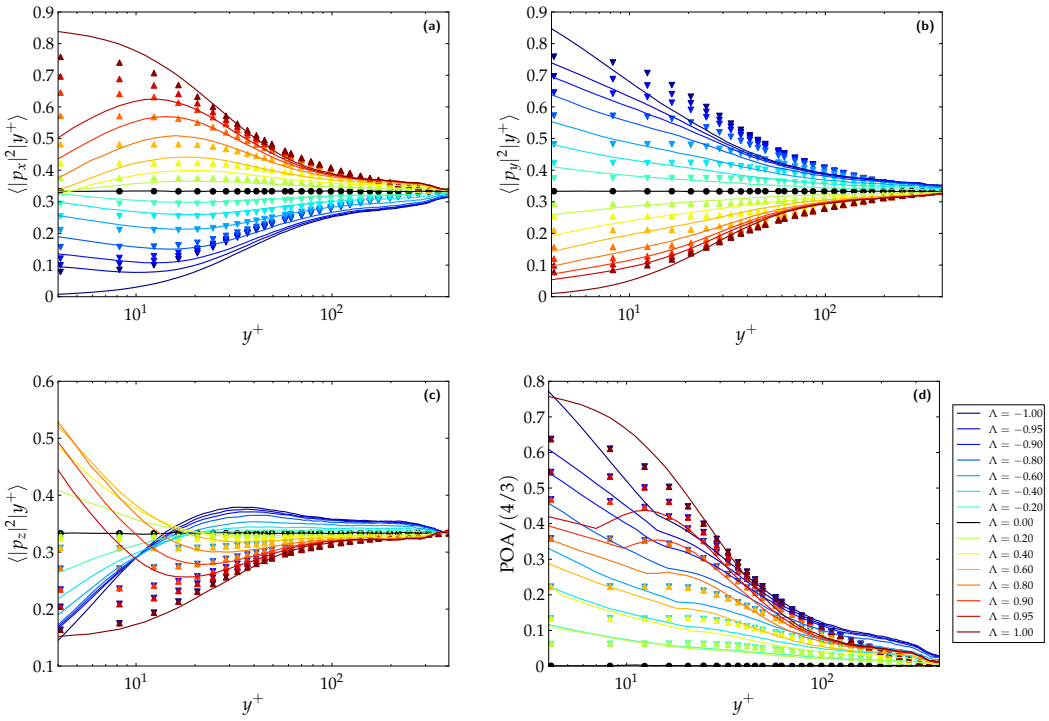

Figure 5.6: Mean-squared components of the orientation vector $\boldsymbol{p}$ as a function of the distance y^+ to the boundary for different values of the shape parameter Λ as labelled. DNS case (continuous lines) and model in A-DNS case (markers: $\Lambda < 0$ in lower triangles, $\Lambda = 0$ in circle, $\Lambda > 0$ in upper triangles). In (a) streamwise, (b) wall-normal and (c) spanwise directions, respectively. In (d) scalar measure of particle orientation anisotropy POA $= |\langle |p_x|^2|y^+\rangle - 1/3| + |\langle |p_y|^2|y^+\rangle - 1/3| + |\langle |p_z|^2|y^+\rangle - 1/3|$ renormalised to its maximum value $(4/3)$.

the model is not easy already in two-dimensional homogeneous shear flow, which becomes even more intricate in a three-dimensional channel flow. Additionally, another possible reason that could explain this difference relies on having considered a constant parameter $1/\tau_\eta^{\text{bulk}}$ for the model fluctuations. Indeed, it is possible that a finer tuning is required, by introducing a dependency on y^+. In our opinion, from a modelling point of view, it could be better to fully explain the employment of this constant factor, that at present is not justified, than to tune the orientation statistics along the wall normal direction.

Figure 5.6a shows the behaviour of the streamwise component. Here, a good agreement is found for prolate particles for $y^+ \gtrsim 30$. In contrast, the change of concavity is not reproduced by the model for $y^+ \lesssim 12$, by the presence of complex turbulent structures within this region. For oblate particles we find that the model is able to qualitatively reproduce DNS results all along the channel, even if flatter disks remain more isotropic than the DNS.

A limit of the model can be observed, regarding the mean squared orientation for the spanwise component in Fig. 5.6c. Indeed, prolate (in upper triangles) and oblate particles (in lower triangles) have the same behaviour (they are exactly superposed). Prolate particles with finite aspect ratio are well reproduced by the model for $y^+ \gtrsim 30$ and an even better behaviour is found for longer rod ($\Lambda = 1$) that matches DNS results all along y^+.

The fact that prolate and oblate particles act in the same manner in the model can be explained by the 'time reversibility' of the model. Indeed, the model considers a Gaussian noise for the velocity gradient fluctuations. In case of Gaussian stochastic processes, there is time symmetry $t \mapsto -t$. This means that the probability of velocity gradient fluctuations

$\boldsymbol{A}'$ and $-\boldsymbol{A}'$ are the same. Moreover, having imposed the isotropy condition means that the probability of $\boldsymbol{A}'$ and $\boldsymbol{A}'^{\intercal}$ are the same (Il'Yn and Zybin (2015)). This implies, in the orientation model (Eq. (5.12)), that changing $|\Lambda| \mapsto -|\Lambda|$ has the effect in Eq. (5.3) (considering only the fluctuations) to obtain $\boldsymbol{A}' = \boldsymbol{O}' + |\Lambda|\boldsymbol{S}'$ and $-\boldsymbol{A}'^{\intercal} = \boldsymbol{O}' - |\Lambda|\boldsymbol{S}'$. This corresponds to have a model for the orientation which behaves in the same manner, having the same probability passing from considering prolate Λ to oblate particles $-\Lambda$.

Conversely, velocity gradient in turbulence is characterised by highly non-Gaussian statistics. As a result, time symmetry is broken, since the time reversal $t \mapsto -t$ would also reverse the direction of energy flux. That is, a real turbulent flow is time irreversible due to the dissipation, with energy that flows from large scales into small scales. In particular, Xu et al. (2014) showed that the motion of a single fluid particle provides a clear manifestation of time irreversibility. Namely, fast moving particles suddenly decelerate into regions where the fluid motion is slow, and the mechanism can be attributed to the presence of rare 'flight-crash' events, as defined by the authors. The implication of time asymmetry on the motion of fluid particles has been extensively studied, being of great interest in Lagrangian turbulence (Falkovich (2009); Jucha et al. (2014); Xu et al. (2014); Il'Yn and Zybin (2015); Xu et al. (2016)).

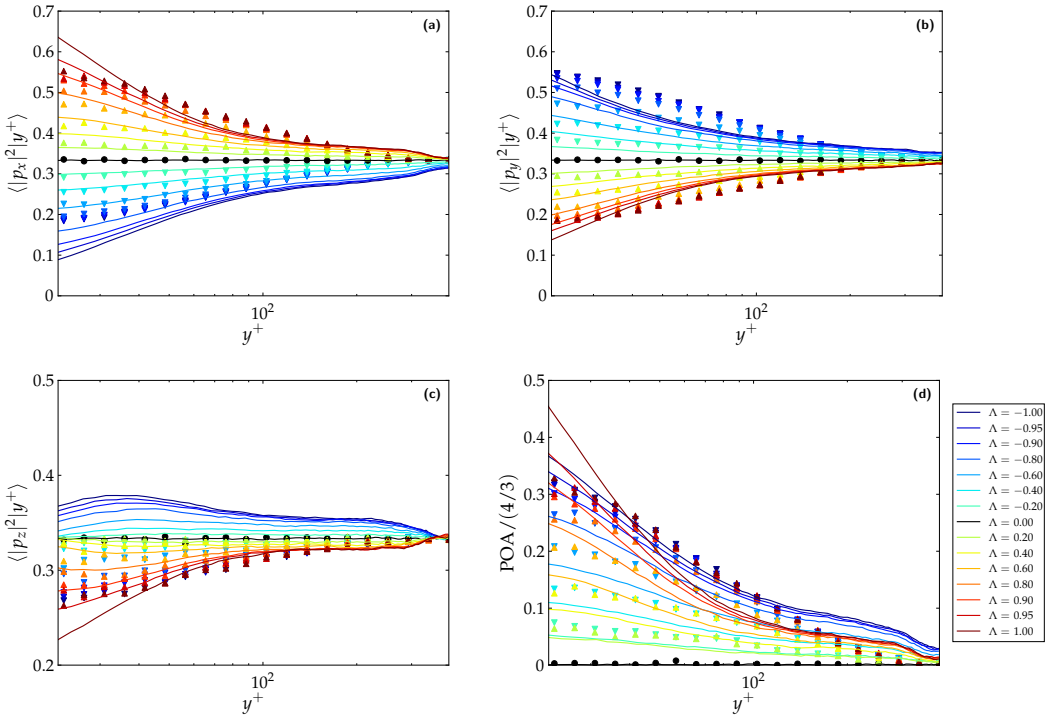

Figure 5.7: Mean-squared components of the orientation vector $\boldsymbol{p}$ as a function of the distance y^+ to the boundary for different values of the shape parameter Λ as labelled. DNS case (continuous lines) and model with RANS (using *Code_Saturne*) case (markers: $\Lambda < 0$ in lower triangles, $\Lambda = 0$ in circle, $\Lambda > 0$ in upper triangles). In (a) streamwise, (b) wall-normal and (c) spanwise directions, respectively. In (d) scalar measure of particle orientation anisotropy
$\mathrm{POA} = |\langle |p_x|^2|y^+\rangle - 1/3| + |\langle |p_y|^2|y^+\rangle - 1/3| + |\langle |p_z|^2|y^+\rangle - 1/3|$ renormalised to its maximum value $(4/3)$.

The comparison between the model (A-DNS) and DNS results for the measurements of the global particle anisotropy with the mean squared orientation is reported in Fig. 5.6d. Firstly, the same behaviour for positive and negative values of Λ confirms the observation in Fig. 5.6c, that was restricted only to the case of the spanwise component. Here, the time reversibility of the

model is more visible since we are considering the global contribution of the three components. We can argue that the anisotropy in the channel flow is driven by two main contributions: the first is given by the mean part of the velocity gradient tensor, which increases getting closer to the channel wall; the second is related to the fluctuations, where the correlations become more and more anisotropic near the wall.

This means that the anisotropy of mean contribution tends to dominate, at least for $y^+ \gtrsim 20$, the contribution of anisotropic fluctuations. Moreover, model results confirm that the presence of fluctuations are still important far from the wall, leading to a different trend for the model and the DNS. In particular, this information highlights that in order to improve the model behaviour the addition of an anisotropic correlation tensor for the fluctuations of the velocity gradient, is needed, as we did in the two dimensional case (Chapter 3).

Following previous results of the model, in the *a priori* case (A-DNS), we want to analyse the behaviour of the mean squared components of the orientation $\boldsymbol{p}$ in the RANS case. These results are presented in Fig. 5.7, for $y^+ \gtrsim 20$. The streamwise and wall-normal directions, in Fig. 5.7a and 5.7b, exhibit a fairly good agreement with DNS data (continuous line). Close to the centre of the channel, the model predicts a slightly more random orientation, in both, long rod ($\lambda > 0$) and flatten disk ($\lambda < 0$), as already observed for the A-DNS case in Fig. 5.7a. Furthermore, for such kind of particles, within the zone $20 \lesssim y^+ \lesssim 50$, the model shows a less steep trend (in both very oblate and very prolate particles) while approaching the wall of the channel with respect to the results obtained for DNS and A-DNS.

A possible explanation of the discrepancy between the RANS and A-DNS results can be given considering the component of the mean velocity gradient tensor $\langle \partial u_x / \partial y \rangle$. In fact, the variation of this component with y^+ from the centre towards the wall of the channel is smoother than the DNS case. In particular, for $y^+ \lesssim 50$ its derivative is steeper than the prediction of RANS.

In the spanwise direction, the behaviour under change of $\Lambda \to -\Lambda$ is still present, which confirms the time reversibility of the model, as pointed out in Fig. 5.5c (DNS case). Finally, the particle anisotropy (POA) in Fig. 5.7d, does not appear very different from the A-DNS case.

We want to remark that the RANS results are obtained without imposing a near-wall model on the orientation. On the other hand, as anticipated in Section 5.2.2.3, the RANS model has been also tested imposing the orientation distribution measured from DNS data. It is clear that this information was too detailed for the modelling. Nonetheless, by using this kind of near-wall model for describing particle orientation at $y^+ \approx 20$, the reversible behaviour observed and discussed in the A-DNS and RANS cases, was broken. In fact, a slightly distinction between oblate and prolate particles was observed. This phenomenon suggests, in perspective, that one possible approach to introduce irreversibility in the model behaviour, consists in the development of near-wall models for particle orientation.

5.4 ROTATION RESULTS

The rotational dynamics of any non-spherical particle strongly depends on how the particle orients itself in a turbulent flow. The various states of particle rotation are therefore distinctly different in isotropic and anisotropic wall turbulence. In the latter, the strong fluid vorticity field in the near-wall region, in combination with the preferential particle orientation observed in Fig. 5.5, makes the rotational dynamics of the spheroidal particles crucially dependent on the shape and on the wall-normal direction y^+ of the channel.

The measurements of the particle, in their 'classical' definitions (Byron et al. (2015)), tumbling rate $\langle \| d\boldsymbol{p}/dt \|^2 \rangle$ and their spinning rate $(1/4) \langle |\boldsymbol{p} \cdot \boldsymbol{\omega}|^2 \rangle$, where $\boldsymbol{\omega}$ is the fluid vorticity at the particle position in the DNS case as a function of the distance from the wall, are reported in Fig. 5.8. The variation of tumbling (left panel) for different values of the shape parameter Λ

(in legend) indicates that the asymmetry between prolate and oblate particles observed in the bulk, which is close to the HIT case, persists in the turbulent boundary layer. Moreover, the tumbling rate is strongly depleted for oblate and prolate particles with zero or infinite aspect ratio ($\Lambda = -1$ or $\Lambda = 1$), when entering in the viscous sub-layer.

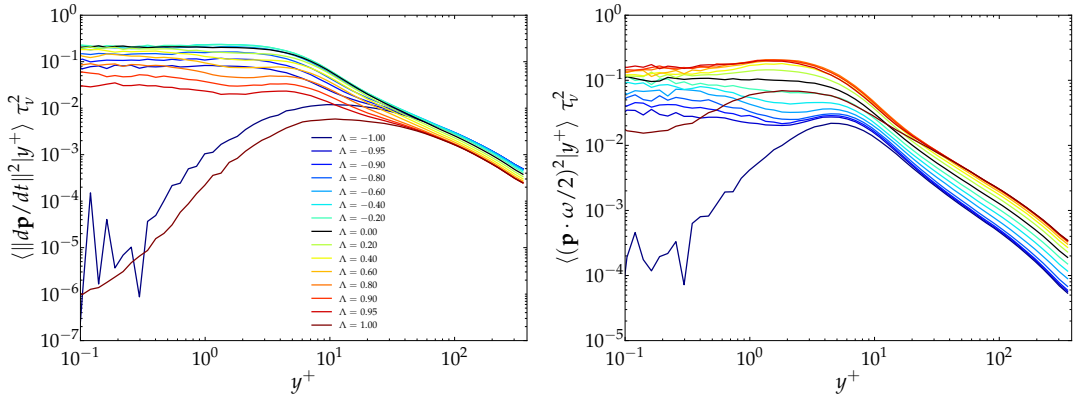

Figure 5.8: DNS results of mean-square tumbling rate (left panel) and spinning rate (right panel) in viscous units τ_ν, as a function of the distance y^+ to the boundary for various values of Λ as labelled.

The spinning rate (right panel) shows as well these asymmetries all along the wall-normal direction, where now the prolate particles tend to spin faster than oblate particles. Moreover, the spinning rate shows a change of sign of the derivative in the interval $1 \lesssim y^+ \lesssim 5$ for both oblate and prolate particles, but not for spherical ones ($\Lambda = 0$). This behaviour happens in the critical zone, i.e. when particles enter in the viscous sub-layer, where there is an interaction between the shear dominant region and the buffer-layer.

We can observe that both tumbling and spinning rates are maximal close to the boundary, and decrease when moving away from the walls. This effect certainly originates from the fact that turbulent shear is maximal at the boundary. A special case is represented by the limit case of the longest rods ($\Lambda = 1$) and flatten disks ($\Lambda = -1$). Finally, it is important to notice that the quasi-discontinuous behaviour is an artefact coming from the choice of the parameters. Indeed, we anticipate that, as we will see from Fig. 5.9 (left panel), the rotation rates in the viscous sublayer show a regular behaviour once represented as a function of the aspect ratio λ, rather than the shape parameter Λ.

In order to shed light on the effect of shear, Fig. 5.9 reports the mean square rotation rates obtained in the bulk (right panel) of the channel and in the viscous sublayer (left panel), as a function of the aspect ratio, rather than of the shape parameter. In the right panel of Fig. 5.9, the tumbling, the spinning and the total rotation, in the bulk of the channel, have been rescaled by the Kolmogorov time $\tau_\eta = \sqrt{\nu/\varepsilon}$.

The various components of the rotation rate reveal that the bulk of the channel is nearly HIT, and measurements confirm similar findings in HIT from other groups, Parsa et al. (2012); Byron et al. (2015). All mean-square rates show similar behaviours, with a higher tumbling for oblate particles (disks with small aspect ratios), and a higher spinning for prolate particles (rods with large aspect ratios). Moreover, the asymmetry between oblate and prolate particles (that is when changing $|\Lambda| \mapsto -|\Lambda|$) is clearly visible, indicating the importance of time-irreversible statistics of the fluid velocity gradients along tracer trajectories, also discussed in Ni et al. (2014); Byron et al. (2015).

On the other hand, on the left panel, the three rotation rates in the viscous sub-layer, rescaled by the viscous time scale τ_ν, show the strong shear effect on the particle aspect ratio. In the viscous sub-layer, the strong preferential orientation of highly elongated aspherical particles

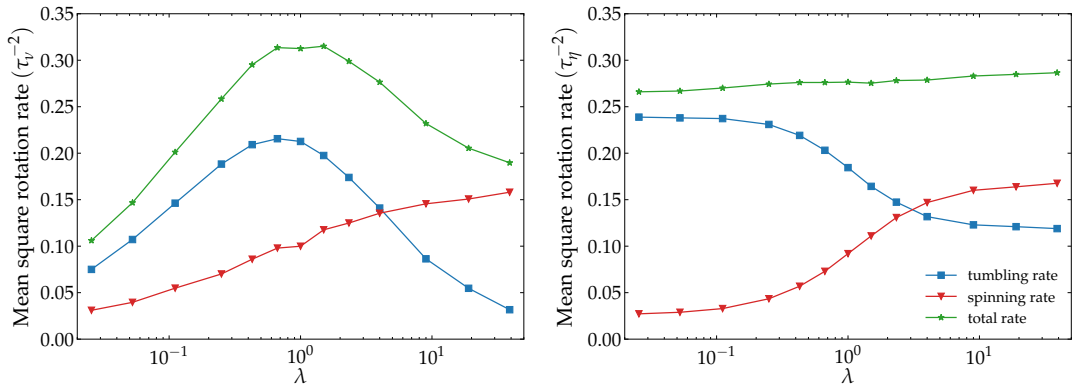

Figure 5.9: Left panel: Mean-square tumbling, spinning, and total rotation rates (in viscous units), in DNS, inside the viscous boundary layer ($y^+ < 0.2$) as a function of particle aspect ratio λ. Right panel: Mean-square tumbling, spinning, and total rotation rate in the flow bulk (at $y = h$) as a function of particle aspect ratio λ.

(i.e. $|\Lambda| \sim 1$), makes the observed rotation rates qualitatively consistent with spheroids in Jeffery orbits, for simple shear flows. Voth (2015) argued that oblate spheroids, bringing their symmetry axis near the wall-normal direction, will spend a long time in this orientation before tumbling. Here, we similarly observe that rod-like particles, having their axis almost aligned in the streamwise direction, rarely tumble.

As discussed in Chapter 4, the tumbling and spinning rates, in their definition used to analyse the DNS results, are not properly defined in the stochastic model for the orientation, due to the presence of a stochastic integral. Therefore, in order to study the rotation behaviour in the stochastic model, alternative definitions for the tumbling and spinning rates have been developed (Section 4.3.3 in Chapter 4). We recall that these two quantities read

$$\Phi_{\perp p}(t, y^+) = \frac{d}{dt}\left[\mathbb{E}\left\|\phi_{\perp p}(t, y^+)\right\|^2 - \left\|\mathbb{E}\left[\phi_{\perp p}(t, y^+)\right]\right\|^2\right], \tag{5.13}$$

$$\Phi_{\parallel p}(t, y^+) = \frac{d}{dt}\left[\mathbb{E}\left[\phi_{\parallel p}^2(t, y^+)\right] - \mathbb{E}\left[\phi_{\parallel p}(t, y^+)\right]^2\right], \tag{5.14}$$

where in the presence of channel flows, due to the inhomogeneity, additional difficulties arise from the dependence of these quantities on y^+. Equation (5.13) and (5.14) represent the extension to the 3D case of the variance of the angular displacement defined in Chapter 3 in the 2D case.

The Lagrangian stochastic model (Eq. (5.12)) provides the measurements of the total rate of the norm squared of angular displacement and its orthogonal and parallel projections along $\boldsymbol{p}$. Moreover, these quantities are cumulated for a certain elapsed time, conversely to the DNS statistics where the rotations modes are represented by the instantaneous change in time of the rotation. Despite the different definition in the model, the rotational dynamics of a spheroids can be understood in terms of the angular variation under the action of both the mean shear and fluctuations.

Equation (5.13) and (5.14) have been conditioned with respect to the position y^+, which means to evaluate

$$\Phi_{\perp p}(t, y^+) = \frac{1}{T^*}\left[\mathbb{E}\left\|\int_0^{T^*} d\phi_{\perp p}(t, y^+)\middle| y^+\right\|^2 - \left\|\mathbb{E}\left[\int_0^{T^*} d\phi_{\perp p}(t, y^+)\middle| y^+\right]\right\|^2\right], \tag{5.15}$$

$$\Phi_{\|p}(t,y^+) = \frac{1}{T^*}\left[\mathbb{E}\left[\left(\int_0^{T^*} d\phi_{\|p}(t,y^+)\Big|y^+\right)^2\right] - \mathbb{E}\left[\int_0^{T^*} d\phi_{\|p}(t,y^+)\Big|y^+\right]^2\right], \tag{5.16}$$

where the integrals have been computed according to their numerical discretization presented in Section 4.4 (Chapter 4). The time T^* has been fixed to ten times the frequency of reading the filtered DNS dataset for the A-DNS case, i.e. $T^* = 2$. Further, the channel half-height has been subdivided in 48 levels along the wall-normal directions to evaluate the integral, in order to cumulate the tumbling and spinning. We want to point out that these quantities can not be directly compared to the DNS results. Indeed, in the model the tumbling and spinning are characterised in terms of angular rate, whereas in DNS, they have been expressed in terms of rotation rate. However, in the model the statistics in Eq. (5.15) and (5.16) represent a first attempt to evaluate the tumbling and spinning along the channel.

The quantitative comparison between rotation dynamics in the model and in DNS is not straightforward. In this respect, how the statistics in the model can be adapted to the DNS remains an open question. Indeed, the simulating statistics in Eq. (5.15) and (5.16) can not be trivially computed in DNS since integration in a finite time interval and conditioning of tumbling and spinning with respect y^+, are two major issues deserving careful scrutiny.

Figure 5.10 shows the variance of the norm of the orthogonal (tumbling) and parallel (spinning) projections on $\boldsymbol{p}$, the orientation vector. These two quantities have been tested in A-DNS case. As we can see in left panel of Fig. 5.10, the Eq. (5.15), which characterises the tumbling, tends to increase approaching the wall of the channel. For $y+ \gtrsim 100$, the tumbling within the model is constant. This observation highlights the importance of the anisotropic fluctuations far from the wall since we are looking at the second order moments that cause a decreasing of tumbling approaching the central region of the channel in DNS. In this respect, it could be possible that a tuning parameter has to be set in order to find such behaviour for $y+ \gtrsim 100$.

Even if, as previously noted, this quantity is not directly comparable to DNS results, some common features may be highlighted. When approaching the wall, the model suggests that spheres ($\Lambda = 0$) are among the various shapes, those are tumbling faster. Furthermore, the way they are classified using the shape as parameter as a function of y^+, is in agreement with results obtained from DNS. Similar considerations hold for the description of the spinning in the model, as shown, in Fig. 5.10 (left panel). A remarkable difference is represented by the fact that, at $y+ \gtrsim 100$ the response of the model is equivalent with respect to the shape Λ. Moreover, these two statistics confirm the time-reversible character of the model. That is, prolate and

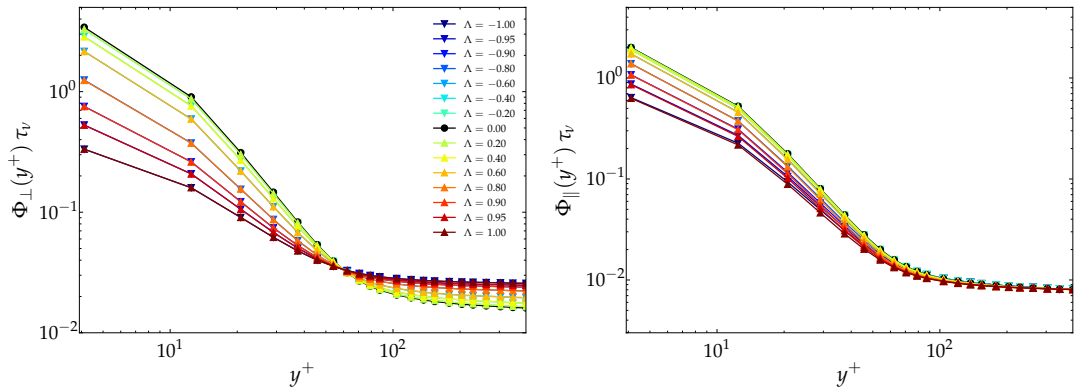

Figure 5.10: A-DNS results of mean-square tumbling rate (left panel) and spinning rate (right panel) A-DNS results in viscous units τ_η, as a function of the distance y^+ to the boundary for various values of Λ as labelled.

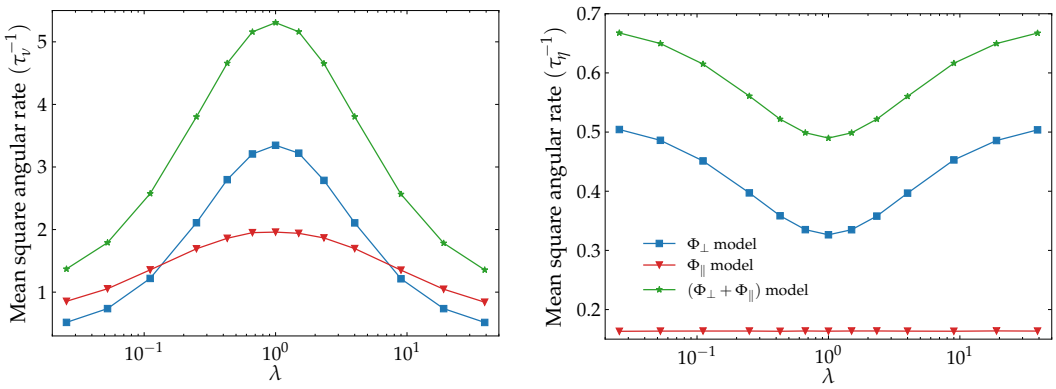

Figure 5.11: Left panel: Mean-square tumbling, spinning, and total rotation rates (in viscous units), in A-DNS, at $y^+ \approx 4$ as a function of particle aspect ratio λ. Right panel: Mean-square tumbling, spinning, and total rotation rate in the bulk region (at $y = h$) as a function of particle aspect ratio λ.

oblate particles behave in the same way for the two statistics. Finally, it is interesting to notice that the significant change in the behaviour of both tumbling and spinning occurs at $y^+ \approx 65$ which corresponds to the point where the mean velocity gradient component $\langle \partial u_x / \partial y \rangle$ rapidly increases. This mean that approaching the channel wall, where the turbulent velocity gradient fluctuations are small and the mean shear rate is large, the diffusion approximation works qualitatively well since the angular dynamics is dominated by the mean shear rate.

As we did for the DNS case, in Fig. 5.11 we show the tumbling, spinning and total rotation rates (in units of τ_η) for $y^+ \approx 4$ (left panel) and in the bulk of the channel (left panel), as a function of particle aspect ratio. As expected, in the bulk region we find the analytical result computed in Chapter 4 for the HIT (Fig. 4.13), which validates both the numerical implementation used to compute these statistics, and the limit of the model. In the left panel of Fig. 5.11, we can appreciate the behaviour of the model when the shear starts to dominate approaching the wall. At least for oblate particles ($\lambda < 1$) a similar qualitative behaviour on the rotation is recorded, when compared to DNS results. Even not willing to confront directly the two different statistics, the above considerations provide a qualitative picture of the rotation modes from the model.

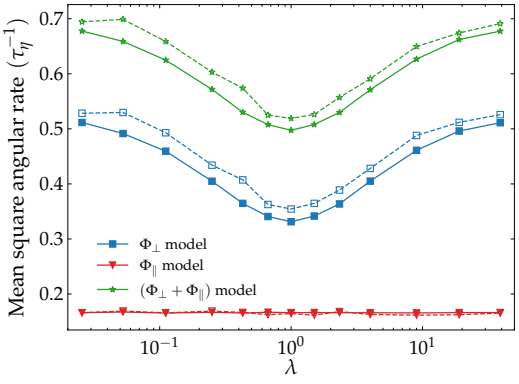

Figure 5.12: Mean-square tumbling, spinning, and total rotation rates (in units of τ_η), in RANS, in the log-layer ($y^+ \approx 20$) (dashed lines) and in the flow bulk ($y = h$) (continuous lines) as a function of particle aspect ratio λ.

The RANS results are reported in Fig. 5.12. In this case, the measurements of tumbling and spinning rate in the model remain constant all along the channel. Indeed, here both the lower magnitude of the mean velocity gradient $\langle \partial_y u_x \rangle$ and looking at $y^+ \gtrsim 20$, make the RANS case similar to the HIT case as in Fig. 5.12, where continuous lines refer to the bulk of the channel and dotted lines to $y^+ \approx 20$ (in units of τ_η).

Moreover, a possible explanation for the discrepancy between RANS and A-DNS could be relied to the trajectories behaviour. The tumbling and spinning statistics for the model, actually, strongly depend on the path-wise attitude and on the time spent by the particles close to the wall (Voth (2015)). This means that a future investigation could be the analysis of the residence time of the spheroids within different regions of the channel, since their asphericity impacts this time. For example, the presence of the Lagrangian coherent structures (Haller (2015)) act as organizers of transport in fluid flow having a clear impact on the particle trajectories. Therefore, it is possible to hypothesize that inertialess spheroids are captured by, and partially move along with, the coherent vortices modifying the residence time, especially in near-wall turbulence.

5.5 CONCLUSIONS

In this work, orientation and rotation statistics of inertia-free spheroidal particles in a turbulent channel flow have been presented. Fifteen different spheroidal tracers were considered, ranging from oblate ($\Lambda = -1$) to prolate particles with $\Lambda = 1$. The orientation model presented in Chapter 4 has been interfaced with the Eulerian/Lagrangian PDF method in order to study the orientation and rotation of spheroidal particles. In particular, the stochastic model and its numerical scheme discussed in Chapter 4 have been implemented in a CFD code (*Code_Saturne*), and detailed comparisons with DNS are carried out. A thorough statistical investigation on the orientation and rotation has been performed by considering mean-field informations obtained by filtering the DNS dataset, which can be treated as a 'perfect' RANS (A-DNS), providing finer details on time-filtered DNS trajectories, as well as on the mean velocity gradient tensor in the buffer layer.

In the near-wall region, for the DNS case, the flattest disks were strongly aligned in the wall-normal direction, whereas the longest rods aligned themselves with the streamwise direction. The inertia-free particles were evenly distributed across the channel, and the shape-dependence of their preferred orientations impact on their angular velocities, such that tumbling and spinning are reduced close to the walls for strong aspherical particles.

The model showed a good agreement with DNS results far from the wall. The variance of the orientation vector $\boldsymbol{p}$ in the A-DNS case reacts in a slightly better way than the RANS. This difference, given by the known limits of RANS in reproducing the mean velocity gradient of the fluid phase, confirms the potential of the model especially if coupled to more refined turbulence models for the fluid phase (which should include near-wall turbulence description). On the other hand, among the limits of the model, the time reversibility is the most significant, having a strong impact on both, orientation and rotation statistics. Indeed, in perspective, addition of time-symmetry breaking effects within the model, or through a wall condition on the orientation, should be really interesting, providing informations on the distinctive behaviour of oblate and prolate particles.

Another important aspect is the characterisation of the rotation in the model. The methodology introduced in Chapter 4 to study the tumbling and spinning modes has revealed that these quantities can be used to describe the rotation in a turbulent channel flow. However, to identify suitable statistics for both tumbling and spinning that provides a direct quantitative comparison between the model and DNS remains an open question.

The tumbling rate observed in DNS for spherical particles ($\Lambda = 0$) decreased with increasing asphericity both for rod-like and disk-like spheroids. Moreover, both tumbling and spinning

rate decrease approaching the centre of the channel, with the exception of very long rods ($\Lambda = -1$) and flattened disks ($\Lambda = -1$). The substantial reduction of the tumble and spin motions of spheroids with high asphericity was attributed to Jeffery-like orbiting.

In general, the model showed the same qualitative behaviour compared with DNS results on the wall, but in terms of angular rate for the A-DNS and in terms of rotation rate for the DNS simulation. In contrast, RANS results were not able to capture the change of tumbling and spinning all along the channel since they remain constant with y^+, reproducing only the HIT character in the bulk of the channel.

Finally, another flow in which the effects of mean shear on particle orientation and rotation can be investigated is the homogeneous shear turbulent flow. A particularly attractive advantage of such flows is that the mean shear is the same everywhere. Indeed, this is also an interesting case where the anisotropies are accounted for, without dealing with the inhomogeneities that complexify the study of the model. Moreover, it would be the natural extension of what we have done in Chapter 3, with a more refined classification of the anisotropies, within the model and in the analytical results.

APPENDIX

APPENDIX: CHAPTER 3

A.1 APPENDIX: ITÔ'S LEMMA ON THE ORIENTATION

Starting from the equation for the separation vector Eq. (3.24), that we rewrite $\langle A_{ij} \rangle = a_{ij}$ to simplify the notation:

$$dr_i = a_{ij} r_j dt + \beta_{ikl} r_l \circ dw^k$$

for $i = 1, 2$, we want to compute the Itô's Lemma for the orientation angle $\theta = \arctan(r_y/r_x)$.

The multidimensional Ito's lemma for θ states:

$$\begin{aligned} d\theta = &\sum_{i,j}^{2} J_i^\theta a_{ij} r_j dt + \frac{1}{2} \sum_{i,j,l,l'}^{2} \sum_{k}^{4} J_i^\theta \beta_{jkl} r_l \frac{\partial}{\partial r_j} \left(\beta_{ikl'} r_{l'} \right) dt \\ &+ \frac{1}{2} \sum_{i,j,l,l'}^{2} \sum_{k}^{4} H_{ij}^\theta \left(\beta_{ikl} r_l \beta_{jkl'} r_{l'} \right) dt + \sum_{i,l}^{2} \sum_{k}^{4} J_i^\theta \beta_{ikl} r_l w_t^k; \end{aligned}$$

where $J_i^\theta = -\sum_j^2 \varepsilon_{ij} r_j \left(\sum_p^2 r_p^2 \right)^{-1}$ and $H_{ij}^\theta = \sum_{l,l'}^2 \left(\varepsilon_{il} r_l r_j + \varepsilon_{jl'} r_{l'} r_i \right) \left(\sum_p^2 r_p^2 \right)^{-2}$ are respectively the gradient and hessian matrix of θ. Here we are denoting with ε_{ij} is the *Levi-Civita symbol*.

Regarding the stochastic integral, applying for example the martingale representation ()Theorem 4.2 in Chapter 3 of Karatzas and Shreve (1998)). This reduction of the noise is true in law only. And their is no direct identification between w_t^k and one dimensional W_t, (except in the isotropic case, maybe). Such that we obtain:

$$\begin{aligned} d\theta \overset{Law}{=} &\sum_{i,j}^{2} J_i^\theta a_{ij} r_j dt + \frac{1}{2} \sum_{i,j,l,l'}^{2} \sum_{k}^{4} J_i^\theta \beta_{jkl} r_l \frac{\partial}{\partial r_j} \left(\beta_{ikl'} r_{l'} \right) dt \\ &+ \frac{1}{2} \sum_{i,j,l,l'}^{2} \sum_{k}^{4} H_{ij}^\theta \left(\beta_{ikl} r_l \beta_{jkl'} r_{l'} \right) dt + \left(\sum_{i,i',l,l'}^{2} \sum_{k}^{4} J_i^\theta \beta_{ikl} r_l J_{i'}^\theta \beta_{i'kl'} r_{l'} \right)^{\frac{1}{2}} dW_t \\ =&\mathrm{I} + \mathrm{II} + \mathrm{III} + \mathrm{IV}, \end{aligned} \tag{A.1}$$

where these four last terms correspond to the four terms of the equation above. The effective correlation tensor in Eq. (3.20) can be rewritten as:

$$\mathbb{C}^{\text{eff}}_{(i,j);(k,l)} = \begin{pmatrix} \mathcal{C}^{\text{eff}}_{1111} & \mathcal{C}^{\text{eff}}_{1112} & \mathcal{C}^{\text{eff}}_{1121} & \mathcal{C}^{\text{eff}}_{1122} \\ \mathcal{C}^{\text{eff}}_{1211} & \mathcal{C}^{\text{eff}}_{1212} & \mathcal{C}^{\text{eff}}_{1221} & \mathcal{C}^{\text{eff}}_{1222} \\ \mathcal{C}^{\text{eff}}_{2111} & \mathcal{C}^{\text{eff}}_{2112} & \mathcal{C}^{\text{eff}}_{2121} & \mathcal{C}^{\text{eff}}_{2122} \\ \mathcal{C}^{\text{eff}}_{2211} & \mathcal{C}^{\text{eff}}_{2212} & \mathcal{C}^{\text{eff}}_{2221} & \mathcal{C}^{\text{eff}}_{2222} \end{pmatrix} = \begin{pmatrix} f & h & j & -f \\ & g & k & -h \\ \text{sym.} & & \ell & -j \\ & & & f \end{pmatrix}. \tag{A.2}$$

We recall the relation $\beta_{jkl}\beta_{ikl'} = 2\mathcal{C}^{\text{eff}}_{jlil'}$. Here the computation will use the general notation of $\mathcal{C}_{ijkl}$ instead of $\mathcal{C}^{\text{eff}}_{ijkl}$ to simply the notation. Moreover, we are going to analyse each term in Eq. (A.1) separately, in order to make easier the presentation.

TERM I The term I in Eq. (A.1) is, by replacing the definition of J_i^θ,

$$\mathrm{I} = \sum_{i,j}^{2} J_i^\theta a_{ij} r_j dt = -\sum_{i\neq m,j}^{2} \varepsilon_{im} r_m a_{ij} r_j \left(\sum_{p}^{2} r_p^2\right)^{-1} dt.$$

Since the only component different from zero of a_{ij} is $a_{12} = \sigma^*$ and by replacing $p_i = r_i \left(\sum_p^2 r_p^2\right)^{-1/2}$, i.e. $\boldsymbol{p} = (\cos\theta, \sin\theta)$, we get:

$$\mathrm{I} = \sum_{i,j}^{2} J_i^\theta a_{ij} r_j dt = -\sigma^* p_2^2 dt = \frac{\sigma^*}{2}\left(\cos(2\theta) - 1\right) dt.$$

TERM II The term II in Eq. (A.1), using the equality $\beta_{jkl}\beta_{ikl'} = 2\mathcal{C}_{jlil'}$ and by replacing the definition of J_i^θ and $\boldsymbol{p} = \boldsymbol{r}/\|\boldsymbol{r}\|$, leads to

$$\begin{aligned}
\mathrm{II} = \frac{1}{2}\sum_{i,j,l,l'}^{2}\sum_{k}^{4} J_i^\theta \beta_{jkl} r_l \frac{\partial}{\partial r_j}\left(\beta_{ikl'} r_{l'}\right) dt &= \sum_{i,j,l,l'}^{2}\sum_{k}^{4} J_i^\theta \beta_{jkl}\beta_{ikl'} r_l \delta_{l'j} dt \\
&= -\sum_{i\neq m}^{2}\sum_{j,l,l'}^{2} \varepsilon_{im} r_m \mathcal{C}_{jlil'} r_l \delta_{l'j} \left(\sum_{p}^{2} r_p^2\right)^{-1} dt \\
&= -\sum_{i\neq m}^{2}\sum_{j,l}^{2} \varepsilon_{im} \mathcal{C}_{jlij} p_m p_l dt
\end{aligned}$$

We develop the computation considering the matrix (A.2):

$$\begin{aligned}
\mathrm{II} &= -\sum_{j,l,}^{2}\left(\mathcal{C}_{jl1j} p_2 p_l - \mathcal{C}_{jl2j} p_1 p_l\right) dt \\
&= -\big(\mathcal{C}_{1111} p_2 p_1 + \mathcal{C}_{2112} p_2 p_1 + \mathcal{C}_{1211} p_2^2 + \mathcal{C}_{2212} p_2^2 \\
&\quad - \mathcal{C}_{1121} p_1^2 - \mathcal{C}_{2122} p_1^2 - \mathcal{C}_{1221} p_1 p_2 - \mathcal{C}_{2222} p_1 p_2\big) dt \\
&= -\left(f p_2 p_1 + k p_2 p_1 + h p_2^2 - h p_2^2 - j p_1^2 + j p_1^2 - k p_1 p_2 - f p_1 p_2\right) dt = 0
\end{aligned}$$

TERM III The term III in Eq. (A.1), using the equality $\beta_{jkl}\beta_{ikl'} = 2\mathcal{C}_{jlil'}$ and by replacing the definition of H_{ij}^θ and $\boldsymbol{p} = \boldsymbol{r}/\|\boldsymbol{r}\|$, leads to

$$\begin{aligned}
\mathrm{III} &= \frac{1}{2}\sum_{i,j,l,l'}^{2}\sum_{k}^{4} H_{ij}^\theta \left(\beta_{ikl}\beta_{jkl'} r_l r_{l'}\right) dt \\
&= \frac{1}{2}\sum_{i\neq m}^{2}\sum_{j\neq n}^{2}\sum_{l,l'}^{2}\sum_{k}^{4}\left(\varepsilon_{im} r_m r_j + \varepsilon_{jn} r_n r_i\right)\beta_{ikl}\beta_{jkl'} r_l r_{l'} \left(\sum_{p}^{2} r_p^2\right)^{-2} dt \\
&= \sum_{i\neq m}^{2}\sum_{j\neq n}^{2}\sum_{l,l'}^{2} \mathcal{C}_{iljl'}\left(\varepsilon_{im} p_m p_j + \varepsilon_{jn} p_n p_i\right) p_l p_{l'} dt
\end{aligned}$$

$$=2\sum_{l,l'}^{2}\left[\left(\mathcal{C}_{1l1l'}-\mathcal{C}_{2l2l'}\right)p_1p_2+\frac{1}{2}\left(\mathcal{C}_{1l1l'}-\mathcal{C}_{2l2l'}\right)\left(p_2^2-p_1^2\right)\right]p_lp_{l'}dt,$$

developing the computation considering the matrix (A.2):

$$\begin{aligned}
\text{III} = 2\Big\{ &\left[\frac{1}{2}(\mathcal{C}_{1121}+\mathcal{C}_{2111})(p_2^2-p_1^2)+(\mathcal{C}_{1111}-\mathcal{C}_{2121})p_1p_2\right]p_1^2\\
&+\left[\frac{1}{2}(\mathcal{C}_{1122}+\mathcal{C}_{2112})(p_2^2-p_1^2)+(\mathcal{C}_{1112}-\mathcal{C}_{2122})p_1p_2\right]p_1p_2\\
&+\left[\frac{1}{2}(\mathcal{C}_{1221}+\mathcal{C}_{2211})(p_2^2-p_1^2)+(\mathcal{C}_{1211}-\mathcal{C}_{2221})p_1p_2\right]p_1p_2\\
&+\left[\frac{1}{2}(\mathcal{C}_{1222}+\mathcal{C}_{2212})(p_2^2-p_1^2)+(\mathcal{C}_{1212}-\mathcal{C}_{2222})p_1p_2\right]p_2^2\Big\}dt\\
=2\Big[&3(j+h)p_1^2p_2^2-jp_1^4-hp_2^4+(2f-\ell-k)p_1^3p_2+(-2f+g+k)p_2^3p_1\Big]dt.
\end{aligned}$$

Now, considering that $\boldsymbol{p}=(\cos(\theta),\sin(\theta))$, the different terms can be rewritten as:

$$\begin{aligned}
p_1^3p_2&=\frac{1}{4}(\sin(2\theta)+\frac{1}{2}\sin(4\theta)), & p_1^4&=\frac{1}{8}(3+4\cos(2\theta)+\cos(4\theta)),\\
p_2^3p_1&=\frac{1}{4}(\sin(2\theta)-\frac{1}{2}\sin(4\theta)), & p_2^4&=\frac{1}{8}(3-4\cos(2\theta)+\cos(4\theta)),\\
p_1^2p_2^2&=\frac{1}{8}(1-\cos(4\theta)).
\end{aligned}$$

So the third term in Eq. (A.1) becomes

$$\begin{aligned}
\text{III} = 2\Big[&\frac{1}{4}(g-\ell)\sin(2\theta)+\frac{1}{8}\left(4f-2k-(\ell+g)\right)\sin(4\theta)\\
&+\frac{1}{2}(h-j)\cos(2\theta)-\frac{1}{2}(h+j)\cos(4\theta)\Big]dt\\
=&\left(-\frac{\gamma_3}{2}\sin(2\theta)-\gamma_4\sin(4\theta)+\frac{\gamma_1}{2}\cos(2\theta)+\gamma_2\cos(4\theta)\right)dt
\end{aligned}$$

with $\gamma_1=2(h-j)$, $\gamma_2=-(h+j)$, $\gamma_3=(\ell-g)$ and $\gamma_4=(-2f+k(\ell+j)/2)/2$.

TERM IV The term IV in Eq. (A.1) using the equality $\beta_{jkl}\beta_{ikl'}=2\mathcal{C}_{jlil'}$ and by replacing the definition of J_i^θ and $\boldsymbol{p}=\boldsymbol{r}/\|\boldsymbol{r}\|$, leads to

$$\begin{aligned}
\text{IV} &= \sum_{i,i',l,l'}^{2}\sum_{k}^{4}\left(J_i^\theta J_{i'}^\theta\beta_{ikl}\beta_{i'kl'}r_lr_{l'}\right)^{\frac{1}{2}}dW_t\\
&=\sqrt{2}\left[\sum_{l,l'}^{2}\sum_{i\neq s}^{2}\sum_{i'\neq s'}^{2}\left(\varepsilon_{is}r_s\varepsilon_{i's'}r'_s\right)\mathcal{C}_{ili'l'}r_lr_{l'}\left(\sum_{p}^{2}r_p^2\right)^{-2}\right]^{\frac{1}{2}}dW_t\\
&=\sqrt{2}\left(\sum_{l,l'}^{2}\sum_{i\neq s}^{2}\sum_{i'\neq s'}^{2}\varepsilon_{is}\varepsilon_{i's'}\mathcal{C}_{ili'l'}p_sp_{s'}p_lp_{l'}\right)^{\frac{1}{2}}dW_t
\end{aligned}$$

developing the computation considering the matrix (A.2):

$$\begin{aligned}
\text{IV} &= \sqrt{2}\left(\sum_{l,l'}^{2}\left[\mathcal{C}_{1s1s'}p_2^2+\mathcal{C}_{2s2s'}p_1^2-\left(\mathcal{C}_{2s1s'}+\mathcal{C}_{1s2s'}\right)p_2p_1\right]p_sp_{s'}\right)^{\frac{1}{2}}dW_t \\
&= \sqrt{2}\Big[\left(\mathcal{C}_{1111}p_2^2+\mathcal{C}_{2121}p_1^2-\left(\mathcal{C}_{1121}+\mathcal{C}_{2111}\right)p_1p_2\right)p_1^2 \\
&\quad+\left(\mathcal{C}_{1212}p_2^2+\mathcal{C}_{2222}p_1^2-\left(\mathcal{C}_{1222}+\mathcal{C}_{2212}\right)p_1p_2\right)p_2^2 \\
&\quad+\left(\mathcal{C}_{1112}p_2^2+\mathcal{C}_{2122}p_1^2-\left(\mathcal{C}_{1122}+\mathcal{C}_{2112}\right)p_1p_2\right)p_1p_2 \\
&\quad+\left(\mathcal{C}_{1211}p_2^2+\mathcal{C}_{2221}p_1^2-\left(\mathcal{C}_{1221}+\mathcal{C}_{2211}\right)p_1p_2\right)p_1p_2\Big]^{\frac{1}{2}}dW_t \\
&= \sqrt{2}\left[(4f-2k)p_1^2p_2^2-4jp_1^3p_2+4hp_2^3p_1+\ell p_1^4+gp_2^4\right]^{\frac{1}{2}}dW_t.
\end{aligned} \tag{A.3}$$

Using the same relations between Cartesian and polar coordinates system introduced for the term III in Eq. (A.1), this leads to,

$$\begin{aligned}
\text{IV} &= \sqrt{2}\Big[\frac{1}{2}\left(f+\frac{k}{2}+\frac{3}{4}(\ell+g)\right)+(h-j)\sin(2\theta)-\frac{1}{2}(h+j)\sin(4\theta) \\
&\quad+\frac{1}{2}(\ell-g)\cos(2\theta)+\frac{1}{2}\left(-f+\frac{k}{2}+\frac{1}{4}(\ell+g)\right)\cos(4\theta)\Big]^{\frac{1}{2}}dW_t \\
&= \left(\gamma_0+\gamma_1\sin(2\theta)+\gamma_2\sin(4\theta)+\gamma_3\cos(2\theta)+\gamma_4\cos(4\theta)\right)^{\frac{1}{2}}dW_t,
\end{aligned}$$

where $\gamma_0 = (f+\frac{k}{2}+\frac{3}{4}(\ell+g))$ and the others already has been defined as $\gamma_1 = 2(h-j)$, $\gamma_2 = -(h+j)$, $\gamma_3 = (\ell-g)$ and $\gamma_4 = (-2f+k+(\ell+j)/2)/2$.

Finally, Eq. (A.1) can be rewritten by summing the four terms as,

$$\begin{aligned}
d\theta &= \left(\frac{\sigma}{2}\left(\cos(2\theta)-1\right)-\frac{\gamma_3}{2}\sin(2\theta)-\gamma_4\sin(4\theta)+\frac{\gamma_1}{2}\cos(2\theta)+\gamma_2\cos(4\theta)\right)dt \\
&\quad+\left(\gamma_0+\gamma_1\sin(2\theta)+\gamma_2\sin(4\theta)+\gamma_3\cos(2\theta)+\gamma_4\cos(4\theta)\right)^{\frac{1}{2}}dW_t
\end{aligned} \tag{A.4}$$

with

$$\begin{aligned}
\gamma_0 &= f+\frac{k}{2}+\frac{3}{4}(\ell+g) \\
\gamma_1 &= 2(h-j) \\
\gamma_2 &= -(h+j) \\
\gamma_3 &= (\ell-g) \\
\gamma_4 &= \frac{1}{2}\left(-2f+k+\frac{1}{2}(\ell+g)\right)
\end{aligned}$$

σ^*		0.00	0.03	0.07	0.15	0.33	0.77	1.26	1.77	2.80	3.79
γ_0	$\mathcal{C}^{\text{aniso}}$	0.7565	0.7559	0.7612	0.7433	0.7311	0.7084	0.7210	0.7223	0.7065	0.7389
	$\mathcal{C}^{\text{int}}$	66.8319	49.3522	36.7193	21.4299	12.3579	7.7984	6.5343	6.0211	6.0748	8.0637
γ_1	$\mathcal{C}^{\text{aniso}}$	0.0033	−0.0008	−0.0160	−0.0734	−0.1642	−0.1883	−0.1665	−0.1518	−0.1165	−0.1007
	$\mathcal{C}^{\text{int}}$	0.6818	0.2007	0.2778	−0.6735	−2.4257	−1.3606	−0.7794	−0.6748	−0.4338	−0.3979
γ_2	$\mathcal{C}^{\text{aniso}}$	−0.0015	−0.0002	−0.0022	−0.0027	0.0052	0.0317	0.0442	0.0455	0.0394	0.0354
	$\mathcal{C}^{\text{int}}$	0.0034	0.0184	−0.0002	−0.0171	0.0581	0.2195	0.1815	0.1779	0.1428	0.149452
γ_3	$\mathcal{C}^{\text{aniso}}$	−0.0095	−0.0014	−0.0032	−0.0179	−0.1031	−0.2961	−0.4134	−0.4818	−0.5741	−0.7004
	$\mathcal{C}^{\text{int}}$	−0.1937	0.0441	−0.2509	−0.5446	−2.1580	−3.6875	−4.4623	−4.9191	−5.9903	−9.2379
γ_4	$\mathcal{C}^{\text{aniso}}$	0.0028	0.0021	0.0004	−0.0004	−0.0057	0.0043	0.0328	0.0528	0.0885	0.1300
	$\mathcal{C}^{\text{int}}$	0.0477	0.0058	0.0460	0.0235	−0.0264	0.2027	0.4348	0.5986	0.9369	1.7944

Table A.1: Values of γ_i (with $i = 0, \dots, 4$) used in the model (in the normalised case, i.e. by multiplying for τ_ω) when we use $\mathcal{C}^{\text{aniso}}$ or $\mathcal{C}^{\text{int}}$ to study the model as a function of the shear rate σ^* . The values of the tuning parameters, here, are $\alpha_{\text{aniso}} = \alpha_{\text{int}} = 1$.

A.2 APPENDIX: POSITIVITY OF DIFFUSION COEFFICIENT

We can compute the positivity of the diffusion coefficient $b^2(\bar{\chi})$ in Eq. (3.27). Considering the result in Eq. (A.3),

$$(\text{IV})^2 = 2((4f - 2k)p_1^2 p_2^2 + 4hp_2^3 p_1 - 4jp_1^3 p_2 + gp_2^4 + lp_1^4).$$

In the case of isotropic tensor $\mathcal{C}^{\text{iso}}_{ijkl}$ (with $\alpha_{\text{iso}} = 1$), considering that $f = -k =, g = l = 3f$, $h = j = 0$, we get

$$(\text{IV})^2 = 2(6fp_1^2 p_2^2 + 3fp_1^4 + 3fp_2^4) = 6f > 0$$

where the diffusion coefficients in the model is constant b^2. For the other cases, i.e. using in the model either $\mathcal{C}^{\text{aniso}}_{ijkl}$ or $\mathcal{C}^{\text{int}}_{ijkl}$, we consider that periodicity of the coefficient $b^2(\bar{\chi})$ in Eq. (3.27). Figure A.1 shows the positivity of $b^2(\bar{\chi})$ when the model uses $\mathcal{C}^{\text{aniso}}_{ijkl}$ (left panel) and $\mathcal{C}^{\text{int}}_{ijkl}$ (right panel).

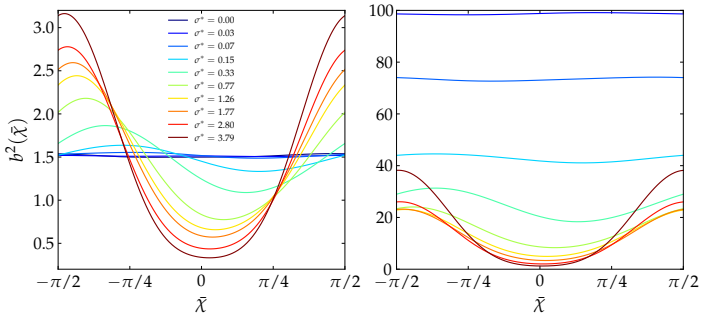

Figure A.1: Measurement of the diffusion coefficient $b^2(\bar{\chi})$ in Eq. (3.27), for all values of the shear rate parameter σ^*, as a function of the unfolded angle. In left panel the results in the case of $\mathcal{C}^{\text{aniso}}_{ijkl}$ and in the right panel the results for $\mathcal{C}^{\text{int}}_{ijkl}$. These results are computed for a value of a tuning parameter $\alpha_{\text{aniso}} = \alpha_{\text{int}} = 1$, for the two cases, respectively.

B

APPENDIX: CHAPTER 4

B.1 APPENDIX: STRATONOVICH–ITÔ CONVENTION

In this section we detail the conversion rule to pass from the Stratonovich stochastic differential equation (SDE) to Itô one. More precisely, the Itô formulation contains an extra drift term (see Øksendal (2003)). Equation (4.10) has been presented in the Stratonovich form, which we rewrite in the more compact form:

$$dq_i(t) = \bar{a}_i dt + \bar{\beta}_{ikj} q_j \circ dw_k, \tag{B.1}$$

and the Itô formulation reads:

$$dq_i(t) = a_i dt + \bar{\beta}_{ikj} q_j dw_k. \tag{B.2}$$

where,

$$a_i := \bar{a}_i + \frac{1}{2} \sum_{j,l,l'}^{d} \sum_{k}^{n} \bar{\beta}_{jkl} q_l \frac{\partial}{\partial q_j} \left(\bar{\beta}_{ikl'} q_{l'} \right), \tag{B.3}$$

having identified from Eq. (4.10),

$$\bar{a}_i = \left(\langle O_{ij} \rangle + \Lambda \langle S_{ij} \rangle \right) q_j.$$

In both Eq. (B.1) and (B.2), we have introduced $\bar{\beta}_{ikj} = \beta^a_{ikj} + \Lambda \beta^s_{ikj}$, being $\beta^s_{ikj} = (\beta_{ikj} + \beta_{jki})/2$ and $\beta^a_{ikj} = (\beta_{ikj} - \beta_{jki})/2$ the symmetric and antisymmetric part of the fluctuation tensor respectively.

In order to pass from Eq. (B.1) to (B.2), we need to compute Eq. (B.3). For $d = 3$ and $n = 9$, since β_{ikj} does not depend on $\boldsymbol{q}$ and recalling that $\partial q_{l'} / \partial q_j = \delta_{l'j}$ (with δ_{ij} to be the Kronecker delta),

$$a_i = \bar{a}_i + \frac{1}{2} \sum_{j,l,l'}^{d} \sum_{k}^{n} \bar{\beta}_{jkl} q_l \frac{\partial}{\partial q_j} \left(\bar{\beta}_{ikl'} q_{l'} \right) = \bar{a}_i + \frac{1}{2} \sum_{j,l,l'}^{d} \sum_{k}^{n} \bar{\beta}_{jkl} \bar{\beta}_{ikl'} q_l \delta_{l'j}$$

We replace the definition of $\bar{\beta}_{ikj}$ and β^a_{ikj}, β^s_{ikj}:

$$a_i = \bar{a}_i + \frac{1}{2} \sum_{j,l,l'}^{d} \sum_{k}^{n} \frac{1}{4} \left[\left(\beta_{jkl} - \beta_{lkj} \right) + \Lambda \left(\beta_{jkl} + \beta_{lkj} \right) \right] \left[\left(\beta_{ikl'} - \beta_{l'ki} \right) + \Lambda \left(\beta_{ikl'} + \beta_{l'ki} \right) \right] q_l \delta_{l'j}.$$

We develop the products:

$$
\begin{aligned}
a_i =& \bar{a}_i + \frac{1}{8}\sum_{j,l,l'}^{d}\sum_{k}^{n}\Big[\Big(\beta_{jkl}-\beta_{lkj}\Big)\left(\beta_{ikl'}-\beta_{l'ki}\right)+\Lambda^2\Big(\beta_{jkl}+\beta_{lkj}\Big)\left(\beta_{ikl'}-\beta_{l'ki}\right)\\
&+\Lambda\Big(\beta_{jkl}-\beta_{lkj}\Big)\left(\beta_{ikl'}+\beta_{l'ki}\right)+\Lambda\Big(\beta_{jkl}+\beta_{lkj}\Big)\left(\beta_{ikl'}-\beta_{l'ki}\right)\Big]q_l\delta_{l'j}\\
=& \bar{a}_i + \frac{1}{8}\sum_{j,l,l'}^{d}\sum_{k}^{n}\Big[\Big(\beta_{jkl}\beta_{ikl'}-\beta_{jkl}\beta_{l'ki}-\beta_{jkl}\beta_{ikl'}+\beta_{lkj}\beta_{l'ki}\Big)\\
&+\Lambda^2\Big(\beta_{jkl}\beta_{ikl'}+\beta_{jkl}\beta_{l'ki}+\beta_{lkj}\beta_{ikl'}+\beta_{jkl}\beta_{ikl'}+\beta_{lkj}\beta_{l'ki}\Big)+2\Lambda\Big(\beta_{jkl}\beta_{ikl'}-\beta_{lkj}\beta_{l'ki}\Big)\Big]q_l\delta_{l'j}\\
=& \bar{a}_i + \frac{1}{8}\sum_{j,l,l'}^{d}\sum_{k}^{n}\Big[\Big(\beta_{jkl}\beta_{ikl'}-\beta_{jkl}\beta_{l'ki}-\beta_{jkl}\beta_{ikl'}+\beta_{lkj}\beta_{l'ki}\Big)\\
&+\Lambda^2\Big(\beta_{jkl}\beta_{ikl'}+\beta_{jkl}\beta_{l'ki}+\beta_{lkj}\beta_{ikl'}+\beta_{jkl}\beta_{ikl'}+\beta_{lkj}\beta_{l'ki}\Big)+2\Lambda\Big(\beta_{jkl}\beta_{ikl'}-\beta_{lkj}\beta_{l'ki}\Big)\Big]q_l\delta_{l'j}.
\end{aligned}
$$

By the fact that $\beta_{ikj}\beta_{mkn} = 2D\,Ku\,\mathcal{C}^*_{ijkl}$ with $\mathcal{C}^*_{ijkl} = 4\delta_{ik}\delta_{jl} - \delta_{ij}\delta_{kl} - \delta_{il}\delta_{kj}$ (see Eq. (4.15)) we get:

$$
\begin{aligned}
a_i =& \bar{a}_i + \frac{D\,Ku}{4}\sum_{j,l,l'}^{d}\Big[\Big(\mathcal{C}^*_{jlil'}-\mathcal{C}^*_{jll'i}-\mathcal{C}^*_{jlil'}+\mathcal{C}^*_{ljl'i}\Big)\delta_{l'j}+\Lambda^2\Big(\mathcal{C}^*_{jlil'}+\mathcal{C}^*_{jll'i}+\mathcal{C}^*_{ljil'}+\mathcal{C}^*_{ljl'i}\Big)\delta_{l'j}\\
&+2\Lambda\Big(\mathcal{C}^*_{jlil'}-\mathcal{C}^*_{ljl'i}\Big)\delta_{l'j}\Big]q_l,
\end{aligned}
$$

that we rewrite as:

$$
\begin{aligned}
a_i =& \bar{a}_i + \frac{D\,Ku}{4}\sum_{l,l'}^{d}\Big[\left(\mathcal{C}^*_{l'lil'}-\mathcal{C}^*_{l'll'i}-\mathcal{C}^*_{ll'il'}+\mathcal{C}^*_{ll'l'i}\right)+\Lambda^2\left(\mathcal{C}^*_{l'lil'}+\mathcal{C}^*_{l'll'i}+\mathcal{C}^*_{ll'il'}+\mathcal{C}^*_{ll'l'i}\right)\\
&+2\Lambda\left(\mathcal{C}^*_{l'lil'}-\mathcal{C}^*_{ll'l'i}\right)\Big]q_l.
\end{aligned}
$$

Using the definition of $\mathcal{C}^*_{ijkl}$, we obtain:

$$
a_i = \bar{a}_i + \frac{D\,Ku}{4}\Big(20\Lambda^2-20\Big)q_i = \bar{a}_i + 5D\,Ku\Big(\Lambda^2-1\Big)q_i.
$$

Thus, if we replace it in Itô formulation (B.2) reads:

$$
dq_i(t) = \Big(\langle O_{ij}\rangle + \Lambda\langle S_{ij}\rangle + 5D\,Ku\Big(\Lambda^2-1\Big)\delta_{ij}\Big)\,q_j\,dt + \bar{\beta}_{ikj}q_j d\mathrm{w}_k. \tag{B.4}
$$

We can go further in the reformulation that will be useful to present the model and developing a numerical scheme, by considering the transformation that we detail in the following remark.

Remark 2 *We can rewrite*

$$
\beta_{jkl}\,q_l\,d\mathrm{w}_k = \mathcal{D}_{jlmn}\,q_l\,d\mathrm{W}_{mn}, \tag{B.5}
$$

where W_{mn} is Wiener matrix. This implies that if w_k is a vector 9×1, W_{mn} it's the correspondent 3 by 3 matrix, issued by its components; which means to map $\mathrm{W}^{mn}_t = \mathrm{w}^{3(m-1)+n}_t$ and schematically to write,

$$
\mathbf{w} = (W_1,\dots W_9)^\intercal \Longleftrightarrow \mathbf{W} = \begin{pmatrix} W_1 & W_2 & W_3\\ W_4 & W_5 & W_6\\ W_7 & W_8 & W_9\end{pmatrix} \tag{B.6}
$$

The diffusion tensor $\mathcal{D}_{ijkl} = \sqrt{2\,D\,Ku}\,\mathcal{D}^*_{ijkl}$ *is derived by imposing* $\mathcal{C}^*_{ijkl} = \mathcal{D}^*_{ijmn}\mathcal{D}^*_{klmn}$. *It maintains the properties of the correlation tensor such as isotropy and incompressibility; its general form reads*

$$\begin{aligned}\mathcal{D}^*_{ijmn} &= d_1\delta_{im}\delta_{jn} + d_2\delta_{ij}\delta_{mn} + d_3\delta_{in}\delta_{jm}\\ \mathcal{D}^*_{klmn} &= d_1\delta_{km}\delta_{ln} + d_2\delta_{kl}\delta_{mn} + d_3\delta_{kn}\delta_{lm}\end{aligned}$$

with d_1, d_2, d_3 *coefficients that have to be computed. Replacing the general form of* $\mathcal{D}^*_{ijmn}$ *into the relation* $\mathcal{C}^*_{ijkl} = \mathcal{D}^*_{ijmn}\mathcal{D}^*_{klmn}$ *brings to:*

$$\begin{aligned}\mathcal{C}^*_{ijkl} =& d_1^2\delta_{ik}\delta_{jl} + d_1d_2\delta_{ij}\delta_{kl} + d_1d_3\delta_{il}\delta_{jk}\\ &+ d_2d_1\delta_{ij}\delta_{kl} + d_2^2\delta_{ij}\delta_{mm} + d_2d_3\delta_{ij}\delta_{lk}\\ &+ d_3d_1\delta_{il}\delta_{jk} + d_3d_2\delta_{ij}\delta_{kl} + d_3^2\delta_{ik}\delta_{jl}\\ =& \left(d_1^2 + d_3^2\right)\delta_{ik}\delta_{jl} + \left(2d_2d_1 + 3d_2^2 + 2d_2d_3\right)\delta_{ij}\delta_{lk} + 2d_1d_3\delta_{il}\delta_{jk}.\end{aligned}$$

Since we know $\mathcal{C}^*_{ijkl} = 4\delta_{ik}\delta_{jl} - \delta_{ij}\delta_{kl} - \delta_{il}\delta_{jk}$, *it leads to solve the linear system composed by* $d_1^2 + d_3^2 = 4$, $2d_2d_1 + 3d_2^2 + 2d_2d_3 = -1$ *and* $2d_1d_3 = -1$. *The solution gives the definition of* $\mathcal{D}_{ijkl} = \sqrt{2\,D\,Ku}\,\mathcal{D}^*_{ijkl}$, *with:*

$$\mathcal{D}^*_{ijkl} = \frac{1}{2}\left(\sqrt{3}+\sqrt{5}\right)\delta_{ik}\delta_{jl} - \frac{\sqrt{3}}{3}\delta_{ij}\delta_{kl} + \frac{1}{2}\left(\sqrt{3}-\sqrt{5}\right)\delta_{il}\delta_{jk}. \tag{B.7}$$

Considering the equivalence in Expr. (B.5) in Remark 2 and the relations $\bar{\beta}_{ikj} = \beta^a_{ikj} + \Lambda\,\beta^s_{ikj}$, being $\beta^s_{ikj} = (\beta_{ikj} + \beta_{jki})/2$ and $\beta^a_{ikj} = (\beta_{ikj} - \beta_{jki})/2$; Eq. (B.4) can be rewritten as:

$$\begin{aligned}dq_i(t) =& \left(\langle O_{ij}\rangle + \Lambda\,\langle S_{ij}\rangle + 5D\,Ku\left(\Lambda^2 - 1\right)\delta_{ij}\right)\,q_j\,dt\\ &+ \frac{1}{2}(\Lambda+1)\mathcal{D}_{ijmn}q_j d\mathrm{W}_{mn} + \frac{1}{2}(\Lambda-1)\mathcal{D}_{jimn}q_j d\mathrm{W}_{mn}.\end{aligned}$$

Expressing the form of the tensor $\mathcal{D}_{ijkl} = \sqrt{2\,D\,Ku}\,\mathcal{D}^*_{ijkl}$, where $\mathcal{D}^*_{ijkl}$ is defined in Expr. (B.7) and simplifying the equation above,

$$\begin{aligned}dq_i(t) =& \left(\langle O_{ij}\rangle + \Lambda\,\langle S_{ij}\rangle + \frac{5}{6}\nu_s^2\left(\Lambda^2 - 1\right)\delta_{ij}\right)\,q_j\,dt\\ &- \frac{\nu_s}{3}\Lambda\sum_{m=1}^{3} d\mathrm{W}_{mm}q_i + \nu_s\Lambda d\mathrm{W}^s_{ij}q_j + \nu_a d\mathrm{W}^a_{ij}q_j,\end{aligned} \tag{B.8}$$

where we have introduced two parameters related to the symmetric and antisymmetric part of the fluctuations $\nu_s = \sqrt{6\,D\,Ku}$ and $\nu_a = \sqrt{10\,D\,Ku}$. Moreover, we have identified the symmetric part and antisymmetric matrices $\mathrm{W}^s_{ij} = \left(\mathrm{W}_{ij} + \mathrm{W}_{ji}\right)/2$, $\mathrm{W}^a_{ij} = \left(\mathrm{W}_{ij} - \mathrm{W}_{ji}\right)/2$ of the Wiener matrix W_{ij} (see Remark 2).

B.2 APPENDIX: ITÔ'S LEMMA ON THE ORIENTATION

In order to recover the orientation vector $\boldsymbol{p}$, we apply Itô's Lemma (see Øksendal (2003)) on Eq. (B.4), since we can write $\boldsymbol{p}$ as a function of $\boldsymbol{q}$; in fact, $\boldsymbol{p} = \boldsymbol{q}/\|q\|$. We obtain:

$$\begin{aligned} dp_i =& \Big(\sum_{j,l}^{d} \mathrm{J}^p_{ij} \left(\left(\langle \Omega_{jl} \rangle + \Lambda \langle S_{jl} \rangle \right) + 5D\, Ku \left(\Lambda^2 - 1 \right) \delta_{jl} \right) q_l \\ &+ \frac{1}{2} \sum_{j,m,l,l'}^{d} \sum_{k}^{n} \mathrm{H}^p_{ijm} \left(\bar{\beta}_{jkl} \bar{\beta}_{mkl'} q_l q_{l'} \right) \Big) dt + \sum_{j,l}^{d} \sum_{k}^{n} \mathrm{J}^p_{ij} \left(\bar{\beta}_{jkl} q_l \right) d\mathrm{w}_k \\ :=& \left(\mathrm{I} + \mathrm{II} + \mathrm{III} \right) dt + \mathrm{IV}, \end{aligned} \tag{B.9}$$

where the first line corresponds to the contribution relied to the first derivative, the second line to the hessian matrix and the quadratic term, while in the last line we have the stochastic contribution, in particular J^p and H^p are the Jacobian and Hessian of $p_i = q_i / (\sum_s^d q_s^2)^{1/2}$ respectively, defined as,

$$\begin{aligned} \mathrm{J}^p_{ij} =& \frac{\partial}{\partial q_j} \left(\frac{q_i}{(\sum_s^d q_s^2)^{1/2}} \right) = \frac{\delta_{ij}}{(\sum_s^d q_s^2)^{1/2}} - \frac{q_i q_j}{(\sum_s^d q_s^2)^{3/2}} \\ \mathrm{H}^p_{ijk} =& \frac{\partial^2}{\partial q_i \partial q_j} \left(\frac{q_k}{(\sum_s^d q_s^2)^{1/2}} \right) \\ =& - q_k q_j \frac{\partial}{\partial q_i} \left(\frac{1}{(\sum_s^d q_s^2)^{3/2}} \right) - \frac{q_j}{(\sum_s^d q_s^2)^{1/2}} \frac{\partial q_k}{\partial q_i} + \frac{\partial}{\partial q_i} \left(\frac{\delta_{kj}}{(\sum_s^d q_s^2)^{1/2}} \right) \\ =& 3 \frac{q_i q_j q_k}{(\sum_s^d q_s^2)^{5/2}} - \frac{q_k}{(\sum_s^d q_s^2)^{3/2}} \delta_{ij} - \frac{q_j}{(\sum_s^d q_s^2)^{3/2}} \delta_{ik} - \frac{q_i}{(\sum_s^d q_s^2)^{3/2}} \delta_{jk} \end{aligned}$$

We now develop the computation. We star by the first term, which comes from the mean velocity gradient:

$$\begin{aligned} \mathrm{I} &= \sum_{j,l}^{d} \mathrm{J}^p_{ij} \left(\langle O_{jl} \rangle + \Lambda \langle S_{jl} \rangle \right) q_l \\ &= \sum_{j,l}^{d} \frac{\delta_{ij}}{(\sum_s^d q_s^2)^{1/2}} \left(\langle \Omega_{jl} \rangle + \Lambda \langle S_{jl} \rangle \right) q_l - \frac{q_i q_j}{(\sum_s^d q_s^2)^{3/2}} \left(\langle \Omega_{jl} \rangle + \Lambda \langle S_{jl} \rangle \right) q_l \\ &= \sum_{l}^{d} \left(\langle \Omega_{il} \rangle + \Lambda \langle S_{il} \rangle \right) p_l - \Lambda p_i p_j \langle S_{jl} \rangle p_l. \end{aligned}$$

Here, we replaced $p_i = q_i / (\sum_s^d q_s^2)^{1/2}$ and we have used the fact that $\frac{q_i q_j}{(\sum_s^d q_s^2)^{3/2}} \langle O_{jl} \rangle q_l = 0$ since the cubic term of the antisymmetric part of the velocity gradient is null.

Passing to the term II, it is easy to prove that $\mathrm{II} = 0$ sice it is fully diagonal.

We then focus on III:

$$\begin{aligned} \mathrm{III} &= \frac{1}{2} \sum_{j,m,l,l'}^{d} \sum_{k}^{n} \mathrm{H}^p_{ijm} \bar{\beta}_{jkl} \bar{\beta}_{mkl'} q_l q_{l'} \\ &= \frac{1}{2} \sum_{j,m,l,l'}^{d} \sum_{k}^{n} \left(3 \frac{q_i q_j q_k}{(\sum_s^d q_s^2)^{5/2}} - \frac{q_k}{(\sum_s^d q_s^2)^{3/2}} \delta_{ij} - \frac{q_j}{(\sum_s^d q_s^2)^{3/2}} \delta_{ik} - \frac{q_i}{(\sum_s^d q_s^2)^{3/2}} \delta_{jk} \right) \bar{\beta}_{jkl} \bar{\beta}_{mkl'} q_l q_{l'} \end{aligned}$$

We recall that $\bar{\beta}_{ikj} = \left(\Gamma^a_{ikj} + \Lambda\, \Gamma^s_{ikj}\right)$, $\Gamma^s_{ikj} = (\beta_{ikj} + \beta_{jki})/2$ and $\Gamma^a_{ikj} = (\beta_{ikj} - \beta_{jki})/2$. Thus we obtain:

$$\begin{aligned}
\text{III} = \frac{1}{8} \sum_{j,m,l,l'}^{d} \sum_{k}^{n} & \left(3p_i p_j p_m p_l p_{l'} - p_i p_l p_{l'} \delta_{jm} - p_j p_l p_{l'} \delta_{im} - p_m p_l p_{l'} \delta_{ij}\right) \\
& \Big[\left(\beta_{jkl}\beta_{mkl'} - \beta_{jkl}\beta_{l'km} - \beta_{lkj}\beta_{mkl'} + \beta_{lkj}\beta_{l'km}\right) \\
& + \Lambda^2 \left(\beta_{jkl}\beta_{mkl'} + \beta_{jkl}\beta_{l'km} + \beta_{lkj}\beta_{mkl'} + \beta_{lkj}\beta_{l'km}\right) \\
& + 2\Lambda \left(\beta_{jkl}\beta_{mkl'} - \beta_{lkj}\beta_{l'km}\right) \Big]
\end{aligned}$$

By the fact that $\beta_{ikj}\beta_{mkn} = 2D\,Ku\,\mathcal{C}^*_{ijkl}$ with $\mathcal{C}^*_{ijkl} = 4\delta_{ik}\delta_{jl} - \delta_{ij}\delta_{kl} - \delta_{il}\delta_{kj}$ (see Eq. (4.15)) we get:

$$\begin{aligned}
\text{III} = \frac{D\,Ku}{4} \sum_{j,m,l,l'}^{d} & \left(3p_i p_j p_m p_l p_{l'} - p_i p_l p_{l'} \delta_{jm} - p_j p_l p_{l'} \delta_{im} - p_m p_l p_{l'} \delta_{ij}\right) \\
& \Big[\left(\mathcal{C}^*_{jlml'} - \mathcal{C}^*_{jll'm} - \mathcal{C}^*_{ljml'} + \mathcal{C}^*_{ljl'm}\right) + \Lambda^2 \left(\mathcal{C}^*_{jlml'} + \mathcal{C}^*_{jll'm} + \mathcal{C}^*_{ljml'} + \mathcal{C}^*_{ljl'm}\right) + 2\Lambda \left(\mathcal{C}^*_{jlml'} - \mathcal{C}^*_{ljl'm}\right) \Big]
\end{aligned}$$

We develop the products:

$$\begin{aligned}
\text{III} = \frac{D\,Ku}{4} \sum_{j,m,l,l'}^{d} & \Big\{ \\
& 3p_i p_j p_m p_l p_{l'} \left[(\Lambda^2+1)\left(\mathcal{C}^*_{jlml'} + \mathcal{C}^*_{ljl'm}\right) + (\Lambda^2-1)\left(\mathcal{C}^*_{jll'm} + \mathcal{C}^*_{ljml'}\right) + 2\Lambda\left(\mathcal{C}^*_{jlml'} - \mathcal{C}^*_{ljl'm}\right)\right] \\
& - p_i p_l p_{l'} \left[(\Lambda^2+1)\left(\mathcal{C}^*_{mlml'} + \mathcal{C}^*_{lml'm}\right) + (\Lambda^2-1)\left(\mathcal{C}^*_{mll'm} + \mathcal{C}^*_{lmml'}\right) + 2\Lambda\left(\mathcal{C}^*_{mlml'} - \mathcal{C}^*_{lml'm}\right)\right] \\
& - p_j p_l p_{l'} \left[(\Lambda^2+1)\left(\mathcal{C}^*_{jlil'} + \mathcal{C}^*_{ljl'i}\right) + (\Lambda^2-1)\left(\mathcal{C}^*_{jll'i} + \mathcal{C}^*_{ljil'}\right) + 2\Lambda\left(\mathcal{C}^*_{jlil'} - \mathcal{C}^*_{ljl'i}\right)\right] \\
& - p_m p_l p_{l'} \left[(\Lambda^2+1)\left(\mathcal{C}^*_{ilml'} + \mathcal{C}^*_{lil'm}\right) + (\Lambda^2-1)\left(\mathcal{C}^*_{ill'm} + \mathcal{C}^*_{liml'}\right) + 2\Lambda\left(\mathcal{C}^*_{ilml'} - \mathcal{C}^*_{lil'm}\right)\right] \Big\}
\end{aligned}$$

Thanks to the definition of $\mathcal{C}^*_{ijkl}$ we obtain:

$$\begin{aligned}
\text{III} = & \frac{D\,Ku}{4} \sum_{j,m,l,l'}^{d} \Big\{ 6p_i p_j p_m p_l p_{l'} \left[\Lambda^2\left(3\delta_{jm}\delta_{ll'} - 2\delta_{jl}\delta_{ml'} + 3\delta_{jl'}\delta_{lm}\right) + 5\left(\delta_{jm}\delta_{ll'} - \delta_{jl'}\delta_{lm}\right)\right] \\
& - 10(\Lambda^2+1)p_i - 4\Lambda^2\left(3p_i - 2p_i + 3p_i\right) \Big\} \\
= & -\frac{D\,Ku}{4}\left(12\Lambda^2 + 20\right) p_i = -\frac{1}{2}\, D\,Ku \left(6\Lambda^2 + 10\right) p_i
\end{aligned}$$

Ultimately, we consider the diffusion term IV,

$$\text{IV} = \sum_{j,l}^{d} \sum_{k}^{n} \mathrm{J}^p_{ij}\, \bar{\beta}_{jkl}\, q_l\, d\mathrm{w}_k.$$

We replace the definition of $\bar{\beta}_{ikj} = \beta^a_{ikj} + \Lambda\, \beta^s_{ikj}$, $\beta^s_{ikj} = (\beta_{ikj} + \beta_{jki})/2$ and $\beta^a_{ikj} = (\beta_{ikj} - \beta_{jki})/2$. Thus, we obtain:

$$\text{IV} = \frac{1}{2} \sum_{j,l}^{d} \sum_{k}^{n} \mathrm{J}^p_{ij} \left[\left(\beta_{jkl} - \beta_{lkj}\right) + \Lambda\left(\beta_{jkl} - \beta_{lkj}\right)\right] q_l d\mathrm{w}_k.$$

Without loss of generality, we apply transformation $\beta_{jkl}\, q_l\, d\mathrm{w}_k = \mathcal{D}_{jlmn}\, q_l\, d\mathrm{W}_{mn}$ (Eq. (B.5)) as detailed in Remark 2. We obtain:

$$\begin{aligned}\mathrm{IV} =& \frac{1}{2}\sqrt{2\,D\,Ku} \sum_{j,l,m,n}^{d} \mathrm{J}^p_{ij} \big[\mathcal{D}^*_{jlmn} q_l d\mathrm{W}_{mn} - \mathcal{D}^*_{ljmn} q_l d\mathrm{W}_{mn} \\ &+ \Lambda \left(\mathcal{D}^*_{jlmn} q_l d\mathrm{W}_{mn} + \mathcal{D}^*_{ljmn} q_l d\mathrm{W}_{mn}\right)\big].\end{aligned}$$

We replace the definition of J^p_{ij} and of $\mathbf{p}$:

$$\begin{aligned}\mathrm{IV} =& \frac{1}{2}\sqrt{2\,D\,Ku} \sum_{j,l,m,n}^{d} \left(\frac{\delta_{ij}}{(\sum_s^d q_s^2)^{1/2}} - \frac{q_i q_j}{(\sum_s^d q_s^2)^{3/2}}\right) \\ &\left[(\Lambda+1)\mathcal{D}^*_{jlmn} + (\Lambda-1)\mathcal{D}^*_{ljmn}\right] q_l d\mathrm{W}_{mn} \\ =& \frac{1}{2}\sqrt{2\,D\,Ku} \sum_{j,l,m,n}^{d} \Big\{ \left[(\Lambda+1)\mathcal{D}^*_{ilmn} + (\Lambda-1)\mathcal{D}^*_{limn}\right] p_l \\ &- \left[(\Lambda+1)\mathcal{D}^*_{jlmn} + (\Lambda-1)\mathcal{D}^*_{ljmn}\right] p_i p_j p_l \Big\} d\mathrm{W}_{mn}.\end{aligned}$$

Using the definition of the tensor $\mathcal{D}^*_{ijkl}$ in Expr. (B.7) and by developing the computations:

$$\begin{aligned}\mathrm{IV} =& \frac{1}{2}\sqrt{2\,D\,Ku} \sum_{j,l,m,n}^{d} \Big\{ \Big[(\Lambda+1)\left(d_1\delta_{im}\delta_{ln} + d_2\delta_{il}\delta_{mn} + d_3\delta_{lm}\delta_{in}\right) \\ &+ (\Lambda-1)\left(d_1\delta_{lm}\delta_{in} + d_2\delta_{li}\delta_{mn} + d_3\delta_{im}\delta_{ln}\right)\Big] p_l \\ &- \Big[(\Lambda+1)\left(d_1\delta_{jm}\delta_{ln} + d_2\delta_{jl}\delta_{mn} + d_3\delta_{lm}\delta_{jn}\right) \\ &+ (\Lambda-1)\left(d_1\delta_{lm}\delta_{jn} + d_2\delta_{lj}\delta_{mn} + d_3\delta_{jm}\delta_{ln}\right)\Big] p_i p_j p_l \Big\} d\mathrm{W}_{mn} \\ =& \frac{1}{2}\sqrt{2\,D\,Ku} \sum_{j,l}^{d} \Big\{ \Lambda(d_1+d_3)\left(d\mathrm{W}_{il} + d\mathrm{W}_{li}\right) p_l \\ &+ 2\Lambda d_2 p_i \sum_m^d d\mathrm{W}_{mm} + (d_1-d_3)\left(d\mathrm{W}_{il} - d\mathrm{W}_{li}\right) p_l \\ &- \Lambda(d_1+d_3)\left(d\mathrm{W}_{jl} + d\mathrm{W}_{lj}\right) p_i p_j p_l \\ &- 2\Lambda d_2 p_i \sum_m^d d\mathrm{W}_{mm} - (d_1-d_3)\left(d\mathrm{W}_{jl} - d\mathrm{W}_{lj}\right) p_i p_j p_l \Big\},\end{aligned}$$

and since $-\frac{1}{2}\sqrt{2\,D\,Ku}(d_1-d_3)\left(d\mathrm{W}_{jl} - d\mathrm{W}_{lj}\right) p_i p_j p_l$ is null,

$$\begin{aligned}\mathrm{IV} =& \frac{1}{2}\sqrt{2\,D\,Ku} \sum_{j,l}^{d} \Big\{ \frac{\Lambda}{2}(d_1+d_3)\left(d\mathrm{W}_{il} + d\mathrm{W}_{li}\right) p_l \\ &+ \frac{1}{2}(d_1-d_3)\left(d\mathrm{W}_{il} - d\mathrm{W}_{li}\right) p_l - \frac{\Lambda}{2}(d_1+d_3)\left(d\mathrm{W}_{jl} + d\mathrm{W}_{lj}\right) p_i p_j p_l \Big\}.\end{aligned}$$

By using (already defined in Eq. (B.8)) the symmetric part and antisymmetric matrices $\mathrm{W}^s_{il} = \left(\mathrm{W}_{il} + \mathrm{W}_{li}\right)/2$ and $\mathrm{W}^a_{il} = \left(\mathrm{W}_{il} - \mathrm{W}_{li}\right)/2$ we get:

$$\mathrm{IV} = \sqrt{2\,D\,Ku} \sum_{j,l}^{d} \Big\{ \Lambda(d_1+d_3) d\mathrm{W}^s_{il} p_l + (d_1-d_3) d\mathrm{W}^a_{il} p_l - \Lambda(d_1+d_3) p_i p_j d\mathrm{W}^s_{jl} p_l \Big\}.$$

We can now put together the results obtained for I, II, III and IV; Eq. (B.9) becomes,

$$dp_i = (\langle O_{il}\rangle + \Lambda \langle S_{il}\rangle)\, p_l dt - \Lambda p_i p_j \langle S_{jl}\rangle\, p_l dt - \frac{1}{2} D\, Ku \left(6\Lambda^2 + 10\right) p_i dt + \sqrt{2\, D\, Ku}\Big\{\Lambda(d_1+d_3) dW^s_{il} p_l + (d_1 - d_3) dW^a_{il} p_l - \Lambda(d_1+d_3) p_i p_j dW^s_{jl} p_l\Big\}.$$

If we replace the values $d_1 = (\sqrt{3}+\sqrt{5})/2$, $d_2 = -\sqrt{3}/3$ and $d_3 = (\sqrt{3}-\sqrt{5})/2$, (from Expr. (B.7)) we finally get:

$$\begin{aligned} dp_i = &(\langle O_{il}\rangle + \Lambda \langle S_{il}\rangle)\, p_l dt - \Lambda p_i p_j \langle S_{jl}\rangle\, p_l dt - \left(\frac{\nu_s}{2}\Lambda^2 + \frac{\nu_a}{2}\right) p_i dt \\ &+ (\nu_a dW^a_{il} + \nu_s \Lambda dW^s_{il})\, p_l - \nu_s \Lambda p_i p_j dW^s_{jl} p_l, \end{aligned} \tag{B.10}$$

and the Stratonovich (∂) form results to be,

$$\begin{aligned} dp_i = &(\langle O_{il}\rangle + \Lambda \langle S_{il}\rangle)\, p_l dt - \Lambda p_i p_j \langle S_{jl}\rangle\, p_l dt \\ &+ (\nu_a \partial W^a_{il} + \nu_s \Lambda \partial W^s_{il})\, p_l - \nu_s \Lambda p_i p_j \partial W^s_{jl} p_l, \end{aligned} \tag{B.11}$$

two parameters related to the symmetric and antisymmetric part of the fluctuations $\nu_s = \sqrt{6\, D\, Ku}$ and $\nu_a = \sqrt{10\, D\, Ku}$ and with the symmetric part and antisymmetric matrices $W^s_{il} = (W_{il} + dW_{li})/2$, $W^a_{il} = (W_{il} - W_{li})/2$ have been used.

B.3 APPENDIX: ITÔ ISOMETRY

In this section we present first the explicit form of Eqs. (4.22) and (4.23); then these expressions will be used to derive the analytical forms of Exprs. (4.28) and (4.29) in the case of homogenous isotropic turbulence. Recalling Eqs. (4.21), (4.23) and (4.22), which are respectively,

$$d\boldsymbol{\phi} = \frac{1}{2}\langle \boldsymbol{\omega}\rangle\, dt + \Lambda(\boldsymbol{p} \times \langle \boldsymbol{S}\rangle\, \boldsymbol{p}) dt + \frac{\nu_a}{2} d\mathbf{w}^a + \nu_s \Lambda\, \boldsymbol{p} \times d\mathbf{W}^s \boldsymbol{p}, \tag{B.12}$$

$$\boldsymbol{\phi}_{\perp p}(t) = \int_0^t \boldsymbol{p} \times (d\boldsymbol{\phi} \times \boldsymbol{p})\,, \tag{B.13}$$

$$\boldsymbol{\phi}_{\parallel p}(t) = \int_0^t \boldsymbol{p} \cdot d\boldsymbol{\phi}. \tag{B.14}$$

Here the mean antisymmetric part of the velocity gradient tensor has been rewritten as $\langle \boldsymbol{O}\rangle\, \boldsymbol{p} = (\langle \boldsymbol{\omega}\rangle \times \boldsymbol{p})/2$, where $\boldsymbol{\omega}$ is the vorticity vector. Analogously the fluctuating part becomes $d\mathbf{W}^a\, \boldsymbol{p} = (d\mathbf{w}^a \times \boldsymbol{p})/2$, where we have identified the vorticity vector fluctuation as $\mathbf{w}^a = 2(\mathbf{W}^a_{32}, \mathbf{W}^a_{13}, \mathbf{W}^a_{21})^\intercal$.

Then replacing Eq. (B.12) into (B.14) and (B.13) respectively, we get

$$\begin{aligned} \boldsymbol{\phi}_{\perp p}(t) &= \int_0^t \boldsymbol{p} \times \left[\frac{1}{2}\langle \boldsymbol{\omega}\rangle \times \boldsymbol{p} + \Lambda\left(\langle S\rangle\, \boldsymbol{p} - \boldsymbol{p}\boldsymbol{p}^\intercal \langle S\rangle\, \boldsymbol{p}\right)\right] ds \\ &\quad + \int_0^t \boldsymbol{p} \times \left[\frac{\nu_a}{2} d\mathbf{w}^a \times \boldsymbol{p} + \nu_s \Lambda\left(d\mathbf{W}^s \boldsymbol{p} - \boldsymbol{p}\boldsymbol{p}^\intercal d\mathbf{W}^s \boldsymbol{p}\right)\right] \\ &= \int_0^t \left[\frac{1}{2}(\mathbb{1} - \boldsymbol{p}\boldsymbol{p}^\intercal)\langle \boldsymbol{\omega}\rangle + \Lambda \boldsymbol{p} \times \langle S\rangle\, \boldsymbol{p}\right] ds \\ &\quad + \int_0^t \frac{\nu_a}{2}(\mathbb{1} - \boldsymbol{p}\boldsymbol{p}^\intercal) d\mathbf{w}^a + \nu_s \Lambda \boldsymbol{p} \times d\mathbf{W}^s \boldsymbol{p}, \end{aligned} \tag{B.15}$$

$$\begin{aligned}\phi_{\|p}(t) =& \int_0^t \boldsymbol{p}\cdot\left[\frac{1}{2}\langle\boldsymbol{\omega}\rangle + \Lambda\boldsymbol{p}\times\langle S\rangle\,\boldsymbol{p}\right] ds \\ &+ \int_0^t \boldsymbol{p}\cdot\left(\frac{\nu_a}{2} d\mathbf{w}^a + \nu_s\Lambda\boldsymbol{p}\times d\mathbf{W}^s\boldsymbol{p}\right) \\ =& \frac{1}{2}\int_0^t \boldsymbol{p}\cdot\langle\boldsymbol{\omega}\rangle\, ds + \frac{\nu_a}{2}\int_0^t \boldsymbol{p}\cdot d\mathbf{w}^a.\end{aligned} \tag{B.16}$$

where $\mathbb{1}$ is the identity matrix. Now we want to focus the attention only on the stochastic part which means to set to zero the mean contributions in Exprs (B.15) and (B.16). In order to compute the expectation of the norm squared for the quantities $\phi_{\perp p}$ and $\phi_{\|p}$, we need to apply the Itô isometry for the stochastic integrals. Recalling the definition of the Itô isometry from the book of Øksendal (2003),

Definition 3 *(Itô isometry) Let $\boldsymbol{B} : [0,T]\times\Omega\to\mathbb{R}^n$ be a standard n-dimensional Brownian motion and $\boldsymbol{M} : [0,T]\times\Omega\to\mathbb{R}^{d\times n}$ be a matrix valued stochastic process adapted to the natural filtration of the Brownian motion. Then*

$$\mathbb{E}\left[\left\|\int_0^T \boldsymbol{M}_t\, d\boldsymbol{B}_t\right\|^2\right] = \mathbb{E}\left[\int_0^T \|\boldsymbol{M}_t\|_F^2\, dt\right],$$

where the norm in the right-hand side is the Frobenious norm of the matrix valued process.

The expectation of the norm squared for the quantity $\phi_{\perp p}$ can be written as,

$$\begin{aligned}\mathbb{E}\left\|\phi_{\perp p}(t)\right\|^2 =& \mathbb{E}\left\|\int_0^t \left(\frac{\nu_a}{2}(\mathbb{1}-\boldsymbol{p}\boldsymbol{p}^\intercal)d\mathbf{w}^a + \nu_s\Lambda\boldsymbol{p}\times d\mathbf{W}^s\boldsymbol{p}\right)\right\|^2 \\ =& \mathbb{E}\left\|\int_0^t \boldsymbol{M}\, d\mathrm{w}\right\|^2 = \mathbb{E}\left[\int_0^t \|\boldsymbol{M}\|^2\, ds\right] = \left(\nu_a^2 + \nu_s^2\Lambda^2\right) t,\end{aligned} \tag{B.17}$$

here we have applied Definition 3. The standard 9-dimensional Brownian vector $\mathbf{w}$ has been used by reshaping the same 9 elements of the matrix $\mathbf{W}$ (see. Remark 2). The matrix $\boldsymbol{M}_{3\times 9}$ has been constructed in order to apply the Itô's isometry and, for sake of simplicity, we will define it by blocks of3 by 3 matrices, so that:

$$\boldsymbol{M}_{1:3,1:9} = \frac{1}{2}[\boldsymbol{M}_{1:3,1:3}\,\boldsymbol{M}_{1:3,4:6}\,\boldsymbol{M}_{1:3,7:9}].$$

We have:

$$\boldsymbol{M}_{1:3,1:3} = \begin{bmatrix} 0 & m^{(-)}p_1p_3 & -m^{(-)}p_1p_2 \\ 2\Lambda\nu_s p_1p_3 & m^{(+)}p_2p_3 & m^{(-)}p_1^2 + m^{(+)}p_3^2 \\ -2\Lambda\nu_s p_1p_2 & -m^{(-)}p_1^2 - m^{(+)}p_2^2 & -m^{(+)}p_2p_3 \end{bmatrix}$$

$$\boldsymbol{M}_{1:3,4:6} = \begin{bmatrix} -m^{(+)}p_1p_3 & -2\Lambda\nu_s p_2p_3 & -m^{(-)}p_2^2 - m^{(+)}p_3^2 \\ -m^{(-)}p_2p_3 & 0 & m^{(-)}p_1p_23 \\ m^{(-)}p_2^2 + m^{(+)}p_1^2 & 2\Lambda\nu_s p_1p_2 & m^{(+)}p_1p_3 \end{bmatrix}$$

$$\boldsymbol{M}_{1:3,7:9} = \begin{bmatrix} m^{(+)}p_1p_2 & m^{(-)}p_3^2 + m^{(+)}p_2^2 & 2\Lambda\nu_s p_2p_3 \\ -m^{(-)}p_1^2 - m^{(+)}p_3^2 & -m^{(+)}p_1p_2 & -2\Lambda\nu_s p_1p_3 \\ m^{(-)}p_2p_3 & -m^{(-)}p_1p_3 & 0 \end{bmatrix}$$

where $m^{(+)} = \nu_a + \Lambda\nu_s$ and $m^{(-)} = \nu_a - \Lambda\nu_s$.

In analogous way, the expectation of the norm squared for the quantity $\phi_{\|p}$ leads to,

$$\mathbb{E}\left[\phi_{\|p}(t)\right]^2 = \mathbb{E}\left[\int_0^t \frac{\nu_a}{2}\boldsymbol{p}d\mathbf{w}^a\right]^2 = \frac{\nu_a^2}{2}\mathbb{E}\left[\int_0^t \|\boldsymbol{p}\|_F^2\, ds\right] = \frac{\nu_a^2}{2}t, \tag{B.18}$$

where $\boldsymbol{p}$ has unitary norm. In addition, we remark that the explicit form of $\mathbf{w}^a$, in terms of the elements of the matrix $\mathbf{W}$, is $\mathbf{w}^a = (W_8 - W_6, W_3 - W_7, W_4 - W_2)$.

B.4 APPENDIX: MOMENTS' EQUATION

In the absence of mean field contribution, it is possible to compute an analytical solution for the first three moments. Recalling that Eq. (4.17) when the mean contribution is zero reads

$$dp_i = -\frac{\nu_s}{2}\Lambda^2 p_i dt + \nu_s\Lambda\left(d\mathrm{W}^s_{il} - p_i p_j d\mathrm{W}^s_{jl}\right)p_l - \frac{\nu_a}{2}p_i dt + \nu_a d\mathrm{W}^a_{il}p_l. \tag{B.19}$$

The latter equation contains the two contribution of Eq. (4.49) and (4.50). Applying the Itô's lemma to the function $f(\boldsymbol{p}_t)$ that takes values p_i, $p_i p_j$ and p_i^3 and then computing the expectation, we get

$$\frac{d}{dt}\mathbb{E}[p_i](t) = -\frac{c}{2}\mathbb{E}[p_i] \tag{B.20}$$

$$\frac{d}{dt}\mathbb{E}[p_i p_j](t) = -\frac{3c}{2}\mathbb{E}[p_i p_j] \tag{B.21}$$

$$\frac{d}{dt}\mathbb{E}[p_i^2](t) = \frac{c}{2}\left(1 - 3\mathbb{E}[p_i^2](t)\right) \tag{B.22}$$

$$\frac{d}{dt}\mathbb{E}[p_i^3](t) = \frac{3}{2}c\left(\mathbb{E}[p_i](t) - 2\mathbb{E}[p_i^3](t)\right) \tag{B.23}$$

These equations have the same structure for the three Eqs. (4.49), (4.50) and (B.19); differing for a constant factor c for the Brownian stretching part, Brownian rotation part and the composition of these two. The coefficient takes the value respectively

$$c = \begin{cases} \Lambda^2\nu_s^2 & \text{for (}\mathbb{B}\text{S) Eq. (4.49)} \\ \nu_a^2 & \text{for (}\mathbb{B}\text{R) Eq. (4.50)} \\ \Lambda^2\nu_s^2 + \nu_a^2 & \text{for (}\mathbb{B}\text{S) + (}\mathbb{B}\text{R) Eq. (4.49)+ (4.50).} \end{cases} \tag{B.24}$$

Then the solution for the moments is

$$\mathbb{E}[p_i](t) = \mathbb{E}[p_i](0)e^{-\frac{c}{2}t} \tag{B.25}$$

$$\mathbb{E}[p_i p_j](t) = \mathbb{E}[p_i p_j](0)e^{-\frac{3c}{2}t} \tag{B.26}$$

$$\mathbb{E}[p_i^2](t) = \mathbb{E}[p_i^2](0)e^{-\frac{3}{2}ct} + \frac{1}{3}(1 - e^{-\frac{3}{2}ct}) \tag{B.27}$$

$$\mathbb{E}[p_i^3](t) = e^{-3ct}\left(\mathbb{E}[p_i^3](0) - \frac{3}{5}\mathbb{E}[p_i](0)\right) + \frac{3}{5}\mathbb{E}[p_i](0)e^{-\frac{c}{2}t} \tag{B.28}$$

easy to see that the resulting equations for the moments have the same structure for the three Eqs. (4.49), (4.50) and (B.19)); differing for a constant coefficient c for the Brownian stretching part, Brownian rotation part and the full Brownian i.e. the composition of the first two.

B.5 SOME SCHEME'S PROPERTIES

In this section we want to compute the expectation of norm of the numerical schemes used in the splitting algorithm. In particular, we want to highlight the difference between the näive approach by using a semi-implicit Euler–Maruyama scheme Eq. (4.67) and the semi-implicit Euler–Maruyama scheme using the quaternion approach Eq. (4.87). Moreover, for the stretching part of the splitting the semi-implicit Euler–Maruyama scheme Eq. (4.93) will be analysed.

B.5.1 *About the näive Brownian rotation scheme*

Recalling the semi-implicit Euler–Maruyama scheme in Eq. (4.67), with a starting initial condition $\widehat{\boldsymbol{p}}_{ba,0}$ such that $\|\widehat{\boldsymbol{p}}_{ba,0}\| = 1$, it reads

$$\begin{aligned}
\tilde{p}_{ba(1),k+1} &= \left[\widehat{p}_{ba(1),k} + \frac{\nu_a}{2}\left(\Delta \mathrm{w}^a_{2,k}\,\widehat{p}_{ba(3),k} - \Delta \mathrm{w}^a_{3,k}\,\widehat{p}_{ba(2),k}\right)\right]\frac{1}{1+\frac{\nu_a^2}{2}\Delta t}\\
\tilde{p}_{ba(2),k+1} &= \left[\widehat{p}_{ba(2),k} + \frac{\nu_a}{2}\left(\Delta \mathrm{w}^a_{3,k}\,\widehat{p}_{ba(1),k} - \Delta \mathrm{w}^a_{1,k}\,\widehat{p}_{ba(3),k}\right)\right]\frac{1}{1+\frac{\nu_a^2}{2}\Delta t}\\
\tilde{p}_{ba(3),k+1} &= \left[\widehat{p}_{ba(3),k} + \frac{\nu_a}{2}\left(\Delta \mathrm{w}^a_{1,k}\,\widehat{p}_{ba(2),k} - \Delta \mathrm{w}^a_{2,k}\,\widehat{p}_{ba(1),k}\right)\right]\frac{1}{1+\frac{\nu_a^2}{2}\Delta t},
\end{aligned}$$

where at each time step we re-normalize and obtain $\widehat{\boldsymbol{p}}_{ba,k+1} = \tilde{\boldsymbol{p}}_{ba,k+1}/\|\tilde{\boldsymbol{p}}_{ba,k+1}\|$.

By computing the expectation of the norm squared we have

$$\mathbb{E}\|\tilde{\boldsymbol{p}}_{ba,k+1}\|^2 = \frac{(1+\nu_a^2\,\Delta t)}{(1+\frac{\nu_a^2}{2}\Delta t)^2}, \tag{B.29}$$

Since the map $x \mapsto \frac{(1+2x)}{(1+x)^2}$ expands around zero as $1 - x^2 + \mathcal{O}(x^3)$, we get for the norm of the semi-implicit Euler–Maruyama scheme for Brownian

$$\mathbb{E}\|\tilde{\boldsymbol{p}}_{ba,k+1}\|^2 = 1 - \frac{\nu_a^4}{4}\Delta t^2 + \mathcal{O}(\Delta t^3). \tag{B.30}$$

So, at least for the mean, the norm is not preserved and the error generated regarding just the norm squared converge with a rate Δt^2.

B.5.2 *About the quaternion Brownian rotation scheme*

Recalling the semi-implicit Euler–Maruyama scheme in Eq. (4.87), that solve the increment of quaternions with respect to the fixed unitary quaternion $\mathrm{q}^{\mathrm{fix}} = (1,0,0,0)$. We recall that the scheme reads

$$\begin{aligned}
&\left(\Delta\tilde{\mathrm{q}}_{0,k+1};\, \Delta\tilde{\mathrm{q}}_{1,k+1};\Delta\tilde{\mathrm{q}}_{2,k+1};\, \Delta\tilde{\mathrm{q}}_{3,k+1};\, \Delta\tilde{\mathrm{q}}_{4,k+1}\right)^{\mathsf{T}}\\
&\qquad = \left(1;\, \frac{\nu_a}{4}\,\Delta \mathrm{w}^a_{1,k};\, \frac{\nu_a}{4}\,\Delta \mathrm{w}^a_{2,k};\, \frac{\nu_a}{4}\,\Delta \mathrm{w}^a_{3,k}\right)^{\mathsf{T}}\frac{1}{1+\frac{3}{16}\nu_a^2\Delta t}.
\end{aligned}$$

In order to preserve the unit constraint, the quaternion $\Delta\tilde{\mathrm{q}}_{k+1}$ requires re-normalisation at each time step, $\Delta\hat{\mathrm{q}}_{k+1} = \Delta\tilde{\mathrm{q}}_{k+1}/\|\Delta\tilde{\mathrm{q}}_{k+1}\|$. Using the same strategy above we have that the expectation of the norm squared is

$$\mathbb{E}\|\Delta\tilde{\mathrm{q}}_{k+1}\|^2 = \frac{1+\frac{3}{8}\nu_a^2\Delta t}{(1+\frac{3}{16}\nu_a^2\Delta t)^2} \tag{B.31}$$

Since the map $x \mapsto \frac{(1+2x)}{(1+x)^2}$ expands around zero as $1 - x^2 + \mathcal{O}(x^3)$, we get for the norm of the semi-implicit Euler–Maruyama scheme for Brownian rotation using quaternions before the renormalization step that

$$\mathbb{E}\|\Delta\tilde{\mathfrak{q}}_{k+1}\|^2 = 1 - \left(\frac{3}{16}\right)^2 \nu_a^4 \, \Delta t^2 + \mathcal{O}(\Delta t^3). \tag{B.32}$$

B.5.3 *About the Brownian stretching scheme*

We consider the stretching sub-part of the splitting scheme and we recall its numerical implementation in the non-linear version in Eq. (4.93) to be,

$$\begin{aligned}
\tilde{p}_{bs(1),k+1} = \Big[& \widehat{p}_{bs(1),k} \\
& + \frac{\nu_s}{2}\Lambda\big[2\widehat{p}_{bs(1),k}(1-\widehat{p}^2_{bs(1),k})\Delta W_1 - 2\widehat{p}_{bs(1),k}\widehat{p}^2_{bs(2),k}\Delta W_5 - 2\widehat{p}_{bs(1),k}\widehat{p}^2_{bs(3),k}\Delta W_9 \\
& + \widehat{p}_{bs(2),k}(1-2\widehat{p}^2_{bs(1),k})(\Delta W_2 + \Delta W_4) + \widehat{p}_{bs(3),k}(1-2\widehat{p}^2_{bs(1),k})(\Delta W_3 + \Delta W_7) \\
& - 2\widehat{p}_{bs(1),k}\widehat{p}_{bs(2),k}\widehat{p}_{bs(3),k}(\Delta W_6 + \Delta W_8)\big]\Big]\frac{1}{1+\frac{\nu_s^2}{2}\Lambda^2\Delta t} \\
\tilde{p}_{bs(2),k+1} = \Big[& \widehat{p}_{bs(2),k} \\
& + \frac{\nu_s}{2}\Lambda\Big[2\widehat{p}_{bs(2),k}(1-\widehat{p}^2_{bs(2),k})\Delta W_5 - 2\widehat{p}_{bs(2),k}\widehat{p}^2_{bs(1),k}\Delta W_1 - 2\widehat{p}_{bs(2),k}\widehat{p}^2_{bs(3),k}\Delta W_9 \\
& + \widehat{p}_{bs(1),k}(1-2\widehat{p}^2_{bs(2),k})(\Delta W_2 + \Delta W_4) + \widehat{p}_{bs(3),k}(1-2\widehat{p}^2_{bs(2),k})(\Delta W_6 + \Delta W_8) \\
& - 2\widehat{p}_{bs(1),k}\widehat{p}_{bs(2),k}\widehat{p}_{bs(3),k}(\Delta W_3 + \Delta W_7)\big]\Big]\frac{1}{1+\frac{\nu_s^2}{2}\Lambda^2\Delta t} \\
\tilde{p}_{bs(3),k+1} = \Big[& \widehat{p}_{bs(3),k} \\
& + \frac{\nu_s}{2}\Lambda\Big[2\widehat{p}_{bs(3),k}(1-\widehat{p}^2_{bs(3),k})\Delta W_9 - 2\widehat{p}_{bs(3),k}\widehat{p}^2_{bs1}\Delta W_1 - 2\widehat{p}_{bs(3),k}\widehat{p}^2_{bs(2),k}\Delta W_5 \\
& + \widehat{p}_{bs(1),k}(1-2\widehat{p}^2_{bs(3),k})(\Delta W_3 + \Delta W_7) + \widehat{p}_{bs(2),k}(1-2\widehat{p}^2_{bs(3),k})(\Delta W_6 + \Delta W_8) \\
& - 2\widehat{p}_{bs(1),k}\widehat{p}_{bs(2),k}\widehat{p}_{bs(3),k}(\Delta W_2 + \Delta W_4)\big]\Big]\frac{1}{1+\frac{\nu_s^2}{2}\Lambda^2\Delta t},
\end{aligned}$$

where at each time step we re-normalize and obtain $\widehat{\boldsymbol{p}}_{bs,k+1} = \tilde{\boldsymbol{p}}_{bs,k+1}/\|\tilde{\boldsymbol{p}}_{bs,k+1}\|$. We want to examine the ability of the equation above into preserve the norm of the corresponding

approximation. Taking the expectation of the square of each coordinates in Eq. (4.93) and summing the result we obtain expectation

$$\begin{aligned}\mathbb{E}\|\tilde{\boldsymbol{p}}_{bs,k+1}\|^2 = \Big[1+\frac{\nu_s^2}{4}\Lambda^2\Delta t\big[&4\widehat{p}^2_{bs(1),k}(1-\widehat{p}^2_{bs(1),k})^2 + 4\widehat{p}^2_{bs(1),k}\widehat{p}^4_{bs(2),k} + 4\widehat{p}^2_{bs(1),k}\widehat{p}^4_{bs(3),k}\\ &+ 2\widehat{p}^2_{bs(2),k}(1-2\widehat{p}^2_{bs(1),k})^2 + 2\widehat{p}^2_{bs(3),k}(1-2\widehat{p}^2_{bs(1),k})^2\\ &+ 8\widehat{p}^2_{bs(1),k}\widehat{p}^2_{bs(2),k}\widehat{p}^2_{bs(3),k}\\ &+ 4\widehat{p}^2_{bs(2),k}(1-\widehat{p}^2_{bs(2),k})^2 + 4\widehat{p}^2_{bs(2),k}\widehat{p}^4_{bs(1),k} + 4\widehat{p}^2_{bs(2),k}\widehat{p}^4_{bs(3),k}\\ &+ 2\widehat{p}^2_{bs(1),k}(1-2\widehat{p}^2_{bs(2),k})^2 + 2\widehat{p}^2_{bs(3),k}(1-2\widehat{p}^2_{bs(2),k})^2\\ &+ 8\widehat{p}^2_{bs(1),k}\widehat{p}^2_{bs(2),k}\widehat{p}^2_{bs(3),k}\\ &+ 4\widehat{p}^2_{bs(3),k}(1-\widehat{p}^2_{bs(3),k})^2 + 4\widehat{p}^2_{bs(3),k}\widehat{p}^4_{bs1} + 4\widehat{p}^2_{bs(3),k}\widehat{p}^4_{bs(2),k}\\ &+ 2\widehat{p}^2_{bs(1),k}(1-2\widehat{p}^2_{bs(3),k})^2 + 2\widehat{p}^2_{bs(2),k}(1-2\widehat{p}^2_{bs(3),k})^2\\ &+ 8\widehat{p}^2_{bs(1),k}\widehat{p}^2_{bs(2),k}\widehat{p}^2_{bs(3),k}\big]\Big]\frac{1}{(1+\frac{\nu_s^2}{2}\Lambda^2\Delta t)^2},\end{aligned}$$

having used the independence of the Brownian vector components, and the fact that $\|\widehat{\boldsymbol{p}}_{bs,k}\| = 1$. We then observe that

$$\begin{aligned}&4\widehat{p}^2_{bs(1),k}(1-\widehat{p}^2_{bs(1),k})^2 + 4\widehat{p}^2_{bs(1),k}\widehat{p}^4_{bs(2),k} + 4\widehat{p}^2_{bs(1),k}\widehat{p}^4_{bs(3),k} + 8\widehat{p}^2_{bs(1),k}\widehat{p}^2_{bs(2),k}\widehat{p}^2_{bs(3),k}\\ &= 4\widehat{p}^2_{bs(1),k}\big((1-\widehat{p}^2_{bs(1),k})^2 + \widehat{p}^4_{bs(2),k} + \widehat{p}^4_{bs(3),k} + 2\widehat{p}^2_{bs(2),k}\widehat{p}^2_{bs(3),k}\big)\\ &= 8\widehat{p}^2_{bs(1),k}(1-\widehat{p}^2_{bs(1),k})^2.\end{aligned}$$

Moreover

$$(2\widehat{p}^2_{bs(2),k} + 2\widehat{p}^2_{bs(3),k})(1-2\widehat{p}^2_{bs(1),k})^2 = 2(1-\widehat{p}^2_{bs(1),k})(1-2\widehat{p}^2_{bs(1),k})^2$$

and the sum of the two last contributions is now

$$\begin{aligned}&8\widehat{p}^2_{bs(1),k}(1-\widehat{p}^2_{bs(1),k})^2 + 2(1-\widehat{p}^2_{bs(1),k})(1-2\widehat{p}^2_{bs(1),k})^2\\ &= (1-\widehat{p}^2_{bs(1),k})(8\widehat{p}^2_{bs(1),k} - 8\widehat{p}^4_{bs(1),k} + 2 - 8\widehat{p}^2_{bs(1),k} + 8\widehat{p}^4_{bs(1),k})\\ &= 2(1-\widehat{p}^2_{bs(1),k}).\end{aligned}$$

So going back to the norm and considering the same results for the other two components we get,

$$\mathbb{E}\|\tilde{\boldsymbol{p}}_{bs,k+1}\|^2 = \frac{(1+\nu_s^2\Lambda^2\Delta t)}{(1+\frac{\nu_s^2}{2}\Lambda^2\Delta t)^2}.$$

Since the map $x \mapsto \frac{(1+2x)}{(1+x)^2}$ expands around zero as $1-x^2+\mathcal{O}(x^3)$, we get for the norm of the semi-implicit Euler–Maruyama scheme for Brownian stretching before the renormalization step that

$$\mathbb{E}\|\tilde{\boldsymbol{p}}_{bs,k+1}\|^2 = 1 - \frac{\nu_s^4}{4}\Lambda^4\Delta t^2 + \mathcal{O}(\Delta t^3). \tag{B.33}$$

B.6 STOCHASTIC TUMBLING AND SPINNING WITH SPHERICAL PARTICLES

Here, the tumbling and spinning rate for the stochastic model in Eq. (4.28) and (4.29), will be compute for a spherical particle ($\Lambda = 0$) and assuming the presence of an homogenous shear flow as the one presented in Section 4.3.3.2. Equation (4.17) for $\Lambda = 0$ reads,

$$\begin{aligned} dp_1 =& \frac{\sigma}{2} p_2 dt - \frac{1}{2}\nu_a^2 p_1 dt + \nu_a d\mathrm{W}_{1l}^a p_l \\ dp_2 =& -\frac{\sigma}{2} p_1 dt - \frac{1}{2}\nu_a^2 p_2 dt + \nu_a d\mathrm{W}_{2l}^a p_l \\ dp_3 =& -\frac{1}{2}\nu_a^2 p_3 dt + \nu_a d\mathrm{W}_{3l}^a p_l. \end{aligned} \tag{B.34}$$

Then, the probability density function, at the stationary regime (that we will call t_0), can be explicitly determined, considering that for a sphere the only possible distribution for the orientation is the uniform law on the sphere. In order to compute explicitly the moments we can pass to spherical coordinates $(p_1, p_2, p_3) \mapsto (\sin\phi\cos\theta, \sin\phi\sin\theta, \cos\phi)$ where $(\varphi, \vartheta) \in [0, \pi] \times [0, 2\pi]$ and the uniform law on the sphere $\rho(\varphi, \vartheta) = \sin\phi/(4\pi)$. In this case the moments can be computed as,

$$\mathbb{E}[f(p_1, p_2, p_3)] = \int_0^{\pi}\int_0^{2\pi} \rho(\phi, \theta) d\theta d\phi. \tag{B.35}$$

The moments involved to compute the stumbling and spinning are, $\mathbb{E}[p_i] = 0$, $\mathbb{E}[p_i^2] = 1/3$, $\mathbb{E}[p_i p_j] = 0$, $\mathbb{E}[p_i^2 p_j^2] = 1/15$, $\mathbb{E}[p_i^4] = 1/5$ and $\mathbb{E}[p_1 p_2 p_3^2] = 0$.

B.6.1 *Stochastic spinning*

In the case of Eq. (4.28), considering that $\mathbb{E}[p_3] = 0$,

$$\Phi_{\|p} = \frac{\sigma^2}{2}\int_0^t \mathbb{E}\left[p_3(t_0)p_3(s)\right] ds + \frac{\nu_a^2}{2}. \tag{B.36}$$

At the stationary regime, considering p_3 in Eq. (B.34), and multiplying it for $p_3(t_0)$, and renaming the stochastic term with $\mathscr{M}$,

$$d(p_3(t_0)p_3(t)) = -\frac{1}{2}\nu_a^2 p_3(t_0)p_3(t)dt + \mathscr{M} p_3(t_0), \tag{B.37}$$

then, considering the solution of this equation and taking the expectation we had $\mathbb{E}[p_3(t_0)p_3(t)] = \mathbb{E}[p_3(t_0)p_3(t_0)]\exp\left(-\nu_a^2 t/2\right)$. By computing the spinning for very long time behaviour,

$$\begin{aligned} \Phi_{\|p} &= \frac{\sigma^2}{2}\int_0^{\infty} \mathbb{E}[p_3(t_0)p_3(t_0)]\exp\left(-\frac{\nu_a^2}{2}s\right) ds + \frac{\nu_a^2}{2} \\ &= -\frac{\sigma^2}{\nu_a^2}\mathbb{E}[p_3^2(t_0)]\exp\left(-\frac{\nu_a^2}{2}s\right)\Big|_0^{\infty} + \frac{\nu_a^2}{2} = \frac{\sigma^2}{3\nu_a^2} + \frac{\nu_a^2}{2} \end{aligned} \tag{B.38}$$

B.6.2 *Stochastic tumbling*

In the case of tumbling the method is equivalent but with the implication of high order moments.

$$\begin{aligned}\Phi_{\perp p} = \frac{\sigma^2}{2}\Big\{ &\int_0^t \mathbb{E}\left[p_1p_3(t_0)p_1p_3(s)\right] - \mathbb{E}\left[p_1p_3(t_0)\right]\mathbb{E}\left[p_1p_3(s)\right] ds \\ &+ \int_0^t \mathbb{E}\left[p_2p_3(t_0)p_2p_3(s)\right] - \mathbb{E}\left[p_2p_3(t_0)\right]\mathbb{E}\left[p_2p_3(s)\right] ds \\ &+ \int_0^t \mathbb{E}\left[p_3^2(t_0)p_3^2(s)\right] - \mathbb{E}\left[p_3^2(t_0)\right]\mathbb{E}\left[p_3^2(s)\right] ds\Big\} + \nu_a^2 \\ = \frac{\sigma^2}{2}\Big\{ &\int_0^t \mathbb{E}\left[p_1p_3(t_0)p_1p_3(s)\right] ds + \int_0^t \mathbb{E}\left[p_2p_3(t_0)p_2p_3(s)\right] ds \\ &+ \int_0^t \mathbb{E}\left[p_3^2(t_0)p_3^2(s)\right] - \mathbb{E}\left[p_3^2(t_0)\right]\mathbb{E}\left[p_3^2(s)\right] ds\Big\} + \nu_a^2,\end{aligned} \tag{B.39}$$

where we have simplified the above equation taking the values at the stationary initial time t_0. Using the Itô's lemma to compute higher polynomial equation for $\boldsymbol{p}$,

$$dp_3^2(t) = \frac{\nu_a^2}{2}(1 - 3p_3^2(t))dt + \mathscr{M}, \tag{B.40}$$

and its solution reads,

$$\mathbb{E}[p_3^2(t)] = \mathbb{E}[p_3^2(t_0)]\exp\left(-\frac{3}{2}\nu_a^2 t\right) + \frac{1}{3}\left(1 - \exp\left(-\frac{3}{2}\nu_a^2 t\right)\right). \tag{B.41}$$

Multiplying Eq. (B.40) for $p_3^2(t_0)$ we get,

$$d(p_3^2(t_0)p_3^2(t)) = \frac{\nu_a^2}{2}(p_3^2(t_0) - 3(p_3^2(t_0)p_3^2(t)))dt + \mathscr{M}(p_3^2(t_0)p_3^2(t)), \tag{B.42}$$

solving this last equation and taking the expectation we had,

$$\mathbb{E}[p_3^2(t_0)p_3^2(t)] = \mathbb{E}[p_3^4(t_0)]\exp\left(-\frac{3}{2}\nu_a^2 t\right) + \frac{1}{3}\mathbb{E}[p_3^2(t_0)]\left(1 - \exp\left(-\frac{3}{2}\nu_a^2 t\right)\right). \tag{B.43}$$

Finally the contribution of this part in Eq. (B.39) can be expressed as,

$$\begin{aligned}&\int_0^t \mathbb{E}\left[p_3^2(t_0)p_3^2(s)\right] ds - \int_0^t \mathbb{E}\left[p_3^2(t_0)\right]\mathbb{E}\left[p_3^2(s)\right] ds \\ &\int_0^t \mathbb{E}\left[p_3^4(t_0)\right]\exp\left(-\frac{3}{2}\nu_a^2 s\right) ds + \frac{1}{3}\mathbb{E}[p_3^2(t_0)]\int_0^t \left(1 - \exp\left(-\frac{3}{2}\nu_a^2 s\right)\right) ds \\ &- \mathbb{E}\left[p_3^2(t_0)\right]\int_0^t \left[\mathbb{E}[p_3^2(t_0)]\exp\left(-\frac{3}{2}\nu_a^2 t\right) + \frac{1}{3}\left(1 - \exp\left(-\frac{3}{2}\nu_a^2 t\right)\right)\right] ds \\ &= \frac{2}{3\nu_a^2}\left(\mathbb{E}\left[p_3^4(t_0)\right] - \mathbb{E}\left[p_3^2(t_0)\right]^2\right) = \frac{8}{135\nu_a^2}\end{aligned} \tag{B.44}$$

The two other contributions of the tumbling are coupled as,

$$dp_1p_3(t) = \frac{\sigma}{2}p_2p_3(t)dt - \frac{3}{2}\nu_a^2 p_1p_3(t)dt + \mathscr{M}, \tag{B.45a}$$

$$dp_2p_3(t) = -\frac{\sigma}{2}p_1p_3(t)dt - \frac{3}{2}\nu_a^2 p_2p_3(t)dt + \mathscr{M}. \tag{B.45b}$$

Computing the expectation

$$\frac{d}{dt}\mathbb{E}[p_1p_3(t)] = \frac{\sigma}{2}\mathbb{E}\left[p_2p_3(t)\right] - \frac{3}{2}\nu_a^2\mathbb{E}[p_1p_3(t)], \tag{B.46a}$$

$$\frac{d}{dt}\mathbb{E}[p_2p_3(t)] = -\frac{\sigma}{2}\mathbb{E}\left[p_1p_3(t)\right] - \frac{3}{2}\nu_a^2\mathbb{E}[p_2p_3(t)], \tag{B.46b}$$

the solution will be,

$$\mathbb{E}[p_1p_3(t)] = \left(\mathbb{E}\left[p_1p_3(t_0)\right]\cos\left(\frac{\sigma t}{2}\right) + \mathbb{E}\left[p_2p_3(t_0)\right]\sin\left(\frac{\sigma t}{2}\right)\right)\exp\left(-\frac{3}{2}\nu_a^2 t\right), \tag{B.47a}$$

$$\mathbb{E}[p_2p_3(t)] = \left(\mathbb{E}\left[p_2p_3(t_0)\right]\cos\left(\frac{\sigma t}{2}\right) - \mathbb{E}\left[p_1p_3(t_0)\right]\sin\left(\frac{\sigma t}{2}\right)\right)\exp\left(-\frac{3}{2}\nu_a^2 t\right). \tag{B.47b}$$

$$d(p_1p_3(t_0)p_1p_3(t)) = \frac{\sigma}{2}p_1p_3(t_0)p_2p_3(t)dt - \frac{3}{2}\nu_a^2 p_1p_3(t_0)p_1p_3(t)dt + \mathscr{M}\,p_1p_3(t_0), \tag{B.48a}$$

$$d(p_2p_3(t_0)p_2p_3(t)) = -\frac{\sigma}{2}p_2p_3(t_0)p_1p_3(t)dt - \frac{3}{2}\nu_a^2 p_2p_3(t_0)p_2p_3(t)dt + \mathscr{M}\,p_2p_3(t_0). \tag{B.48b}$$

We need to add two more equations in order to solve the full system,

$$(p_1p_3(t_0)p_1p_3(t), p_1p_3(t_0)p_2p_3(t), p_2p_3(t_0)p_1p_3(t), p_2p_3(t_0)p_2p_3(t)) \mapsto (x_1, x_2, x_3, x_4)$$

This system is coupled two by two,

$$dx_1 = \frac{\sigma}{2}x_2dt - \frac{3}{2}\nu_a^2 x_1dt + \mathscr{M}\,p_1p_3(t_0), \tag{B.49a}$$

$$dx_2 = -\frac{\sigma}{2}x_1dt - \frac{3}{2}\nu_a^2 x_2dt + \mathscr{M}\,p_1p_3(t_0), \tag{B.49b}$$

solving the system and taking the expectation,

$$\mathbb{E}[x_1(t)] = \left(\mathbb{E}\left[x_1(t_0)\right]\cos\left(\frac{\sigma t}{2}\right) + \mathbb{E}\left[x_2(t_0)\right]\sin\left(\frac{\sigma t}{2}\right)\right)\exp\left(-\frac{3}{2}\nu_a^2 t\right), \tag{B.50a}$$

$$\mathbb{E}[x_2(t)] = \left(\mathbb{E}\left[x_2(t_0)\right]\cos\left(\frac{\sigma t}{2}\right) - \mathbb{E}\left[x_1(t_0)\right]\sin\left(\frac{\sigma t}{2}\right)\right)\exp\left(-\frac{3}{2}\nu_a^2 t\right). \tag{B.50b}$$

The contribution of tumbling for this term in the long time limit,

$$\begin{aligned}\int_0^t \mathbb{E}\left[p_1p_3(t_0)p_1p_3(s)\right]ds &= \int_0^t \mathbb{E}\left[p_1^2p_3^2(t_0)\right]\cos\left(\frac{\sigma}{2}s\right)\exp\left(-\frac{3}{2}\nu_a^2 s\right)ds \\ &= \mathbb{E}\left[p_1^2p_3^2(t_0)\right]\left(\frac{3}{2}\nu_a^2\right)\left(\frac{4}{\sigma^2+9\nu_a^4}\right) = \frac{2}{5}\left(\frac{\nu_a^2}{\sigma^2+9\nu_a^2}\right)\end{aligned} \tag{B.51}$$

For the second term,

$$dx_3 = \frac{\sigma}{2}x_4dt - \frac{3}{2}\nu_a^2 x_3dt + \mathscr{M}\,p_2p_3(t_0), \tag{B.52a}$$

$$dx_4 = -\frac{\sigma}{2}x_3dt - \frac{3}{2}\nu_a^2 x_4dt + \mathscr{M}\,p_2p_3(t_0), \tag{B.52b}$$

solving the system and taking the expectation,

$$\mathbb{E}[x_3(t)] = \left(\mathbb{E}\left[x_3(t_0)\right]\cos\left(\frac{\sigma t}{2}\right) + \mathbb{E}\left[x_4(t_0)\right]\sin\left(\frac{\sigma t}{2}\right)\right)\exp\left(-\frac{3}{2}\nu_a^2 t\right), \tag{B.53a}$$

$$\mathbb{E}[x_4(t)] = \left(\mathbb{E}\left[x_4(t_0)\right]\cos\left(\frac{\sigma t}{2}\right) - \mathbb{E}\left[x_3(t_0)\right]\sin\left(\frac{\sigma t}{2}\right)\right)\exp\left(-\frac{3}{2}\nu_a^2 t\right). \tag{B.53b}$$

The contribution of tumbling for this term in the long time limit,

$$\begin{aligned}\int_0^t \mathbb{E}\left[p_2 p_3(t_0) p_1 p_3(s)\right] ds &= \int_0^t \mathbb{E}\left[p_2^2 p_3^2(t_0)\right]\cos\left(\frac{\sigma s}{2}\right)\exp\left(-\frac{3}{2}\nu_a^2 s\right) ds \\ &= \mathbb{E}\left[p_2^2 p_3^2(t_0)\right]\left(\frac{3}{2}\nu_a^2\right)\left(\frac{4}{\sigma^2 + 9\nu_a^4}\right) = \frac{2}{5}\left(\frac{\nu_a^2}{\sigma^2 + 9\nu_a^2}\right).\end{aligned} \tag{B.54}$$

Summing all contribution in Eq. (B.39), the stochastic tumbling for a sphere ($\Lambda = 0$) in the long-time limit reads,

$$\Phi_{\perp p} = \sigma^2\left[\frac{2}{5}\left(\frac{\nu_a^2}{\sigma^2 + 9\nu_a^2}\right) + \frac{4}{135\nu_a^2}\right] + \nu_a^2 \tag{B.55}$$

B.7 APPENDIX: COMPLEMENT MATERIAL CONVERGENCE

Here the additional plots on the strong and weak convergence error all along the numerical results is reported. We resume the parameters used to study the strong and weak convergence. The case of spheroidal particles with a shape parameter $\Lambda = 1$ in Eq. (4.17) has been considered. Each test case is integrated on $t \in [0, T]$ for different time steps $\Delta t = 2^{-h}$, with $h = 1, .., 12$, and the stopping time $T = 0.5$ is the same for all choices, in order to show the asymptotic convergence with respect to the time step Δt. We perform the convergence test for each simulation trial using the same number of particles $N_p = 5 \cdot 10^8$, and repeat the trials independently 10 times. A total of four different values of the characteristic time scale parameter $\tau_\eta = 0.01, 0.1, 1, 10$ are considered, fixing the Kubo number $Ku = 1$ (see, Eq. (4.17)); in this way we aim to estimate the influence of τ_η both on weak and strong convergence. Moreover, two different choices of initial conditions have been used: $\boldsymbol{p}_a^0 = (1, 0, 0)$ and $\boldsymbol{p}_b^0 = (1, 1, 1)/\sqrt{3}$.

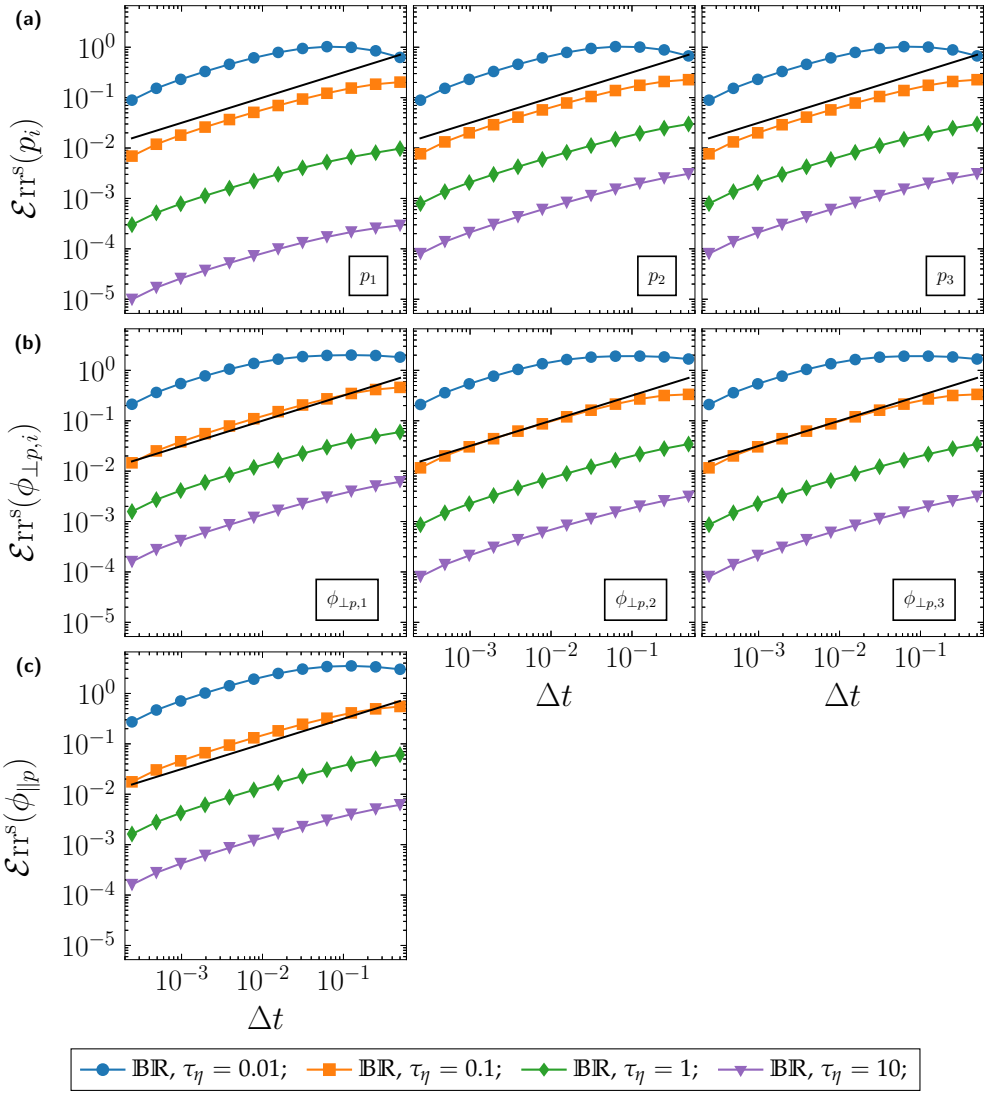

Figure B.1: Stochastic rotation sub-step ($\mathbb{BR}$): Strong error ($\mathcal{E}\mathrm{rr}^s$) of the numerical scheme in Eq. (4.89) ($\mathbb{BR}$) against the time step Δt for different values of τ_η. In (a) the three components of $\boldsymbol{p}_{bs}$, (b) the three components of $\boldsymbol{\phi}_{\perp p}$ of tumbling and (c) the spinning $\boldsymbol{\phi}_{\parallel p}$. Black line indicates the slope $1/2$; and the initial condition of particle orientation is $\boldsymbol{p}_a^0 = (1, 0, 0)$.

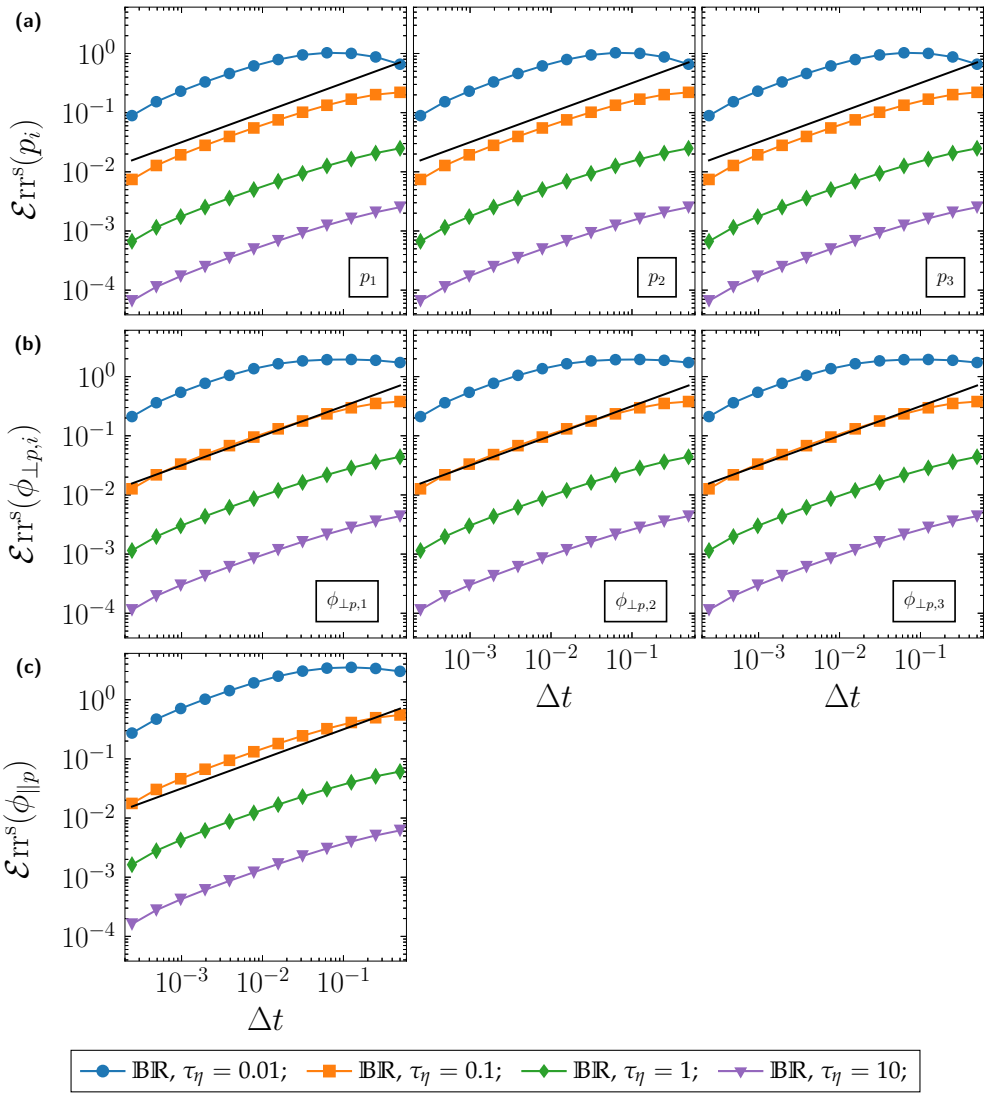

Figure B.2: Stochastic rotation sub-step ($\mathbb{BR}$): Strong error ($\mathcal{E}\mathrm{rr}^{\mathrm{s}}$) of the numerical scheme in Eq. (4.89) ($\mathbb{BR}$) against the time step Δt for different values of τ_η. In (a) the three components of $\boldsymbol{p}_{bs}$, (b) the three components of $\boldsymbol{\phi}_{\perp p}$ of tumbling and (c) the spinning $\boldsymbol{\phi}_{\parallel p}$. Black line indicates the slope $1/2$; and the initial condition of particle orientation is $\boldsymbol{p}_b^0 = (1,1,1)/\sqrt{3}$.

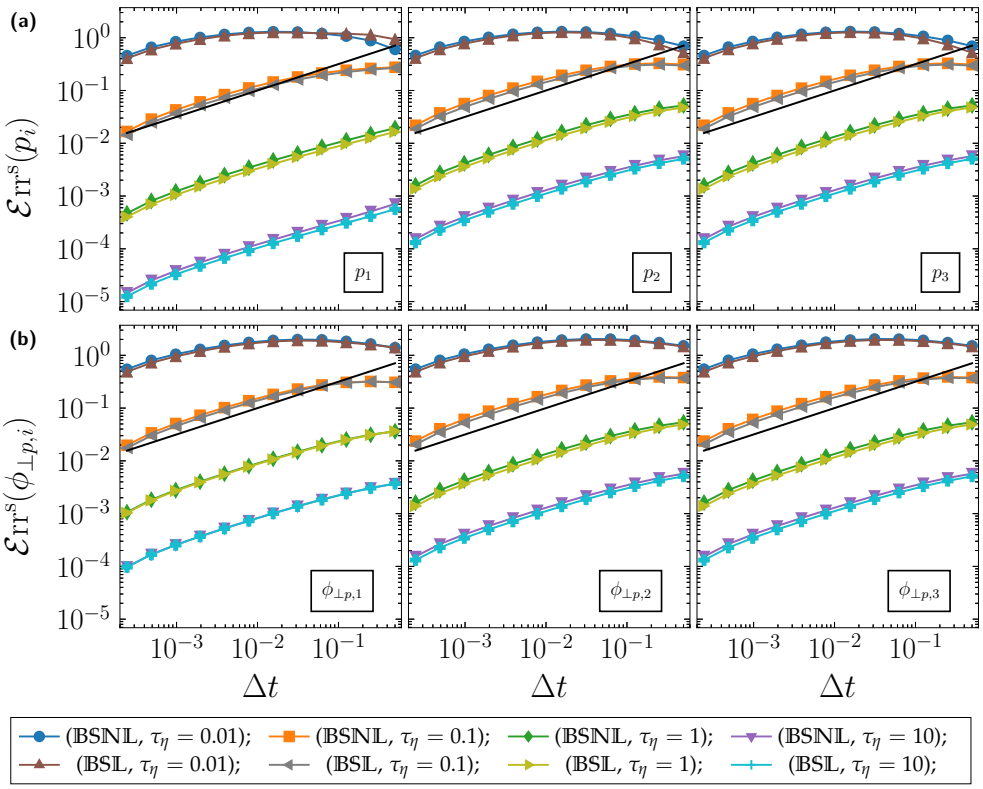

Figure B.3: Stochastic stretching sub-step (𝔹𝕊): Strong error ($\mathcal{E}\mathrm{rr}^{\mathrm{s}}$) of the numerical scheme in Eq. (4.93) (𝔹𝕊ℕ𝕃) and Eq. (4.95) (𝔹𝕊𝕃) against the time step Δt for different values of τ_η. In (a) the three components of $\boldsymbol{p}_{bs}$, (b) the three components $\phi_{\perp p}$ of tumbling. Black line indicates the slope $1/2$; and the initial condition of particle orientation is $\boldsymbol{p}_a^0 = (1, 0, 0)$.

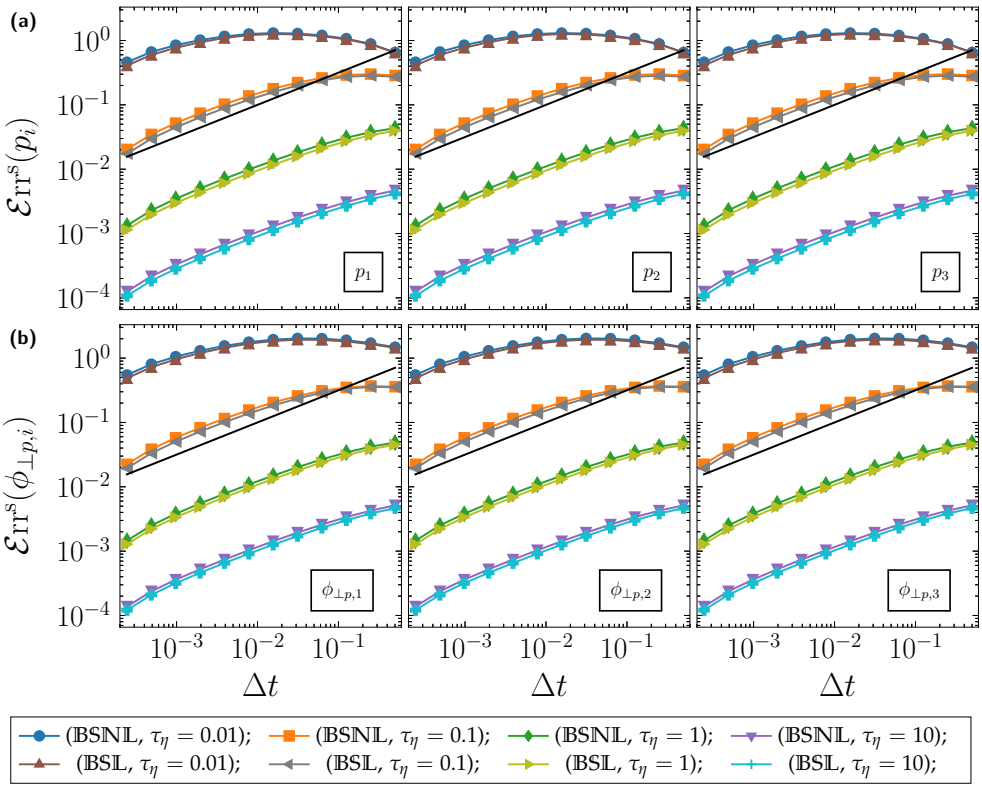

Figure B.4: Stochastic stretching sub-step (𝔹𝕊): Strong error ($\mathcal{E}\mathrm{rr}^{\mathrm{s}}$) of the numerical scheme in Eq. (4.93) (𝔹𝕊ℕ𝕃) and Eq. (4.95) (𝔹𝕊𝕃) against the time step Δt for different values of τ_η. In (a) the three components of $\boldsymbol{p}_{bs}$, (b) the three components $\phi_{\perp p}$ of tumbling. Black line indicates the slope $1/2$; and the initial condition of particle orientation is $\boldsymbol{p}_b^0 = (1,1,1)/\sqrt{3}$.

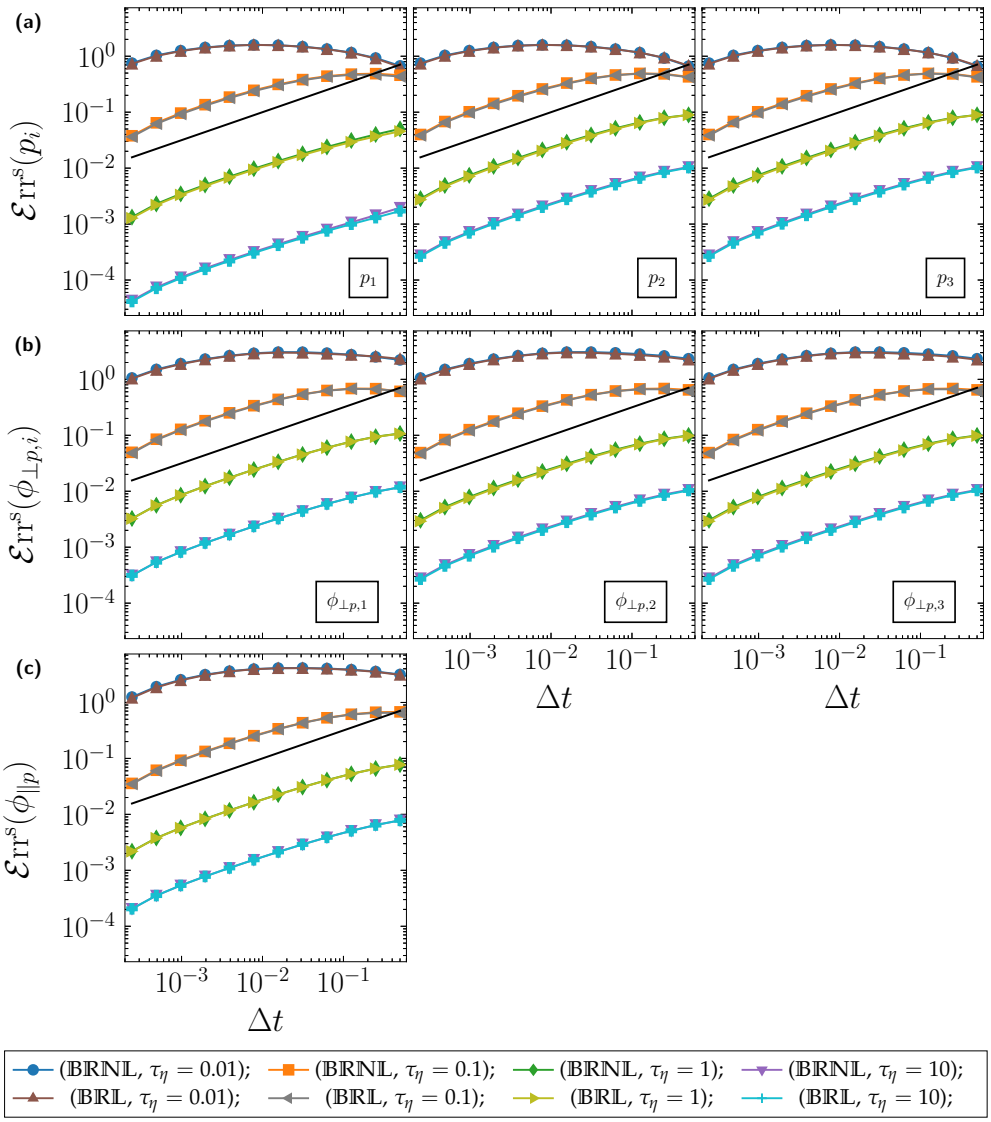

Figure B.5: Splitting scheme in HIT: Strong error ($\mathcal{E}\mathrm{rr}^s$) of the splitting algorithm Eq. (4.96) using the numerical scheme in Eq. (4.93) followed by Eq. (4.89) ($\mathbb{BR} - \mathbb{BSNL}$) and Eq. (4.95) followed by Eq. (4.89) ($\mathbb{BR} - \mathbb{BSL}$), against the time step Δt for different values of τ_η. In (a) the three components of $\boldsymbol{p}$, (b) the first component $\phi_{\perp p}$ of tumbling and (c) the spinning $\phi_{\parallel p}$. Black line indicates the slope 1/2; and the initial condition of particle orientation is $\boldsymbol{p}_a^0 = (1, 0, 0)$.

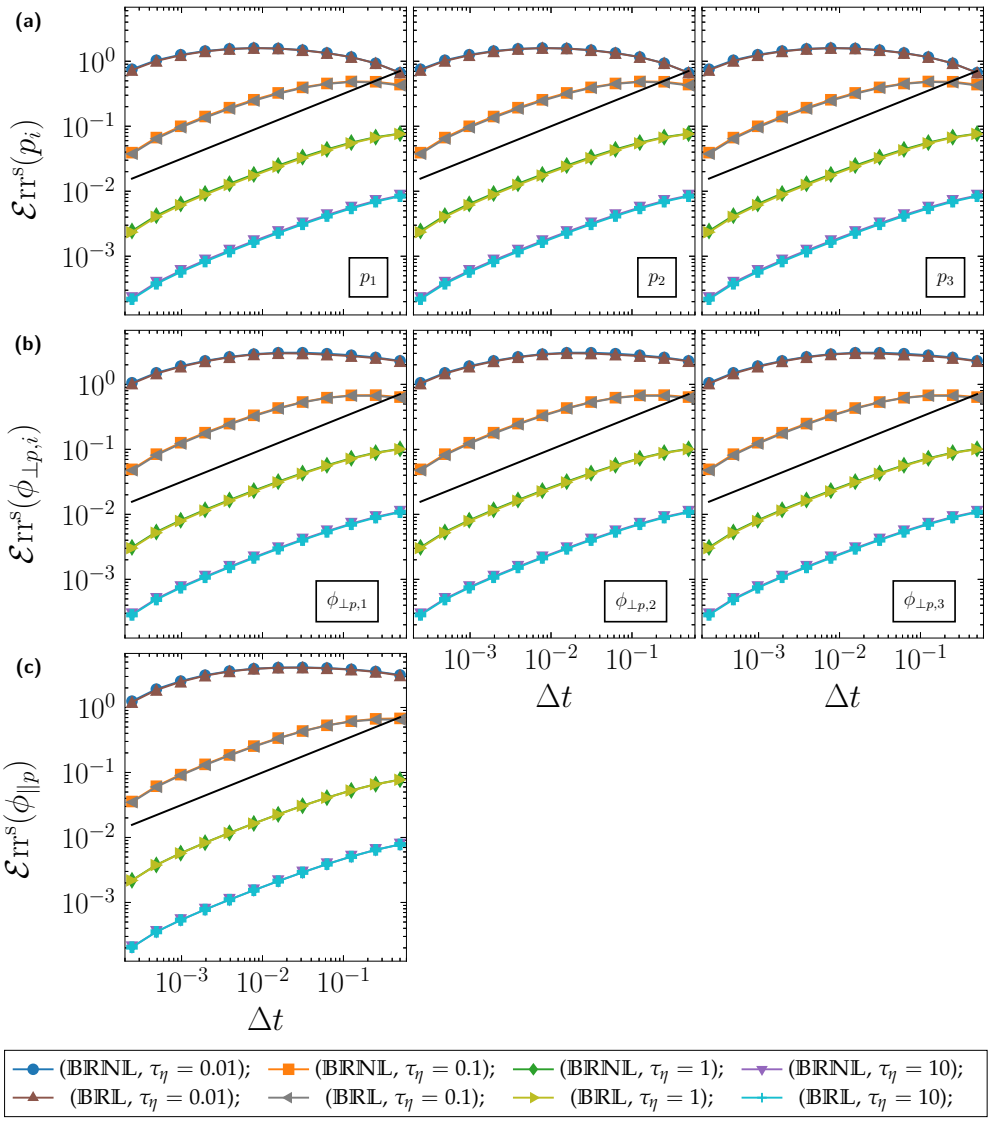

Figure B.6: Splitting scheme in HIT: Strong error ($\mathcal{E}\mathrm{rr}^s$) of the splitting algorithm Eq. (4.96) using the numerical scheme in Eq. (4.93) followed by Eq. (4.89) ($\mathbb{BR} - \mathbb{BSNL}$) and Eq. (4.95) followed by Eq. (4.89) ($\mathbb{BR} - \mathbb{BSL}$), against the time step Δt for different values of τ_η. In (a) the three components of $\boldsymbol{p}$, (b) the first component $\phi_{\perp p}$ of tumbling and (c) the spinning $\phi_{\parallel p}$. Black line indicates the slope $1/2$; and the initial condition of particle orientation is $\boldsymbol{p}_b^0 = (1,1,1)/\sqrt{3}$.

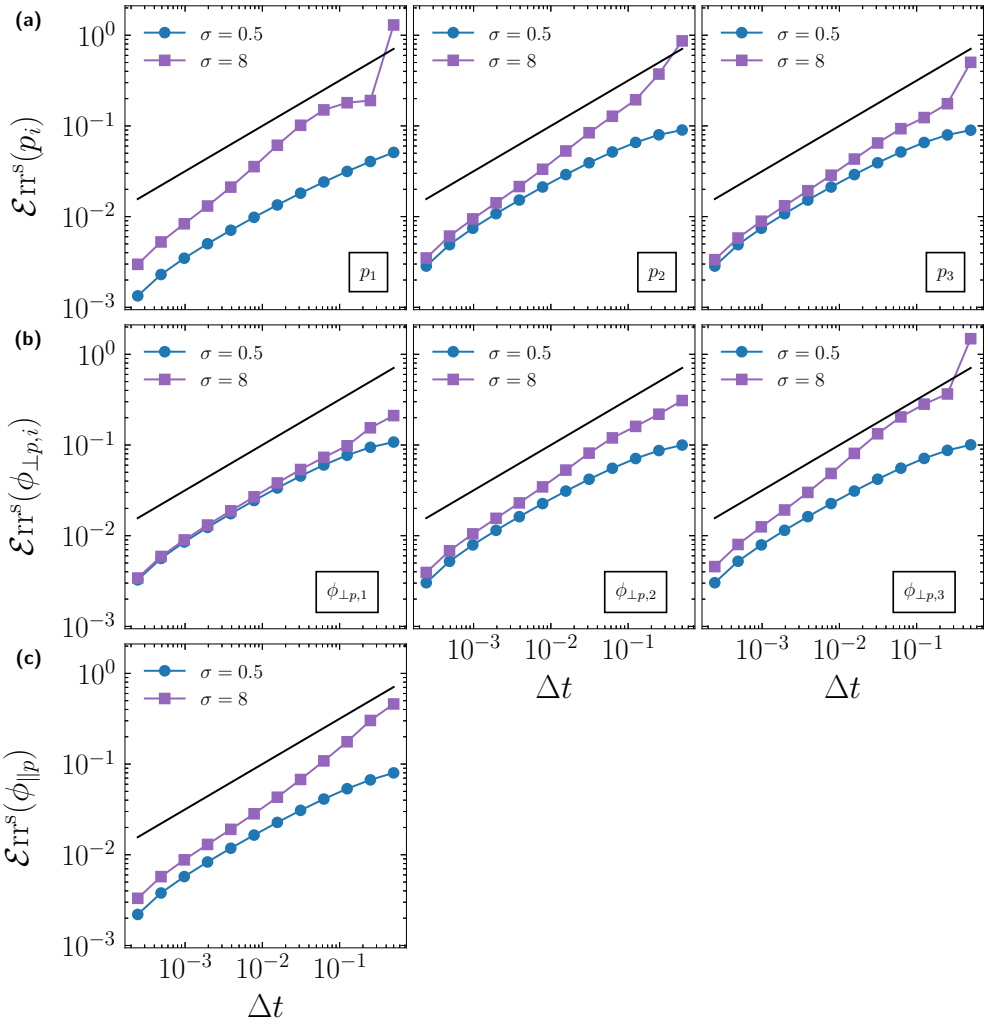

Figure B.7: Splitting scheme in HSF: Strong error ($\mathcal{E}\mathrm{rr}^{\mathrm{s}}$) of the splitting algorithm Eq. (4.96) using the numerical scheme in Eq. (4.93) followed by Eq. (4.89) ($\mathbb{BR} - \mathbb{BSNL}$) followed by Eq. (4.89) ($\mathbb{BR} - \mathbb{BSL}$), against the time step Δt for different values of τ_η. In (a) the three components of $\boldsymbol{p}$, (b) the first component $\boldsymbol{\phi}_{\perp p}$ of tumbling and (c) the spinning $\phi_{\parallel p}$. Black line indicates the slope 1/2; and the initial condition of particle orientation is $\boldsymbol{p}_a^0 = (1, 0, 0)$.

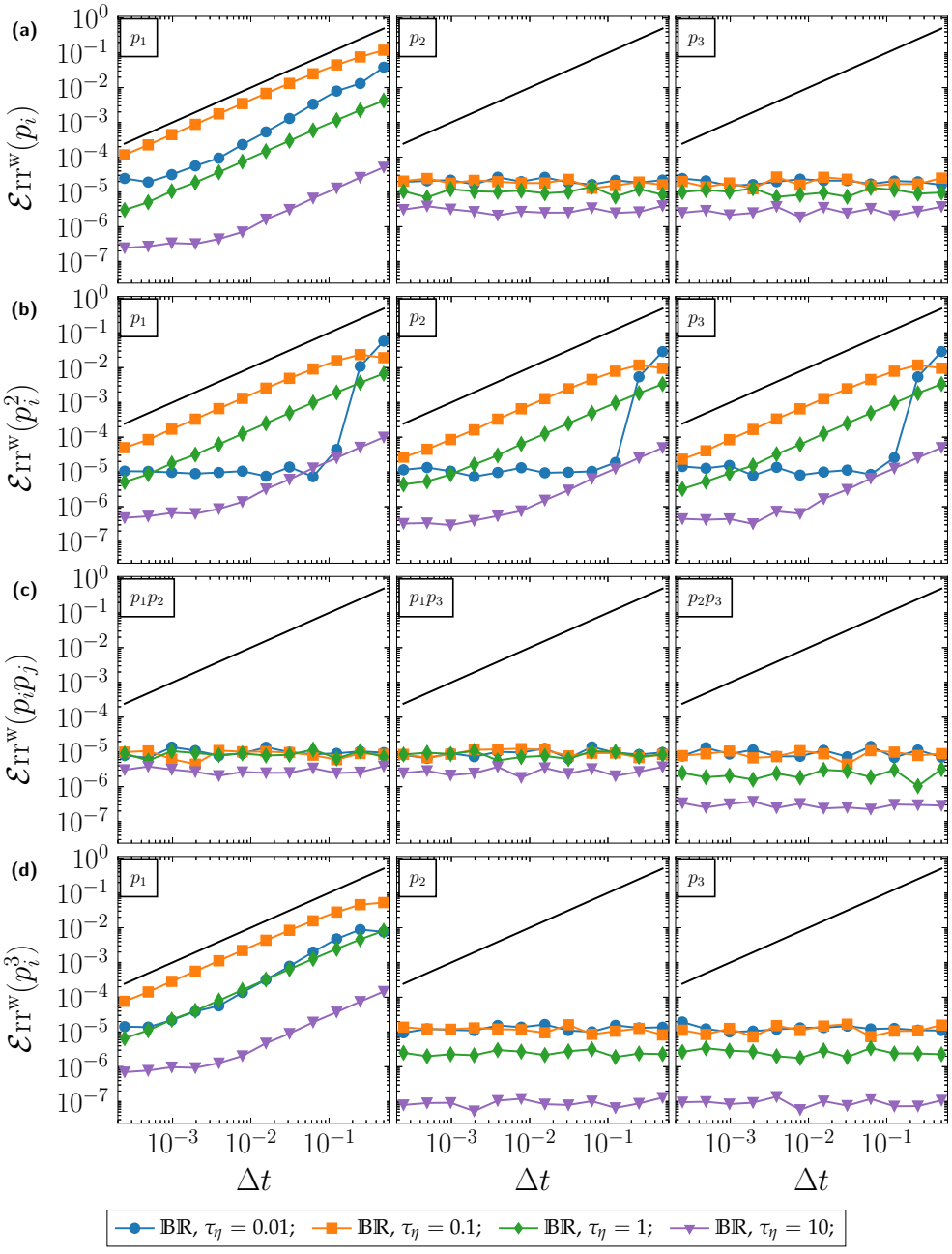

Figure B.8: Stochastic rotation sub-step ($\mathbb{BR}$): Weak error ($\mathcal{E}\mathrm{rr}^{\mathrm{w}}$) of the numerical scheme in Eq. (4.89) ($\mathbb{BR}$) against the time step Δt for different values of τ_η. In (a) the three components of $\mathbb{E}[p_i]$, (b) the three components of $\mathbb{E}[p_i^2]$, (c) the three components of $\mathbb{E}[p_ip_j]$ and (d) the three components of $\mathbb{E}[p_i^3]$ for the initial condition of particle orientation $\boldsymbol{p}_a^0 = (1,0,0)$. Black line indicates the slope 1.

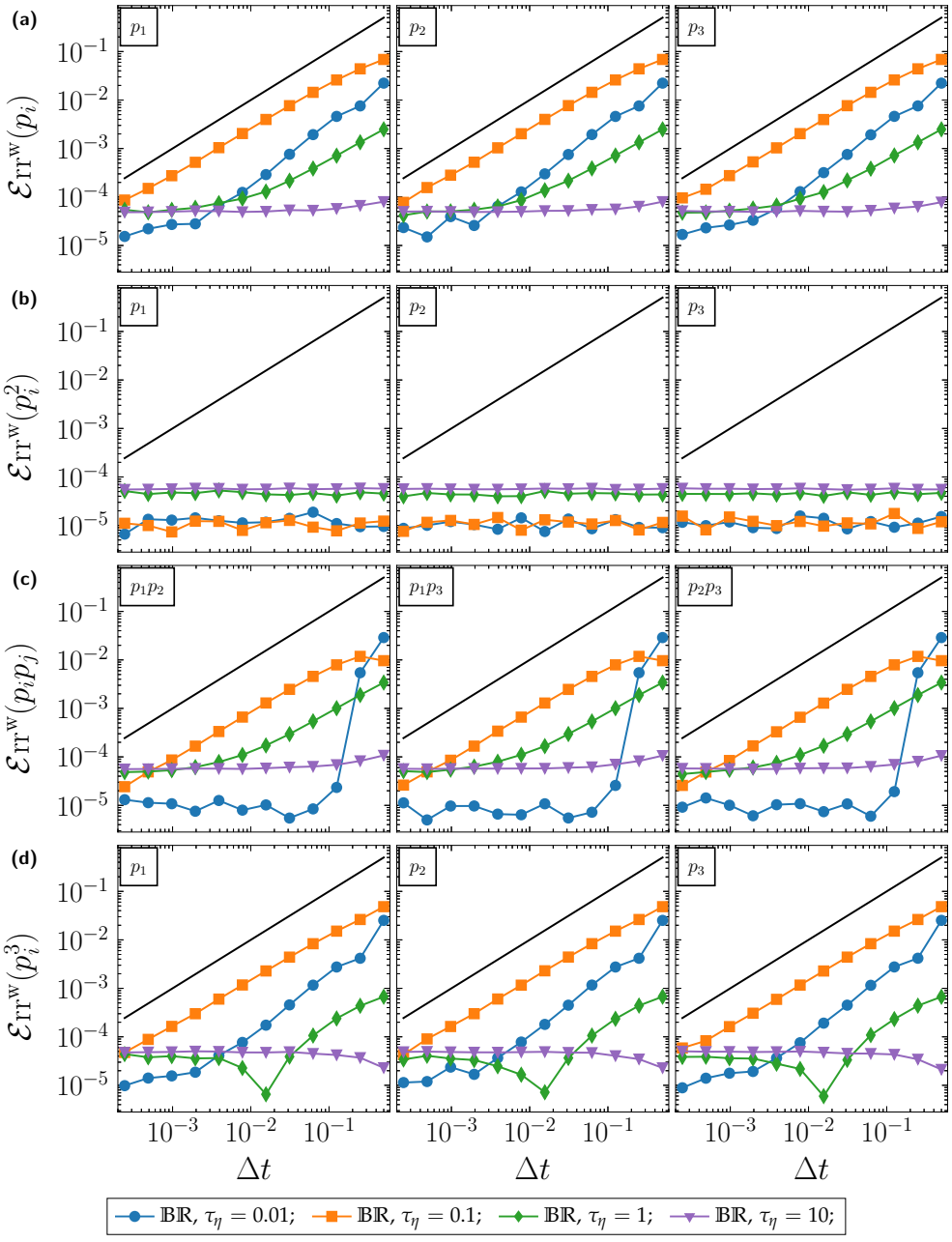

Figure B.9: Stochastic rotation sub-step ($\mathbb{BR}$): Weak error ($\mathcal{E}\mathrm{rr}^{\mathrm{w}}$) of the numerical scheme in Eq. (4.89) ($\mathbb{BR}$) against the time step Δt for different values of τ_η. In (a) the three components of $\mathbb{E}[p_i]$, (b) the three components of $\mathbb{E}[p_i^2]$, (c) the three components of $\mathbb{E}[p_ip_j]$ and (d) the three components of $\mathbb{E}[p_i^3]$ for the initial condition of particle orientation $\boldsymbol{p}_b^0 = (1,1,1)/\sqrt{3}$. Black line indicates the slope 1.

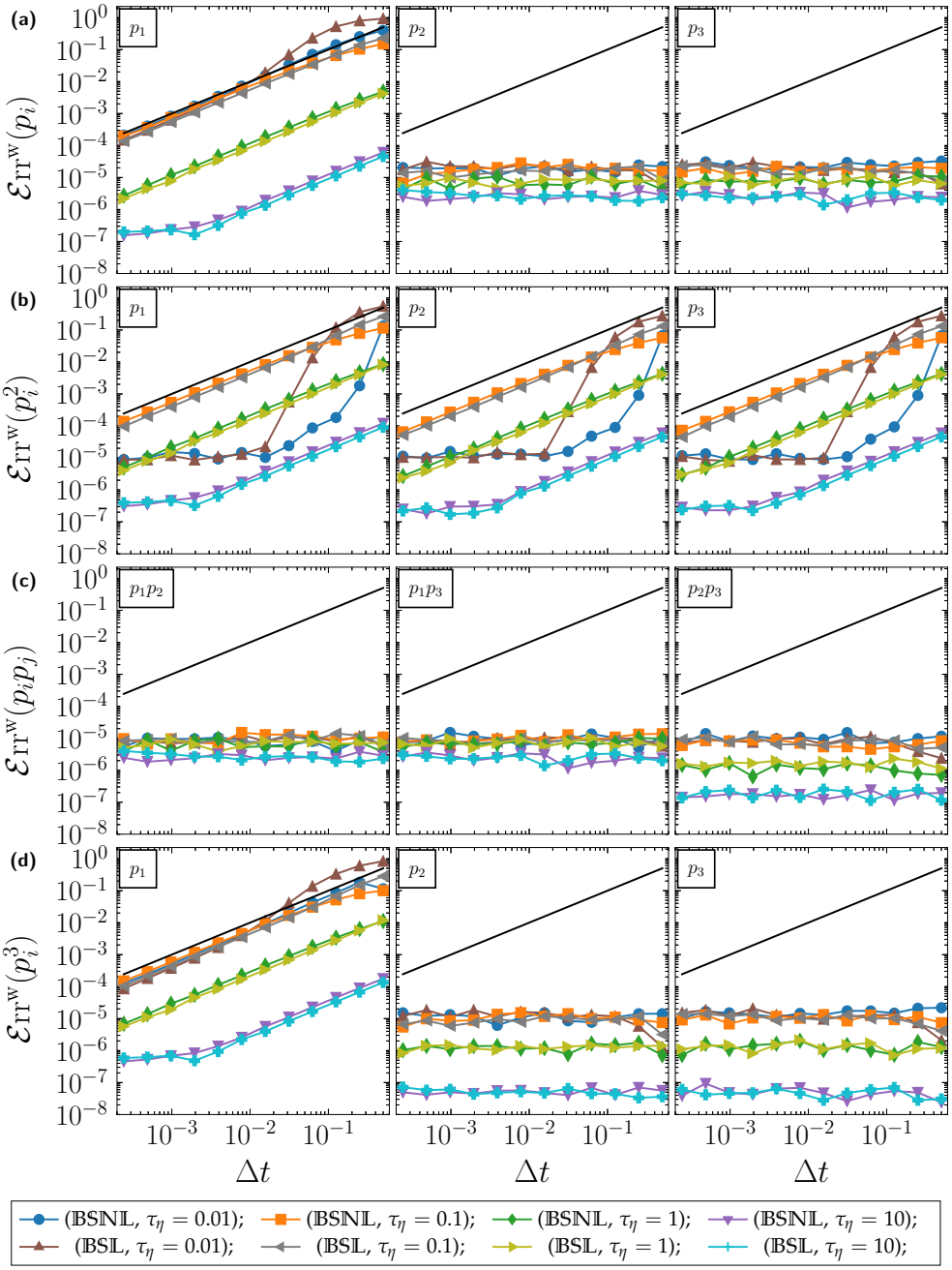

Figure B.10: Stochastic stretching sub-step (𝔹𝕊): Weak error ($\mathcal{E}\mathrm{rr}^{\mathrm{w}}$) of the numerical scheme in Eq. (4.93) (𝔹𝕊ℕ𝕃) and Eq. (4.95) (𝔹𝕊𝕃) against the time step Δt for different values of τ_η. In (a) the three components of $\mathbb{E}[p_i]$, (b) the three components of $\mathbb{E}[p_i^2]$, (c) the three components of $\mathbb{E}[p_ip_j]$ and (d) the three components of $\mathbb{E}[p_i^3]$ for the initial condition of particle orientation $\boldsymbol{p}_a^0 = (1, 0, 0)$. Black line indicates the slope 1.

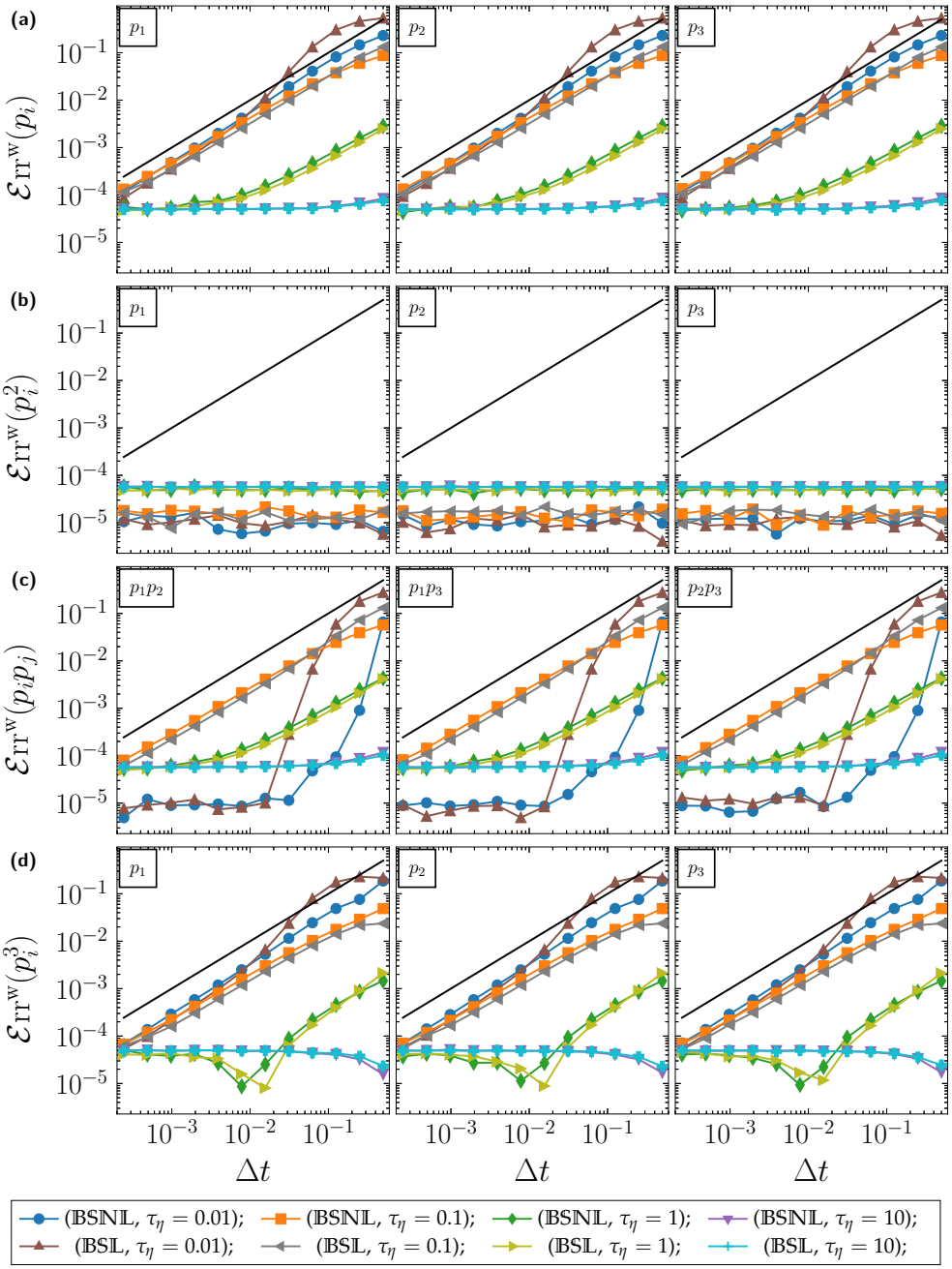

Figure B.11: Stochastic stretching sub-step (𝔹S): Weak error ($\mathcal{E}\mathrm{rr}^{\mathrm{w}}$) of the numerical scheme in Eq. (4.93) (𝔹S𝕀N𝕃) and Eq. (4.95) (𝔹S𝕀𝕃) against the time step Δt for different values of τ_η. In (a) the three components of $\mathbb{E}[p_i]$, (b) the three components of $\mathbb{E}[p_i^2]$, (c) the three components of $\mathbb{E}[p_ip_j]$ and (d) the three components of $\mathbb{E}[p_i^3]$ for the initial condition of particle orientation $\boldsymbol{p}_b^0 = (1,1,1)/\sqrt{3}$. Black line indicates the slope 1.

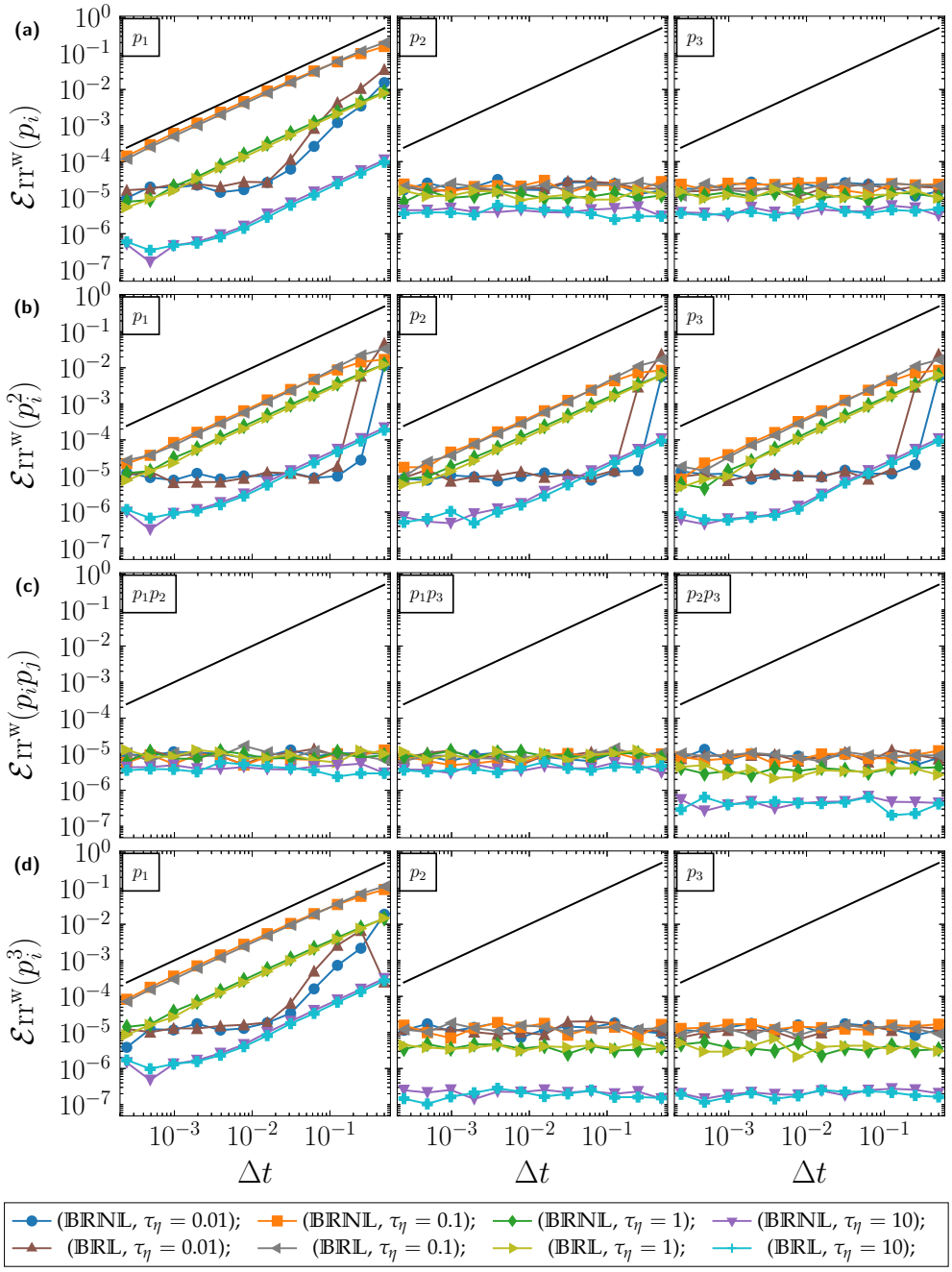

Figure B.12: Splitting scheme in HIT: Weak error ($\mathcal{E}\mathrm{rr}^{\mathrm{w}}$) of the splitting algorithm Eq. (4.96) using the numerical scheme in Eq. (4.93) followed by Eq. (4.89) ($\mathbb{BR} - \mathbb{BSNL}$) and Eq. (4.95) followed by Eq. (4.89) ($\mathbb{BR} - \mathbb{BSL}$), against the time step Δt for different values of τ_η. In (a) the three components of $\mathbb{E}[p_i]$, (b) the three components of $\mathbb{E}[p_i^2]$, (c) the three components of $\mathbb{E}[p_i p_j]$ and (d) the three components of $\mathbb{E}[p_i^3]$ for the initial condition of particle orientation $\boldsymbol{p}_a^0 = (1, 0, 0)$. Black line indicates the slope 1.

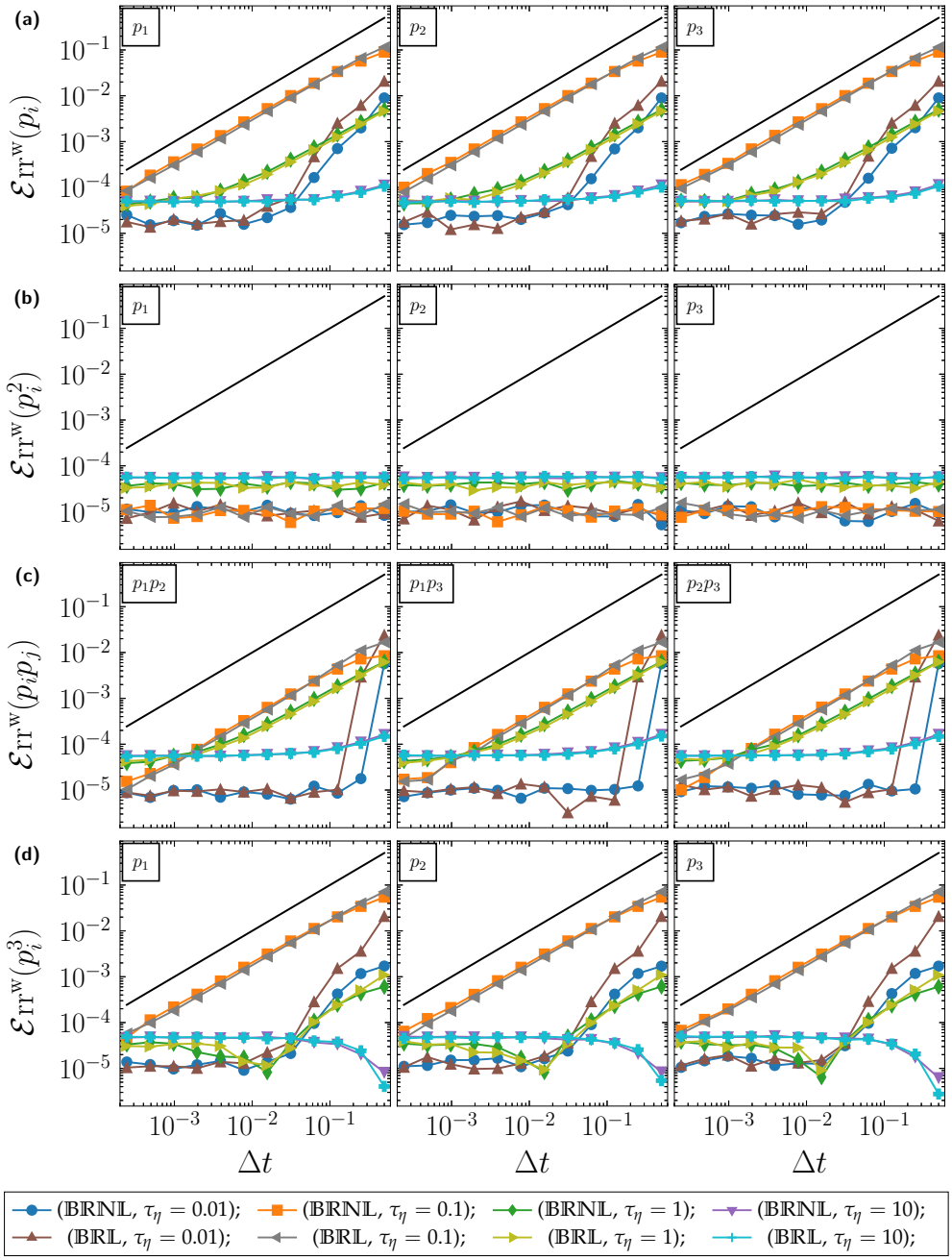

Figure B.13: Splitting scheme in HIT: Weak error ($\mathcal{E}\mathrm{rr}^{\mathrm{w}}$) of the splitting algorithm Eq. (4.96) using the numerical scheme in Eq. (4.93) followed by Eq. (4.89) ($\mathbb{BR} - \mathbb{BSNL}$) and Eq. (4.95) followed by Eq. (4.89) ($\mathbb{BR} - \mathbb{BSL}$), against the time step Δt for different values of τ_η. In (a) the three components of $\mathbb{E}[p_i]$, (b) the three components of $\mathbb{E}[p_i^2]$, (c) the three components of $\mathbb{E}[p_ip_j]$ and (d) the three components of $\mathbb{E}[p_i^3]$ for the initial condition of particle orientation $\boldsymbol{p}_b^0 = (1,1,1)/\sqrt{3}$. Black line indicates the slope 1.

BIBLIOGRAPHY

C

REFERENCES

A. Abdulle, E. Weinan, B. Engquist, and E. Vanden-Eijnden. The heterogeneous multiscale method. *Acta Numerica*, 21:1–87, 2012.

R. J. Adrian. Hairpin vortex organization in wall turbulence. *Physics of Fluids*, 19(4):041301, 2007.

A. Alexakis. Two-dimensional behavior of three-dimensional magnetohydrodynamic flow with a strong guiding field. *Physical Review E*, 84(5):056330, 2011.

H. I. Andersson, L. Zhao, and E. A. Variano. On the anisotropic vorticity in turbulent channel flows. *Journal of Fluids Engineering*, 137(8), 2015.

M. S. Andrle and J. L. Crassidis. Geometric integration of quaternions. *Journal of Guidance, Control, and Dynamics*, 36(6):1762–1767, 2013.

M. Antoine, A. Comtet, J. Desbois, and S. Ouvry. Magnetic fields and brownian motion on the 2-sphere. *Journal of Physics A: Mathematical and General*, 24(11):2581, 1991.

J. Armstrong, D. Brigo, and E. R. Ferrucci. Projections of sdes onto submanifolds. *arXiv preprint arXiv:1810.03923*, 2018.

B. Asgharian and S. Anijilvel. Movement and deposition of fibers in an airway with steady viscous flow. *Aerosol science and technology*, 22(3):261–270, 1995.

N. T. Baker, A. Pothérat, L. Davoust, F. Debray, and R. Klein. Controlling the dimensionality of low-rm mhd turbulence experimentally. *Experiments in Fluids*, 58(7):1–14, 2017.

S. Balachandar and J. K. Eaton. Turbulent dispersed multiphase flow. *Annual review of fluid mechanics*, 42:111–133, 2010.

E. Balkovsky and A. Fouxon. Universal long-time properties of lagrangian statistics in the batchelor regime and their application to the passive scalar problem. *Physical Review E*, 60(4): 4164, 1999.

G.-K. Batchelor. *The theory of homogeneous turbulence*. Cambridge university press, 1953.

G. K. Batchelor. Small-scale variation of convected quantities like temperature in turbulent fluid part 1. general discussion and the case of small conductivity. *Journal of Fluid Mechanics*, 5(1):113–133, 1959.

J. Bec, L. Biferale, G. Boffetta, M. Cencini, S. Musacchio, and F. Toschi. Lyapunov exponents of heavy particles in turbulence. *Physics of Fluids*, 18(9):091702, 2006.

S. J. Benavides and A. Alexakis. Critical transitions in thin layer turbulence. *arXiv preprint arXiv:1701.05162*, 2017.

O. Bernstein and M. Shapiro. Direct determination of the orientation distribution function of cylindrical particles immersed in laminar and turbulent shear flows. *J. Aerosol Sci.*, 25(1): 113–136, 1994.

V. Bezuglyy, B. Mehlig, and M. Wilkinson. Poincaré indices of rheoscopic visualisations. *EPL (Europhysics Letters)*, 89(3):34003, 2010.

L. Biferale, L. Chevillard, C. Meneveau, and F. Toschi. Multiscale model of gradient evolution in turbulent flows. *Physical review letters*, 98(21):214501, 2007.

L. Biferale, C. Meneveau, and R. Verzicco. Deformation statistics of sub-kolmogorov-scale ellipsoidal neutrally buoyant drops in isotropic turbulence. *Journal of fluid mechanics*, 754: 184–207, 2014.

S. Blanes, F. Casas, and A. Murua. Splitting and composition methods in the numerical integration of differential equations. *arXiv preprint arXiv:0812.0377*, 2008.

S. Blanes, F. Casas, J.-A. Oteo, and J. Ros. The magnus expansion and some of its applications. *Physics reports*, 470(5-6):151–238, 2009.

G. Boffetta and R. E. Ecke. Two-dimensional turbulence. *Annu. Rev. Fluid Mech.*, 44:427–451, 2012.

M. Bossy, J.-F. Jabir, and K. Martínez. On the weak convergence rate of an exponential Euler scheme for SDEs governed by coefficients with superlinear growth. *Bernoulli*, 27(1):312 – 347, 2021. doi: 10.3150/20-BEJ1241.

C. L. Bottasso and M. Borri. Integrating finite rotations. *Computer Methods in Applied Mechanics and Engineering*, 164(3):307–331, 1998. ISSN 0045-7825. doi: https://doi.org/10.1016/S0045-7825(98)00031-0.

H. Brenner. The stokes resistance of an arbitrary particle. *Chemical Engineering Science*, 18(1): 1–25, 1963.

H. Brenner. The stokes resistance of an arbitrary particle—ii: an extension. *Chemical Engineering Science*, 19(9):599–629, 1964a.

H. Brenner. The stokes resistance of an arbitrary particle—iv arbitrary fields of flow. *Chemical Engineering Science*, 19(10):703–727, 1964b.

F. P. Bretherton. The motion of rigid particles in a shear flow at low reynolds number. *Journal of Fluid Mechanics*, 14(2):284–304, 1962.

D. R. Brillinger. *A Particle Migrating Randomly on a Sphere*, pages 73–87. Springer New York, New York, NY, 2012. ISBN 978-1-4614-1344-8. doi: 10.1007/978-1-4614-1344-8_7.

R. D. Brown, Z. Warhaft, and G. A. Voth. Acceleration statistics of neutrally buoyant spherical particles in intense turbulence. *Physical review letters*, 103(19):194501, 2009.

B. K. Brunk, D. L. Koch, and L. W. Lion. Observations of coagulation in isotropic turbulence. *Journal of fluid mechanics*, 371:81–107, 1998.

C. Budd and M. Piggott. Geometric integration and its applications. In *Handbook of numerical analysis, Vol.\XI*, pages 35–139. North-Holland Publishing Co., 2003.

K. Burrage and P. Burrage. High strong order methods for non-commutative stochastic ordinary differential equation systems and the magnus formula. *Physica D: Nonlinear Phenomena*, 133 (1-4):34–48, 1999.

K. Burrage and T. Tian. The composite euler method for stiff stochastic differential equations. *Journal of computational and applied mathematics*, 131(1-2):407–426, 2001.

K. Burrage and T. Tian. Predictor-corrector methods of runge–kutta type for stochastic differential equations. *SIAM Journal on Numerical Analysis*, 40(4):1516–1537, 2002.

J. E. Butler and B. Snook. Microstructural dynamics and rheology of suspensions of rigid fibers. *Annu. Rev. Fluid Mech.*, 50:299–318, 2018. doi: 10.1146/annurev-fluid-122316-045144.

D. Byrne and J. A. Zhang. Height-dependent transition from 3-d to 2-d turbulence in the hurricane boundary layer. *Geophysical research letters*, 40(7):1439–1442, 2013.

M. Byron, J. Einarsson, K. Gustavsson, G. Voth, B. Mehlig, and E. Variano. Shape-dependence of particle rotation in isotropic turbulence. *Phys. Fluids*, 27(3):035101, 2015.

W. Cai, H. Li, and Y. Wang. Partitioned averaged vector field methods. *Journal of Computational Physics*, 370:25–42, 2018.

E. Calzavarini, A. Donini, V. Lavezzo, C. Marchioli, E. Pitton, A. Soldati, and F. Toschi. On the error estimate in sub-grid models for particles in turbulent flows. In *Direct and Large-Eddy Simulation VIII*, pages 171–176. Springer, 2011.

E. Calzavarini, L. Jiang, and C. Sun. Anisotropic particles in two-dimensional convective turbulence. *Physics of Fluids*, 32(2):023305, 2020.

L. Campana, S. Allende, J. Bec, M. Bossy, M. Ferran, C. Henry, and J.-P. Minier. Dynamics of inertialess spheroids in a channel flow: orientation, tumbling and spinning statistics. (in preparation).

B. J. Cantwell. Exact solution of a restricted euler equation for the velocity gradient tensor. *Physics of Fluids A: Fluid Dynamics*, 4(4):782–793, 1992.

F. Carbonell, J. Jimenez, and R. Biscay. A class of orthogonal integrators for stochastic differential equations. *Journal of computational and applied mathematics*, 182(2):350–361, 2005.

A. Carlsson, L. D. Söderberg, and F. Lundell. Fibre orientation measurements near a headbox wall. *Nordic Pulp & Paper Research Journal*, 25(2):204–212, 2010a.

T. Carlsson, T. Ekholm, and C. Elvingson. Algorithm for generating a brownian motion on a sphere. *Journal of physics A: Mathematical and theoretical*, 43(50):505001, 2010b.

F. Castell. Asymptotic expansion of stochastic flows. *Probability theory and related fields*, 96(2): 225–239, 1993.

A. Celani, A. Puliafito, and K. Turitsyn. Polymers in linear shear flow: a numerical study. *EPL (Europhysics Letters)*, 70(4):464, 2005.

E. Celledoni and B. Owren. Lie group methods for rigid body dynamics and time integration on manifolds. *Computer Methods in Applied Mechanics and Engineering*, 192(3-4):421–438, 2003.

N. R. Challabotla, L. Zhao, and H. I. Andersson. Orientation and rotation of inertial disk particles in wall turbulence. *Journal of Fluid Mechanics*, 766, 2015a.

N. R. Challabotla, L. Zhao, and H. I. Andersson. Shape effects on dynamics of inertia-free spheroids in wall turbulence. *Physics of Fluids*, 27(6):061703, 2015b.

J. G. Charney. Geostrophic turbulence. *Journal of the Atmospheric Sciences*, 28(6):1087–1095, 1971.

J. Chen, G. Jin, and J. Zhang. Large eddy simulation of orientation and rotation of ellipsoidal particles in isotropic turbulent flows. *Journal of Turbulence*, 17(3):308–326, 2016.

M. Chertkov. Polymer stretching by turbulence. *Physical review letters*, 84(20):4761, 2000.

M. Chertkov, A. Pumir, and B. I. Shraiman. Lagrangian tetrad dynamics and the phenomenology of turbulence. *Physics of fluids*, 11(8):2394–2410, 1999.

M. Chertkov, I. Kolokolov, V. Lebedev, and K. Turitsyn. Polymer statistics in a random flow with mean shear. *Journal of Fluid Mechanics*, 531:251–260, 2005.

L. Chevillard and C. Meneveau. Lagrangian dynamics and statistical geometric structure of turbulence. *Physical review letters*, 97(17):174501, 2006.

L. Chevillard and C. Meneveau. Orientation dynamics of small, triaxial–ellipsoidal particles in isotropic turbulence. *Journal of Fluid Mechanics*, 737:571–596, 2013.

L. Chevillard, C. Meneveau, L. Biferale, and F. Toschi. Modeling the pressure hessian and viscous laplacian in turbulence: comparisons with direct numerical simulation and implications on velocity gradient dynamics. *Physics of Fluids*, 20(10):101504, 2008.

S. Chibbaro and J.-P. Minier. Langevin pdf simulation of particle deposition in a turbulent pipe flow. *Journal of aerosol science*, 39(7):555–571, 2008.

S. Chibbaro and J.-P. Minier. A note on the consistency of hybrid eulerian/lagrangian approach to multiphase flows. *International Journal of Multiphase Flow*, 37(3):293–297, 2011.

S. A. Chin and J. Geiser. Multi-product operator splitting as a general method of solving autonomous and nonautonomous equations. *IMA Journal of Numerical Analysis*, 31(4):1552–1577, 2011.

J.-I. Choi, K. Yeo, and C. Lee. Lagrangian statistics in turbulent channel flow. *Physics of Fluids*, 16(3):779–793, 2004.

P. E. Crouch and R. Grossman. Numerical integration of ordinary differential equations on manifolds. *Journal of Nonlinear Science*, 3(1):1–33, 1993.

M. Daghooghi and I. Borazjani. The influence of inertia on the rheology of a periodic suspension of neutrally buoyant rigid ellipsoids. *Journal of Fluid Mechanics*, 781:506–549, 2015.

S. Delong, F. Balboa Usabiaga, and A. Donev. Brownian dynamics of confined rigid bodies. *The Journal of chemical physics*, 143(14):144107, 2015.

E. Deusebio, G. Boffetta, E. Lindborg, and S. Musacchio. Dimensional transition in rotating turbulence. *Physical Review E*, 90(2):023005, 2014.

P. Devinant, T. Laverne, and J. Hureau. Experimental study of wind-turbine airfoil aerodynamics in high turbulence. *Journal of Wind Engineering and Industrial Aerodynamics*, 90(6):689–707, 2002.

P. H. Diamond, S. Itoh, K. Itoh, and T. Hahm. Zonal flows in plasma—a review. *Plasma Physics and Controlled Fusion*, 47(5):R35, 2005.

J. Diebel. Representing attitude: Euler angles, unit quaternions, and rotation vectors. *Matrix*, 58(15-16):1–35, 2006.

X. Ding, Q. Ma, and L. Zhang. Convergence and stability of the split-step θ-method for stochastic differential equations. *Computers & Mathematics with Applications*, 60(5):1310–1321, 2010.

M. Dong, S. Li, J. Xie, and J. Han. Experimental studies on the normal impact of fly ash particles with planar surfaces. *Energies*, 6:3245–3262, 07 2013. doi: 10.3390/en6073245.

E. Dresselhaus and M. Tabor. The kinematics of stretching and alignment of material elements in general flow fields. *Journal of Fluid Mechanics*, 236:415–444, 1992.

D. G. Dritschel and B. Legras. Modeling oceanic and atmospheric vortices. *Physics Today*, 46(3): 44–51, 1993.

A. Dullweber, B. Leimkuhler, R. Mclachlan, E. C. Ew, A. Dullweber, B. Leimkuhler, and R. Mclachlan. Split-hamiltonian methods for rigid body molecular dynamics. *J. Chem. Phys*, 107:5840–5852, 1997.

F. J. Dyson. The radiation theories of tomonaga, schwinger, and feynman. *Physical Review*, 75 (3):486, 1949.

J. K. Eaton. Two-way coupled turbulence simulations of gas-particle flows using point-particle tracking. *International Journal of Multiphase Flow*, 35(9):792–800, 2009.

J. Einarsson, A. Johansson, S. Mahato, Y. Mishra, J. Angilella, D. Hanstorp, and B. Mehlig. Periodic and aperiodic tumbling of microrods advected in a microchannel flow. *Acta Mechanica*, 224(10):2281–2289, 2013.

G. L. Eyink. Exact results on stationary turbulence in 2d: consequences of vorticity conservation. *Physica D: Nonlinear Phenomena*, 91(1-2):97–142, 1996.

G. Falkovich. Symmetries of the turbulent state. *Journal of Physics A: Mathematical and Theoretical*, 42(12):123001, 2009.

G. Falkovich and V. Lebedev. Vorticity statistics in the direct cascade of two-dimensional turbulence. *Phys. Rev. E*, 83(4):045301, 2011.

G. Falkovich, K. Gawedzki, and M. Vergassola. Particles and fields in fluid turbulence. *Reviews of modern Physics*, 73(4):913, 2001.

S. Faltinsen, A. Marthinsen, and H. Z. Munthe-Kaas. Multistep methods integrating ordinary differential equations on manifolds. *Applied numerical mathematics*, 39(3-4):349–365, 2001.

F.-G. Fan and G. Ahmadi. A sublayer model for wall deposition of ellipsoidal particles in turbulent streams. *Journal of Aerosol Science*, 26(5):813–840, 1995.

J. Faraudo. Diffusion equation on curved surfaces. i. theory and application to biological membranes. *The Journal of chemical physics*, 116(13):5831–5841, 2002.

B. Favier, F. S. Godeferd, C. Cambon, and A. Delache. On the two-dimensionalization of quasistatic magnetohydrodynamic turbulence. *Physics of Fluids*, 22(7):075104, 2010.

R. O. Fox. Large-eddy-simulation tools for multiphase flows. *Annual Review of Fluid Mechanics*, 44(1):47–76, 2012. doi: 10.1146/annurev-fluid-120710-101118.

A. Friedman. Stochastic differential equations and applications. In *Stochastic differential equations*, pages 75–148. Springer, 2010.

U. Frisch. *Turbulence: The Legacy of A. N. Kolmogorov*. Cambridge University Press, 1995. doi: 10.1017/CBO9781139170666.

U. Frisch, S. Kurien, R. Pandit, W. Pauls, S. S. Ray, A. Wirth, and J.-Z. Zhu. Hyperviscosity, galerkin truncation, and bottlenecks in turbulence. *Phys. Rev. Lett.*, 101(14):144501, 2008.

E. García-Portugués, M. Sørensen, K. V. Mardia, and T. Hamelryck. Langevin diffusions on the torus: estimation and applications. *Statistics and Computing*, 29(1):1–22, 2019.

S. Girimaji and S. Pope. A diffusion model for velocity gradients in turbulence. *Physics of Fluids A: Fluid Dynamics*, 2(2):242–256, 1990.

F. Godeferd and L. Lollini. Direct numerical simulations of turbulence with confinement and rotation. *Journal of Fluid Mechanics*, 393:257–308, 1999.

H. Gould, J. Tobochnik, D. C. Meredith, S. E. Koonin, S. R. McKay, and W. Christian. An introduction to computer simulation methods: applications to physical systems. *Computers in Physics*, 10(4):349–349, 1996.

A. Greiner, W. Strittmatter, and J. Honerkamp. Numerical integration of stochastic differential equations. *Journal of Statistical Physics*, 51(1):95–108, 1988.

O. Gressel and M. E. Pessah. Characterizing the mean-field dynamo in turbulent accretion disks. *The Astrophysical Journal*, 810(1):59, 2015.

M. Guala, B. Lüthi, A. Liberzon, A. Tsinober, and W. Kinzelbach. On the evolution of material lines and vorticity in homogeneous turbulence. *Journal of Fluid Mechanics*, 533:339–359, 2005.

J. S. Guasto, R. Rusconi, and R. Stocker. Fluid mechanics of planktonic microorganisms. *Annual Review of Fluid Mechanics*, 44:373–400, 2012.

K. Gustavsson, J. Einarsson, and B. Mehlig. Tumbling of small axisymmetric particles in random and turbulent flows. *Physical review letters*, 112(1):014501, 2014.

E. Hairer, M. Hochbruck, A. Iserles, and C. Lubich. Geometric numerical integration. *Oberwolfach Reports*, 3(1):805–882, 2006.

M. Hairer. Ergodicity of stochastic differential equations driven by fractional brownian motion. *The Annals of Probability*, 33(2):703–758, 2005.

G. Haller. Lagrangian coherent structures. *Annual Review of Fluid Mechanics*, 47(1):137–162, 2015. doi: 10.1146/annurev-fluid-010313-141322.

W. R. Hamilton. Lxxviii. on quaternions; or on a new system of imaginaries in algebra: To the editors of the philosophical magazine and journal. *The London, Edinburgh, and Dublin Philosophical Magazine and Journal of Science*, 25(169):489–495, 1844.

J. Happel and H. Brenner. *Low Reynolds number hydrodynamics with special applications to particulate media; 2nd ed.* Monographs and textbooks on mechanics of solids and fluids. Noordhoff, Liége, 1973.

J. Harris and J. Pittman. Equivalent ellipsoidal axis ratios of slender rod-like particles. *Journal of Colloid and Interface Science*, 50(2):280–282, 1975.

N. E. L. Haugen and A. Brandenburg. Inertial range scaling in numerical turbulence with hyperviscosity. *Phys. Rev. E*, 70(2):026405, 2004.

B. Hejazi, B. Mehlig, and G. A. Voth. Emergent scar lines in chaotic advection of passive directors. *Physical Review Fluids*, 2(12):124501, 2017.

C. Henry, J.-P. Minier, and G. Lefèvre. Towards a description of particulate fouling: From single particle deposition to clogging. *Advances in colloid and interface science*, 185:34–76, 2012.

A. J. Heymsfield. Precipitation development in stratiform ice clouds: A microphysical and dynamical study. *J. Atmos. Sci.*, 34(2):367–381, 1977. doi: 10.1175/1520-0469(1977)034<0367:PDISIC>2.0.CO;2.

D. J. Higham, X. Mao, and A. M. Stuart. Strong convergence of euler-type methods for nonlinear stochastic differential equations. *SIAM Journal on Numerical Analysis*, 40(3):1041–1063, 2002.

M. Hinsberg, van, J. Thije Boonkkamp, ten, F. Toschi, and H. Clercx. Optimal interpolation schemes for particle tracking in turbulence. *Physical Review E*, 87(4):043307, 2013.

W. Hundsdorfer and J. G. Verwer. *Numerical solution of time-dependent advection-diffusion-reaction equations*, volume 33. Springer Science & Business Media, 2013.

M. Hutzenthaler, A. Jentzen, and P. E. Kloeden. Strong and weak divergence in finite time of euler's method for stochastic differential equations with non-globally lipschitz continuous coefficients. *Proceedings of the Royal Society A: Mathematical, Physical and Engineering Sciences*, 467(2130):1563–1576, 2011. doi: 10.1098/rspa.2010.0348.

A. Il'Yn and K. Zybin. Material deformation tensor in time-reversal symmetry breaking turbulence. *Physics Letters A*, 379(7):650–653, 2015.

M. Izakov. Large-scale quasi-two-dimensional turbulence and a inverse spectral flux of energy in the atmosphere of venus. *Solar System Research*, 47(3):170–181, 2013.

L. Jarecki, S. Blonski, A. Blim, and A. Zachara. Modeling of pneumatic melt spinning processes. *Journal of applied polymer science*, 125(6):4402–4415, 2012.

G. B. Jeffery. The motion of ellipsoidal particles immersed in a viscous fluid. *Proc. Royal Soc. Lond. A*, 102(715):161–179, 1922.

E. Jeong and S. S. Girimaji. Velocity-gradient dynamics in turbulence: effect of viscosity and forcing. *Theoretical and computational fluid dynamics*, 16(6):421–432, 2003.

Y. Jie, L. Zhao, C. Xu, and H. I. Andersson. Preferential orientation of tracer spheroids in turbulent channel flow. *Theoretical and Applied Mechanics Letters*, 9(3):212–214, 2019.

P. L. Johnson and C. Meneveau. A closure for lagrangian velocity gradient evolution in turbulence using recent-deformation mapping of initially gaussian fields. *Journal of Fluid Mechanics*, 804:387–419, 2016.

P. L. Johnson and C. Meneveau. Predicting viscous-range velocity gradient dynamics in large-eddy simulations of turbulence. *Journal of Fluid Mechanics*, 837:80–114, 2018.

W. P. Jones. Turbulence modelling and numerical solution methods for variable density and combusting flows. *Turbulent reacting flows*, (309-347), 1994.

J. Jucha, H. Xu, A. Pumir, and E. Bodenschatz. Time-reversal-symmetry breaking in turbulence. *Physical review letters*, 113(5):054501, 2014.

P. A. Jumars, J. H. Trowbridge, E. Boss, and L. Karp-Boss. Turbulence-plankton interactions: a new cartoon. *Marine Ecology*, 30(2):133–150, 2009.

M. Junk and R. Illner. A new derivation of jeffery's equation. *Journal of Mathematical Fluid Mechanics*, 9(4):455–488, 2007.

K. Kamm, S. Pagliarani, and A. Pascucci. On the stochastic magnus expansion and its application to spdes. *arXiv preprint arXiv:2001.01098*, 2020.

I. Karatzas and S. E. Shreve. *Brownian Motion and Stochastic Calculus*. Springer New York, New York, NY, 1998. ISBN 978-1-4612-0949-2. doi: 10.1007/978-1-4612-0949-2_1.

A. Karnis, H. Goldsmith, and S. Mason. Axial migration of particles in poiseuille flow. *Nature*, 200(4902):159–160, 1963.

A. Karnis, H. Goldsmith, and S. Mason. The kinetics of flowing dispersions: I. concentrated suspensions of rigid particles. *Journal of Colloid and Interface Science*, 22(6):531–553, 1966.

R. Khasminskii. *Stochastic stability of differential equations*, volume 66. Springer Science & Business Media, 2011.

G. P. King, J. Vogelzang, and A. Stoffelen. Upscale and downscale energy transfer over the tropical p acific revealed by scatterometer winds. *Journal of Geophysical Research: Oceans*, 120 (1):346–361, 2015.

J. R. Klauder and W. P. Petersen. Numerical integration of multiplicative-noise stochastic differential equations. *SIAM journal on numerical analysis*, 22(6):1153–1166, 1985.

M. Kleppmann. Simulation of colliding constrained rigid bodies. Technical Report UCAM-CL-TR-683, University of Cambridge, Computer Laboratory, apr 2007.

P. E. Kloeden and E. Platen. Higher-order implicit strong numerical schemes for stochastic differential equations. *Journal of statistical physics*, 66(1-2):283–314, 1992.

A. N. Kolmogorov. A refinement of previous hypotheses concerning the local structure of turbulence in a viscous incompressible fluid at high reynolds number. *Journal of Fluid Mechanics*, 13(1):82–85, 1962.

A. V. Korolev, G. A. Isaac, S. G. Cober, J. W. Strapp, and J. Hallett. Microphysical characterization of mixed-phase clouds. *Quarterly Journal of the Royal Meteorological Society: A journal of the atmospheric sciences, applied meteorology and physical oceanography*, 129(587):39–65, 2003.

R. Kraichnan. Rh kraichnan, phys. fluids 11, 945 (1968). *Phys. Fluids*, 11:945, 1968.

R. H. Kraichnan. Inertial ranges in two-dimensional turbulence. *The Physics of Fluids*, 10(7): 1417–1423, 1967.

R. H. Kraichnan and D. Montgomery. Two-dimensional turbulence. *Reports on Progress in Physics*, 43(5):547, 1980.

M. Krishna, J. Samuel, and S. Sinha. Brownian motion on a sphere: distribution of solid angles. *Journal of Physics A: Mathematical and General*, 33(34):5965, 2000.

E. Krushkal and I. Gallily. On the orientation distribution function of nonspherical aerosol particles in a general shear flow—ii. the turbulent case. *Journal of Aerosol Science*, 19(2): 197–211, 1988.

J. G. Kuerten. Point-particle dns and les of particle-laden turbulent flow-a state-of-the-art review. *Flow, turbulence and combustion*, 97(3):689, 2016.

B. E. Launder. Phenomenological modelling: Present.... and future? In *Whither Turbulence? Turbulence at the Crossroads*, pages 439–485. Springer, 1990.

B. E. Launder, G. J. Reece, and W. Rodi. Progress in the development of a reynolds-stress turbulence closure. *Journal of fluid mechanics*, 68(3):537–566, 1975.

M. Lesieur. *Turbulence in fluids: stochastic and numerical modelling*, volume 488. Nijhoff Boston, MA, 1987.

G. Li, L.-K. Tam, and J. X. Tang. Amplified effect of brownian motion in bacterial near-surface swimming. *Proceedings of the National Academy of Sciences*, 105(47):18355–18359, 2008.

H. Li, Z. Mu, and Y. Wang. An energy-preserving crank–nicolson galerkin spectral element method for the two dimensional nonlinear schrödinger equation. *Journal of Computational and Applied Mathematics*, 344:245–258, 2018a.

X. Li, C. Zhang, Q. Ma, and X. Ding. Discrete gradient methods and linear projection methods for preserving a conserved quantity of stochastic differential equations. *International Journal of Computer Mathematics*, 95(12):2511–2524, 2018b.

E. Lindborg and K. Alvelius. The kinetic energy spectrum of the two-dimensional enstrophy turbulence cascade. *Phys. Fluids*, 12(5):945–947, 2000.

H. Lu and Y. Shao. Toward quantitative prediction of dust storms: an integrated wind erosion modelling system and its applications. *Environmental Modelling & Software*, 16(3):233–249, 2001.

F. Lundell, L. D. Söderberg, and P. H. Alfredsson. Fluid mechanics of papermaking. *Annu. Rev. Fluid Mech.*, 43:195–217, 2011. doi: 10.1146/annurev-fluid-122109-160700.

B. Lüthi, A. Tsinober, and W. Kinzelbach. Lagrangian measurement of vorticity dynamics in turbulent flow. *Journal of Fluid mechanics*, 528:87–118, 2005.

N. Machicoane, F. Moisy, and P.-P. Cortet. Two-dimensionalization of the flow driven by a slowly rotating impeller in a rapidly rotating fluid. *Physical Review Fluids*, 1(7):073701, 2016.

V. Mackevičius and J. Navikas. Second order weak runge–kutta type methods for itô equations. *Mathematics and computers in simulation*, 57(1-2):29–34, 2001.

S. J. Malham and A. Wiese. Stochastic lie group integrators. *SIAM Journal on Scientific Computing*, 30(2):597–617, 2008.

R. Maniero, O. Masbernat, E. Climent, and F. Risso. Modeling and simulation of inertial drop break-up in a turbulent pipe flow downstream of a restriction. *International journal of multiphase flow*, 42:1–8, 2012.

X. Mao. *Stochastic differential equations and applications*. Elsevier, 2007.

C. Marchioli. Large-eddy simulation of turbulent dispersed flows: a review of modelling approaches. *Acta Mechanica*, 228(3):741–771, 2017.

C. Marchioli and A. Soldati. Rotation statistics of fibers in wall shear turbulence. *Acta Mechanica*, 224(10):2311–2329, 2013.

C. Marchioli, M. Fantoni, and A. Soldati. Orientation, distribution, and deposition of elongated, inertial fibers in turbulent channel flow. *Physics of fluids*, 22(3):033301, 2010.

G. I. Marchuk. Some application of splitting-up methods to the solution of mathematical physics problems. *Aplikace matematiky*, 13(2):103–132, 1968.

G. G. Marcus, S. Parsa, S. Kramel, R. Ni, and G. A. Voth. Measurements of the solid-body rotation of anisotropic particles in 3d turbulence. *New journal of physics*, 16(10):102001, 2014.

G. Marjanovic, M. J. Piggott, and V. Solo. A simple approach to numerical methods for stochastic differential equations in lie groups. In *2015 54th IEEE Conference on Decision and Control (CDC)*, pages 7143–7150. IEEE, 2015.

N. Markatos. The mathematical modelling of turbulent flows. *Applied Mathematical Modelling*, 10(3):190–220, 1986. ISSN 0307-904X. doi: https://doi.org/10.1016/0307-904X(86)90045-4.

I. Marusic and R. Adrian. The eddies and scales of wall turbulence. In *Ten chapters in turbulence*, pages 176–220. Cambridge University Press, 2010.

J. C. Mattingly, A. M. Stuart, and D. J. Higham. Ergodicity for sdes and approximations: locally lipschitz vector fields and degenerate noise. *Stochastic processes and their applications*, 101(2): 185–232, 2002.

R. I. McLachlan and G. R. W. Quispel. Splitting methods. *Acta Numerica*, 11:341–434, 2002.

R. I. McLachlan, G. R. W. Quispel, and N. Robidoux. Geometric integration using discrete gradients. *Philosophical Transactions of the Royal Society of London. Series A: Mathematical, Physical and Engineering Sciences*, 357(1754):1021–1045, 1999.

C. Meneveau. Lagrangian dynamics and models of the velocity gradient tensor in turbulent flows. *Annual Review of Fluid Mechanics*, 43:219–245, 2011.

A. Mijatović, V. Mramor, and G. U. Bravo. A note on the exact simulation of spherical brownian motion. *arXiv preprint arXiv:1811.12107*, 2018.

G. N. Milstein. *Numerical integration of stochastic differential equations*, volume 313. Springer Science & Business Media, 1994.

G. N. Milstein, E. Platen, and H. Schurz. Balanced implicit methods for stiff stochastic systems. *SIAM Journal on Numerical Analysis*, 35(3):1010–1019, 1998.

J.-P. Minier. Statistical descriptions of polydisperse turbulent two-phase flows. *Physics Reports*, 665:1–122, 2016.

J.-P. Minier and E. Peirano. The pdf approach to turbulent polydispersed two-phase flows. *Physics reports*, 352(1-3):1–214, 2001.

J.-P. Minier, E. Peirano, and S. Chibbaro. Pdf model based on langevin equation for polydispersed two-phase flows applied to a bluff-body gas-solid flow. *Physics of fluids*, 16(7): 2419–2431, 2004.

J.-P. Minier et al. Probabilistic approach to turbulent two-phase flows modelling and simulation: theoretical and numerical issues. *Monte Carlo Methods and Applications*, 7(3/4):295–310, 2001.

M. Moakher. Fourth-order cartesian tensors: old and new facts, notions and applications. *The Quarterly Journal of Mechanics & Applied Mathematics*, 61(2):181–203, 2008.

R. C. Moffet and K. A. Prather. In-situ measurements of the mixing state and optical properties of soot with implications for radiative forcing estimates. *Proceedings of the National Academy of Sciences*, 106(29):11872–11877, 2009.

A. S. Monin and A. M. Yaglom. *Statistical fluid mechanics, volume II: mechanics of turbulence*, volume 2. Courier Corporation, 2013.

P. Mortensen, H. Andersson, J. Gillissen, and B. Boersma. Dynamics of prolate ellipsoidal particles in a turbulent channel flow. *Physics of Fluids*, 20(9):093302, 2008.

H. Munthe-Kaas. Runge-kutta methods on lie groups. *BIT Numerical Mathematics*, 38(1):92–111, 1998.

M. Muradoglu, S. B. Pope, and D. A. Caughey. The hybrid method for the pdf equations of turbulent reactive flows: consistency conditions and correction algorithms. *Journal of Computational Physics*, 172(2):841–878, 2001.

M. M. Musielak, L. Karp-Boss, P. A. Jumars, and L. J. Fauci. Nutrient transport and acquisition by diatom chains in a moving fluid. *J. Fluid. Mech.*, 638:401–421, 2009. doi: 10.1017/S0022112009991108.

M. Nelkin. Universality and scaling in fully developed turbulence. *Advances in physics*, 43(2): 143–181, 1994.

R. Newsom and C. Bruce. Orientational properties of fibrous aerosols in atmospheric turbulence. *Journal of aerosol science*, 29(7):773–797, 1998.

R. Ni, N. T. Ouellette, and G. A. Voth. Alignment of vorticity and rods with lagrangian fluid stretching in turbulence. *Journal of Fluid Mechanics*, 743, 2014.

R. Ni, S. Kramel, N. T. Ouellette, and G. A. Voth. Measurements of the coupling between the tumbling of rods and the velocity gradient tensor in turbulence. *Journal of Fluid Mechanics*, 766:202–225, 2015.

J. Nissfolk, T. Ekholm, and C. Elvingson. Brownian dynamics simulations on a hypersphere in 4-space. *The Journal of chemical physics*, 119(13):6423–6432, 2003.

D. Njobuenwu and M. Fairweather. Dynamics of single, non-spherical ellipsoidal particles in a turbulent channel flow. *Chemical Engineering Science*, 123:265–282, 2015.

D. O. Njobuenwu and M. Fairweather. Simulation of inertial fibre orientation in turbulent flow. *Physics of Fluids*, 28(6):063307, 2016.

A. M. Oboukhov. Some specific features of atmospheric tubulence. *Journal of Fluid Mechanics*, 13(1):77–81, 1962.

B. Øksendal. Stochastic differential equations. In *Stochastic differential equations*, pages 65–84. Springer, 2003.

J. A. Olson and R. J. Kerekes. The motion of fibres in turbulent flow. *Journal of Fluid Mechanics*, 377:47–64, 1998.

N. T. Ouellette, P. O'Malley, and J. P. Gollub. Transport of finite-sized particles in chaotic flow. *Physical review letters*, 101(17):174504, 2008.

G. Pagés. Numerical probability. In *Universitext*. Springer, 2018.

G. Parisi and U. Frisch. On the singularity structure of fully developed turbulence in turbulence and predictability in geophysical fluid dynamics and climate dynamics. *NTurbulence and Predictability of Geophysical Flows and Climate Dynamics*, 88, 01 1985.

S. Parsa, J. S. Guasto, M. Kishore, N. T. Ouellette, J. Gollub, and G. A. Voth. Rotation and alignment of rods in two-dimensional chaotic flow. *Physics of Fluids*, 23(4):043302, 2011.

S. Parsa, E. Calzavarini, F. Toschi, and G. A. Voth. Rotation rate of rods in turbulent fluid flow. *Phys. Rev. Lett.*, 109(13):134501, 2012.

E. Peirano, S. Chibbaro, J. Pozorski, and J.-P. Minier. Mean-field/pdf numerical approach for polydispersed turbulent two-phase flows. *Progress in energy and combustion science*, 32(3): 315–371, 2006.

R. M. Pereira, L. Moriconi, and L. Chevillard. A multifractal model for the velocity gradient dynamics in turbulent flows. *Journal of Fluid Mechanics*, 839:430–467, 2018.

W. Petersen. A general implicit splitting for stabilizing numerical simulations of itô stochastic differential equations. *SIAM journal on numerical analysis*, 35(4):1439–1451, 1998.

R. T. Pierrehumbert and H. Yang. Global chaotic mixing on isentropic surfaces. *Journal of Atmospheric Sciences*, 50(15):2462–2480, 1993.

M. J. Piggott. *Stochastic algorithms in Riemannian manifolds and adaptive networks*. PhD thesis, Ph. D. dissertation, Univ. of New South Wales, Sydney, NSW, Australia, 2016.

M. J. Piggott and V. Solo. Geometric euler–maruyama schemes for stochastic differential equations in so (n) and se (n). *SIAM Journal on Numerical Analysis*, 54(4):2490–2516, 2016.

M. Pinsky and A. Khain. Some effects of cloud turbulence on water–ice and ice–ice collisions. *Atmospheric research*, 47:69–86, 1998.

E. L. C. V. M. Plan and D. Vincenzi. Tumbling of a brownian particle in an extensional flow. *Proc. Royal Soc. Lond. A*, 472(2194):20160226, 2016.

E. Platen. On weak implicit and predictor-corrector methods. *Mathematics and computers in simulation*, 38(1-3):69–76, 1995.

J. I. Polanco. *Lagrangian properties of turbulent channel flow: a numerical study*. Theses, Université Claude Bernard Lyon 1 ; Université de Lyon, Mar. 2019.

S. Pope. On the relationship between stochastic lagrangian models of turbulence and second-moment closures. *Physics of Fluids*, 6(2):973–985, 1994.

S. Pope. Particle method for turbulent flows: Integration of stochastic model equations. *Journal of Computational Physics*, 117(2):332–349, 1995.

S. B. Pope. *Turbulent Flows*. Cambridge University Press, 2001.

W. H. Press, W. T. Vetterling, S. A. Teukolsky, and B. P. Flannery. *Numerical recipes in C*, volume 818. Cambridge university press Cambridge, 1986.

I. Procaccia, V. S. L'vov, and R. Benzi. Colloquium: Theory of drag reduction by polymers in wall-bounded turbulence. *Reviews of Modern Physics*, 80(1):225, 2008.

A. Pumir. Turbulence in homogeneous shear flows. *Phys. Fluids*, 8(11):3112–3127, 1996.

A. Pumir. Structure of the velocity gradient tensor in turbulent shear flows. *Physical Review Fluids*, 2(7):074602, 2017.

A. Pumir and M. Wilkinson. Orientation statistics of small particles in turbulence. *New journal of physics*, 13(9):093030, 2011.

G. Quispel and D. I. McLaren. A new class of energy-preserving numerical integration methods. *Journal of Physics A: Mathematical and Theoretical*, 41(4):045206, 2008.

N. M. Qureshi, M. Bourgoin, C. Baudet, A. Cartellier, and Y. Gagne. Turbulent transport of material particles: an experimental study of finite size effects. *Physical review letters*, 99(18): 184502, 2007.

G. O. Roberts and R. L. Tweedie. Exponential convergence of langevin distributions and their discrete approximations. *Bernoulli*, pages 341–363, 1996.

R. Rogallo. Numerical experiments in homogeneous turbulence. Technical Report TM-81315, NASA Ames Research Center, California, 1981.

M. M. Rogers and P. Moin. The structure of the vorticity field in homogeneous turbulent flows. *J. Fluid Mech.*, 176:33–66, 1987.

A. Rößler. Second order runge–kutta methods for itô stochastic differential equations. *SIAM Journal on Numerical Analysis*, 47(3):1713–1738, 2009.

C. Rucker. Integrating rotations using nonunit quaternions. *IEEE Robotics and Automation Letters*, 3(4):2979–2986, 2018.

L. Sabban, A. Cohen, and R. van Hout. Temporally resolved measurements of heavy, rigid fibre translation and rotation in nearly homogeneous isotropic turbulence. *Journal of Fluid Mechanics*, 814:42–68, 2017.

Y. Saito and T. Mitsui. Stability analysis of numerical schemes for stochastic differential equations. *SIAM Journal on Numerical Analysis*, 33(6):2254–2267, 1996.

M. Samie, I. Marusic, N. Hutchins, M. Fu, Y. Fan, M. Hultmark, and A. Smits. Fully resolved measurements of turbulent boundary layer flows up to $Re_\tau = 20,000$. *Journal of Fluid Mechanics*, 851:391–415, 2018.

B. Sawford. Turbulent relative dispersion. *Annual review of fluid mechanics*, 33(1):289–317, 2001.

I. F. Sbalzarini, A. Hayer, A. Helenius, and P. Koumoutsakos. Simulations of (an) isotropic diffusion on curved biological surfaces. *Biophysical journal*, 90(3):878–885, 2006.

A. Shalchi. Applicability of the taylor-green-kubo formula in particle diffusion theory. *Physical Review E*, 83(4):046402, 2011.

M. Shapiro and M. Goldenberg. Deposition of glass fiber particles from turbulent air flow in a pipe. *Journal of aerosol science*, 24(1):65–87, 1993.

T. Shardlow. Splitting for dissipative particle dynamics. *SIAM Journal on Scientific computing*, 24 (4):1267–1282, 2003.

Q. Sheng. Solving linear partial differential equations by exponential splitting. *IMA Journal of numerical analysis*, 9(2):199–212, 1989.

M. Shin and D. L. Koch. Rotational and translational dispersion of fibres in isotropic turbulent flows. *Journal of Fluid Mechanics*, 540:143–173, 2005.

I. Snook. *The Langevin and generalised Langevin approach to the dynamics of atomic, polymeric and colloidal systems*. Elsevier, 2006.

J. Sola. Quaternion kinematics for the error-state kalman filter. *arXiv preprint arXiv:1711.02508*, 2017.

A. Soldati and C. Marchioli. Physics and modelling of turbulent particle deposition and entrainment: Review of a systematic study. *International Journal of Multiphase Flow*, 35(9): 827–839, 2009.

O. Stein, G. Olenik, A. Kronenburg, F. C. Marincola, B. Franchetti, A. Kempf, M. Ghiani, M. Vascellari, and C. Hasse. Towards comprehensive coal combustion modelling for les. *Flow, turbulence and combustion*, 90(4):859–884, 2013.

N. Stelzenmuller, J. I. Polanco, L. Vignal, I. Vinkovic, and N. Mordant. Lagrangian acceleration statistics in a turbulent channel flow. *Physical Review Fluids*, 2(5):054602, 2017.

D. E. Stock. Particle dispersion in flowing gases–1994 freeman scholar lecture. *Journal of fluids engineering*, 118(1), 1996.

G. Strang. On the construction and comparison of difference schemes. *SIAM journal on numerical analysis*, 5(3):506–517, 1968.

A. J. Szeri and L. G. Leal. Microstructure suspended in three-dimensional flows. *Journal of Fluid Mechanics*, 250:143–167, 1993.

P. Tabeling. Two-dimensional turbulence: a physicist approach. *Physics reports*, 362(1):1–62, 2002.

G. I. Taylor. Diffusion by continuous movements. *Proceedings of the london mathematical society*, 2 (1):196–212, 1922.

S. Tenneti and S. Subramaniam. Particle-resolved direct numerical simulation for gas-solid flow model development. *Annual review of fluid mechanics*, 46:199–230, 2014.

L. Tian, G. Ahmadi, Z. Wang, and P. K. Hopke. Transport and deposition of ellipsoidal fibers in low reynolds number flows. *Journal of Aerosol Science*, 45:1–18, 2012.

T. Tian and K. Burrage. Two-stage stochastic runge-kutta methods for stochastic differential equations. *BIT Numerical Mathematics*, 42(3):625–643, 2002.

H. F. Trotter. On the product of semi-groups of operators. *Proceedings of the American Mathematical Society*, 10(4):545–551, 1959.

I. Tubikanec, M. Tamborrino, P. Lansky, and E. Buckwar. Qualitative properties of numerical methods for the inhomogeneous geometric brownian motion. *arXiv preprint arXiv:2003.10193*, 2020.

K. Turitsyn. Polymer dynamics in chaotic flows with a strong shear component. *Journal of Experimental and Theoretical Physics*, 105(3):655–664, 2007.

M. Van Den Berg and J. Lewis. Brownian motion on a hypersurface. *Bulletin of the London Mathematical Society*, 17(2):144–150, 1985.

T. J. van Terwisga, M. van Rijsbergen, E. van Wijngaarden, J. Bosschers, S. Schenke, and T. Melissaris. Chapter 3 - cavitation nuisance in ship propulsion: A review of developments. In P. Koukouvinis and M. Gavaises, editors, *Cavitation and Bubble Dynamics*, pages 73–109. Academic Press, 2021. ISBN 978-0-12-823388-7. doi: https://doi.org/10.1016/B978-0-12-823388-7.00011-4.

K. Vercruysse, R. C. Grabowski, and R. Rickson. Suspended sediment transport dynamics in rivers: Multi-scale drivers of temporal variation. *Earth-Science Reviews*, 166:38–52, 2017.

D. Vincenzi. Orientation of non-spherical particles in an axisymmetric random flow. *Journal of Fluid Mechanics*, 719:465–487, 2013.

D. Vincenzi, S. Jin, E. Bodenschatz, and L. R. Collins. Stretching of polymers in isotropic turbulence: a statistical closure. *Physical review letters*, 98(2):024503, 2007.

G. A. Voth. Disks aligned in a turbulent channel. *Journal of Fluid Mechanics*, 772:1–4, 2015.

G. A. Voth and A. Soldati. Anisotropic particles in turbulence. *Annu. Rev. Fluid Mech.*, 49: 249–276, 2017.

J. M. Wallace. Twenty years of experimental and direct numerical simulation access to the velocity gradient tensor: What have we learned about turbulence? *Physics of Fluids*, 21(2): 021301, 2009.

O. Walton and R. Braun. Simulation of rotary-drum and repose tests for frictional spheres and rigid sphere clusters. Technical report, Lawrence Livermore National Lab., CA (United States), 1993.

P. Wang and Z. Liu. Split-step backward balanced milstein methods for stiff stochastic systems. *Applied Numerical Mathematics*, 59(6):1198–1213, 2009.

D. Waugh, R. Plumb, R. Atkinson, M. Schoeberl, L. Lait, P. Newman, M. Loewenstein, D. Toohey, L. Avallone, C. Webster, et al. Transport out of the lower stratospheric arctic vortex by rossby wave breaking. *Journal of Geophysical Research: Atmospheres*, 99(D1):1071–1088, 1994.

N. Wax. *Selected papers on noise and stochastic processes*. Courier Dover Publications, 1954.

E. Weinan, B. Engquist, and Z. Huang. Heterogeneous multiscale method: a general methodology for multiscale modeling. *Physical Review B*, 67(9):092101, 2003.

D. C. Wilcox et al. *Turbulence modeling for CFD*, volume 2. DCW industries La Canada, CA, 1998.

M. Wilkinson and B. Mehlig. Path coalescence transition and its applications. *Physical Review E*, 68(4):040101, 2003.

M. Wilkinson and B. Mehlig. Caustics in turbulent aerosols. *EPL (Europhysics Letters)*, 71(2):186, 2005.

M. Wilkinson, V. Bezuglyy, and B. Mehlig. Fingerprints of random flows? *Physics of Fluids*, 21 (4):043304, 2009.

M. Wilkinson, V. Bezuglyy, and B. Mehlig. Emergent order in rheoscopic swirls. *Journal of fluid mechanics*, 667:158–187, 2011.

H. Xia, M. Shats, and G. Falkovich. Spectrally condensed turbulence in thin layers. *Physics of Fluids*, 21(12):125101, 2009.

H. Xu, A. Pumir, G. Falkovich, E. Bodenschatz, M. Shats, H. Xia, N. Francois, and G. Boffetta. Flight–crash events in turbulence. *Proceedings of the National Academy of Sciences*, 111(21): 7558–7563, 2014.

H. Xu, A. Pumir, and E. Bodenschatz. Lagrangian view of time irreversibility of fluid turbulence. *Science China Physics, Mechanics & Astronomy*, 59(1):1–9, 2016.

K. Yang, L. Zhao, and H. I. Andersson. Particle segregation in turbulent couette–poiseuille flow with vanishing wall shear. *International Journal of Multiphase Flow*, 98:45–55, 2018.

S. Yashiro, H. Sasaki, and Y. Sakaida. Particle simulation for predicting fiber motion in injection molding of short-fiber-reinforced composites. *Composites Part A: Applied Science and Manufacturing*, 43(10):1754–1764, 2012.

A. Yoshizawa, S. I. Itoh, and K. Itoh. Plasma and fluid turbulence: Theory and modelling, 2003.

H. Zhang, G. Ahmadi, F.-G. Fan, and J. B. McLaughlin. Ellipsoidal particles transport and deposition in turbulent channel flows. *International Journal of Multiphase Flow*, 27(6):971–1009, 2001.

F. Zhao and B. Van Wachem. Direct numerical simulation of ellipsoidal particles in turbulent channel flow. *Acta Mechanica*, 224(10):2331–2358, 2013a.

F. Zhao and B. Van Wachem. A novel quaternion integration approach for describing the behaviour of non-spherical particles. *Acta Mechanica*, 224(12):3091–3109, 2013b.

L. Zhao and H. I. Andersson. Why spheroids orient preferentially in near-wall turbulence. *Journal of Fluid Mechanics*, 807:221–234, 2016.

L. Zhao, N. R. Challabotla, H. I. Andersson, and E. A. Variano. Rotation of nonspherical particles in turbulent channel flow. *Physical review letters*, 115(24):244501, 2015.

L. Zhao, N. R. Challabotla, H. I. Andersson, and E. A. Variano. Mapping spheroid rotation modes in turbulent channel flow: effects of shear, turbulence and particle inertia. *Journal of Fluid Mechanics*, 876:19–54, 2019.

W. Zhou, L. Zhang, J. Hong, and S. Song. Projection methods for stochastic differential equations with conserved quantities. *BIT Numerical Mathematics*, 56(4):1497–1518, 2016.